Towards Chemical Control of Photoisomerization: Substituent Effects on the Excited-state Dynamics of Conjugated Polyenes

Submitted by
Ryan J. MacDonell

In partial fulfillment of the requirements
for the Doctorate of Philosophy degree in Chemistry

Department of Chemistry and Biomolecular Sciences
Faculty of Science
University of Ottawa

Abstract

The photochemical isomerization of alkenes is an important aspect of many light-sensitive processes in chemistry and biology. It involves the internal conversion from an excited electronic state of a molecule to its ground state via geometries which twist about a carbon-carbon bond. In nature, the electronic environment around the molecule influences photoisomerization to occur at specific locations in conjugated polyenes, *i.e.* molecules with multiple adjacent carbon-carbon double bonds. Without the environmental influences, polyenes may undergo isomerization at many competing sites. A potential alternative approach to influencing photoisomerization is the use of functional group substituents. A substituent may lead to significant changes in the electronic excitation energies and the nuclear dynamics at or near the substituted site. For alkenes, substituents can be used to influence the electron density by favouring or inhibiting charge at specific positions in a molecule.

The mechanism of photoisomerization is exemplified by the smallest alkene, ethylene. After photoexcitation to the lowest absorption band, carbon-carbon bond torsion is followed by a pyramidalization at one carbon atom to reach a conical intersection (*i.e.* a point of degeneracy between two electronic states) with a concurrent "sudden polarization" across the carbon-carbon bond, such that there is a lone pair at the pyramidalized site. Conjugated polyenes have excited-state decay pathways similar to that of ethylene. They also have "kinked-diene" pathways, which involve conical intersection regions with no significant polarization. These pathways are barrierless and lead to competing relaxation processes during a photochemical reaction.

Being able to predict isomerization sites and design photochemical reactions is desirable for many applications in light-driven chemical properties and chemical synthesis. We show that the principles of chemical substitution to favour or inhibit electron density (and thus pyramidalization) at specific sites can be applied to excited-state processes of cyano-substituted ethylenes through *ab initio* molecular dynamics simulations, verified experimentally by ultrafast spectroscopy techniques. The effect of these electronic substituents is consistent for a range of substituted ethyenes, and the form of the excited-state potential can be qualitatively predicted by modification of a biradical model of ethylene.

The ability to significantly alter the branching ratios of photochemical reactions is the most unambiguous demonstration of substituent effects in excited-state processes. We simulate the excited-state dynamics of 1,3-butadiene and its cyano-substituted analogs to show how the conical intersection energies are predictably lowered and raised for pyramidalization at the subsituted and adjacent sites, respectively. Dynamics simulations reveal a more important change in the potential energies: the gradients of the exicted-state surface direct nuclear rearrangement towards the favoured ethylenic conical intersection region, despite

the fact that the kinked-diene conical intersections are lower in energy. We use methyl-substituted butadienes to show how this change in gradients compares to the change in the masses and thus the frequencies of motion relevant to dynamics. Dynamical simulation of mass-weighted butadienes reveal that, despite having a minor effect on potential energies, the difference in excited-state gradients caused by the electronic effect of methyl groups plays an important role in the decay pathway.

Analysis of the rearrangement of charge caused by substitution and by nuclear dynamics towards a conical intersection require methods which show differences in electron density of electronic excited states. We show how partial atomic charge methods, particularly real-space methods, can be used to characterize the complex evolution of excited-state electronic character. As an example, we show that the polarization effect is consistent for alkenes ranging from ethylene to 1,3,5-hexatriene with and without cyano and amino substituents. These results give a consistent picture of how substituents may be employed to achieve site-specificity in photochemical isomerization, and to tailor photochemical properties of conjugated polyenes with potential applications in light-harvesting, molecular motors and chemical synthesis.

Résumé

L'isomérisation photochimique des alcènes est un aspect important de plusieurs processus photosensibles en chimie et en biologie. Cela implique la conversion interne d'un état excité électronique d'une molécule à son état fondamental par des geométries qui tournent autour d'un liaison carbone-carbone. En nature, l'environnement électronique autour de la molécule cause la photoisomérisation de se produire à des endroits précis en polyènes conjugés, *i.e.* des molécules avec plusieurs liaisons doubles carbone-carbone adjacentes. Sans les influences de l'environnement, les polyènes peuvent réaliser l'isomérisation à plusieurs sites concurrents. Une approche alternative potentillle pour influencer la photoisomérisation est l'usage des substituants de groupes fonctionnels. Un substituant peut engendrer des changes signicatifs en énergies d'excitation électroniques et en dynamique nucléaire à ou proche du site substitué. Pour les alcènes, les substituants peuvent être utilisés pour influencer la densité électronique en favorisant ou en inhibant la charge à des positions spécifiques dans une molécule.

Le méchanisme de la photoisomérisation est illustré par l'alcène le plus pétit, l'éthylène. Après la photoexcitation à la bande d'absorption le plus bas, la torsion de la liaison carbone-carbone est suivi par une pyramidalisation à un atome de carbone pour acceder à une intersection conique (*i.e.* un point de dégénérescence entre deux états électroniques) avec une « polarisation soudaine » concomitante à travers la liaison carbone-carbone, telle qu'il existe un doublet libre au site pyramidalisé. Les polyènes conjugés ont des voies de décomposition similaires à celui d'éthylène. Ils ont ausse des voies « dienes-pliés », qui compte des intersections coniques avec des régions sans polarisation significative. Ces voies n'ont pas de barrières énergiques, et entraînent des processes de rélaxation compétitifs lors d'une réaction photochimique.

La capacité de prédire les sites d'isomérisation et de concevoir des réactions photochimiques est souhaitable pour beaucoup des applications en propriétés régies par la lumière et en synthèse chimique. Nous affichons que les principles de substitution chimiques pour favoriser ou inhiber la densité électronique (et ainsi la pyramidalisation) à des sites spécifiques peuvent être appliqués aux processus des états exités des éthylènes cyano-substitués en utilisant des simulations *ab initio* de la dynamique moléculaire, verifiées par des experiments de la spectroscopie ultrarapide. L'effet de ces substituants électroniques est uniforme pour une variété des éthylènes substitués, et la forme du potential de l'état excité peut être prévu qualitativement en modifiant un modèle biradical d'éthylène.

Le potentiel de modifier les rapports d'embranchement des réactions photochimiques substantiellement est la démonstration la plus claire des effets des substituants en processes des états exités. Nous simulons la dynamique des états excités de buta-1,3-diène et ces

analogues substitués pour montrer comment les énergies des intersections coniques sont réduits et élevés pour la pyramidalisation aux sites substitués et adjacents respectivement. La simulation dynamique dévoile un changement plus important dans les éenergies potentiels: les pentes de la surface de l'état excité dirige le réaménagement nucléaire vers la région de l'intersection conique éthylènique favorisée, malgré le fait que les intersections coniques diènes-pliés sont plus bas en énergie. Nous utilisons les butadiènes méthyl-substitués pour démontrer comment ce changement en pentes compare au changement en masses et donc en fréquences de motion pertinents aux dynamiques. La simulation dynamique des butadiènes alourdis révéle que, malgré les effets mineurs en énergies potentiels, la différence en pentes des états excités causée par l'effet électronique des groupes méthyles joue une rôle important dans sa voie de décomposition.

L'analyse de la réaménagement de charge causée par la substitution et par la dynamique nucléaire vers une intersection conique nécissite des méthodes qui montrent les différences en densité électronique pour les états excités. Nous illustrons comment les méthodes des charge partielles atomiques, en particulier les méthodes en espace réel, peuvent êtres utilisées pour charactériser l'évolution complexe du charactère des états excités électroniques. À titre d'exemple, nous montrons que l'effet de polarisation est uniforme pour les alcènes allant d'éthylène à hexa-1,3,5-triène avec et sans substituants amino et cyano. Ces résultats donne une image cohérente de comment les substituants peuvent être employés pour atteindre l'isomérisation photochimique spécifique par site, et pour adapter les propriétés photochimiques des polyènes conjugés avec des applications potentielles dans la collecte de lumière, les moteurs moléculaires et la synthèse chimique.

Acknowledgements

This thesis and the past five years of work wouldn't be possible without the support of so many people. Mostly important for the work in this thesis is my advisor. Thank you Michael for putting up with me since the summer of 2013. I still remember getting a call (on a friend's cellphone) and you describing your research in terms of molecules like balls rolling on potential energy landscapes, which at the time was something I'd never thought about. On a side note, I also remember you asking if I was "finding it too easy" during my toughest semester of my undergrad. Considering the fact that I dropped the summer position that I had accepted the day before, you certainly got my attention! You gave me the freedom to try (and often fail) many different projects, but in the end I think we told some nice stories. I couldn't have asked for a better student-supervisor dynamic.

While I'm on the topic of supervisors, thank you Albert for serving as my supervisor (on paper) in my first year. You have provided me with so much advice over the years, and your perspective of spectroscopy, ultrafast dynamics and science in general has been invaluable. I always appreciated your open-door policy and your willingness to discuss all topics in depth, science or otherwise. In a similar vein, thank you to Bob Burk for all of the guidance during my undergraduate degree and helping me get to graduate school. Your love of teaching chemistry was an enormous inspiration to me. To my past supervisors: Kenny, Randall and Ewa, thank you for helping me find my way and teaching me research skills that I use to this day.

Thank you to all of my group mates. Simon, I have really appreciated being able to talk over my ideas with you throughout my degree. I am always amazed by how quickly you understand theoretical concepts and by your careful and meticulous approach to research. I hope that even a bit of it has rubbed off on me. Issaka, thanks for being the local DFT and transition metal expert! Your unique perspective has been so helpful over the past couple years, and I'm happy that you're always willing to let me bounce ideas off of you (even if you don't like all the "fuzzy concepts"). Coates, keep being you. I have zero regrets for suggesting that you look into the NRC position, and your hard-working spirit is something that I aspire to. I have no doubt that you will go far wherever you end up. Katherine, thank you for helping me out in the past year. Working with you has really helped me to solidify my understanding of our research, and I am sure that you will do well in whatever field you choose. And the other summer and co-op students: Liam, Ashley, Joscelyn and Adam, thank you for offering your own perspectives and for putting up with my late-PhD moods.

A huge thanks to all of my co-workers and collaborators at NRC and abroad (most of whom were once at NRC). There are too many names for me to list here without worrying

about leaving out someone. I will mention a couple though: thank you so much to Anja and Andrey. I really valued all of the discussions we had at work, and it was great to spend time with you outside of work as well. We collectively came up with more projects than any of us have time for, but that's a great excuse to keep in touch. Much of this thesis would not have been possible without feedback from you two.

Thank you to all of my friends from uOttawa and Carleton chemistry. I may not have always understood what you do, but I appreciated the fact that you were willing to spend the time with an "outsider" from NRC. Working in student government positions was made a lot smoother with relaxed atmosphere of the C(B)GSA at uOttawa. A special thanks to Frank, Shady Tom, Tom with the guns, Terry, and Nate for spending so much time with me and tolerating my sobriety. The world of chemistry is small enough that I expect to see you all soon.

To all of my uOttawa XC/track teammates over the past 4.5 years: thank you for being my family away from home. I never could have predicted that running would become such an important aspect of my life during grad school, but a big part of it was from spending so much time with people who aren't afraid to grind in practices and in races. There are again too many names, but two important people come to mind: Thank you Ray for giving me the opportunity to run with your group in the first place, and for being my coach through it all. Your patience and your positive attitude made a huge difference in my appreciation for the sport, qualities that I think would be difficult for any coach to live up to. And to my training partner/assistant coach/former roommate/best friend Tom, thank you for being all of those things. I look forward to seeing you more in your future travels, and to hopefully running with you too.

Last of all, and certainly the most important for getting me here in the first place, is my family. Thank you for being supportive of my research career so far, even if some aspects aren't always easy to explain (no, I still don't work on quarks, gluons or string theory). Mom and Dad, thank you for being my heroes for all of my life. I feel like I am still learning more from you and about you to this day. I'm sorry that I didn't become an engineer but I think you've come around to the idea of having a scientist as a son (I'm kidding, of course!). When I came home in third grade and said I wanted to be a "tchemist" (IPA: /tʃɛmɪst/, or "ch" pronounced as in "cheese"), I don't think you expected me to follow through, but your support has kept me going for 18 years now. Brendan, thank you for being an amazingly talented and hard-working older brother and a role model to this day. As it turns out, you were right when you said I should learn to program, so thanks for giving me the push in the right direction.

Contents

Appendix:

List of Schemes

List of Figures

List of Tables

Chapter 1
Introduction

1.1 Unimolecular photochemistry

1.1.1 Non-radiative processes

Photochemistry involves the use of the energy of light in chemical reactions. A reaction is typically deemed "photochemical" if it involves an electronic excitation, which corresponds to visible, UV or near-infrared light in organic photochemistry, whereas excitations with longer wavelengths (*i.e.* infrared and microwave) are considered "thermal". Following photoexcitation, a molecule will have a high potential energy relative to the ground electronic state, which can be converted to other forms of energy by two types excited-state decay: radiative and non-radiative. Radiative decay (fluorescence and phosphorescence for spin-allowed and spin-forbidden transitions, respectively) involves the emission of a photon with an energy equal to the energy gap between initial and final states. The coupling between the energetically-separated ground and excited states typically results in excited-state lifetimes on the order of nanoseconds to milliseconds (ns–ms) or longer. Conversely, nonradiative decay (internal conversion and intersystem crossing for spin-allowed and spin-forbidden transitions, respectively) involves the conversion of electronic potential energy to vibrational kinetic energy to access the ground state. The timescale of internal conversion depends on the coupling of ground and excited states as well as the relevant molecular vibrational frequencies, which have periods on the order of femtoseconds to picoseconds (fs–ps, known as "ultrafast" timescales) for most organic molecules.[1,2] Thus, in cases where ultrafast internal conversion is possible, it takes place preferentially relative to fluorescence. Other than excited-state to ground-state transitions, the density of electronic states is generally sufficiently high that radiative transitions only take place from the first excited state. This preference for internal conversion between excited states is formally known as Kasha's rule.[1]

On the ground state, reactions are described by transition state theory (TST), whereby rates of reactions and product distributions are accurately predicted using only the energies of reactants, products and "transition states", *i.e.* the minimum energy barriers between reactants and products.[3–6] A chemical reaction can be thought of as occuring within the phase space (a coordinate system of nuclear positions and momenta) of a molecule or group of molecules, where the evolution of phase-space variables is determined by the underlying potential energy surface (PES), *i.e.* a surface of potential energies expressed in terms of all atomic motions in a molecule. In the absence of external thermal energy, the system interconverts potential and kinetic energy much like a classical trajectory on a surface. The success of TST is due to the nature of thermal chemistry: an increase in the thermal energy (vibrational kinetic energy via molecular collisions) leads to a complete sampling of the phase space of a system over a period much greater than that of molecular vibrations

(*e.g.* milliseconds to minutes). The molecules can thus proceed to any region that is energetically accessible at that thermal energy. TST also readily explains the effects of adding substituents, catalysts and co-reagents by raising or lowering the relative energies of reactants, products and transition states. It can be used for certain excited-state reactions where there is an excited-state minimum in the vicinity of the ground state minimum and significant potential energy barriers on the excited state.[6]

Many molecules have steep potential energy gradients on their excited states which, in the absence of greater energy barriers, will direct the excited molecule to internal conversion. This leads to a breakdown of the phase space sampling assumed by TST, because the excited molecule does not spend sufficient time in a single potential energy region. Instead, gradient-directed internal conversion lends itself well to a trajectory-based picture of a quantum mechanical wavepacket.[2,7,8] Evolution on the PES corresponds to the atoms within a molecule displacing to reduce the potential energy, with forces corresponding to the gradients of the PES. Internal conversion thus takes place in regions of the PES where two electronic states are strongly coupled, particularly where the potential energy surfaces of two states are degenerate, known as "conical intersections".[9–11] The conical intersection picture of internal conversion can be used as a partial analogy to TST due to the presence of a phase-space bottleneck through which the excited wavepacket passes. In this picture, a transition state is analogous to a minimum energy conical intersection (MECI), *i.e.* the minimum-energy degeneracy between states.[7,8,12,13] Figure 1.1 shows an example of ground-state and excited-state potential energy surfaces. In this example, and in subsequent sections, MECIs are marked with the symbol ⧖ analogous to the ‡ symbol used for transition states. A more formal definition of potential surfaces and conical intersection is given in Section 1.2. Thus, a better understanding of internal conversion can be gained by observing trends in terms of excited-state gradients and MECI geometries.

1.1.2 Photoisomerization

The photochemical isomerization of carbon-carbon double bonds is one of the best studied examples of internal conversion in organic molecules.[2,7,14,15] Ethylene (ethene), as the smallest alkene, thus serves an important role in understanding the mechanism and implications of photochemical isomerization. Excitation of ethylene with a 200 nm (6.2 eV) photon leads to promotion of an electron from the π-bonding orbital to the π^*-antibonding orbital, yielding a net single carbon-carbon bond which may freely rotate. This bond rotation is driven by repulsion between the now non-bonding p-orbital lobes at each carbon. After the bond torsion, gradients on the ethylene PES cause a single CH_2 group to pyramidalize, leading to the so-called twist-pyramidalization MECI between the $\pi\pi^*$ excited state and the ground state (shown in Figure 1.2a).[7,16] Photoexcited ethylene also has sufficient potential

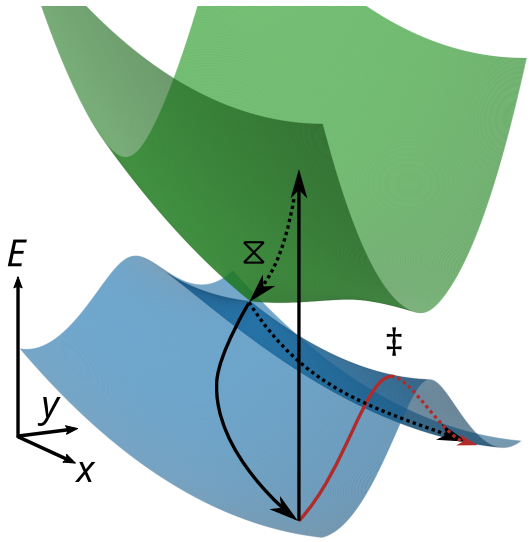

Figure 1.1: An example of a ground- (blue) and excited-state (green) potential energy surfaces with a transition state (‡) and a conical intersection (⧖). Coordinates x and y represent atomic displacements of the molecule. Pathways of thermal and photochemical reactions are shown by red and black arrows, respectively.

energy to overcome the barrier to hydrogen atom migration, leading to the ethylidene MECI region. Branching ratios of decay to the ground state between twist-pyramidalization and ethylidene geometries vary with the excitation energy, but twist-pyramidalization is the dominant pathway at lower photon energies.[17–19]

Concurrent with the change in geometry during twist-pyramidalization is a change in the electronic character of ethylene. As pyramidalization takes place at either carbon atom, the symmetry between atoms is broken as is the π and π^* orbital degeneracy. The electronic character changes from an open-shell configuration ($\pi\pi^*$) at the initially excited geometry to a doubly occupied orbital with a lobe at the pyramidalized carbon atom. This leads to the loss of electron density from the planar carbon site and an increase in density at the pyramidalized site. The shift in electron density is characterized by a dipole across the molecule, an effect known as the "sudden polarization" of ethylene.[14,16,20–22] Although the reaction products of larger dienes point towards a polarized intermediate,[23–25] the transient nature of the polarized conical intersection region make it difficult to observe experimentally.[14,26]

The twist-pyramidalization mechanism is not limited to ethylene. It plays a role in many photochemical isomerization processes where rotation of a C=C bond is otherwise uninhibited. Photochemical isomerization has been used in the design of molecular-scale devices such as photoswitches and molecular motors.[27–29] It is used in light-harvesting materials to convert photon energy into vibrational kinetic energy,[27,30] such as the isomerization of stilbene and azobenzene moieties about a central bond.[15] The nature of substituents on

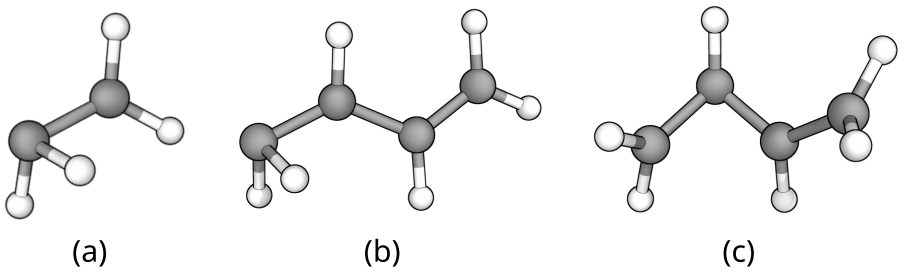

Figure 1.2: Twist-pyramidalized MECIs of (a) ethylene and (b) 1,3-butadiene as well as (c) the transoid (kinked-diene) MECI of 1,3-butadiene.

the C=C bond influences the excitation energy and relaxation properties. In the example of molecular motors, subsequent photochemical and thermal relaxation leads to a net 360° rotation. This principle has been used to achieve controlled motion on surfaces as well as asymmetric catalysis.[27,28,30,31]

In polyenes, *i.e.* molecules with multiple C=C bonds, photoisomerization is governed by the electronic character of the excited state. Conjugated polyenes have low-lying $(\pi^*)^2$ and $\pi\pi^*$ states that are delocalized across the full π-orbital system. The $\pi\pi^*$ state is optically "bright", meaning it has a large oscillator strength with the ground state, whereas the doubly-excited state is typically "dark". Photoexcitation thus primarily leads to population of the $\pi\pi^*$ state, and the coupling between the bright and dark states proceeds via carbon-carbon bond alternation across the molecule.[32–35] The subsequent dynamics of the excited polyene depend on its size and polarity. In larger, nonpolar polyenes the $(\pi^*)^2$ state is low in energy and typically has a potential energy minimum at which the molecular wavepacket is trapped, requiring fluorescense to reach the ground state. Smaller polyenes and polar polyenes are exemplified by the dynamics of 1,3-butadiene.[36,37] There exist conical intersection regions connecting both the $\pi\pi^*$ and $(\pi^*)^2$ states to the ground state. The $\pi\pi^*$ MECIs closely resemble that of ethylene, with twisting at one of the C=C bonds and pyramidalization of one carbon site (Figure 1.2b). The $(\pi^*)^2$ MECIs, known as "kinked-diene" or "cisoid" and "transoid" MECIs, involve the pyramidalization at a central carbon atom and the twisting of both carbon-carbon bonds at the pyramidalized site (Figure 1.2c). The kinked-diene geometries have a complex electronic character with the highest occupied orbitals resembling a tetraradical across the four carbon atoms.[33,38,39] In butadiene, these conical intersection regions are nearly degenerate and both have significant contributions to the excited-state dynamics.[37]

1.1.3 Environmental effects

The photoisomerization of alkenes is ubiquitous in light-driven biological processes. The prototypical example is the retinal chromophore in the rhodopsin family of proteins. Retinal is one of the forms of vitamin A, and it includes a 10-atom conjugated carbon chain which binds to a lysine unit in the rhodopsin protein backbone. In humans and other mammals, retinal is enzymatically isomerized to generate 11-*cis*-retinal. Absorption of a visible-light photon leads to photochemical isomerization via a conical intersection, twisting the *cis*-bonded site to form all-*trans* retinal, which is then hydrolyzed and remade into the 11-*cis* form. This geometric change leads to a signalling cascade and is responsible for the vision process of mammals.[40,41] In other organisms, retinal may start from its all-*trans* form and photochemically isomerize about a specific C=C bond in the conjugated chain. Microbial rhodopsins are responsible for other light-driven processes such as ion pumping and locomotion.[15,40]

The local electronic environment plays an important role in the localization of isomerization to a single site. Theoretical studies have shown that the introduction of ions near ethylene[42,43] and retinal Schiff bases[44,45] cause significant changes in the relative energies of conical intersection regions. Quantum chemical simulations of retinal with atomic and amino acid counter-ions revealed that the site specificity is strongly influenced by the electrostatic interactions of the chromophore with nearby charged amino acids in the protein cavity, as opposed to steric interactions with the surrounding cavity alone.[46] Conversely, steric inhibition of isomerization plays an important role in bioluminescence. The green fluorescent protein family contains small, conjugated chromophores which readily absorb light in the visible spectrum. In the abscence of the protein, the chromophores decay nonradiatively by isomerization of a C=C bond. The protein cavity hinders this rotation, effectively trapping the molecule on the excited state and leading to fluorescence.[45,47]

Biomolecules which undergo internal conversion typically have a much higher quantum yield for specific reaction outcomes, such as isomerization. This is in sharp contrast to the outcomes of photoexcitation of polyenes or biological chromophores in the absence of the electronic environment of the protein cavity. The many C=C bonds of polyenes make up many sites at which an excited molecule may isomerize, yielding a mixture of photochemical products.[15,48,49] The site-specificity of biomolecular photochemistry is a desirable trait with applications in organic synthesis, light-harvesting and photoswitching.[15] Achieving similarly high quantum yields in a laboratory requires an understanding of how the electronic environment of a molecule can be influenced and what are its consequences for the excited-state dynamics of internal conversion.

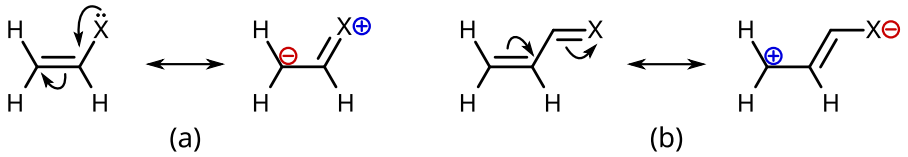

Figure 1.3: Examples of the resonance structures and expected charges of (a) π-donor and (b) π-acceptor substituents on ethylene.

1.1.4 Substituent effects

The standard approach to influencing ground- and excited-state chemistry is the use of functional group substituents. Chemical substitution plays an important role in altering the electronic potential energies and the electron density distributions of a molecule.[50–52] For the most part, substituents do not lead to large enough changes in vibrational frequencies to hinder thermal processes, and their masses are thus not important for ground-state reactions. The addition of a substituent causes changes to the PES of a molecule, the most obvious of which are steric effects from bulky substituents due to repulsion with neighbouring nuclei. On the PES, steric repulsion leads to an increase in potential energies for motions around the substituted site with the possibility of introducing barriers to specific reactions. In contrast, electronic (or potential) substituents affect the PES by electronic interactions between the substituent and the molecular backbone.[53]

Strongly electronegative functional groups act as σ-electron acceptors by withdrawing electron density from the substituted atom, where as electropositive substituents have the opposite effect. If the substituent is added to a π-bonded site, it may also have a π-acceptance or π-donation effect which is typically stronger than σ interactions. The π-electron donation or withdrawl is dictated by resonance of electrons of the substituent (*e.g.* lone pairs or π-electrons) with the π electrons in the substituted molecule.[50,53] It is characterized by an increase/decrease in electron density at the β-atoms, *i.e.* the site(s) adjacent to the substituted atom, as shown in Figure 1.3. For example, NH_2 contains a lone pair and acts as a strong π-donor, whereas CN contains a triple bond and acts as a strong π-acceptor. Alkyl groups such as methyl (CH_3) have neither lone pairs nor π-bonds, but they have a weak π-donor effect. Halogens are typically π-donors due to their lone pairs, but the σ-withdrawing effect of fluorine is stronger than its π-donor effect due to its extreme electronegativity.[52,53]

Our intuition for the effect of substituents is largely based on ground-state properties such as changes to reaction rates with selective substitution, and it provides a basis for "arrow-pushing" mechanisms of chemical synthesis. In excited-state studies, the dynamical nature of internal conversion leads to a different effect: "inertial" effects take into account the difference in mass, and thus in the vibrational frequencies, of substituents.[8,54–56] The

non-ergodic nature of ultrafast internal conversion means that a faster reaction pathway may dominate a slower one, even in cases where the slower pathway is more energetically favourable. This is most obvious with isotopic substitution of small molecules which give rise to changes in pathway and timescales proportional to the change in mass.[19,57] In other cases, substituents with weak electronic and steric effects (*e.g.* methyl groups) can be assumed to simply "weigh down" motions at the substituted site.[43,55,56] In reality, all functional group substituents lead to inertial, steric and electronic effects on internal conversion. Whereas inertial and steric effects are largely state-independent, electronic effects by their nature depend on the character of electronic states. Developing theories and predicting outcomes of substituent effects on internal conversion thus requires an understanding of electronic effects with the relatively exotic electronic characters involved in excited states.

1.2 Excited-state molecular dynamics simulation

Quantum mechanical simulations of most organic molecules and systems of molecules are governed by the non-relativistic molecular Hamiltonian,

$$\begin{aligned}\hat{H} &= \hat{T}_e + \hat{T}_N + \hat{V}_{ee} + \hat{V}_{eN} + \hat{V}_{NN} \\ &= -\frac{1}{2}\sum_i \nabla_i^2 - \sum_\alpha \frac{1}{2M_\alpha}\nabla_\alpha^2 + \sum_{ij}\frac{1}{|r_i - r_j|} - \sum_{i\alpha}\frac{Z_\alpha}{|r_i - R_\alpha|} + \sum_{\alpha\beta}\frac{Z_\alpha Z_\beta}{|R_\alpha - R_\beta|},\end{aligned} \tag{1.1}$$

given in atomic units ($\hbar = e = m_e = 4\pi\varepsilon_0 = 1$). $\hat{T}$ and $\hat{V}$ are kinetic and potential energy operators, respectively, for electronic (e) and nuclear (N) terms. The kinetic energy terms are expressed in terms of the Laplacians ∇^2 and nuclear masses M_α, whereas potential energy terms depend on electronic and nuclear positions, r and R, respectively, as well as nuclear charges Z_α. Obtaining time-independent molecular wavefunctions involves finding solutions of the time-independent Schrödinger equation (TISE), $\hat{H}\Psi(\mathbf{r},\mathbf{R}) = E\Psi(\mathbf{r},\mathbf{R})$, where E is the energy and Ψ is the corresponding wavefunction. E and Ψ are eigenvalues and eigenfunctions of $\hat{H}$, respectively. The electronic degrees of freedom can be isolated by removing the purely nuclear terms from Equation 1.1, yielding the electonic Hamiltonian:

$$\hat{H}_e = \hat{T}_e + \hat{V}_{ee} + \hat{V}_{eN}. \tag{1.2}$$

The electronic potential energy is thus the solution of $\hat{H}_e\psi_I(\mathbf{r};\mathbf{R}) = E_I^e(\mathbf{R})\psi_I(\mathbf{r};\mathbf{R})$, with electronic wavefunctions ψ_I and energies E_I^e for each electronic state I. These wavefunctions and energies are parametrically dependent on $\mathbf{R}$, making $E_I^e(\mathbf{R})$ the PES for state I. The

full wavefunction can then be expressed as

$$\Psi(\mathbf{r}, \mathbf{R}) = \sum_I \psi_I(\mathbf{r}; \mathbf{R}) \chi_I(\mathbf{R}), \tag{1.3}$$

with nuclear wavefunctions χ_I.[58] Even without including nuclear degrees of freedom, an exact solution of the electronic TISE requires an exponential number of terms which scales exponentially with the number of electrons.

Many chemical properties, including reactivities and rates of reaction, can be computed by static calculations at stationary points on the PES using TST; however, the dynamical nature of internal conversion requires an understanding of the shape of the PES. A molecular PES is expressed in terms of $3N - 6$ "internal" degrees of freedom, where six degrees of freedom correspond to the "external" translations and rotations of the molecules as a whole. Gradients on the PES depend on its electronic character, *i.e.* the form of the electronic wavefunction specific to an electronic state and set of nuclear positions. Motion of a wavepacket on the PES thus corresponds to motion towards a more stable nuclear configuration for the electronic state, much like the classical picture of a ball taking a steepest-descent path on a surface. The classical view of a wavepacket is often suitable until it reaches a region where two potential energy surfaces approach. Couplings between surfaces are found by considering the action of the nuclear gradient operator on an electronic eigenstate,

$$\hat{\Lambda}_{IJ} = \frac{1}{M} \mathbf{F}_{IJ} \cdot \nabla_{\mathbf{R}} + \frac{1}{2M} G_{IJ}, \tag{1.4}$$

$$\mathbf{F}_{IJ} = \langle \psi_I | \nabla_{\mathbf{R}} | \psi_J \rangle = \frac{\langle \psi_I | \nabla_{\mathbf{R}} \hat{H} | \psi_J \rangle}{E_I - E_J}, \tag{1.5}$$

$$G_{IJ} = \langle \psi_I | \nabla^2_{\mathbf{R}} | \psi_J \rangle = \nabla_{\mathbf{R}} \cdot \mathbf{F}_{IJ} - \mathbf{F}^2_{IJ}, \tag{1.6}$$

where M is the reduced mass, $\mathbf{F}_{IJ}$ is known as the derivative coupling and G_{IJ} is known as the scalar coupling between states I and J. The coupling is inversely dependent on the energy difference between electronic states (or its square) and is thus important in regions where two states approach each other. Otherwise, the approximation $\hat{\Lambda}_{IJ} = 0$ is appropriate for many single-state processes and is known as the Born-Oppenheimer approximation, or the adiabatic approximation. Potential energies obtained using the Born-Oppenheimer approximation are thus said to correspond to an adiabatic PES.[58]

1.2.1 Conical intersections

For molecules with more than two atoms, potential energy surfaces may reach points of degeneracy where the coupling between adiabatic potential energy surfaces is singular. These points are known as conical intersections, because it can be shown that the degeneracy can

only be linearly lifted in a two-dimensional space, defined by the directions

$$\mathbf{h}_{IJ} = \langle\psi_I|\,\nabla_{\mathbf{R}}\hat{H}\,|\psi_J\rangle = \mathbf{F}_{IJ}(E_I - E_J) \tag{1.7}$$

$$\mathbf{g}_{IJ} = \langle\psi_I|\,\nabla_{\mathbf{R}}\hat{H}\,|\psi_I\rangle - \langle\psi_J|\,\nabla_{\mathbf{R}}\hat{H}\,|\psi_J\rangle = \nabla_{\mathbf{R}}(E_I - E_J), \tag{1.8}$$

where $\mathbf{h}_{IJ}$ and $\mathbf{g}_{IJ}$ are known as nonadiabatic coupling and gradient difference vectors, respectively. Together, they make up the branching space and can be orthogonalized to obtain branching space coordinates. The degeneracy is lifted by quadratic and higher-order terms along the remaining $3N - 8$ internal degrees of freedom, which together with external degrees of freedom (translation and rotation) are known as the seam space. Conical intersections are not isolated points on the PES, but make up a seam where the degeneracy is maintained.[11] A MECI thus corresponds to a local minimum in the seam space, and can serve a role similar to transition states in the sense that it may act as a limiting nuclear geometry for transitions between states, *i.e.* a bottleneck for internal conversion processes. The excited-state gradients may also direct the molecular wavepacket to regions of the conical intersection seam far from a MECI, similar to non-kinetic reactions which take place via a region of a reaction dividing surface far from a transition state. For certain molecules such as ethylene and butadiene, the minimum energy structure of the first excited state is a MECI to which the excited molecule is directed following photoexcitation, effectively funneling the excited molecular wavepacket to the ground state.

1.2.2 Electronic structure

Much of past and present research in quantum chemistry is dedicated to finding suitable approximations for the form of $\hat{H}_e$ and ψ_I to calculate molecular properties with contemporary hardware. The fundamental approach for most quantum chemistry methods is the Hartree-Fock (HF) approximation. It uses a set of one-electron wavefunctions known as "orbitals" to find an approximate multi-electron wavefunction based on mean-field interactions of each orbital with all other orbitals.[59,60] The HF wavefunction is expressed as a single Slater determinant, which gives a sum of products of HF orbitals with the correct antisymmetry for indistinguishable fermions. The Slater determinant describes a single configuration of electrons filling orbitals starting from the lowest-energy orbital.[60,61] HF theory typically gives a reasonable description of the ground state PES of molecules near the ground-state minimum energy point, but the approximations involved can lead to large errors for geometries for nuclear geometries displaced from the minimum. The antisymmetry of the HF wavefunction correctly accounts for the zero probability of finding two electrons with the same spin at the same position in space, but fails to account for repulsion between electrons of opposite spin. The difference between exact and HF wavefunctions and energies is known

as "electron correlation". As a mean-field approach, HF neglects instantaneous interactions between electrons known as "dynamic" electron correlation. The choice of a single determinant as the wavefunction neglects "static" electron correlation where a multi-determinant description is required. Quantum chemistry methods typically aim to improve on HF results by re-expressing the wavefunction to include dynamic and static correlation.[60]

A natural extension of HF is the expansion of the electronic wavefunction in terms of multiple Slater determinants. These components are restricted to different configurations of the electrons within the full set orbitals, known as the "configuration interaction" approach. Expansion in terms of all possible configurations, known as full configuration interaction, is formally exact for a basis but is only feasible for small molecules and small basis sets because the expansion scales exponentially with the basis.[62,63] Complete active space self-consistent field (CASSCF) reduces the number of configurations to a manageable level by defining an "active space" of occupied and unoccupied orbitals in which all possible electron rearrangements are considered. The active space can be chosen in such a way that it includes only important valence orbitals for a given study, such as σ-bonding orbitals for dissociation or π-bonding orbitals for low-lying electronic transitions. When multiple electronic states are considered, state-averaged CASSCF is used to optimize the orbitals and coefficients of different electron configurations for an averaged state energy, yielding a balanced description for all states of interest. CASSCF is said to recover static correlation and can have qualitatively different surfaces and potential energies than HF.[60,64]

Increased accuracy of electronic energies and properties are achieved using dynamic correlation methods. CASSCF results can be improved by considering perturbations to the electronic Hamiltonian to include the effects of electronic excitations outside of the active space. This approach is known as complete active space second-order perturbation theory (CASPT2),[65] and it has a multi-state extension (MS-CASPT2) in which all CASPT2 states are coupled by an effective Hamiltonian.[66] Alternatively, additional configurations can be included using the CASSCF wavefunctions as a reference. Multi-reference single-excitation configuration interaction (MR-CIS) includes all single-electron excitations from the CASSCF configurations to unoccupied or partially occupied orbitals. The computational cost of MR-CIS scales significantly worse than CASSCF with basis set size, but its inclusion of dynamic correlation can lead to important improvements on potential energy gradients or barrier heights.[60,67]

Time-dependent evolution on a potential energy surface requires calculation of the forces on the nuclei, which are found from the nuclear gradients of the potential energy surfaces. Simulations with multiple electronic states also require a measure of the coupling between states. Both terms include finding the solution of the integral $\langle\psi_I|\,\nabla_{\mathbf{R}}\,|\psi_J\rangle$, where $I = J$ for gradients and $I \neq J$ for coupling terms. CASSCF and MR-CIS methods express the wavefuntion in terms of sums of electronic configuration terms with coefficients which are not

dependent on nuclear coordinates, meaning the analytical derivatives of both approaches can be derived as sums of single-configuration terms with the corresponding CASSCF-optimized orbitals.[68,69] Note that this approach only accounts for the derivative coupling term in Equation 1.4, whereas the scalar coupling is assumed to be relatively small and is thus often neglected from excited-state dynamics simulations.

1.2.3 Electron density characterization

Over the course of dynamical evolution on an excited state, the electronic character of a molecule can change significantly. For example, ethylene undergoes a change in electron configuration and orbital shape during its characteristic twist-pyramidalization. The changes undergone by a molecule in a time-dependent simulation can be better understood by measuring local changes to molecular properties. Partial atomic charges are commonly used to quantify electrostatic properties of molecules on an atomic scale.[70] A partial charge is assigned to each atom by integrating or fitting an observable value. For example, charges can be fit to dipoles and higher-order multipoles,[71,72] or to the electrostatic potential of a molecule.[73,74] These two examples use external properties on the scale of the molecule, meaning they best describe long-range electrostatic forces between molecules.

For short-range or intramolecular properties, the electron density is the observable quantity of choice for calculating atomic charges.[70] Atomic charges are not observable quantities, and thus there are many ways of partitioning electron densities into atomic components without a physically "correct" solution. Mulliken and other orbital-based schemes use the nuclear centres of atomic orbital basis functions for the atomic assignment.[75–77] These approaches suffer from differences in atomic basis sizes, and may lead to diverging charge values with increasingly diffuse basis sets. They also lack the ability to assign density that is not centred at an atomic site, such as dummy-atom and plane-wave bases.[70] Grid-based methods and real-space methods correct for this by calculating total electron densities in 3D space with no knowledge of the basis. One of the best-known examples is Bader's quantum theory of atoms in molecules (QTAIM), where atomic sites are divided by hard boundaries at local minima in the electron densities.[78] Alternatively, the Hirshfeld approach weights atomic contributions based on densities of non-interacting, spherically symmetric atoms at the nuclear sites.[79] If the atomic densities are weighted by atomic charges and iterated until self-consistent, this yields iterative Hirshfeld charges with similar charges to QTAIM.[80] Both approaches provide a coarse-grained view of the electron density which readily show localized changes in electronic character.

1.2.4 The time-dependent Schrödinger equation

The dependence of internal conversion on non-stationary initial conditions necessitates a dynamical approach to accurately predict properties such as excited-state lifetimes and branching ratios, as opposed to the kinetic models such as TST used for ground-state chemistry. Time-dependent systems in quantum mechanics are described by the time-dependent Schrödinger equation (TDSE),

$$i\frac{\partial}{\partial t}\Psi\left(\mathbf{r},\mathbf{R},t\right)=\hat{H}\Psi\left(\mathbf{r},\mathbf{R},t\right), \tag{1.9}$$

where i is the imaginary number, Ψ is the molecular wavefunction in terms of electronic coordinates $\mathbf{r}$, nuclear coordinates $\mathbf{R}$ and time t, and $\hat{H}$ is the molecular Hamiltonian given in Equation 1.1. Solving the TDSE requires the simultaneous evolution of nuclear and electronic coordinates, which is prohibitively computationally expensive for numerical simulation of molecules larger than diatomics. Fortunately, the time-dependent wavefunction can also be expressed in terms of electronic an nuclear components as in Equation 1.3. This yields time-independent potential energy surfaces $E_e^I\left(\mathbf{R}\right)$, with the nuclear TDSE given by

$$i\frac{\partial}{\partial t}\chi_I\left(\mathbf{R},t\right)=\left[\hat{T}_N+E_e^I\left(\mathbf{R}\right)\right]\chi_I\left(\mathbf{R},t\right)-\sum_J\hat{\Lambda}_{IJ}\chi_J\left(\mathbf{R},t\right), \tag{1.10}$$

where $\hat{\Lambda}_{IJ}$ is the nonadiabatic coupling term given in Equation 1.4. Simulation of the time-evolving wavefunction in this form thus requires accurate surfaces $E_e^I\left(\mathbf{R}\right)$ on which the nuclear wavefunction χ_I evolves.[58]

1.2.5 Ab initio multiple spawning

Quantum molecular dynamics calculations with a wavefunction expressed as Equation 1.3 involve the evolution of nuclear wavefunctions, $\chi_I(\mathbf{R},t)$, on a set of potential energy surfaces. For small molecules with few (1–10) degrees of freedom this can be done by pre-computing accurate potential energies, gradients and couplings on a grid to form an analytical vibronic (vibrational and electronic) Hamiltonian for numerically exact nuclear wavefunction evolution.[81,82] Larger molecules can be studied by expressing the Hamiltonian in terms of only the most important degrees of freedom, and by careful choice of the form of the nuclear basis; however, calculation of the vibronic Hamiltonian suffers from the need for a pre-calculated surface with an exponentially growing number of grid points with each degree of freedom.[82,83]

Direct dynamics methods overcome the exponential scaling with degrees of freedom by using localized nuclear basis functions. Rather than needing to pre-calculate potential energy surfaces, direct dynamics methods interrogate the potential energy surface at each

time-step and use that information to propagate the nuclear basis functions and/or the approximate surface.[84–87] Ab initio multiple spawning (AIMS) expresses the full molecular wavefunction as

$$\mathbf{\Psi}(\mathbf{r},\mathbf{R},t) = \sum_{I=1}^{N_s} \sum_{j=1}^{N_I(t)} c_j^I(t)\psi_j^I(\mathbf{r},\mathbf{R})\chi_j^I(\mathbf{R},t), \tag{1.11}$$

where I is the index over the number of electronic states N_s, and j is the index over the number of trajectories $N_I(t)$. Each trajectory involves a nuclear Gaussian basis function χ_j^I evolving on the electronic wavefunction on state I, ψ_j^I. The coefficients $c_j^I(t)$ are solutions of the TDSE at each time step found by substituting the AIMS wavefunction into Equation 1.9. When a trajectory reaches a region of strong coupling between electronic states, a trajectory basis function is spawned on the coupled state, leading to an increase in the nuclear basis size $N_I(t)$ with time. The nuclear basis functions are given by

$$\chi_j^I(\mathbf{R},t) = \exp\left(i\gamma_j^I(t)t\right) \prod_q \left(\frac{2\alpha_{j,q}^I}{\pi}\right)^{1/4} \exp\left[-\alpha_q\left(R_q - R_{j,q}^I(t)\right)^2 + iP_{j,q}^I(t)\left(R_q - R_{j,q}^I(t)\right)\right], \tag{1.12}$$

with time-dependent centroids $\mathbf{R}_j^I(t)$, momenta $\mathbf{P}_j^I(t)$, and phases $\gamma_j^I(t)$ which evolve on the PES with nuclear coordinates q using classical equations of motion, as well as frozen nuclear Gaussian widths $\boldsymbol{\alpha}$. AIMS is thus a quantum mechanical approach which uses a time-dependent, classical nuclear basis.[85,88,89] The basic steps of an AIMS simulation are illustrated in Figure 1.4.

A series of approximations are important to further reduce the computational complexity of AIMS simulations. The most common coupling parameter used to determine spawning is the magnitude of the inner product of the derivative coupling and the nuclear velocities, $|\mathbf{F}_{IJ} \cdot \mathbf{v}|$. The cutoff for spawning is arbitrary, but can be chosen to only include regions of the PES where the value of $|\mathbf{F}_{IJ} \cdot \mathbf{v}|$ is peaked and population transfer is localized; however, this approach does not account for gradual changes in population due to small coupling values.[85] To reduce the total number of coupled trajectories, all initial conditions are assumed to be uncoupled and treated as separate simulations for which observable values are averaged. This is known as the independent first-generation approximation, and is justified given the generally rapid decoherence time that originates from the large number of vibrational degrees of freedom that exist in typical organic molecules.[90,91] Finally, the potential energy terms in the Hamiltonian used to find trajectory coefficients require integration over nuclear coordinates $\mathbf{R}$, but the electronic wavefunction is only known at the centroid geometries of the trajectory basis functions. The saddle point method is used to approximate this integral by

$$\left\langle \chi_j^I \right| \left\langle \psi_j^I(\mathbf{R}) \right| \hat{H}_e \left| \psi_k^J(\mathbf{R}) \right\rangle \left| \chi_k^J \right\rangle \approx \left\langle \psi_j^I(\bar{\mathbf{R}}_{jk}) \right| \hat{H}_e \left| \psi_k^J(\bar{\mathbf{R}}_{jk}) \right\rangle \left\langle \chi_j^I \middle| \chi_k^J \right\rangle \tag{1.13}$$

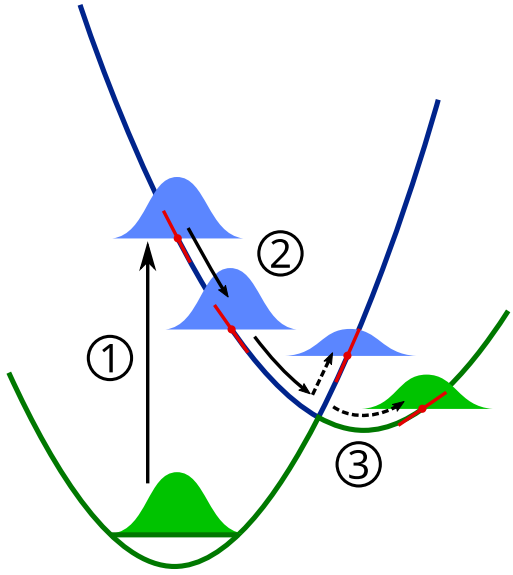

Figure 1.4: Basic scheme of an AIMS simulation: 1. A nuclear basis function is placed on an excited state with an initial geometry and momentum. 2. The electronic potential energy gradients (shown in red) are used to evolve the basis function trajectory classically. 3. When the coupling between electronic states exceeds a set threshold, a new basis function is spawned on the coupled state. Their coefficients are updated as solutions of the TDSE for the system.

Where $\bar{\mathbf{R}}_{jk}$ the average position of the nuclear basis functions j and k. Thus, the potential energy integration can be approximated with one additional calculation per pair of trajectory basis functions.[85,91]

1.3 Experimental observables of internal conversion

1.3.1 Time-resolved photoelectron spectroscopy

Theoretical simulation of microscopic systems provides valuable insight into their properties and dynamics. Experimental observations show the behaviour of real systems in a controlled setting by measuring an observable quantity. The coevolution of electronic and nuclear degrees of freedom in ultrafast photochemistry make it difficult to obtain a full understanding of the properties of internal conversion processes (*e.g.* products, timescales and mechanisms) using either theory or experiment alone. For this reason it is important to be able to compare between the two and to understand the advantages and shortcomings of both approaches. Accuracy of a simulated experiment is assessed in terms of the agreement between experimental and theoretical observations.

Studying the evolution of a molecular wavepacket on a PES involves simulating isolated molecules without intermolecular interactions, which is the same type of system as gas-phase experiments with low enough pressures to avoid molecular clusters. Conical in-

tersection mediated processes are considered ultrafast because they involve nuclear motions with timescales of femtoseconds to picoseconds. This is too fast for multiple observations of the decay process following a single excitation event. Instead, pump-probe experiments employ two laser pulses at different frequencies with a femtosecond time width: a "pump" pulse which prepares the excited state of the molecule, and a "probe" pulse which projects the excited wavepacket onto a set of final states. Changing the time delay between pump and probe gives the time from initial excitation (initiating the excited-state dynamics) to observation.[92–96]

In time-resolved photoelectron spectroscopy (TRPES), the pump and probe pulses are both in the visible to UV range. The pump excites to low-lying molecular electronic states, while the probe pulse ionizes the molecule and ejects an electron. The kinetic energy of the outgoing electron is detected as a function of the pump-probe delay to give a spectrum in time and energy. The experiment uses a supersonic gas jet to obtain vibrationally cold, isolated molecules in a molecular beam which intersects with the path of the pump and probe lasers. Only a fraction of the molecules are excited by the pump pulse, so experiments typically use probe energies that do not ionize the ground state to avoid a large ground state background spectrum. Thus, the probe prepares low-lying states of the molecular cation and the TRPES is dominated by valence contributions. Changes in electronic potential energies of the excited wavefunction lead to shifts in energy with respect to time, whereas changes in electronic character cause time-dependent changes in band intensities.[95–98] The convolution of these two effects, as well as the lack of resolution for events occuring on the same timescale as the pulse widths, make features of the spectrum difficult to assign without simulated results.[8]

1.3.2 Simulating spectra

Ideally, a comparison between experimental and theoretical results should have the same "setup", *e.g.* initial conditions and local environment. The latter is solved by comparing theoretical results to molecular beam experiments, where the molecule is assumed to be mostly in its vibrational ground state. The intial conditions thus depend only on the vibrational distribution and its excitation to higher electronic states. The ground-state vibrational distribution in ordinary AIMS simulations is approximated by a Wigner distribution of the form

$$w(\mathbf{R},\mathbf{P}) = \frac{1}{(\pi\hbar)^{3N-6}} \prod_{q}^{3N-6} \exp(-(R_q/\sigma_q^R)^2 - (P_q/\sigma_q^P)^2), \tag{1.14}$$

where $(\sigma_q^R)^2 = \hbar/(\sqrt{2}\mu_q\omega_q)$ is the normal mode position weight based on reduced mass μ_q and frequency ω_q, and $(\sigma_q^P)^2 = \hbar\mu_q\omega_q/\sqrt{2}$ is the normal mode momentum weight. Excitation by a photon can then be considered "lifting" ground-state wavefunction (given by the

Wigner distribution) by the photon energy. In practice, the Wigner distribution is sampled and the geometries and momenta are used as initial conditions.[85] In most cases, the laser bandwidth is sufficient small ($\sim$150 cm^{-1}) that only a single electronic state is prepared by the laser pulse.[98] In cases such as polyenes with spectroscopically bright and dark states, the bright state is selected by transition dipole and its energy gap to the ground state is compared to the experimental value, including an energetic shift due to errors in the calculated excitatation energy.

With matching conditions for experiment and theory, direct comparison of the two requires simulation of the same observable the experimental measurement. The TRPES signal is, as the name suggests, made up of snapshots of the photoelectron spectrum for each pump-probe delay. Thus, it can be simulated theoretically from the AIMS wavefunction by finding

$$S(E,t) = \sum_{I=1}^{N_s^0} \sum_{j=1}^{N_I(t)} |c_j^I(t)|^2 \sum_{\alpha=1}^{N_s^+} W_{I\alpha}(\mathbf{R}_j^I(t))\, \delta\left(E - \left[n\omega_2 - \Delta E_{I\alpha}(\mathbf{R}_j^I(t))\right]\right), \tag{1.15}$$

where t is the simulation time starting from the pump pulse, N_s^0 and N_s^+ are the number of states for the neutral and cationic molecule, respectively, n is the number of photons, ω_2 is the probe photon energy and $\Delta E_{I\alpha}$ is the energy difference between the trajectory state I and cation states α. The weight factor $W_{I\alpha}$ represents the photoionization cross section, and all other variables are components of the AIMS wavefunction. A complete treatment of the photoionization requires calculating the transition moments between the neutral molecule and the cation states plus the outgoing single-electron wavefunction. For simplicity, $W_{I\alpha}$ can be approximated by norm of the Dyson orbital, which is found by integrating out the overlap of neutral and cationic electronic wavefunctions over all but the ionized electron.[99] The resulting spectrum is given by delta functions $\delta(E)$ which are then convoluted with a two-dimensional Gaussian depending on the energy and time resolution of the experimental setup.

1.4 Outline

The aim of this thesis is to gain a better understanding of the role of substituent effects on nonadiabatic excited-state dynamics using theoretical simulations. Small polyenes, particularly ethylene and 1,3-butadiene, are used as model systems because they demonstrate excited-state decay pathways characteristic of larger, chemically and biologically relevant chromophores but are sufficiently small for accurate *ab initio* simulation. The work is motivated by the findings of Chapter 2 (the strong electronic effect of cyano substitution), as well as previous work on inertial and steric effects with time-resolved simulation and

spectroscopy.[8,54–56] We hope to develop a set of rules and guidelines for how excited-state dynamics can be influenced to achieve desirable properties such as site-specific isomerization, controllable decay timescales and tuneable electronic properties. If achieved, these rules could offer new possibilities for chemical synthesis, light-harvesting, molecular motors and much more.

The outline of the remaining chapters is as follows: Chapter 2 is a collaborative work which details the excited-state dynamics of acrylonitrile (cyano-ethylene) and its methylated derivatives, including our first observation of a strong electronic substituent effect on the dynamics from the cyano group. Chapter 3 demonstrates the extent of electronic substituent effects for a range of substituted ethylenes with known π-donor and π-acceptor substituents, including dynamical results for acrylonitrile and vinylamine (amino-ethylene). In Chapter 4, the use of electronic substituents on photochemical reactions is demonstrated by comparing simulations of 1,3-butadiene with cyano-substituted butadienes. The use of a π-accpetor substituent causes a change in the PES which directly affects the atomic site at which the molecule distorts. Chapter 5 is another collaboration with time-resolved spectroscopy experiments which shows the relevance of weak electronic substituents on excited-state dynamics: the branching ratios of methylated butadienes are compared to artificially mass-weighted butadienes to compare the magnitudes of inertial, steric and electronic effects. Chapter 6 gives an overview of the characterization of partial charges on excited states and their utility, including a demonstration of the similarity of electronic character for ethylene, butadiene, hexatriene, cyclohexadiene and their substituted derivatives. Finally, Chapter 7 provides the summary and conclusions of the thesis as well as future work.

Chapter 2

Excited state dynamics of acrylonitrile: Substituent effects at conical intersections interrogated via time-resolved photoelectron spectroscopy and *ab initio* simulation

R.J. MacDonell,[1] O. Schalk,[2] T. Geng,[2] R.D. Thomas,[2] R. Feifel,[3] T. Hansson,[2] and M.S. Schuurman[1,4]

Reprinted with permission from *J. Chem. Phys.* **2016**, *145*, 114306.
https://doi.org/10.1063/1.4962170.

This work represents our first observation of electronic effects directing the excited-state decay mechanism of a molecule. Note the erroneous use of the term "electron donor" instead of π-acceptor in reference to the cyano group. Other minor typos were fixed in the text. I (RJM) was responsible for characterizing potential energy surfaces, simulating excited-state dynamics, simulating the TRPES spectra and writing the body of the work. OS was responsible for performing the TRPES experiment, fitting the spectra and interpreting experimental results. TG, RDT, RF and TH helped with the experiment and provided feedback for the manuscript. MSS supervised the theoretical work and provided feedback.

[1] Department of Chemistry and Biomolecular Sciences, University of Ottawa, Ottawa, Ontario K1N 6N5, Canada
[2] Department of Physics, AlbaNova University Centre, Stockholm University, Roslagstullsbacken 21, 106 91 Stockholm, Sweden
[3]Department of Physics, University of Gothenburg, Origovägen 6B, 412 96 Gothenburg, Sweden
[4]National Research Council of Canada, 100 Sussex Drive, Ottawa, Ontario K1A 0R6, Canada

Abstract

We report a joint experimental and theoretical study on the photoinitiated ultrafast dynamics of acrylonitrile (AN) and two methylated analogs: crotonitrile (CrN) and methacrylonitrile (MeAN). Time-resolved photoelectron spectroscopy (TRPES) and *ab initio* simulation are employed to discern the conical intersection mediated vibronic dynamics leading to relaxation to the ground electronic state. Each molecule is pumped with a femtosecond pulse at 200 nm and the ensuing wavepackets are probed by means of one and two photon ionization at 267 nm. The predominant vibrational motions involved in the de-excitation process, determined by *ab initio* trajectory simulations, are an initial twisting about the C=C axis followed by pyramidalization at a carbon atom. The decay of the time-resolved photoelectron signal for each molecule is characterized by exponential decay times for the passage back to the ground state of 60 ± 17, 86 ± 23 and 97 ± 33 fs for AN, CrN and MeAN, respectively. As these results show, the excited state dynamics are sensitive to the choice of methylation site and the explanation for the observed trend may be found in the trajectory simulations. Specifically, since the pyramidalization motion leading to the conical intersection with the ground state is accompanied by the development of a partial negative charge at the central atom of the pyramidal group, the electron donation of the cyano group ensures that this occurs exclusively at the medial carbon atom. In this way, the donated electron density from the cyano group "directs" the wavepacket to a particular region of the intersection seam. The excellent agreement between the experimental and simulated TRPES spectra, the latter determined by employing trajectory simulations, demonstrates that this mechanistic picture is consistent with the spectroscopic results.

2.1 Introduction

Interest in the photochemistry of α,β-enenitriles, here exemplified by acrylonitrile (AN, 2-propenenitrile), crotonitrile (CrN, 2-butenenitrile) and methacrylonitrile (MeAN, 2-methyl-2-propenenitrile) illustrated in Figure 2.1, stems in part from their unusual photodissociation dynamics. Whereas most nitriles eliminate radical CN following UV excitation,[100–102] acrylonitrile is observed to release molecular HCN and H_2. These photodissociation dynamics were first studied by Gandini and Hackett using a 213.9 nm excitation wavelength to prepare the $\tilde{A}\,^1A'$ state. They observed the aforementioned molecular dissociation products, as well as significant hydrogen/deuterium scrambling in the HCN and H_2 products when the 2-carbon was deuterated, which they ascribed to an excited state H/D scrambling process.[103] The observations of HCN and H_2 dissociation products were consistent with more recent theoretical determinations of the expected photoproducts following 193 nm photoexcitation.[104] However, CN elimination was also observed for AN, CrN and MeAN following

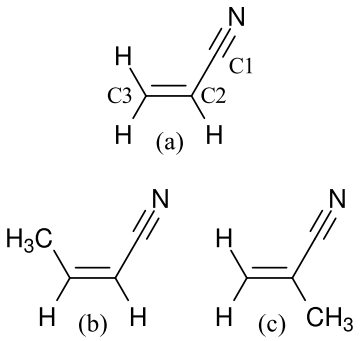

Figure 2.1: Molecular structures of (a) acrylonitrile, (b) *cis*-crotonitrile and (c) methacrylonitrile. Carbon atoms labels are consistent for all three molecules.

excitation at 193 nm.[105,106] *Ab initio* calculations show that MeAN, unlike AN and CrN, may overcome the barrier to CN and H migration before dissociation.[106]

The conjugated π system of α,β-enenitriles gives rise to several low-lying electronic states, resulting in a complex electronic structure that has been the subject of numerous spectroscopic characterization studies.[103,107–109] In the first reported absorption spectrum of acrylonitrile, the two overlapping absorption bands were observed to lie between 159 and 213 nm (5.8–7.8 eV)[107] and were assigned to $n \rightarrow \pi^*$ and $\pi \rightarrow \pi^*$ transitions.[103,107] Using electron energy loss spectroscopy and high resolution photoabsorption spectroscopy, these peaks were later reassigned to the π_2(C=C−C≡N) $\rightarrow \pi_1^*$(C=C−C≡N) transition ($\tilde{A}\,^1A'$) and the π_2(C=C−C≡N) $\rightarrow \pi^*$(C≡N) transition ($\tilde{B}\,^1A''$). An additional band in the range of 138–177 nm (7.0–9.0 eV) was assigned to the $\tilde{C}\,^1A'$ (π_2(C=C−C≡N) $\rightarrow \pi_2^*$(C=C−C≡N)) transition, while higher energy bands were attributed to a Rydberg series.[108,109] To date, high-resolution characterizaton of the electronic spectra has not been performed for crotonitrile and methacrylonitrile, but low resolution UV-Vis spectra show similar broad overlapping bands in the 200–225 nm (5.5–6.2 eV) range.[106]

The potential energy surfaces of the ground state and low lying excited states of AN have been extensively studied to characterize and enumerate the dissociative pathways associated with excitation at 193 nm. Du *et al.*[104] optimized potential energy minima, transition states and minimum energy conical intersections (MECIs) for singlet and triplet states in the Franck-Condon (FC) region. They found that minimum energy structures were not present for the first and second singlet excited states (S_1 and S_2, respectively) in the FC region. Instead, gradients on both surfaces direct the molecule to a conical intersection (CI) to the lower energy state. The S_2-S_1 MECI corresponds to the ground state equilibrium geometry with 90° torsion about the C=C bond, while the MECI between S_1 and the ground state involves both the C=C torsion as well as a C=C−C bend. Thus, after excitation to S_2 the molecule was predicted to decay through both CIs to the ground state. The molecule in the ground state would then have sufficient internal energy to dissociate.[104]

Acrylonitrile has also been studied as a model system for near edge x-ray absorption fine structure spectroscopy (NEXAFS).[110,111] The two low-lying π^* orbitals give rise to high intensity peaks corresponding to excitation into these anti-bonding orbitals from the N 1s orbital. Assignment of the vibrational structure was achieved using density functional theory (DFT) to determine the Franck-Condon transition amplitudes, providing good agreement between theoretical and experimental spectra.[110,111] A further study with a higher energy probe found a closely spaced doublet corresponding to N 1s excitation to a diffuse Rydberg type orbital and an additional $\pi^*(A'')$ orbital. Excitation to the Rydberg-type orbital led to out-of-plane motion of CCN and CH_2 groups, whereas excitation to the π^* orbital caused in-plane CCC and CCN bending.[111]

In order to more definitively address the mechanism of ultrafast relaxation in α,β-enenitriles, this study uses time-resolved photoelectron spectroscopy (TRPES) together with *ab initio* molecular dynamics simulations to discern the excited state dynamics of AN. The timescales associated with electronic de-excitation are probed directly via experiment, while the atomic motions associated with the molecular dynamics are obtained using on-the-fly *ab initio* calculations.[56,112,113] Using methyl substitution, the relative importance of different internal motions can be discerned from excited state decay timescales by experimental and theoretical means. This technique has been previously used in, for example, time-resolved studies of ethylene,[114] 1,3-cyclopentadiene[55,115] and α,β-enones.[54,116] Here, we employ a pump wavelength of 200 nm for all molecules which prepared molecules in both the first and second excited states, $\tilde{A}\,^1A'$ and $\tilde{B}\,^1A''$, and perform *ab initio* molecular dynamics simulations that are then employed to generate a theoretical TRPES signal for direct comparison to experimental results.

2.2 Methods

2.2.1 Experimental Methods

AN, MeAN and CrN were purchased from Sigma-Aldrich with stated purities of 99% and were used without further purification. CrN was delivered and used as a mixture of *cis*- and *trans*-isomers. However, within the present experimental conditions we expect the *cis*-isomer to be predominant (see below). Absorption spectra were taken in a 1 cm quartz cuvette (Hellma) at saturated vapor pressure using a Cary 5e photospectrometer (Varian). The magnetic bottle electron spectrometer setup used in the present study for time-resolved measurements was described before.[117,118] Briefly, it consists of a 5.6-m long flight tube with an energy ($E/\Delta E$) resolution of better than 100, which implies that the resolution for slow photoelectrons is limited by the spectral resolution of the laser pulses. Femtosecond laser pulses were obtained from a Ti:sapphire regenerative amplifier (Coherent Legend USP-HE)

with an output energy of 4 mJ pulse^{-1} at a repetition rate of 1 kHz. Pump and probe pulses at 200 and 267 nm were generated by frequency doubling and consecutive mixing with the fundamental laser beam in β-barium borate crystals. In the experiments, the laser beams were attenuated to 100 nJ for the 200 nm pump and 3 μJ for the 267 nm probe pulses. They were focused weakly into the interaction region by a concave spherical aluminum mirror ($f/150$ for the pump and $f/125$ for the probe pulse). The cross-correlation between pump and probe pulses was measured in xenon and was 160 ± 15 fs for a [1+1′] experiment. The spectral bandwidth of both pump and the probe pulses was around 25 meV. The time delay between the two pulses was controlled by a motorized linear translation stage. At each delay, the measured pump-probe signal was corrected by subtracting the background signals due to the pump and probe laser pulses alone. Perpendicular to the incoming laser pulses, the sample was inserted in the interaction region of the magnetic bottle spectrometer by means of an effusive gas needle using the vapor pressure of the investigated liquids. Within the present experimental conditions a *cis-trans* mixture of CrN is expected with ∼62% of the molecules in the *cis*-configuration.

2.2.2 Computational Methods

Excited state trajectory simulations were performed employing *ab initio* potential energy surfaces determined on-the-fly and propagated using the *ab initio* multiple spawning (AIMS) method.[88,89,119] Here, the wavefunction is the product of electronic and nuclear functions as expressed by

$$\mathbf{\Psi}(\mathbf{r},\mathbf{R},t) = \sum_{I=1}^{N_s} \sum_{j=1}^{N_I(t)} c_j^I(t)\psi_j^I(\mathbf{r};\mathbf{R}_j^I(t))\chi_j^I(\mathbf{R};\mathbf{R}_j^I(t),\mathbf{P}_j^I(t),\gamma_j^I(t)), \tag{2.1}$$

where $\mathbf{r}$ and $\mathbf{R}$ represent electronic and nuclear coordinates, respectively. The wavefunction expansion includes the number of states N_s relevant to the dynamics with electronic wavefunctions $\psi^I(\mathbf{r};\mathbf{R})$. The nuclear component of the trajectory basis function, χ_j^I, is expanded as a direct product of frozen Gaussian basis functions with a time-dependent position $\mathbf{R}_j^I(t)$, momentum $\mathbf{P}_j^I(t)$ and phase $\gamma_j^I(t)$, which evolve according to classical equations of motion. When trajectories enter a region with nonadiabatic coupling beyond a given threshold, they may spawn new basis functions on the coupled state. As a result, the number of basis functions on electronic state I, $N_I(t)$, is time-dependent. The complex amplitudes $c_j^I(t)$ of each trajectory are determined variationally at each time step according to the time-dependent Schrödinger equation.

The initial geometries and momenta of each molecule were sampled from the $v = 0$ vibrational Wigner distribution with the constraint that the excitation energy at a given point was within the pump pulse energy ± twice the laser bandwidth. In the FC region,

the first and second excited states (S_1 and S_2, both $\pi\pi^*$ states) were nearly degenerate and had transition dipole moments on the same order of magnitude. For each initial condition the probability of populating I is proportional to the oscillator strength scaled by the detuning from the central frequency of the pump envelope. More details can be found in the supplementary material (Appendix A). In order to correct for the theoretical and experimental energy differences between electronic states at the S_0 minimum, the S_1 energy was calculated using Davidson-corrected second-order multireference configuration interaction (MR-SOCI) with a 4s3p2d1f ANO basis set and using first-order multireference configuration interaction (MR-FOCI) with a 6-31G* basis. The difference in energies was then added to the the pump energy of 6.20 eV (200 nm) during the selection of initial conditions. These energy shifts were 0.71, 0.74 and 0.69 eV for AN, CrN and MeAN, respectively.

The trajectory simulations employed 31 (30) initial conditions for AN (MeAN), yielding a total of 559 (351) trajectories. To account for the mix of *cis* and *trans* CrN geometries, 29 initial conditions were *cis* geometry and 18 were *trans*. This gave rise to 505 and 285 trajectories, respectively.

At each time step, electronic wavefunctions necessary to propagate each basis function were calculated using the COLUMBUS electronic structure package.[120] The dynamics calculations were performed at the MR-FOCI/6-31G* level of theory.[121] The geometries of the S_0 minimum as well as S_2-S_1 and S_1-S_0 minimum energy conical intersections were optimized at this level of theory and checked with complete active space second-order perturbation theory (CASPT2) with a correlation-consistent triple zeta basis (cc-pVTZ) calculations. Comparison of energy trends from MR-FOCI results with CASPT2 results was used to establish the accuracy of MR-FOCI/6-31G* for the dynamics simulation, as shown in Table A4. Although CASPT2 and MR-FOCI excitation energies differ by as much as 0.9 eV, the energy differences relevant to the dynamics (*i.e.* S_1 and S_2 at the S_0 minimum, the S_2-S_1 MECI and the S_1-S_0 Tw-C2P MECI) are within 0.3 eV. Calculations for all three molecules employed an active space of six electrons in three π and three π^* orbitals for the CASSCF reference, with electronic character defined at the S_0 minimum geometry.

Direct comparison with the experimental spectra were undertaken by calculating the time-resolved photoelectron spectrum using the data produced from the AIMS trajectories. At each time step of each trajectory, MR-FOCI calculations were performed to determine the energy from the state of the trajectory to several doublet ion states. The total signal for ionization from electronic state I of the neutral to state α of the cation is given by the expression:[56,122–124]

$$S(E,t) = \sum_{I=1}^{N_s^0} \sum_{j=1}^{N_I(t)} |c_j^I(t)|^2 \sum_{\alpha=1}^{N_s^+} W_{I\alpha}(\mathbf{R}_j^I(t))\, \delta\left(E - (n\omega_2 - \Delta E_{I\alpha}(\mathbf{R}_j^I(t))\right), \qquad (2.2)$$

where N_s^0 and N_s^+ denote the number of neutral and cationic states, respectively, and $W_{I\alpha}$ is the probability of ionization from neutral state I to cationic state α. The energy portion of the spectrum includes the number of probe photons n (for one- or two-photon ionization), the probe pulse energy ω_2 and the ionization potential $\Delta E_{I\alpha}$. Thus, the energy for each trajectory j at time t is defined by the electron kinetic energy, $E = n\omega_2 - \Delta E_{I\alpha}$. Since the measurement we seek to simulate is angle-integrated, we chose to represent the ionization cross-section arising from the matrix element above using the norm of the corresponding Dyson orbital, such that

$$W_{I\alpha}(\mathbf{R}_j^I(t)) \propto N \left|\langle\psi_j^\alpha(\mathbf{R}_j^I(t))|\psi_j^I(\mathbf{R}_j^I(t))\rangle\right|^2 = \left|\phi_{I\alpha}^D(\mathbf{R}_j^I(t))\right|^2, \tag{2.3}$$

for an N-electron system. In this way, we are limited to approximating the relative rates of ionization to different final cationic states. For 2-photon ionization, the transition corresponds to a set of intermediate neutral states and a transition probability of $W_{I\alpha} = 1$ was found to be a better approximation of the 2-photon signal. The final simulated spectrum was obtained by applying a Gaussian filter with full widths at half maxima of 160 fs (140 fs in the 2-photon region) and 50 meV corresponding to the experimental time cross-correlation and energy resolution, respectively.

2.3 Results

2.3.1 UV-Vis absorption

The UV-Vis absorption spectra of AN, CrN and MeAN are shown in Figure 2.2. These spectra are in agreement with more detailed spectra in the literature.[108,109] The broad absorption band of AN was found to originate at 211 nm (5.88 eV) and was assigned to a $\pi\pi^*$ state. Higher energy peaks were assigned to a vibrational progression.[109] The absorption spectra of MeAN and CrN are not as readily assigned. Their corresponding absportion maxima are slightly red-shifted relative to AN and the broad band near 200 nm is similarly assigned to $\pi\pi^*$ excitation.

2.3.2 Potential energy surfaces

In the Franck-Condon region, the first two excited states both have $\pi\pi^*$ character. The optimization of minima on the pertinent potential energy surfaces, as well as minimum energy conical intersections between those surfaces, yields similar structural motifs for AN and its methylated analogs. Those that were found to be relevant to the dynamics after excitation to S_2 are shown in Figure 2.3, with geometries of each structure given in Figure A1. As noted by Du *et al.*[104] for acrylonitrile, no potential energy minima were found near the FC region on S_1 and S_2 for any of the molecules.

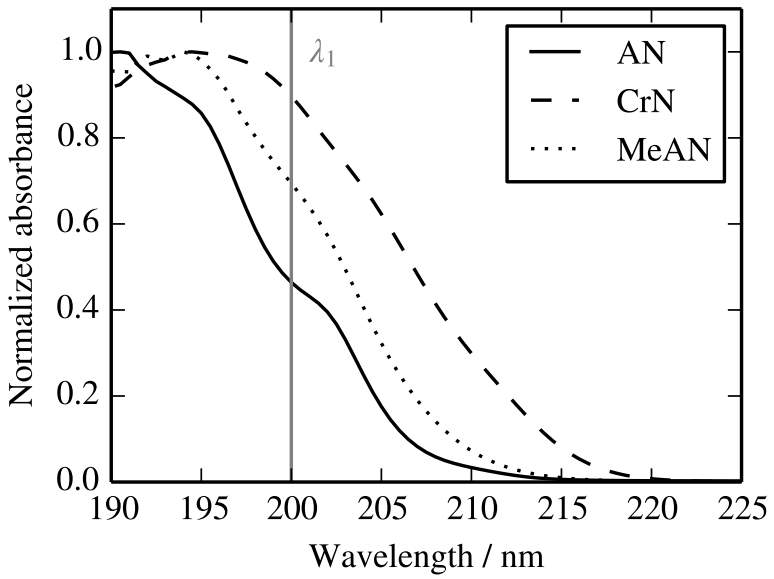

Figure 2.2: Absorption spectra of acrylonitrile (AN), crotonitrile (CrN) and methacrylonitrile (MeAN). The pump wavelength (λ_1) of all three experiments is given by the vertical line.

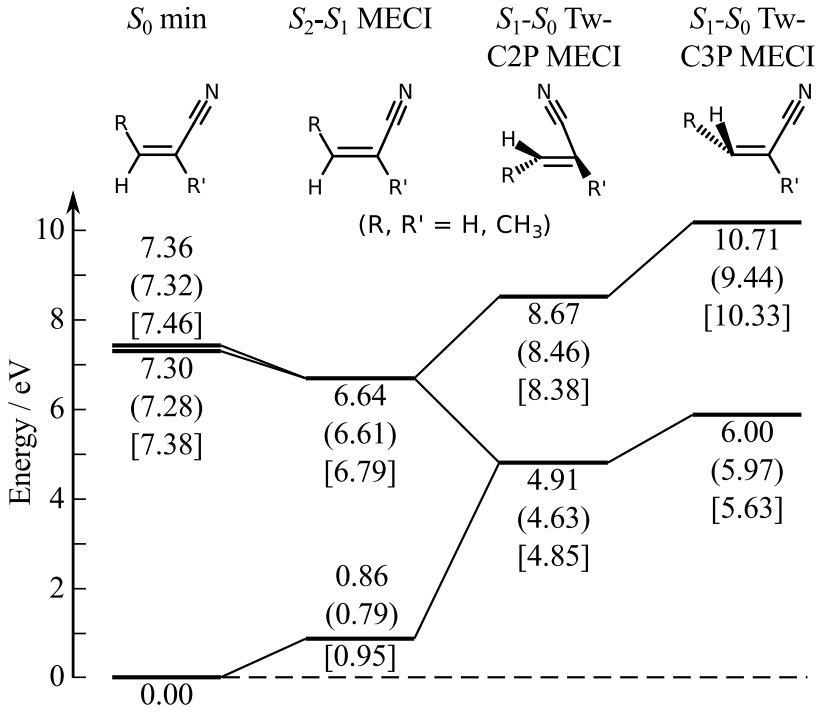

Figure 2.3: Electronic energies of acrylonitrile (crotonitrile) [methacrylonitrile] at the critical points on the potential energy surface calculated at the MR-FOCI/6-31G* level of theory. The solid lines represent potential energies of each state averaged over the three molecules.

From Figure 2.3 it can be seen that the relative energies between the ground and low-lying excited states remain relatively unchanged upon methyl substitution for the regions of the potential energy surfaces relevant to this study. This is a desirable result in the sense that the effect of the methyl groups can be considered as primarily inertial or dynamical and does not appreciably change the contours of the electronic surfaces (in non-mass weighted coordinates). Each of the molecules have nearly degenerate first and second excited states in the Franck-Condon region. A S_2-S_1 MECI is found 0.7 eV below the S_2 energy at the FC point and is accessed through the elongation of the C=C bond. Likewise, each of the α,β-enenitriles have a S_1-S_0 MECI 1.7–2.0 eV lower in energy involving a C=C torsion, a C=C−C bend and pyramidalization at carbon C2 relative to the ground state minimum. Additional MECIs corresponding to torsion and pyramidalization at C3 exist at a higher potential energy. These two MECI types will hereby be referred to as the Tw-C2P and Tw-C3P MECIs, respectively. The twist-pyramidalization S_1-S_0 MECI type is a common motif for CIs of molecules with a vinyl group.[36,54,114,124]

The CASPT2 values presented in Table A4 are within 0.15 eV of the energies calculated by Du *et al.*. Of note is the difference in optimized S_2-S_1 MECI geometries. Du *et al.* report a MECI involving a C=C torsion. In this work, two S_2-S_1 MECI geometries corresponding to the same conical intersection were optimized. Due to the strong coupling between S_2 and S_1 states in the Franck-Condon region, the geometry shown in Figure 2.3 was favoured. The same conical intersection is expected to mediate $S_2 \rightarrow S_1$ decay in the results of Du *et al.*.[104]

2.3.3 Nonadiabatic dynamics simulation

Using the initial condition filtering procedure described in Section 2.2.2 resulted in significant initial population on both S_1 and S_2 as a result of the nearby C=C stretch CI. The initial fraction of the wavepacket amplitude on S_2 varied between 0.5 and 0.9.

Figure 2.4 presents the adiabatic populations of the α,β-enenitriles as a function of time. For each of the three molecules, the initial population on S_2 decays rapidly to S_1 due to the easily accessible CI. The similarity in $S_2 \rightarrow S_1$ transitions is evinced by the time taken for the S_1 population to reach a maximum, which occurs around $t_{off} = 60$ fs for each of the molecules. There is a small increase in the S_2 decay timescale for MeAN relative to AN and CrN which may be related to an increase in the C=C bond length of the S_2-S_1 MECI as well as random errors in the data. The S_1 population then transitions to the ground state. The slow timescales relative to $S_2 \rightarrow S_1$ decay can be attributed to the large amplitude C=C torsion, C=C−C bend and C2 pyramidalization. Interestingly, MeAN showed a much slower decay to the ground state despite the methyl group only undergoing a small out-of-plane motion to reach the Tw-C2P conical intersection. This can be seen quantitatively

Table 2.1: Decay offsets, time constants, and total excited state lifetimes for single exponential fits to the total adiabatic excited state population. Standard deviations for least-squares fits are on the order of 1 fs for all values.

Molecule	t_{off} / fs	τ_{ex} / fs	τ_{tot} / fs
AN	53	53	106
CrN	58	87	145
MeAN	67	99	166

from the excited state lifetimes shown in Table 2.1, where a single exponential fit to the total excited state population (S_1 + S_2) yields increasing excited state lifetimes from AN to CrN to MeAN. The values given in Table 2.1 correspond to an exponential decay of the form $f(t) = \exp[-(t - t_{off})/\tau_{ex}]$ with a total excited state lifetime of $\tau_{tot} = t_{off} + \tau_{ex}$.

Despite both Tw-C2P and Tw-C3P being energetically accessible, ∼95% of the population was found to travel through the S_2-S_1 CI followed by the Tw-C2P S_1-S_0 CI for AN and MeAN. CrN exhibited similar behaviour, with the exception that 15% of the *trans* population passed through the alternate CI. The C=C torsional angle was unimportant for the S_2-S_1 seam, with spawn geometry values varying from 0 to 90°. This can be seen in Figure 2.5, which plots the Monte Carlo integrated wavepacket density as a function of internal coordinate motion. Most of the initial S_2 wavepacket amplitude decays after a single C=C stretch. The remaining density stays on the S_2 state for multiple vibrational periods as the molecule simultaneously undergoes torsion about the C=C bond (see Figure 2.5b). The density plots corresponding to the wavepacket evolution for CrN and MeAN show the same trend; however, the decay to S_1 after a single C=C stretch is nearly quantitative. Also shown in Figure 2.5 is the S_1 population along the C=C−C bend and C=C torsion degrees of freedom, whereby most of the wavepacket transitions to the ground state following a single twist and bend.

A two dimensional cross section of the potential energy surfaces of acrylonitrile is given in Figure 2.6, with arrows indicating the pathway taken to reach the ground state. As can be seen from the figure, after excitation to S_1 or S_2 the C=C−C bending motion is inhibited by a potential energy barrier. The barrier to the C=C−C bend indicates that torsion occurs initially followed by bending. As noted earlier, the first and second excited states are nearly degenerate along the C=C torsion from the FC region. In the case of the methyl substituted analogs, a similar picture can be expected with a higher barrier to torsional motion on the second excited state.

2.3.4 Time-resolved photoelectron spectroscopy

The photoelectron spectra of AN, CrN and MeAN are shown in Figures 2.7a, 2.7c and 2.7e. The time zero spectrum mainly exhibits a broad band that decays toward higher

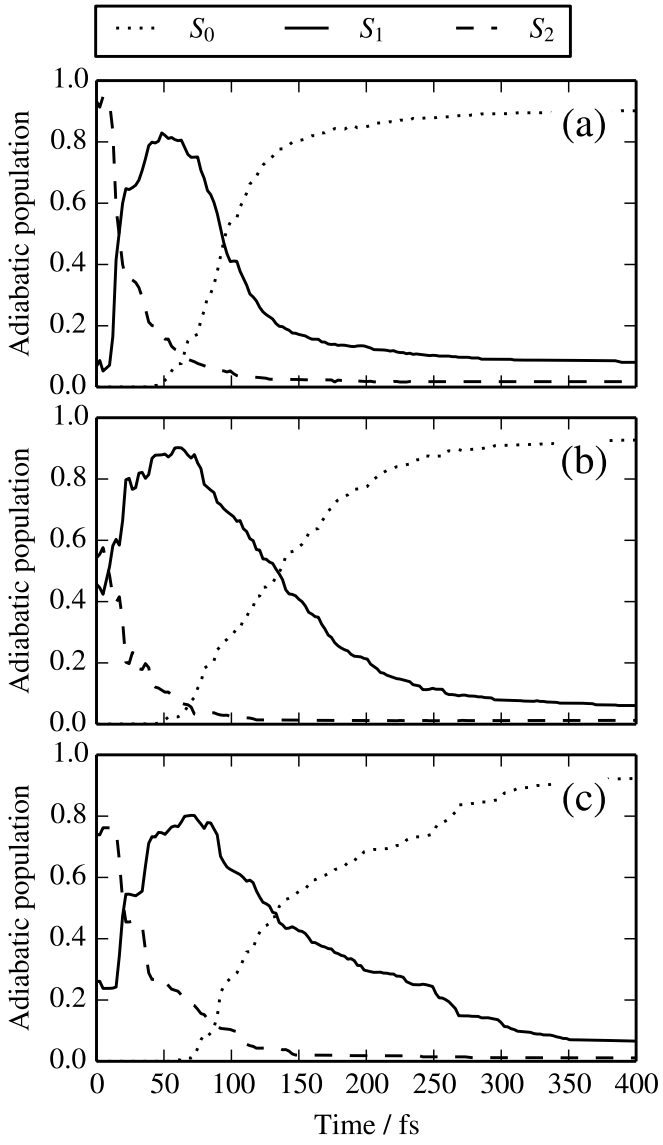

Figure 2.4: Adiabatic populations *vs.* time for (a) AN, (b) CrN and (c) MeAN. S_2 population rapidly transfers to the lower S_1 state, while the S_1 population must go through large amplitude motions to reach S_0.

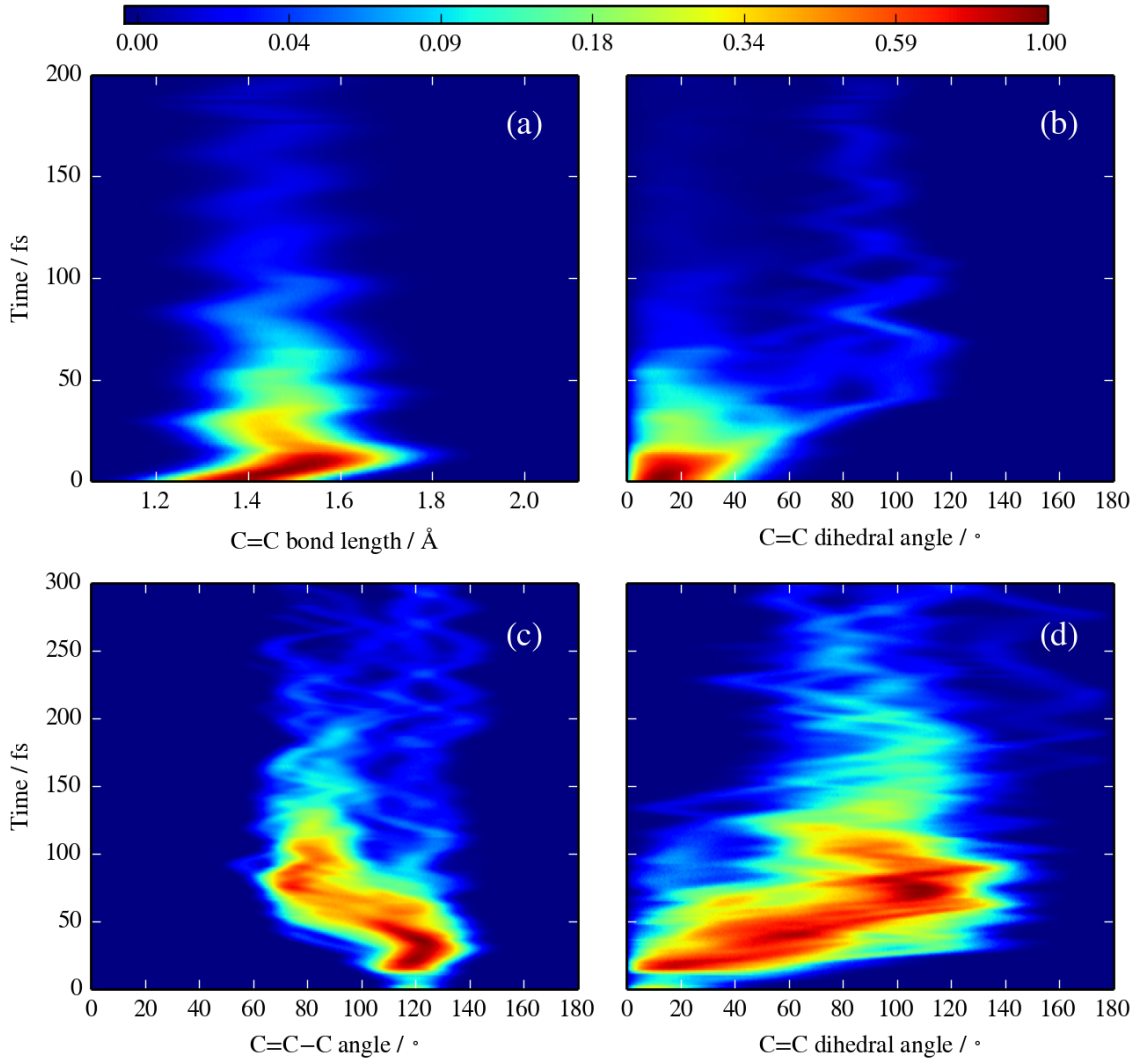

Figure 2.5: Wavepacket density of AN along (a) the C=C bond length on S_2, (b) the C=C torsion on S_2, (c) the C=C−C bend on S_1 and (d) the C=C torsion on S_1. Most of the wavepacket on S_2 undergoes a single C=C stretch to reach S_1, followed by a C=C−C bend and C=C twist to reach S_0.

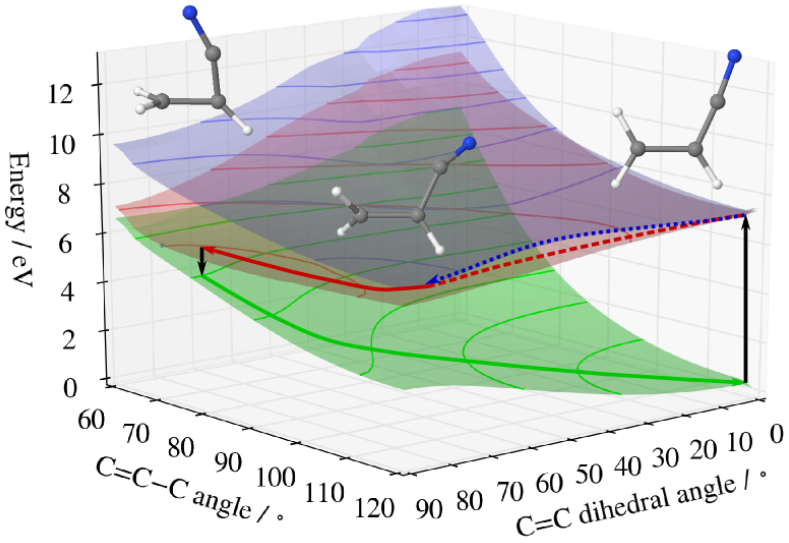

Figure 2.6: 2D cross-section of the acrylonitrile potential energy surfaces along the C=C torsion and C=C−C bend coordinates. Following excitation to S_2, the wavepacket follows a twist followed by a bend to reach S_0. Contours lines on the surfaces are given every 1 eV.

photoelectron kinetic energies and disappears around 4.5 eV (not shown). The ionization potential of AN is 10.92 eV[125,126] which is slightly more than the energy delivered by one pump (6.20 eV) and one probe photon (4.65 eV). Therefore, with the exception of the peak at 0 eV, ionization requires two probe photons which results in a total absorbed energy of 15.5 eV. More discussion on the photoelectron spectrum assignments can be found in the supplementary material (Appendix A).

The ionization potentials of MeAN and CrN have values of 10.34[125,127] and 10.23 eV,,[125,128] respectively, both of which are below the [1+1′] threshold. This corresponds to the energy cutoffs at 0.51 and 0.62 eV in the photoelectron spectra, which agrees with the values found in our experiment (0.49 and 0.62 eV), although we note a minor peak at 0.61 eV in the MeAN spectrum. The signal at higher photoelectron kinetic energies (inset) originates from two-photon ionization. As in AN, we found that the amplitude of the photoelectron spectrum in the [1+2′] region decreases with increasing photoelectron kinetic energies.

Photoelectron spectra are commonly fit using a Levenberg-Marquart 2D global fitting routine using the function

$$S(E, \Delta t) = \sum_{i=0}^{N_{max}} A_i(E) P_i(E, \Delta t) \otimes g(\Delta t). \tag{2.4}$$

Here, N_{exp} is the number of exponential functions used. $A_i(E)$ is the so-called *decay associated spectrum* which is associated with an exponential decay $P_i(\Delta t)$ of the form

$$P_i(E, \Delta t) = \exp(-\Delta t/\tau_i), \tag{2.5}$$

where $\Delta t = t - t_0$ is the pump-probe delay. The cross correlation $g(\Delta t)$ is determined independently (see Section 2.2.1).

This method of fitting is not able to describe all experimental data sets sufficiently well.[115,116,129] A temporal shift of the photoelectron band is observed which cannot be described satisfactorily with a set of exponentials, especially in the case where the Franck-Condon region exhibits a steep gradient on the excited state potential energy surface and the molecule undergoes large amplitude motion. This shift may lead to an increase in the ionization potential as the molecule deforms, yielding a "chirp" of the observed photoelectron kinetic energy signal. It has been previously demonstrated that one suitable way to describe this shift is by using time zero (t_0) of the experiment as a fitting parameter.[115,116,129] Assuming a monoexponential decay ($i = 1$), the spectrum is fit to the function

$$S(E, \Delta t) = A(E) \exp(-(t - t_0(E))/\tau_1) \otimes g(t - t_0). \tag{2.6}$$

The maximum shift therefore indicates the total electron kinetic energy signal modulation due to a dominant large amplitude vibrational mode. Note that the determined exponential decay time may be a varying function of the photoelectron kinetic energy as ionic channels may image the dynamics differently due to windowing effects.

The photoelectron spectra of AN, CrN and MeAN could be fit with one exponential decay function, a non-zero offset that does not decay during the course of the experiment, and a shift in time zero for each energy channel. Time constants and maximum time zero shifts are summarized in Table 2.2.

2.3.5 Simulation of the time-resolved photoelectron spectrum and comparison to the experimental data

In order to directly compare experimental and theoretical results, time-resolved photoelectron spectra were calculated from *ab initio* multiple spawning data as detailed in Section 2.2.2. The theoretical spectra are shown alongside experimental results in Figure 2.7. Other than signal from the 1-photon cutoff, data presented in the spectrum of AN are exclusively from two photon ionization as the ionization potential in the FC region is greater than that of [1+1′] ionization.[130] Spectra of CrN and MeAN contain both one and two photon signals, with insets showing the two photon regions of the spectra. The two photon ionization intensities in the calculated spectra were given a 1% weight relative to single photon results.

Table 2.2: Maximum time zero shifts and global exponential decay time constants for fits of 2-photon experimental and theoretical TRPES spectra.

	Experimental		Theoretical	
Molecule	t_0^{max} / fs	τ_1 / fs	t_0^{max} / fs	τ_1 / fs
AN	37 ± 11	60 ± 10	55 ± 6	50 ± 2
CrN	44 ± 27	86 ± 11	59 ± 7	68 ± 3
MeAN	50 ± 28	97 ± 9	70 ± 9	81 ± 2

The energy correction of the dominant $S_1 \rightarrow D_0$ channel was found by comparing the experimental energy difference of 5.04 eV[109,130] to the calculated value of 2.56 eV. To account for errors in the *ab initio* ionization potentials, the difference (2.49 eV) was subtracted from the computed photoelectron kinetic energies. However, in comparison to the experimental spectrum the shift was changed to 1.96 eV for the 1-photon signal and 2.66 eV for the 2-photon signal to give the spectrum shown in Figure 2.7b. For CrN and MeAN, spectra were adjusted to have approximately the same single photon energy cutoff as experimental results, yielding shifts of 1.87 for both CrN and MeAN in the 1-photon region and 2.06 and 2.19 eV, respectively, in the 2-photon region. The difference in energy shift is likely due to errors of calculated ionization energies for different transitions.

A detailed comparison of the experimental and simulated photoelectron spectra can be made by examining the fit parameters that are determined for both quantities using the model functions shown in Equations 2.4 and 2.6. Figure 2.8 provides a comparison of the time zero shifts as a function of electron kinetic energy for experiment and theory. The sum of the maximum shift of time zero and the corresponding time constant (t_0^{max} and τ_1, respectively) may be used as a lower bound of the excited state lifetime. The fit values of t_0^{max} for AN, CrN and MeAN are 37 ± 11, 44 ± 27 and 50 ± 28 fs, and 60 ± 10, 86 ± 11 and 97 ± 9 fs for τ_1 as can be found in Table 2.2. The combined maximum time zero shift plus the exponential decay accurately reproduce the total excited state lifetime of the molecules evinced in Table 2.1. The error bars on the experimental quantites reflect the uncertainty in both the exponential fit as well as the data points in the photoelectron spectrum. The theoretical error bars were determined via repeated sampling of a subset of trajectories to quantify the uncertainty associated with employing a finite number of initial conditions.

These time constants can be compared to the experimental fitting in order to interpret the time constants observed in the experiments and to check the validity of the computations. The trend for the relaxation time of the molecules for the simulations is confirmed by the experiment both for the time zero shift as well as for the exponential decay time. In that sense, the experimental and simulated data of all three molecules agree in a satisfactory way. The total time for energy shifts plus exponential decays are 97, 130 and 147 fs, respectively, while the simulated spectra are slightly longer (105, 127 and 151 fs).

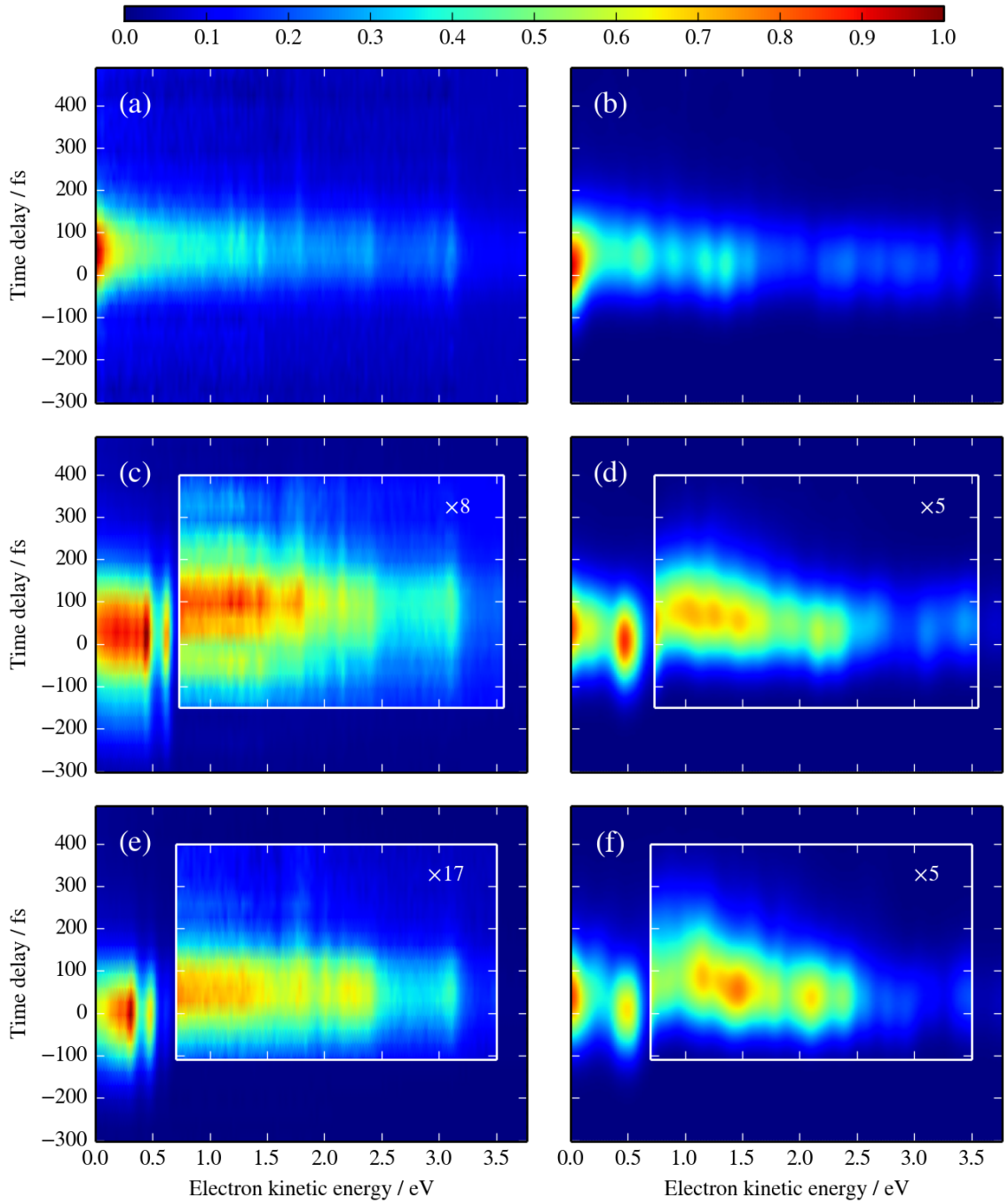

Figure 2.7: (a, c, e) Experimental and (b, d, f) theoretical time-resolved photoelectron spectra of AN, CrN and MeAN, respectively, using 200 nm pump and 267 nm probe wavelengths. Insets in CrN and MeAN spectra provide underlying data scaled by the given factor in order to show the 2-photon signals.

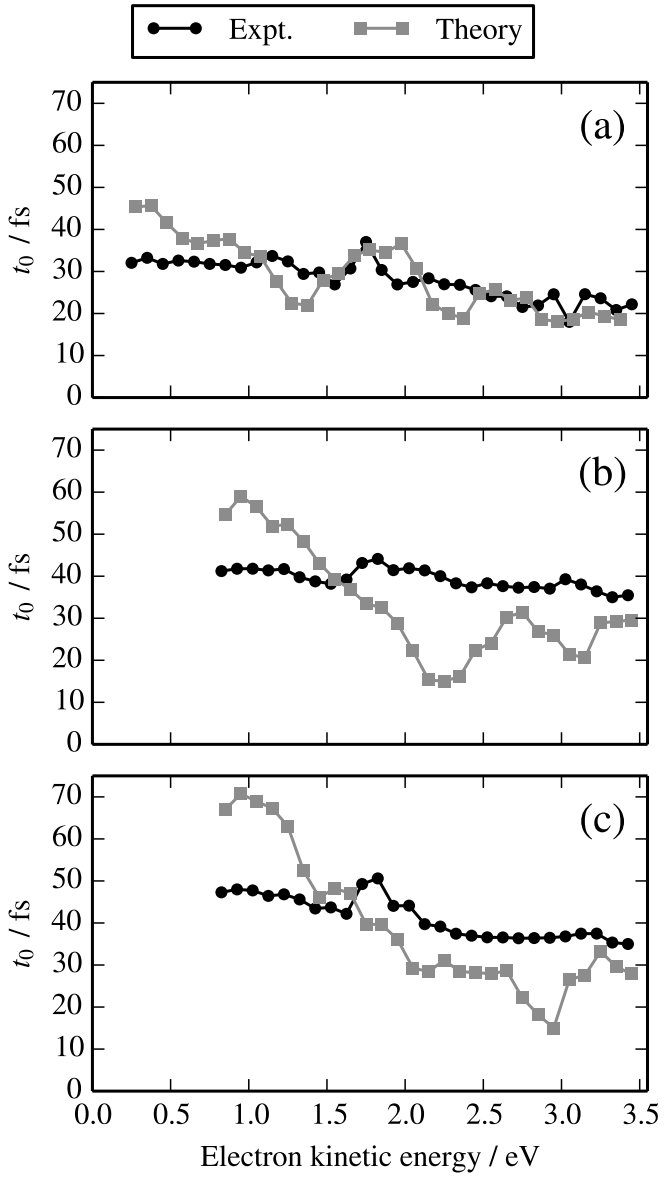

Figure 2.8: Time zero shifts t_0 as a function of photoelectron kinetic energy for the 2-photon region of (a) AN, (b) CrN and (c) MeAN.

Time zero represents the time of an initial signal with a given electron kinetic energy. Thus, in each spectrum the point $t_0 = 0$ occurs at the 1- and 2-photon energy cutoffs. The 1-photon cutoff can be seen as an energy localized peak in the spectra of CrN and MeAN at 0.49 and 0.62 eV, respectively. As the wavepacket evolves, its reduction in potential energy can be seen by a "chirp" towards lower electron kinetic energy at longer time delays (see Figure 2.8). The difference between the experimental and theoretical time zero shifts and exponential decay constants in Figure 2.8 occurs at energies near the maximum time zero shift. This suggests an overestimation of the change in potential energy during the low amplitude motion which causes the shift in t_0.

2.4 Discussion

The addition of a methyl group to AN infleunces the nonadiabatic dynamics by slowing the decay, as inferred from time constants for the decay of adiabatic populations and the TRPES signal. The excited state decay slowed from AN to CrN to MeAN. Considering the importance of torsional motion of the methylene (CH_2) group in AN in particular, it may be expected that methyl substitution of a methylene hydrogen should significantly affect the decay to S_0 by slowing rotation about the C=C bond. For this reason, intuition might suggest that substitution of one of the methylene hydrogens (yielding CrN) would have a more significant impact on the decay of the excited state population than replacement of a methine hydrogen (to form MeAN).

This analysis fails to account for the fact, however, that the requisite pyramidalization occurs almost exclusively at the 2-carbon. As discussed previously in studies of butadiene[36] and ethylene,[124] pyramidalization is accompanied by a sudden polarization across the unsaturated C=C bond. This polarization is engendered by the torsion about the internuclear axis which "decouples" the p-orbitals that form a π-bond. The presence of the electron donating cyano group bonded to C2 *ensures* that the negative charge develops almost exclusively at this site. Figure 2.9 clearly shows this effect by constructing a histogram of the partial (Mulliken) charges at both the 2- and 3-carbons computed at each of the spawn geometries. As the figure evinces, the predilection for the molecules to pyramidalize at C2 is strongly correlated to the partial negative charge developed at this atomic site.

Furthermore, the dynamics simulations show that the longer lived excited state in MeAN is due to more than just a slowed pyramidalization vibration at the C2 site. As Figure 2.10 shows, appreciable wavepacket density is trapped on the S_1 excited state for multiple vibrational periods of the C=C−C angle bend and the methylene torsion mode. In contrast, over half of the AN population transfers to S_0 after a C=C−C bend in Figure 2.5. However, the fact that multiple passes through the coupling region are required to transfer amplitude to the ground state suggests that the region of the intersection seam accessed by the MeAN

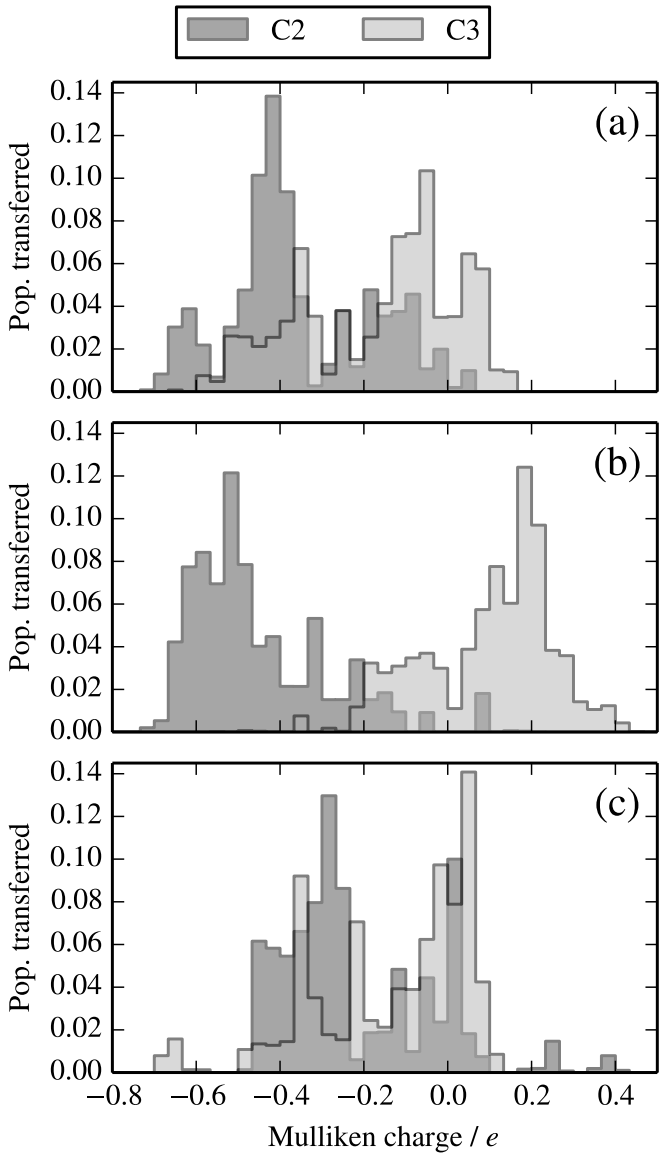

Figure 2.9: Distribution of Mulliken point charges on S_1 at the Tw-C2P spawn points of (a) AN, (b) CrN and (c) MeAN.

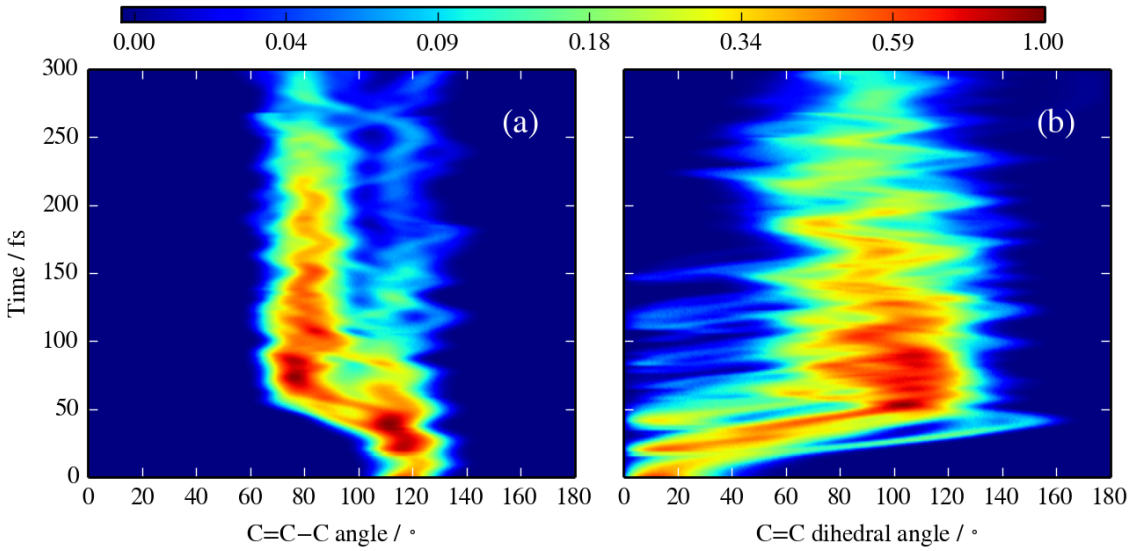

Figure 2.10: MeAN wavepacket density projected onto S_1 along (a) the C=C torsion and (b) the C=C−C bend degrees of freedom. Unlike AN and CrN, the MeAN density takes multiple vibrations to fully transfer to S_0.

wavepacket is less efficient at mediating the nonadiabatic transition.

To elucidate this issue, we plot S_1 and S_0 potential contours along the C=C−C bending, C=C torsion and H (CH_3) out-of-plane motion about the Tw-C2P MECIs, shown in Figure 2.11. The seam of intersection is plotted as a solid blue line and the point of MECI as a blue triangle. The spawn geometries are plotted as dots, the opacity of which indicate the amplitude of population transferred to S_0. To summarize: these plots show *where* population is transferred to the ground state and the relation of these points to the seam of intersection.

The results for AN and CrN (first two rows of Figure 2.11, respectively) show that the spawn points cluster *about* the MECI, with arguably a slight preference for larger out-of-plane angles than those displaying at the minimum energy crossings (26.6° and 33.6° for AN and CrN respectively). In contrast, Figures 2.11e and 2.11f show that in the case of MeAN, the spawn points occur at uniformly larger pyramidalization angles than that of the MECI and thus at higher energies of the seam of intersection. This is likely due to the comparatively small CH_3 out-of-plane angle at the MECI for MeAN. Homoconjugation between the methyl C−H σ bond and the π orbitals on the C-backbone is a stabilizing influence as long as the CH_3 group remains in plane so that overlap can be maintained. For this reason, the corresponding pyramidalization angle at the S_1-S_0 MECI in MeAN is only 9.3° (compared to 26.6° and 33.6° for AN and CrN, respectively). The ensuing wavepacket dynamics are thus sampling higher energy regions of the intersection seam,

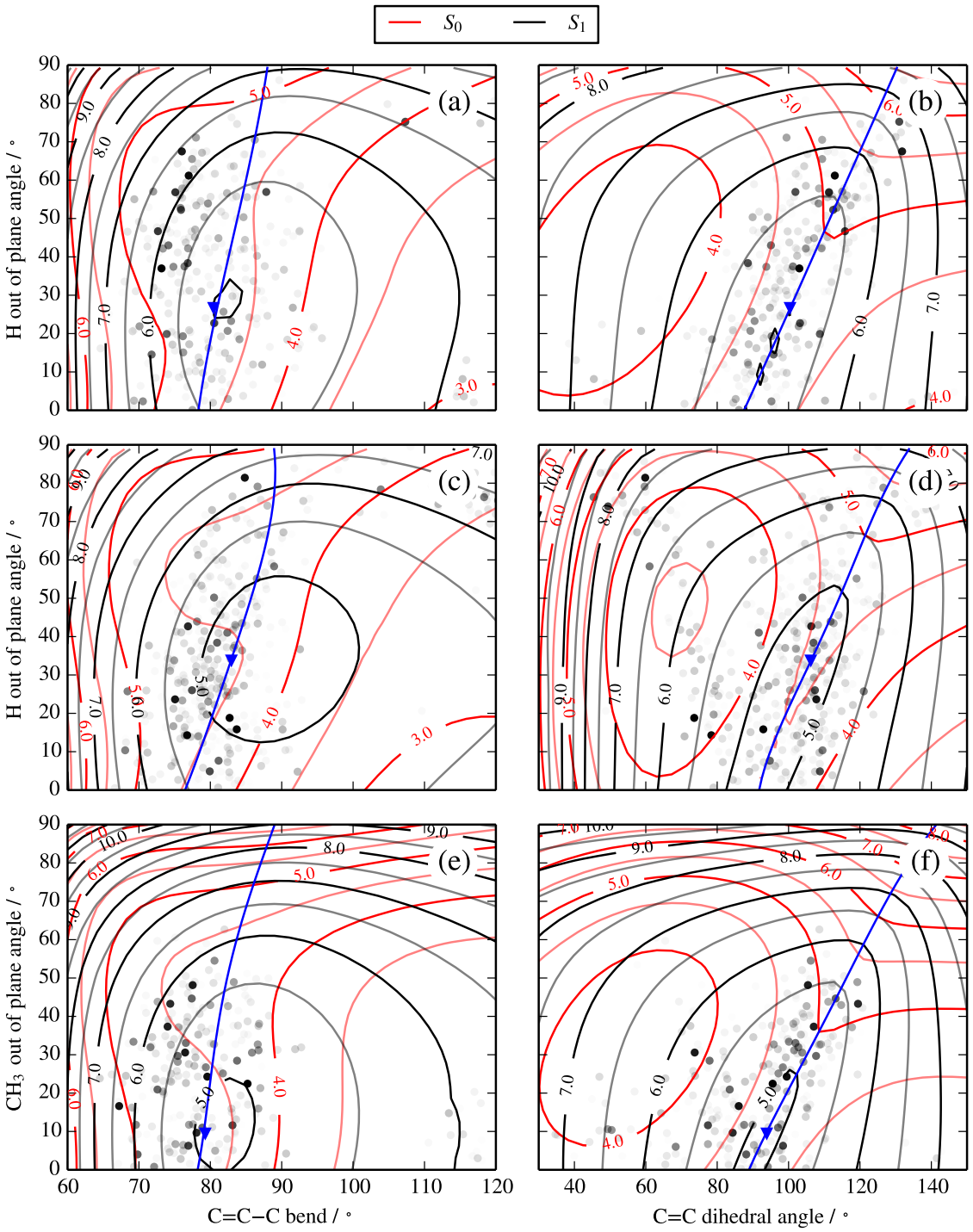

Figure 2.11: S_1 and S_0 potential energy surfaces along (a, c, e) C=C−C angle and H (CH_3) out-of-plane angle and (b, d, f) C=C dihedral angle and H (CH_3) out-of-plane angle for AN, CrN and MeAN, respectively. Blue triangles represent the Tw-C2P MECIs and blue lines are the paths of minimum energy difference between surfaces. Black dots are shown at AIMS spawn geometries with opacity representing the total population transferred.

with less symmetric intersection topologies (see supplementary material, Appendix A), and thus lower nonadiabatic transition efficiencies.

2.5 Conclusions

In previous work,[56,114] we have examined the how methyl substitution can be used to alter the frequency of particular vibrational modes, thereby influencing how an excited state wavepacket approaches a CI and thus the excited state lifetime. The premise in that work is that inertial substituents can be employed to direct wavepacket dynamics to some degree and engender some degree of "chemical control". In this work, the effect of methyl substitution was clearly observed in the measured (and simulated) excited state decay constants, significantly lengthening the excited state lifetime when placed at the medial carbon, as is the case for MeAN. From a purely dynamical perspective the pyramidalization in the "twisted-pyramidalized" CIs would be predicted to occur at the *terminal* methylene carbon, given that the vibrational frequency for this mode (939 cm^{-1}) is significantly higher than at the medial carbon (672 cm^{-1}). However, it is the capacity for electron donation of the cyano group which forces the partial negative charge (a key facet of pyramidalization) to develop at the medial carbon that drives the dynamics, not the inertial effects of the substituents. In other words, it is an electronic structure effect created by the cyano group that determines the relative rates of internal conversion and not the dynamical effect engendered by the increased inertia of the methyl groups. These results demonstrate that a general understanding of the dynamics at CIs will need to consider the interplay of these potentially competing effects.

Acknowledgments

R.J.M. and M.S.S. acknowledge financial support from the Natural Sciences and Engineering Research Council of Canada (NSERC). R.J.M. acknowledges the Government of Ontario for support in the form of an Ontario Graduate Scholarship. O.S. thanks the Wenner-Gren foundation for a research fellowship. R.F. acknowledges financial support by the Swedish Research Council (VR) and the Knut and Alice Wallenberg Foundation, Sweden. We would also like to thank Andrey Boguslavskiy for help with the uncertainty analysis.

Chapter 3
Substituent effects on the nonadiabatic dynamics of ethylene: π-donors and π-acceptors

R.J. MacDonell,[1] and M.S. Schuurman[1,2]

Reprinted with permission from *Chem. Phys.* **2018**, *515*, 360–368.
https://doi.org/10.1016/j.chemphys.2018.09.012.

This work demonstrates the trends in substituted ethylenes and how they can be used to affect excited-state decay mechanisms. All figures with partial atomic charges were modified from the published version due to an error in the charge calculation, detailed in Chem. Phys. ***2020****, 515, 360–368. I (RJM) developed the modified diradical model, performed electronic structure and nonadiabatic dynamics calculations and interpreted the results in the text. MSS supervised the work and provided feedback.*

[1] Department of Chemistry and Biomolecular Sciences, University of Ottawa, Ottawa, Ontario K1N 6N5, Canada
[2] National Research Council of Canada, 100 Sussex Drive, Ottawa, Ontario K1A 0R6, Canada

Abstract

The energetic and structural trends in the minimum energy conical intersections of a series of substituted ethylenes are explained by the degree to which the chemical substituents polarize electron density across the C=C double bond. The addition of a substituent that significantly polarizes the electron density also reduces the magnitude of the large-amplitude pyramidalization motions required to reach a conical intersection and can thus very effectively "direct" these motions to occur at a specific carbon atom. These observations are summarized via the construction of a reduced dimensionality representation of the relevant potential energy surfaces inspired by a previously reported 3-state model for biradical systems. On-the-fly nonadiabatic dynamics simulations reveal that this effect dictates the dominant excited state decay pathway for acrylonitrile (π-acceptor CN substituent) and vinylamine (π-donor NH_2 substituent). The *ab initio* multiple spawning simulations show that population transfer to the ground electronic state for both molecules occurs primarily in the regions around the substituent-altered minimum energy conical intersections, demonstrating that chemical substitution may be used to selectively alter photochemical pathways.

3.1 Introduction

Ethylene is an exhaustively studied model system for nonadiabatic dynamics involving conical intersections.[20,21,131,132] This molecule continues to be the subject of extensive theoretical and experimental investigation due to the prevalence of ultrafast electronic deexcitation in electronically conjugated systems, such as the site-specific isomerization in retinal,[44,45,85,133,134] or the motions that enable molecular switches such as stilbene.[135–137] The photo-absorption process that initiates the excited state dynamics examined here involves excitation to the lowest energy electronic absorption band which is described by two strongly coupled states: the Rydberg $\pi 3s$ ($^1B_{3u}$) and the valence $\pi\pi^*$ ($^1B_{1u}$). Following vertical excitation to the $\pi\pi^*$ state, the primary electronic decay pathway involves twisting about the C=C bond to minimize the overlap between the lobes of the π^* orbital. This involves a combination of C=C stretch, C=C torsion and CH_2 wagging normal modes. The electronic structure associated with nuclear geometries for which the two methylene groups are fully rotated is characterized by the formation of a biradical involving the two now perpendicular *p*-type orbitals.[16]

Following 90° torsion about the C=C bond, Domcke and co-workers[22] showed that nuclear deformations involving pyramidalization or skewed CH_2 scissoring motions at one methylene can lead to a "sudden polarization" across the C=C bond,[16,20,21] and the formation of a sizeable dipole moment. Furthermore, it is precisely these gradient-directed motions that lead to a conical intersection with the ground electronic state and that facil-

itate ultrafast electronic relaxation. Additional intersection moieties involve excited state H-transfer (*i.e.* ethylidene) and H-bridged structures. These geometries have been shown to lie on the same seam of intersection, where the relative energies of these structures depend primarily on the tilt of the CH_2 group relative to the C=C bond.[18] Recently, advances in the experimental techniques have enabled time-resolved spectroscopic experiments in which the nonradiative decay pathways following direct preparation of the $\pi\pi^*$ state can be interrogated and compared directly to computational simulations.[17,138,139]

Chemical substitution has been used previously to influence both the nuclear motions leading to a region of conical intersection, as well as passage through it.[54,56,114,140] One approach is typified by the addition of massive substituents, such as methyl (CH_3) groups, to affect the nuclear momenta along select vibrational modes. The assumption is that such groups are electronically "inert" and do not meaningfully affect the topography of the intersecting potential energy surfaces. For example, the series comprised of allene, 1,2-butadiene, 1,1-dimethylallene and tetramethylallene were studied experimentally and theoretically to assess the effect of inertial substituents on the excited state dynamics following excitation to the bright $\pi\pi^*$ state. The lifetime of the S_1 state population, as simulated using *ab initio* multiple spawning (AIMS) calculations, increased from ∼50 fs for allene to ∼160 fs for 1,1-dimethylallene as the relevant twisting and bending motions about the C=C=C backbond were slowed due to the mass of the methyl substituents. Little ultrafast decay of S_1 population was observed for tetramethylallene, as the steric interaction of the methyl groups prevented access to the conical intersection region. These results were in agreement with time-resolved photoelectron spectroscopic (TRPES) experiments, particularly the long time decay signals.[56]

A more standard utilization of chemical substitution, particularly for ground state chemistry, involves controlled alterations to the underlying potential energy surfaces in order to energetically favour particular reactive outcomes. In the context of excited state processes, this would correspond to altering the relevant conical intersection topographies or differentially shifting the energy of one intersection motif relative to another.[8] For example, the TRPES signal lifetimes of acrylonitrile showed a somewhat counter-intuitive dependence on the location of methyl substitution: the terminal substituted species displayed a reduction in decay lifetime relative to the central substituted species. Using nonadiabatic molecular dynamics simulations, the cause of the slowed decay of methacrylonitrile was found to be a shift in the potential energy surface such that the S_1-S_0 conical intersection from pyramidalization at the CN-substituted carbon was always energetically favoured.[140]

The observation that different types of π-conjugation in unsaturated hydrocarbons can have profound effects on the nonadiabatic dynamics may be rationalized using a simple 3-state configuration interaction biradical model originally proposed by Michl and Bonačić-Koutecký.[42,141] The model describes an ideal biradical in an orthogonal basis, such as

the two p-orbitals of 90° twisted ethylene. The biradical system is represented by the Hamiltonian

$$H = E_0\,\mathbf{I} + \begin{pmatrix} 2K_{AB} & 0 & \gamma \\ 0 & 2K'_{AB} & \delta \\ \gamma & \delta & 2(K'_{AB} + K_{AB}) \end{pmatrix}. \tag{3.1}$$

The terms in H are defined by

$$E_0 = h_{AA} + h_{BB} + J_{AB} - K_{AB}, \tag{3.2}$$

$$K'_{AB} = (J_{AA} + J_{BB})/4 - J_{AB}/2, \tag{3.3}$$

$$\gamma = 2h_{AB} + \langle AA|AB\rangle^* + \langle BB|BA\rangle\,, \tag{3.4}$$

$$\delta = h_{AA} - h_{BB} + (J_{AA} - J_{BB})/2, \tag{3.5}$$

where h, J and K are one electron, Coulomb and exchange integrals, respectively. The model is parameterized by two variables: δ, which quantifies the polarization between the basis functions (*e.g.* across the C=C bond) and γ, which quantifies the off-diagonal mixing of the basis (*e.g.* deviation of the π orbitals from orthogonality via C=C torsion). Notably, the model predicts a degeneracy between the two singlet states at $\delta = 2\sqrt{K'_{AB}(K'_{AB} - K_{AB})}$ and $\gamma = 0$. A non-zero value of δ may arise from, for example: the sudden polarization arising from pyramidalization (*e.g.* in ethylene), the replacement of a carbon atom by a heteroatom, or the addition of a local point charge near one carbon atom.[42,141] Chemical substituents may cause a similar effect, where electron withdrawing or donating groups cause asymmetry about a double bond.[16,142] The ability of point charges to selectively shift the energy of points on the seam of conical intersection has been observed in retinal, where otherwise degenerate conical intersections are shifted by the addition of a Cl^- ion used to represent the local environment in the rhodopsin protein.[44,45]

In π-electron systems, one effect that leads to a polarization across a double bond is the electronic resonance between the electrons of the π-system and a substituent. Substituents may interact with the π-electron system by either contributing excess additional π-electrons (π-donors) or by acting as a sink for electron density (π-acceptors). Examples of these two types of substituents are illustrated in Figure 3.1. In general, π-donors consist of groups with an excess of electrons, often in the form of lone pairs, while π-acceptors extend the conjugation of the π-system with one or more unsaturated bonds to a heteroatom. In the ground state picture the result is an increase in the electron density at the unsubstituted carbon for π-donors and an decrease in the same position for π-acceptors.[53] This arrow-pushing resonance picture is not applicable in general for excited states, but it is clear that the stability of zwitterion configurations (right side of Figure 3.1) in the specific case of the $\pi\pi^*$ state will be dependent on the electronic structure of the substituent. The relative

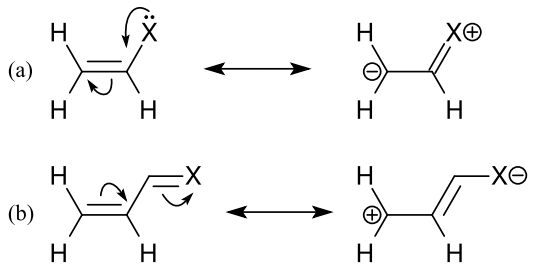

Figure 3.1: Examples of resonance leading to partial charges for (a) π-donors and (b) π-acceptors.

electronegativity of the functional group to the carbon atom may also play a role in the electron withdrawing/donating ability. For example, halides are a poor electron donating group because they act as π-donors and σ-acceptors.[53]

The compact conjugated π-system of acrylonitrile has led to several studies of its electronic structure by experimental[103,107–111] and theoretical[104,140] means. Characterization of the low-lying excited states shows that there are $\pi\pi^*$ states that correspond to excitation of the conjugated π orbital to the π^* orbital spanning the molecule as well as the π^* orbital localized on the CN group. Above these states in energy is a series of Rydberg states.[108,109] There have been relatively few experimental studies on vinylamine due to its instability at ambient conditions from polymerization and reactions with solvents. As a result, it is typically prepared using pyrolysis of small alkyl amines such as ethylamine, cyclobutylamine or diaminoethane. Interest in the structure of vinylamine arose particularly due to the prediction of a pyramidal NH_2 group leading to an overall C_1 symmetry.[143,144] The electronic spectrum of vinylamine remains largely unassigned. A UV absorption study attributed a set of peaks between 4.9 and 5.1 eV to a vibrational progression in the π3s Rydberg state below the $\pi\pi^*$ state,[145] while an MR-DCI/DZP study predicted the $\pi\pi^*$ state to have an excitation energy of 7.1 eV.[146]

In this study we show the effects of resonance and polarity on the accessible conical intersection mediated decay pathways of some substituted ethylenes. The trend in the observed MECI geometries, particularly with respect to pyramidalization, can be justified using an empirical model inspired by the previous biradical configuration interaction study.[42,141] We also demonstrate how these differences manifest in the complex nonadiabatic dynamics for π-donor and π-acceptor substituted ethylenes using on-the-fly dynamics simulations of acrylonitrile and vinylamine.

3.2 Computational Methods

The set of π-acceptor and π-donor substituted ethylenes studied here is given by: ethylene (ET, ethene); four π-donors: vinylamine (VAm, ethenamine), vinylalcohol (VOH, ethenol), vinylchloride (VCl, chloroethene), and propene (VMe); and four π-acceptors: acrylonitrile

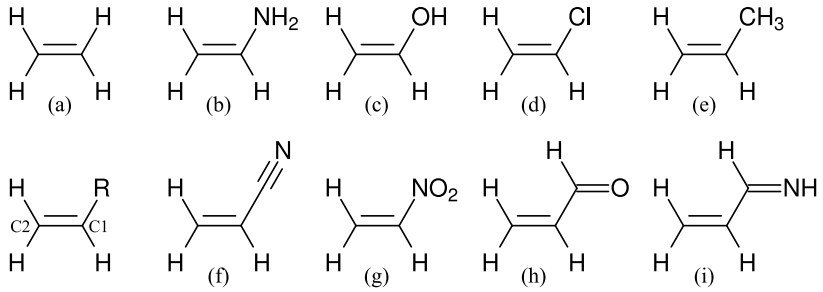

Figure 3.2: Molecular structures of (a) ET, (b) VAm, (c) VOH, (d) VCl, (e) VMe, (f) VCN, (g) VNt, (h) VAl, and (i) VIm. The inset structure on the bottom left shows the carbon labelling conventions for all molecules.

(VCN, 2-propenenitrile), nitroethylene (VNt, nitroethene), acrolein (VAl, 2-propenal), and propenimine (VIm, 2-propen-1-imine). The structures of all 9 molecules are shown in Figure 3.2.

Each of the molecules listed above were optimized at their ground-state minimum geometry as well as the minimum energy conical intersection (MECI) geometries corresponding to the intersection between the ethylene-type $\pi\pi^*$ with the ground state, namely pyramidalization at C1 and C2. Optimizations were performed using multi-reference first-order configuration interaction (MR-FOCI) which uses single excitations from a multiconfigurational self-consistent field (MCSCF) calculation in the COLUMBUS electronic structure package.[120] Potential energies of the ground state were then calculated using complete active space 2nd order perturbation theory with a triple-zeta basis (CASPT2/cc-pVTZ) with the Molcas electronic structure package.[147,148] An appropriate active space was chosen for each molecule based the orbitals required to describe the $\pi\pi^*$ state and lower-lying states in the Franck-Condon (FC) region. Further details on these computations, such as the chosen active space and details of the state-averaged MCSCF procedure can be found in Table B1. The computed ground state and $\pi\pi^*$ state energies can be found in Table B2 in the supporting information (Appendix B). To quantify the degree of polarization between adjacent atoms for specific electronic states, iterative Hirshfeld charges were determined using the MR-FOCI wavefunctions.[79,80] The iterative Hirshfeld method was chosen for the stability of the calculated charges with respect to the level of electronic structure employed and its ease of implementation for partitioning the MR-FOCI electron density.

The effects of π-donation and π-acceptance were also compared using nonadiabatic dynamics calculations for VAm and VCN, respectively. These two molecules were chosen for their small size and lack of low-lying valence states in comparison to the other molecules. The total wavefunction $\mathbf{\Psi}(\mathbf{r}, \mathbf{R}, t)$ was expanded according to the formalism of the AIMS

method,[88,89,119]

$$\mathbf{\Psi}(\mathbf{r},\mathbf{R},t)=\sum_{I=1}^{N_s}\sum_{j=1}^{N_I(t)}c_j^I(t)\psi_j^I(\mathbf{r},\mathbf{R})\chi_j^I(\mathbf{R};\mathbf{R}_j^I(t),\mathbf{P}_j^I(t),\gamma_j^I(t)), \tag{3.6}$$

where c_j^I are expansion coefficients, ψ_j^I are electronic wavefunctions and χ_j^I are nuclear basis functions for trajectory j on electronic state I. The nuclear component of the wavefunction is made up of Gaussian trajectories with centroid $\mathbf{R}_j^I$, momentum $\mathbf{P}_j^I$ and phase γ_j^I which are evolved using classical equations of motion on a single adiabatic potential energy surface. The electronic wavefunction is calculated on-the-fly at the centres of the basis functions. Each time a trajectory reaches a point of strong coupling determined by the vector product of the momentum and the nonadiabatic coupling, a new trajectory is "spawned" on the coupled state leading to a basis set expansion. At each step, the coefficients c_j^I are calculated using the time-dependent Schrödinger equation.

Initial geometries and momenta for both molecules were selected from a $v=0$ vibrational distribution about the ground state minima. The state with the greatest transition dipole moment for vertical excitation was selected as the initial state. The 30 initial conditions for VCN gave rise to 530 trajectories, whereas 43 initial conditions for VAm resulted in 1103 trajectories. The on-the-fly electronic structure calculations were performed at the MR-FOCI/6-31G* level of theory in the COLUMBUS electronic structure package.[120] For VAm, a diffuse 3s function centred at the nitrogen atom was added to the basis set. A 4 electron, 4 orbital active space was selected for VAm consisting of n, π, Rydberg 3s and π^* orbitals. A larger 6 electron, 6 orbital active space was necessary for VCN with the three occupied π and three virtual π^* orbitals. The relevant energy gaps for the dynamics simulations calculated at the MR-FOCI/6-31G* level of theory were found to be within 0.3 eV of CASPT2/cc-pVTZ results, as shown in Table B2 and Figures B3 and B4 in the supporting information.

The complex dynamics involved in both molecules necessitated a robust treatment of the populations involved in a given spawning event. The time-dependent population of a trajectory was defined analogously to Mulliken populations in electronic structure by[149]

$$n_j^I(t)=\sum_{i}^{N_I(t)}\mathrm{Re}\left[c_i^{I*}(t)S_{ij}(t)c_j^I(t)\right], \tag{3.7}$$

where S_{ij} is the overlap between basis functions. During a spawning event, the changes in population $\mathrm{d}n_j^I$ are negatively correlated between parent and child trajectories. In the absence of other coupled trajectories, $\mathrm{d}n_p^I=-\mathrm{d}n_c^J$ for parent p and child c. In order to exclude coupling to other trajectories, we define the correlated population change $\mathrm{d}n_{p\to c}$

and the population transferred to a child Δn_c^J as

$$\mathrm{d}n_{p\to c} = \mathrm{Re}\left(\sqrt{-\mathrm{d}n_p^I \mathrm{d}n_c^J}\right), \tag{3.8}$$

$$\Delta n_c^J = \int_{t=t_i^c}^{t=t_f} \mathrm{sign}(\mathrm{d}n_c^J)\, \mathrm{d}n_{p\to c}. \tag{3.9}$$

For practical purposes, after the spawning event ($t = t_i^c$) the integration occurs within a small time window which is sufficiently long that $\mathrm{d}n_{p\to c} \approx 0$. This method compares favourably with the threshold procedure defined previously,[149] and has the advantage of differentiating between back-transfer of population and coupling to other trajectories. It should be noted that this treatment excludes cases where the population of the child and parent increase simultaneously and damps the population change when multiple trajectories on state I are coupled to the child on state J; however, contributions from such cases were negligible due to the near-orthogonality of the nuclear basis.

3.3 Comparison of minimum energy conical intersections

A chemical substituent can be considered "useful" if it selectively lowers the barrier to a desired reactive outcome. In the case of excited state photochemistry, where multiple reactive channels are energetically accessible on vibrational timescales, substituents may be employed to "tilt" a specific potential energy surface towards the desired reaction pathway. In Figure 3.3, the potential energy of each substituted ethylene is shown by a normalized potential given by the potential energy divided by the $\pi\pi^*$ excitation energy at the S_0 minimum. Thus, a normalized energy value of 0.5 lies halfway between the ground state minimum energy and the $\pi\pi^*$ state in the Franck-Condon region. At the S_1-S_0 C1Pyr geometries, the normalized energy varies by roughly 0.15 across all of the molecules. The highest and lowest C1Pyr normalized energies are a π-donor and a π-acceptor, respectively; however, intermediate values do not show a trend.

In contrast, the S_1-S_0 C2Pyr energies are clearly divided into π-acceptors with greater normalized energies and π-donors with smaller normalized energies in comparison to ethylene. The shift from strongly π-accepting VNt to strongly π-donating VAm is 0.32, which corresponds to a 2.24 eV (7×0.32) difference assuming a $\pi\pi^*$ excitation energy of 7.0 eV in the FC region. The greater difference in energies at the C2Pyr geometry may be in some way related to the localization of charge at C2 in the resonance picture, as illustrated in Figure 3.1.

The origin of the energetic differences at the two pyramidalization conical intersections was previously postulated to be caused by the relative stabilization or destabilization of electron density at the pyramidalizing carbon, as seen for acrylonitrile.[140] This difference

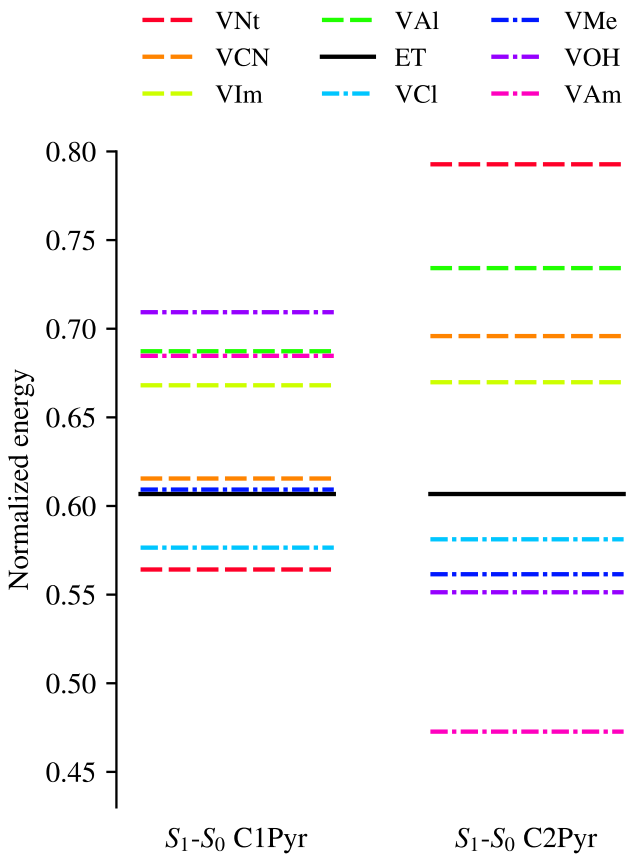

Figure 3.3: Comparison CASPT2/cc-pVTZ C1Pyr and C2Pyr MECI energies normalized by the $\pi\pi^*$ excitation energy. Dashed lines represent π-acceptors and dash-dotted lines represent π-donors.

in electron density at the Franck-Condon point is shown in Figure 3.4a, where the local electron density is represented by the Hirshfeld charge difference of C2 and C1 on the $\pi\pi^*$ state, *i.e.* $q_{C2} - q_{C1}$. For π-donors, the MECI energy difference has a positive correlation with the charge difference which suggests a greater electron density on C2 leads to a more stable MECI from pyramidalization at that carbon. The charge of vinylchloride deviates from this line due to its competing σ-acceptor ability.[53] This trend appears to break down entirely for all π-acceptors other than VCN. This may suggest that the resonance picture poorly predicts the $\pi\pi^*$ state properties in the FC region; however, the consistency of trends across all molecules at the pyramidalized geometries suggests that the issue may come from the charge determination itself. The charge difference for acrolein is in agreement with CHELPG charges[150,151] but disagrees with Bader charges.[152,153] The strong correlation of iterative Hirshfeld and CHELPG charges has been noted previously.[80] Figure B1 in the supporting information shows that the breakdown of the trend also occurs for ground state converged Hirshfeld charges and Mulliken charges. The Hirshfeld charges at the conical intersections are consistent for all molecules as shown in Figure B2 with no significant substituent trend.

Inspection of the pyramidalization conical intersection geometries also revealed a trend in the pyramidalization angles, τ_{Ci}, defined in the same way as an out-of-plane angle of a carbon atom with the plane corresponding to the CH_2 group of the opposite carbon. Figure 3.4b shows both C1Pyr (filled) and C2Pyr (open) MECIs by differences in pyramidalization angles. As suggested by the geometry labels, C1Pyr geometries pyramidalize primarily at C1 and C2Pyr geometries at C2. More importantly, the difference in pyramidalization angles decrease to near zero with greater π-acceptance in the C1Pyr case or greater π-donation at the C2Pyr case. The C1Pyr geometry of VNt and the C2Pyr geometry of VAm resemble that of the formaldimium cation which has a conical intersection at a structure corresponding to a 90° twist about the central C−N bond.[42,141] Although the many-dimensional conical intersection seam likely extends to greater pyramidalization angles as seen with substituted acrylonitriles,[140] the correlation between geometric differences and shifts in the potential energies of the MECIs has an important implication for the shape of the surface between conical intersections, as discussed in the next section.

3.4 Revisiting the biradical model

A reduced dimensionality treatment of the potential energy surfaces in the region of the MECI, inspired by the model of Michl and Bonačić-Koutecký for biradicals and biradicaloids[42,141] can be used to more explicitly illustrate the effect of different chemical substituents on the nonadiabatic dynamics of ethylenic systems. Since our main interest here is in the nonadiabatic dynamics that result from absorption of an ultrafast excitation pulse,

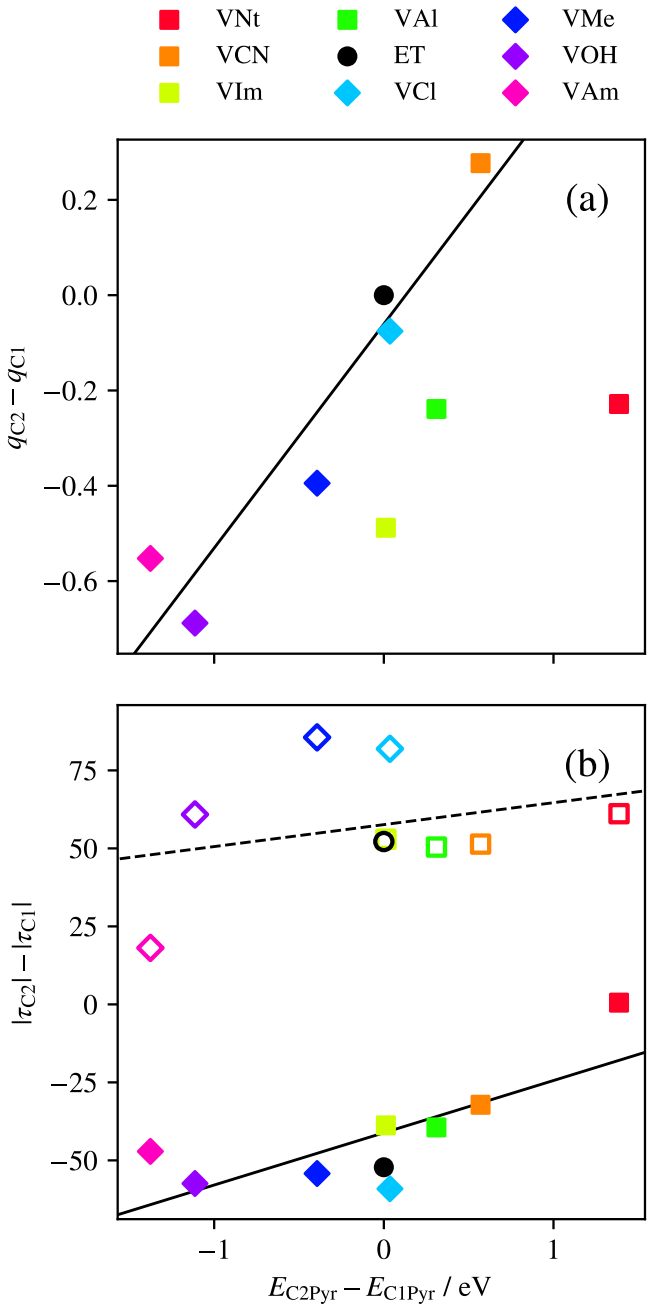

Figure 3.4: Correlation between potential energy differences of MECIs and (a) charges on the $\pi\pi^*$ state at the S_0 minimum geometry as well as (b) differences in pyramidalization angles at the two carbons. Lines indicate a linear least-squares fit excluding VNt, VIm and VAl in (a), and including all molecules in (b). Squares represent π-acceptors and diamonds represent π-donors. The filled shapes and solid line in (b) are C1Pyr geometries and the open shapes and dashed line are C2Pyr geometries.

the curvature of the pertinent excited state potential energy surface in the FC region is of particular import since it will determine the short time evolution of the wave packet. Furthermore, in the presence of large potential gradients these initial motions are often essentially irreversible. We will thus define δ_0 and γ_0 to be the magnitude of polarization and the orthogonality of the p-orbitals of the FC structure, respectively.

Furthermore, the coordinate dependence of the original model was implicit in the values of the molecluar integrals that defined the coupling parameters. Here, we replace configuration interaction matrix elements with coordinate dependent functions assuming only three degrees of freedom are relevant: the torsional coordinate (ϕ_{CC}) about the C=C bond which modulates the orthogonality of the two p-orbitals (γ), and two effective coordinates comprised of pyramidalization and CH_2 scissoring ($\tau_{\mathrm{C}i}$) at each of the carbon atoms which modulate the polarization (δ). We expand these parameters using a Taylor series truncated at second order. This yields an energy for state I given by

$$E'_I(\phi_{\mathrm{CC}}, \tau_{\mathrm{C1}}, \tau_{\mathrm{C2}}) = E_I(\gamma, \delta) + a_0(\phi_{\mathrm{CC}} - \pi/2)^2 + a_1\tau_{\mathrm{C1}}^2 + a_2\tau_{\mathrm{C2}}^2, \tag{3.10}$$

$$\gamma(\phi_{\mathrm{CC}}) = b_0(\phi_{\mathrm{CC}} - \pi/2) + \gamma_0, \tag{3.11}$$

$$\delta(\tau_{\mathrm{C1}}, \tau_{\mathrm{C2}}) = b_1|\tau_{\mathrm{C2}}| - b_2|\tau_{\mathrm{C1}}| + \delta_0, \tag{3.12}$$

where $E_I(\gamma, \delta)$ is the Ith eigenvalue of Equation 3.1, and a_i and b_i are scaling factors. In the case of ethylene, $\delta_0 = 0$, and thus polarization across the C=C bond can only occur via displacements in $\tau_{\mathrm{C}i}$. For the substituted species discussed in the previous section, the chemical substituent will generally result in $\delta_0 \neq 0$, thereby introducing a zeroth order polarization and a corresponding differential shift of the potential energies.

The utility of the model can be illustrated with reference to the molecules studied in the previous section. In Figure 3.5c, values to the right of the vertical line denote C2 pyramidalization and values to the left of the line indicate C1 pyramidalization. Based on the difference in energies, the figure must represent a π-donor because the postive δ_0 implies a greater electron density on C2. If the coordinate assignment is switched the figure would represent a π-acceptor. Here the origin of the potential energy differences of the two conical intersections can be clearly seen. The additional amount of polarization required decreases for one conical intersection and increases for the other. This was seen for substituted ethylenes in the previous section where a stronger π donation or acceptance effect leads to a smaller pyramidalization angle at the corresponding MECI geometry. Thus, the addition of a substituent leads to a shift of the potential energy surface in terms of the proximity of the conical intersections in addition to their relative potential energies.

Additive and subtractive effects of a π-donor and a π-acceptor should also be possible to predict from the model. A 1,1-substitution of a functional group of each type should reduce the polarization at the Franck-Condon geometry and thus reduce the initial polarization,

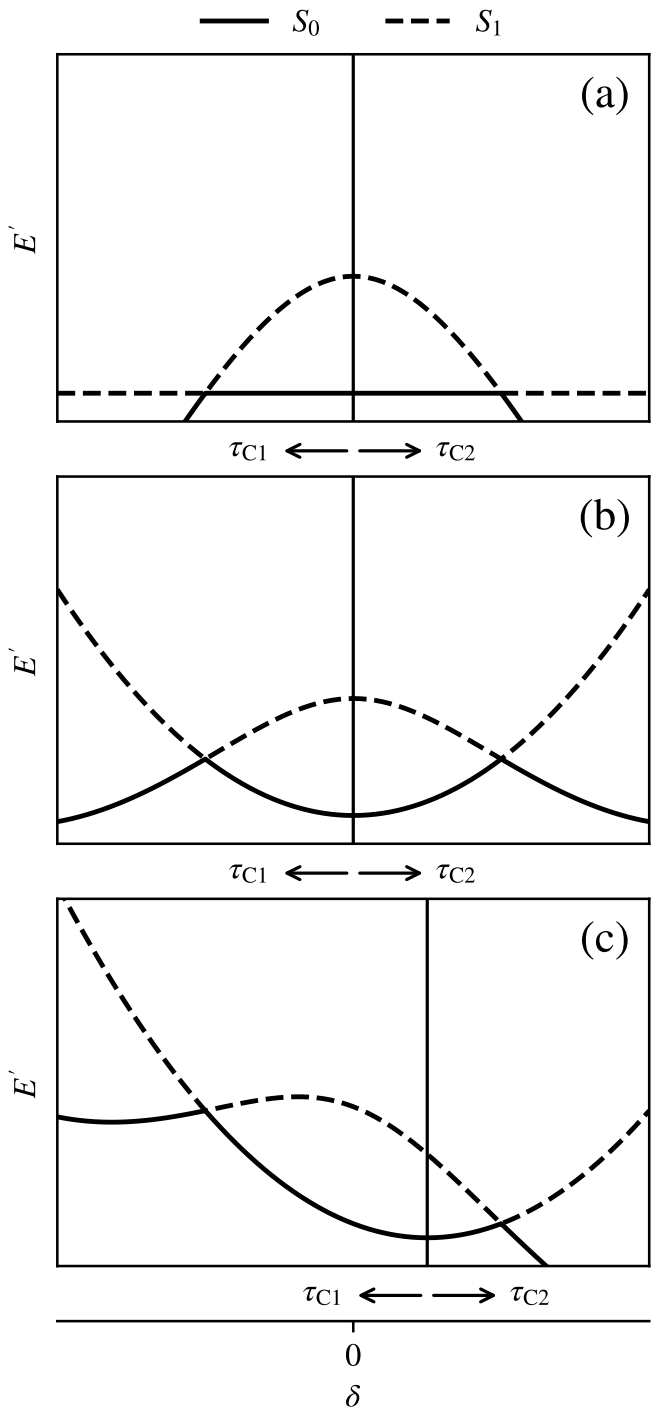

Figure 3.5: Biradical model for (a) no second order dependence ($a_i = 0$) as in the original model, (b) energy dependence representing no initial polarization across the double bond ($a_i \neq 0$, $\delta_0 = 0$) and (c) energy dependence with the initial polarization at the equilibrium geometry ($\delta_0 \neq 0$). Note that motion to the right and to the left of the vertical black lines represents different internal coordinates.

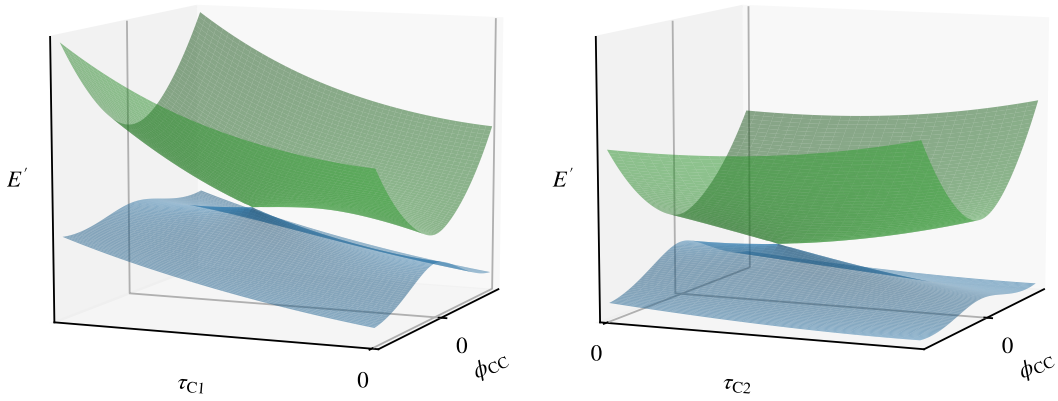

Figure 3.6: The biradical model extension for a π-donor all three degrees of freedom shown.

while a 1,2-substitution should increase the initial polarization. Indeed, a closer inspection of the potential energies of methyl-substituted acrylonitrile show the weak π-donor effect of the methyl group:[140] Compared to the VCN MECI energy difference of 1.09 eV (calculated at the MR-FOCI/6-31G* level of theory), 1-substitution (methacrylonitrile) has an energy difference of 0.78 eV and 2-substitution (crotonitrile) has a difference of 1.34 eV. Such an additive/subtractive effect could be used to effectively localize dynamics to a desired site in the case of a larger conjugated molecule.

This extension to the previous model has other interesting implications for ethylene systems. The non-zero δ_0 value gives rise to a gradient on the potential energy surface along the two coordinates which suggests that substituents can have a local effect on the initial gradients following a vertical excitation to the $\pi\pi^*$ state. It should be noted that this effect is less pronounced than Figure 3.5c suggests because of the non-zero value of γ in the Franck-Condon region, as illustrated in Figure 3.6. This has interesting implications for systems with other non-ethylene-type conical intersections where a substituent may "push" an excited wavepacket along a particular coordinate. In addition, in highly polarized systems (or "strongly heterosymmetric biradicaloids"[42,141]) the value of δ_0 may occur at a δ greater than that of the conical intersection. In such a system, pyramidalization would serve to decrease the polarization between the two carbons, and both conical intersections are predicted to occur along the same pyramidalization coordinate.

3.5 Nonadiabatic dynamics simulations

Two molecular systems, namely VCN and VAm, were selected from the series of molecules above in order to show how the effects of π-donor *vs.* π-acceptor substitution manifest in

a complex nonadiabatic dynamics simulation. Figure 3.7 shows the AIMS adiabatic state populations as a function of time for VCN and VAm. The timescales are the opposite of the expected results from dynamical arguments in the previous section. It was expected that the π-donation effect of VAm should favour C2 pyramidalization, which has a greater frequency than C1 pyramidalization in VCN and thus should lead to faster excited state decay; however, this does not take two additional effects into account: (1) coupling to lower-lying states and (2) the energetic difference between the FC region and the pyramidalized conical intersection. The relevant points on the potential energy surfaces are given in Figures B3 and B4 in the supporting information.

The present dynamics simulations for VCN closely resemble previous results that employed different initial condition selection criteria. In that study, the intial conditions were chosen to be consistent with the experiment pump energy and bandwidth.[140] The S_2 and S_1 states are strongly coupled in the FC region with spawning between the states arising from C=C stretch vibrations. However, the overall decay of the initially prepared S_2 state is associated with torsion about the C=C bond. After passage to the first excited state, over 95% of the population was transferred to the ground state at geometries in the region of the C1Pyr MECI. This result is a very clear example of directed dynamics, whereby the π-accepting cyano group tilts the potential energy surface towards a single decay pathway.

The AIMS simulations of the VAm excited state dynamics reveal that the influence of the π-donor amino group on this process is more nuanced than in the case of the cyano substituent. Figure 3.8a shows the S_1 adiabatic state wavepacket density as a function of the C2 pyramidalization angle. The initial decay from S_2 to S_1 is dominated by C=C torsion and a rapid pyramidalization at C2, leading to most of S_1 population initially at a pyramidalization angle of between 60° and 80°. Note that this is somewhat different from what is observed for ET and VCN, where torsion about the C=C bond largely preceeds pyramidalization at one of the carbon atoms. In this case, the curvature of the PES in the FC region is so distorted by the steep gradients to the C2Pyr MECI that pyramidalization and torsion occur simultaneously.

This initial, and strongly gradient-directed, pyramidalization results in an initial distortion that is much greater than the pyramidalization angle observed for the S_1-S_0 MECI, leading to "ringing" in the CH_2 group vibrations for the duration of the excited state dynamics. Much of the population appears to decay to S_0 around a pyramidalization angle of 20–40°, but the remaining population has sufficient kinetic energy for other decay pathways to be accessed. In addition to the expected C2 pyramidalization and nonradiative decay to the ground electronic state, excited state H and H_2 dissociation may also occur. In certain cases, spawning to the ground state occurred with a hydrogen atom well separated from the remaining fragment. To determine the relative importance of these two pathways, the molecular geometries were characterized using a bond connectivity criteria

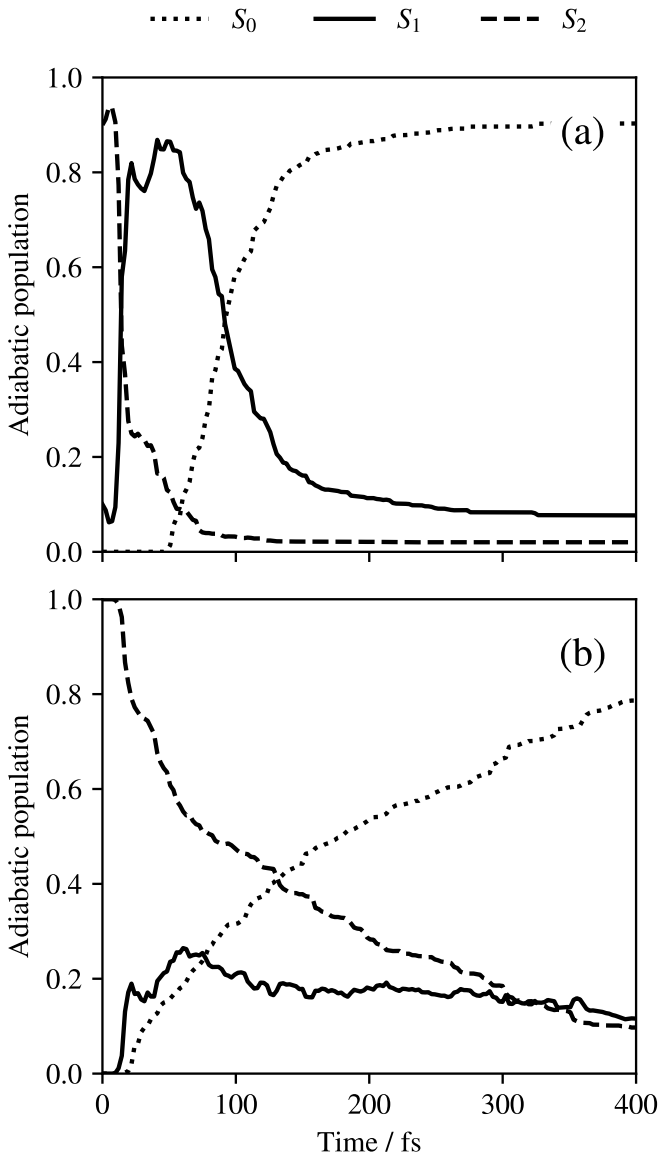

Figure 3.7: Adiabatic populations as a function of time for (a) VCN and (b) VAm.

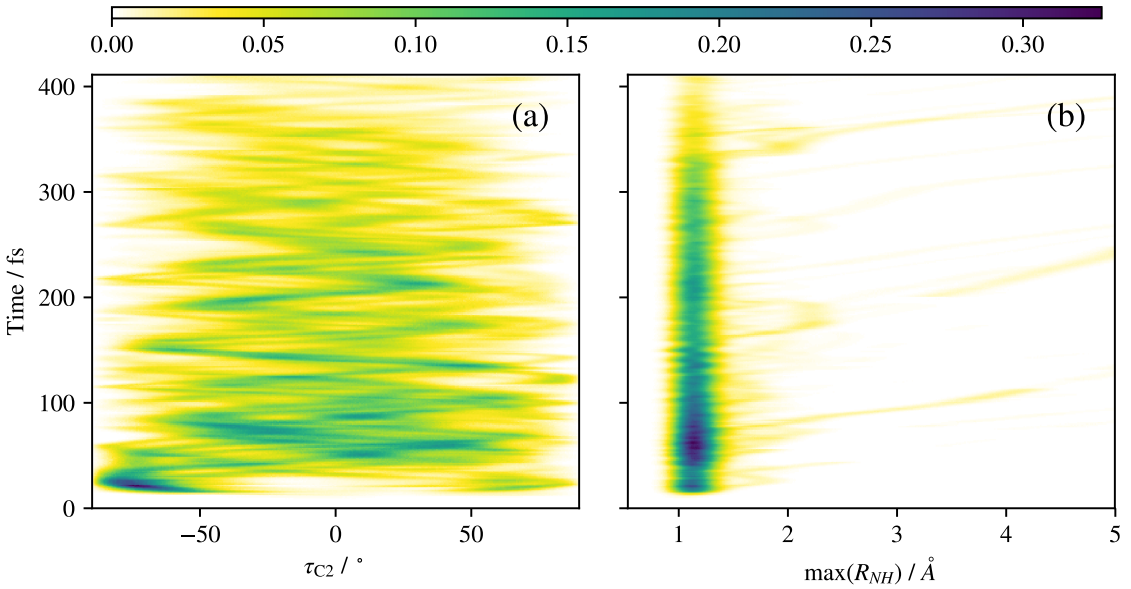

Figure 3.8: VAm wavepacket density on the S_1 surface as a function of time along (a) the C2 pyramidalization angle and (b) the maximum of the N−H stretch.

(determined solely from interatomic distances). The connectivity of each atom in each spawn geometry was then compared to the ground state minimum geometry. Additional details on assignment of connectivity can be found in the supporting information. Cases with a lower connectivity than the ground state structure were labelled as "dissociated" geometries. Using the same analysis for VCN, only 0.1% of the population transferred to the ground state was found to have corresponded to structures with a different connectivity than the S_0 minimum and corresponded to CN migration.

Much of the H dissociation occurs at the NH_2 group. This is illustrated by the maximum N−H bondlength of the wavepacket on the S_1 state as a function of time in Figure 3.8b. Multiple dissociation events can be seen within the figure, with some population returning to bonded geometries after a separation of more than 2 Å. The dominant dissociation paths appear to occur every 150 fs which is arises due to coupling of these nuclear displacements to the C2 pyramidalization coordinate on the S_2 state.

Roughly 32% of the decay of VAm occurred via structures with some degree of bond cleavage, whereas the remaining population was transferred to the ground state in regions about the C2Pyr MECI geometry. The amount of population transferred as a function of time is shown in Figure 3.9. There is a gradual decay in the amount of population transferred via bonded geometries, whereas the population transferred through dissociated geometries remains constants throughout. Performing a similar bonding analysis for S_2-S_1 spawn geometries reveals that 99.5% of the population transfers through geometries

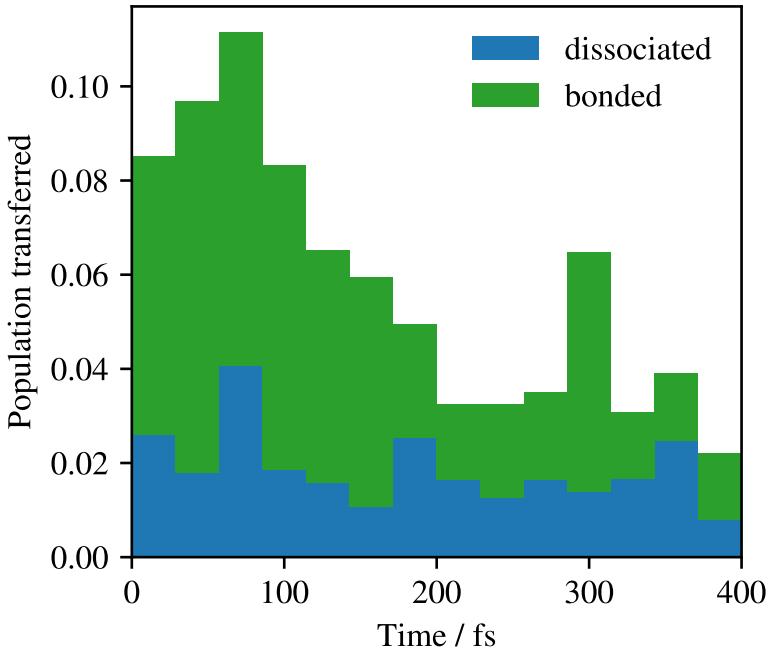

Figure 3.9: Stacked bar plot of VAm population transferred from S_1 to S_0 as a function of time for the two geometry types.

resembling C1 and C2 pyramidalization. Figure 3.3 provides the basis for the rationalization of these results. In particular, the amino substituent is particularly effective at "tilting" the potential energy surfaces toward the C2Pyr MECI, such that the energy difference between the C1Pyr and C2Pyr MECI is 1.2 eV and the amount of momentum acquired by a trajectory basis function before it reaches the conical intersection is sizeable. Any population that is deflected by the initial pass through the coupling region will have sufficient internal energy to sample large swaths of phase space, including those regions that lead to dissociation.

Despite the additional decay pathways for VAm, the fact remains that the C2Pyr path is dominant, especially at earlier times. The partial charge difference and the difference in pyramidalization angle at the spawn geometries of the two molecules are shown in Figure 3.10, excluding the dissociated geometries of VAm. The differences in partial charge can clearly be seen from the figure, with VCN geometries tending towards more negative charge on C1 and VAm having more negative charge on C2. As expected, the carbon with the greater charge density also shows a greater pyramidalization angle. The average charge between the two different molecules appears to have a slightly negative value which is consistent with a greater polarization on the β-carbon. In both cases, there is an additional distribution of pyramidalized geometries with near zero difference in charge. The lack

of polarization likely results from the change in electronic character in the region of the conical intersections. The values of $|\tau_{\mathbf{C2}}| - |\tau_{\mathbf{C1}}|$ *vs.* $q_{\mathbf{C2}} - q_{\mathbf{C1}}$ for MECI geometries of substituted ethylenes are given in Figure B2 in the supporting information, which shows that the dominant distribution corresponds to a closed shell configuration. The distribution with little polarization is thus a result of an open-shell singlet configuration.

3.6 Conclusions

We have shown that functional groups which induce selective polarization in π-bonded structures may be used to influence the $\pi\pi^*$ (bright) excited state dynamics in a predictive manner. Previously, we showed how this effect dominates in acrylonitrile and its methyl-substituted derivatives.[140] The influence of polarization across the C=C bond gives rise to consistent trends in not only the differential energies of particular minimum energy conical intersections, but also in the relative magnitude of the nuclear displacements required to access such structures. A reduced dimensionality description of the dynamics, inspired by a previously reported biradical model, is shown to predict the dominant decay pathway of both VCN and VAm after excitation to the ethylene $\pi\pi^*$ state. In the absence of competing effects from intermediate states, the relative geometric changes from the ground state minimum to the MECIs could be used to predict decay timescales. These results demonstrate that it may be possible to understand photochemical reactions based on local perturbations of the electron density, which will enable predictive models for internal conversion mechanisms of $\pi\pi^*$ systems. The potential applications of such models are numerous: In systems with competing decay pathways from different internal motions, selective substitution could be used to produce desired photoproducts in a predictable manner. This has the potential to be used in organic synthesis, particularly in cases where competing thermal reactions may lead to unwanted products. In addition, organic photoswitches could be tailored for desired geometric and energetic changes using chemical substitution leading to fine-tuned properties in photoharvesing and artificial photosynthesis. Further work is required to extend these results to more complicated systems including multiple competing substituents and solvent molecules in order to determine their use in real-world applications.

Acknowledgments

R.J.M. and M.S.S. acknowledge financial support from the Natural Sciences and Engineering Research Council of Canada (NSERC).

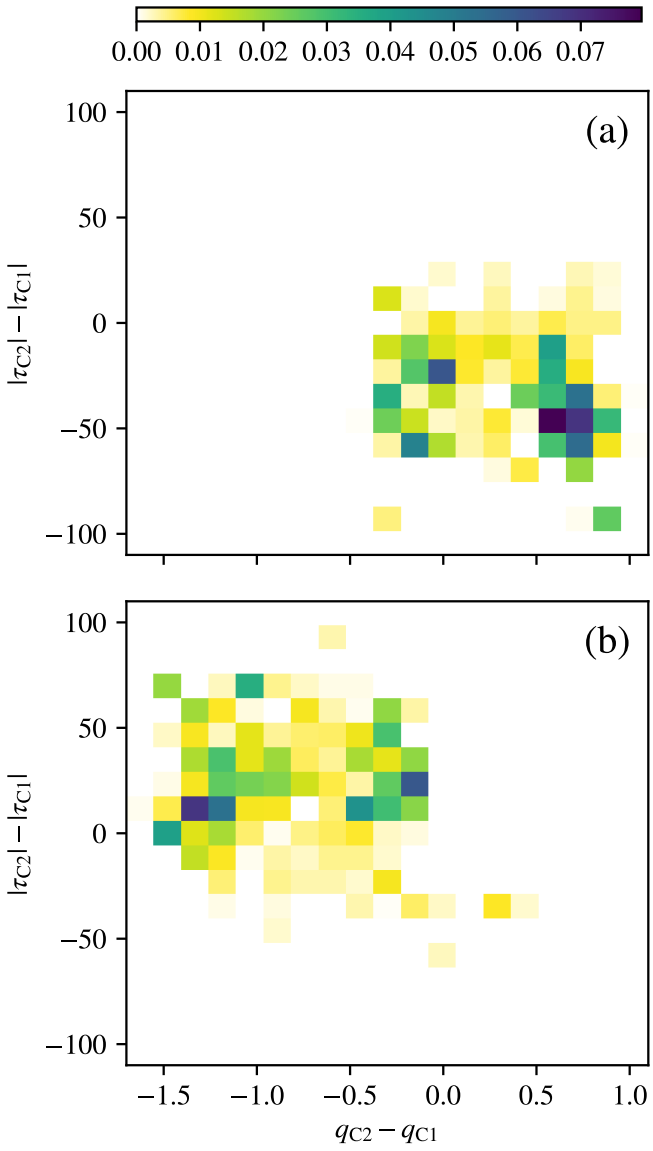

Figure 3.10: Partial charge differences and differences in pyramidalization angles at the AIMS spawning geometries of (a) VCN and (b) VAm. Populations are normalized to the total of the bonded spawn geometries.

Chapter 4
Site-selective isomerization of cyano-substituted butadienes: Chemical control of nonadiabatic dynamics

R.J. MacDonell,[1] and M.S. Schuurman[1,2]

Reprinted with permission from *J. Phys. Chem. A* **2019**, *123*, 4693–4701.
https://doi.org/10.1021/acs.jpca.9b02446.

This work helped us to understand how a cyano-substituent can be used to affect excited-state dynamics and photoisomerization is a site-specific way. I (RJM) characterized potential energy surfaces, performed nonadiabatic dynamics simulations and wrote the interpretation in the text. MSS supervised the work and provided feedback.

[1] Department of Chemistry and Biomolecular Sciences, University of Ottawa, Ottawa, Ontario K1N 6N5, Canada
[2]National Research Council of Canada, 100 Sussex Drive, Ottawa, Ontario K1A 0R6, Canada

Abstract

The photochemistry of organic chromophores generally involves the co-evolution of the electronic and nuclear degrees of freedom. To obtain a specific and predetermined photochemical reaction outcome, chemical substitution can be used to selectively alter the underlying electronic potential energy surfaces to favour a particular reaction pathway. We show using *ab initio* simulation that substitution of *s-trans*-1,3-butadiene with a cyano group can effectively "direct" a molecular wavepacket to particular regions of the seam of conical intersection and either favour or inhibit photo-initiated *cis-trans* isomerization. The substituent is able to effect this control due to the formation of transient charge-separated electronic structures that arise during the nonadiabatic dynamical process. The atomic site at which this charge develops can be selectively stabilized (or destabilized) depending on the location of the cyano substituent and gives rise to a single dominant decay pathway. This work aims to demonstrate how the application of known electron density effects to ultrafast dynamics may be used to obtain desired photochemical reactions and properties.

4.1 Introduction

The photochemistry of conjugated organic molecules is ubiquitous in natural light-driven processes such as vision,[44,45,85,133,134,154,155] bioluminescence,[156–158] and light harvesting.[159–161] Many of these systems share a common feature of isomerization leading to a biochemical signalling cascade, thus transferring the energy of a photon into mechanical motion. For these processes to be repeatable and reversible, isomerization typically occurs at a specific atom or bond, in contrast to the highly varied gas phase photochemistry of analogous molecules. This site-specificity is largely attributed to the chemical environment of the photoactive molecule or chromophore.[42,44,45] For example, simulations and, more recently, experimental evidence have shown that the photoisomerization of the retinal chromophone in the rhodopsin class of proteins is indeed sensitive to electronic effects at highly specific positions in the surrounding environment.[44,45,155] Retinal appears to be optimized for a maximum quantum yield from isomerization at a single C=C bond due to the steric and electronic effects of the protein cavity; however, the details of how similarly high quantum yields can be achieved synthetically remain elusive.

Photochemical isomerization of polyenes has long been studied due to changes in structure and easily observable spectroscopic quantities following the absorption of a photon. The electronic structures of these molecules are characterized by low-lying electronic states with $\pi\pi^*$ and $(\pi^*)^2$ character. The $\pi\pi^*$ state has a large transition dipole moment with the ground state and is considered spectroscopically "bright", whereas the doubly-excited $(\pi^*)^2$ state is spectroscopically "dark", *i.e.* its transition dipole moment with the ground state

is small. In nonpolar conjugated polyenes, the $(\pi^*)^2$ state is typically stabilized relative to the $\pi\pi^*$ state and can have a stable excited state minimum-energy geometry in larger molecules. As a result, photoexcitation of larger polyenes to the $\pi\pi^*$ state is characterized by rapid relaxation to the $(\pi^*)^2$ state followed by relatively slow fluorescence to the ground state. Conversely, in shorter polyenes the $\pi\pi^*$ and $(\pi^*)^2$ states may be close in energy and, following photoexcitation, both electronic states can couple to the ground state via conical intersections.

In polar conjugated polyenes and shorter nonpolar polyenes, the $\pi\pi^*$ state is relatively low in energy and can play an important role in their excited state dynamics. Their decay typically involves isomerization about one C=C double bond and thus closely resembles the behaviour of ethylene.[36,56,162,163] Repulsion between the out-of-phase lobes of the π^* orbital leads to a 90° torsion about the C−C bond. The molecule then undergoes a barrierless pyramidalization at one carbon with a concurrent increase in charge density to reach the so-called twist-pyramidalization conical intersection between the ground state and the $\pi\pi^*$ state.[16,21,124] This twist-pyramidalization conical intersection is found in the dynamics of systems with at least one vinyl group, such as acrolein,[54] acrylonitrile,[140,163] vinylamine,[163] 1,3-butadiene,[36,37,164] 1-(trifluoromethyl)butadiene,[165] and 1,4-cyclohexadiene.[129]

In addition to twist-pyramidalization-type conical intersections ($\pi\pi^*$–S_0), longer polyenes have lower-energy conical intersections with a tetraradical character ($(\pi^*)^2$–S_0). These conical intersections are characterized by three- and four-body interactions involving large scale deformations of the carbon backbone such as the "transoid", "cisoid" (or "kinked-diene") and ring closure conical intersections of 1,3-butadiene and 1,3,5-hexatriene.[33,37–39,166,167] There remains some debate over the influence of the different conical intersections on the dynamics and photoproducts. The transoid and cisoid geometries are often associated with a "hula-twist" pathway, which is volume-conserving in nature and involves the isomerization of adjacent single and double bonds.[167,168] This association is motivated by the similarity of minimum energy conical intersection (MECI) geometries to an intermediate structure in the rotation of the two carbon–carbon bonds,[36,166] and the involvement of a dark band in the transient absorption spectra of previtamin D suggests this pathway for *cis–trans* isomerization.[167,169] Alternatively, it has been suggested that the transoid MECI involves additional torsion about a second C=C double bond and cannot be involved in a hula-twist pathway for larger polyenes. Instead, a pathway was proposed involving the ethylenic pyramidalization and H bridging MECI for *cis–trans* isomerization of polyenes.[38,39]

1,3-Butadiene (BD) is an intermediate model system between ethylene and longer-chain, nonpolar conjugated polyenes. Theoretical studies of *s-trans*-BD have revealed that the first and second singlet excited states (S_1 and S_2, respectively) are nearly degenerate and have the expected $\pi\pi^*$ and $(\pi^*)^2$ characters. These two states are coupled along the bond alternation coordinate,[37,170] and accurate simulation of the absorption spectrum has been

performed excluding in-plane vibrational modes.[171] Spectral simulations employing a vibronic coupling model that included out-of-plane vibrational modes were able to reproduce the absorption spectrum and predicted that non-radiative decay occurs near the transoid conical intersection region.[34,35] Not included were the motions directing towards ethylenic conical intersections involving pyramidalization at the terminal (C1) and central (C2) carbons, the former of which is close in energy to the transoid intersection.[36] Recently, the nonadiabatic decay of BD was measured by time-resolved photoelectron spectroscopy[164] and simulated with ab initio multiple spawning (AIMS).[37] The AIMS simulations included all nuclear degrees of freedom and revealed a competition between the transoid and ethylenic decay pathways, which could be modulated by selectively stabilizing/destabilizing the $\pi\pi^*$ and $(\pi^*)^2$ states.[37]

In synthetic organic chemistry, ground-state reactions can be optimized by altering the electron density and potential energy landscapes in a predictive fashion using functional group substitution. A functional group may either withdraw electron density from an adjacent site (electron withdrawing group, EWG) or donate electrons to an adjacent site (electron donating group, EDG). In π-bonded molecules, these may also be called π-acceptors and π-donors, respectively. Furthermore, EWGs and EDGs alter the electron density and thus the electronic potential energy surfaces, and the addition of bulky ligands can lead to the destabilizing of certain motions through steric hindrance. In dynamics, the mass associated with a functional group has an inertial effect, which modulates the period of important motions in a molecule and can influence the outcomes of barrierless reaction pathways.

Chemical substitution has been employed previously to influence the nonadiabatic dynamics of photoexcited molecules. In particular, different functional groups can be used to either affect the momentum along important vibrational coordinates, or to affect shape of the potential energy surfaces including the relative energies of different conical intersection moieties. For example, methyl substitution of ethylene causes stabilization of the Rydberg-type states leading to longer decay times in addition to the inertial effect characterized by slowing the C=C dihedral motion.[114] Conversely, methyl-substituted allene shows mostly inertial effects by favouring central carbon bending with increasing substitution.[56] The methyl group is not an electronically inert ligand, as it can also significantly alter the stability of $\pi\sigma^*$ states[172] and it acts as a weak π-donor.[140,163] Recently, we have studied the effects of π-accpeting and π-donating substituents on the potential energy surfaces of substituted ethylenes and shown that there is a trend in the geometry, atomic charge and energy of minimum-energy conical intersections as a function of the donor or acceptor strength. The AIMS simulations of π-acceptor and π-donor molecules revealed that the dominant decay pathway could be predicted from the substituent.[163] Steric[173] and electronic[165,174] substituents exhibit the predicted effects for the potential energy surfaces of butadiene, but, to date, the dynamical effects have not been simulated.

Here, we employ functional group substitution on *s-trans*-butadiene to influence the photochemical reaction outcomes following photoexcitation. We compare substitution of a cyano (CN) group at C1 (terminal carbon) or C2 (central carbon) to unsubstituted butadiene to demonstrate this effect, based on the mechanism shown in Scheme 4.1. After photoexcitation, the molecule undergoes a twist about the C1–C2 bond (**C1Tw**) before heading toward distinct regions on the conical intersection seam: H1 bridging (**H1Br**), R1 bridging (**R1Br**, equivalent to **H1Br** if R1 = H), R2 bridging (**R2Br**) and C2 transoid (**C2Tr**). Note that we use the bridging notation since the CN group tends to bend in-plane towards the opposite carbon (as seen for acrylonitrile[140]) as opposed to the H pyramidalization motion of ethylene and polyenes.[16,36,39] We use the symbol ⧖ to denote minimum-energy conical intersections, analogous to the symbol ‡ for transition states.[7,8,12,13] As previously shown for acrylonitrile,[140] the cyano group is a π-acceptor and is expected to favour the pyramidalization or bridging at the substituted site. Substitution on C1 should favour photoproduct **2** due to the localization of dynamics to the terminal carbon; however, the ultimate reaction products are not possible to measure from gas-phase simulation due to the excess kinetic energy of the molecule on the ground state. The ability of the cyano group to influence the potential energy surfaces and photochemical yields are revealed by on-the-fly AIMS simulations of all three molecules.

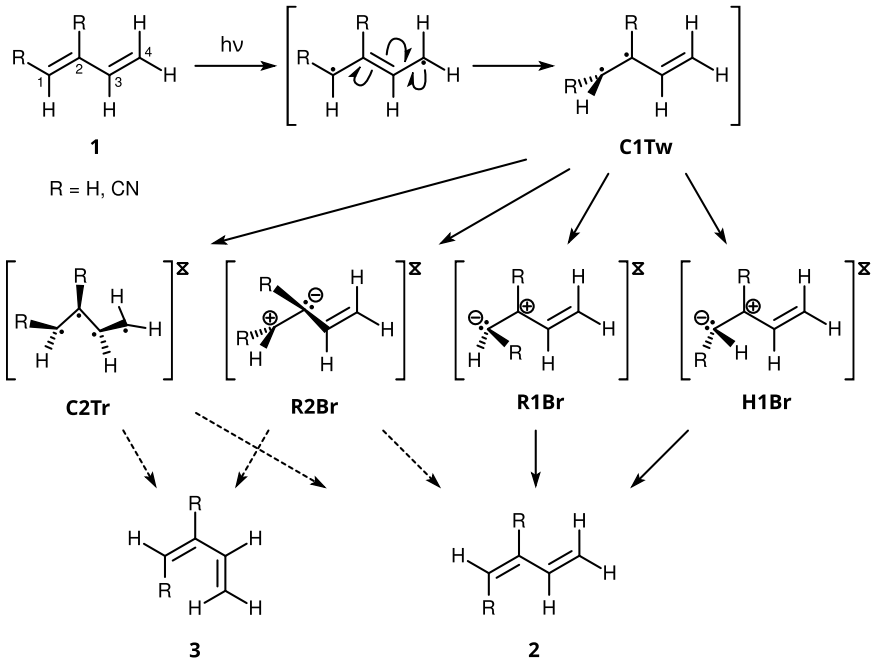

Scheme 4.1

4.2 Computational Methods

Critical points on the potential energy surface of (all *trans*) 1,3-butadiene (BD), 1-cyano-1,3-butadiene (1-CNBD) and 2-cyano-1,3-butadiene (2-CNBD) were optimized using single-excitation multireference configuration interaction with a 6-31G* basis (MR-CIS/6-31G*) using the COLUMBUS electronic structure package.[120] A four-electron, four-orbital active space was employed for BD and the complete active space self consistent field (CASSCF) reference was averaged over three states. For both cyano-substituted species, a six-electron, six-orbital active space was used with a five state average. Single point energies were compared with multistate complete active space second order perturbation theory calculations with a cc-pVTZ basis (MS-CASPT2/cc-pVTZ) using the Molcas electronic structure package,[147,148] with the full 8 electron, 8 π orbital active space for the cyanobutadienes.

Ab initio simulation of the excited-state dynamics of all three molecules were performed using the on-the-fly *ab initio* multiple spawning (AIMS) method.[88,89,119] The AIMS wavefunction $\mathbf{\Psi}(\mathbf{r}, \mathbf{R}, t)$ is expressed in terms of electronic coordinates $\mathbf{r}$, nuclear coordinates $\mathbf{R}$ and time t in a basis of electronic functions ψ_j^I and nuclear functions χ_j^I for all trajectories j and electronic states I as

$$\mathbf{\Psi}(\mathbf{r}, \mathbf{R}, t) = \sum_{I=1}^{N_s} \sum_{j=1}^{N_I(t)} c_j^I(t) \psi_j^I(\mathbf{r}, \mathbf{R}) \chi_j^I(\mathbf{R}; \mathbf{R}_j^I(t), \mathbf{P}_j^I(t), \gamma_j^I(t)). \tag{4.1}$$

The centres of the Gaussian nuclear basis functions χ_j^I are associated with a time-dependent position $\mathbf{R}_j^I(t)$, momentum $\mathbf{P}_j^I(t)$ and phase $\gamma_j^I(t)$, which evolve on the electronic potential according to classical equations of motion. The complex amplitudes $c_j^I(t)$ are solved at each time step using the time-dependent Schrödinger equation. The electronic potential energies and their gradients are determined up to a maximum number of states N_s predetermined for the dynamics of interest. The nonadiabatic coupling is also evaluated at each time step, and when the product of coupling and nuclear velocity cross a threshold, a new basis function may be introduced on the coupled state, leading to an increase in the number of trajectories $N_I(t)$ over time.

For each molecule, 40 initial geometries and momenta were sampled from a $v = 0$ vibrational distribution centred around the RI-MP2/cc-pVDZ ground state minimum geometry optimized with the Turbomole electronic structure package.[175,176] The initial state was selected by the greatest transition dipole out of S_1 and S_2. Each initial geometry was treated as an independent simulation starting with a single trajectory basis function with $\gamma(0) = 0$ (*i.e.* the "independent first-generation approximation"), and the wavefunction was taken as the incoherent sum over all simulations.[90,91] This yielded a total of 577, 289 and 530 trajectories for BD, 1-CNBD and 2-CNBD, respectively. The AIMS potential energy was

calculated for all trajectories at the MR-CIS/6-31G* level of theory. Iterative Hirshfeld atomic charges and spawn populations were determined for AIMS spawn geometries at the same level of theory, as detailed previously.[163]

4.3 Results

4.3.1 Potential energy surfaces

The main critical points on the MR-CIS/6-31G* potential energy surfaces of the three molecules are shown in Figure 4.1, including minimum-energy structures and local minima on the conical intersection seams, *i.e.* minimum energy conical intersections (MECI). Comparison of these and other optimized geometries to MS-CASPT2/cc-pVTZ energies show qualitative agreement, as seen in Figures C3–C8 in the supporting information (SI, Appendix C). The lowest two excited states of BD correspond to $(\pi^*)^2$ and $\pi\pi^*$ characters, respectively. In contrast, the excited states of cyanobutadiene (ordered by increasing vertical excitation energy) are $\pi\pi^*$, $\pi_{CN}\pi^*$ and $(\pi^*)^2$, while the MS-CASPT2 calculations interchange the ordering of the $\pi_{CN}\pi^*$ and $(\pi^*)^2$ electronic states. This most notably has an effect on the energies of the S_2–S_1 MECIs of 1-CNBD, for which the **C4Tw** MECI is lower in energy than the **C1Tw** MECI using MS-CASPT2, in agreement with results for the electron withdrawing substituent CF_3.[165] Fortunately, the first excited state of both cyanobutadienes is of $\pi\pi^*$ character, and the relative energies of the S_2 and S_3 states in the Franck-Condon region is expected to be minimal.

The resonance effects from CN π-acceptance are immediately clear from the relative energies of the conical intersection moieties, as shown in Figure 4.1. Energies of **H1Br** and **R1Br** are lowered by 0.5–0.7 eV by cyano substitution at carbon 1 and raised by 0.2 eV following substution at C2. A more pronounced difference is seen for **R2Br**, where 1-CNBD and 2-CNBD energies are raised and lowered by nearly 1 eV, respectively. Cyano-substitution also appears to have an effect on the nonpolar transoid MECIs, where **C2Tr** is stabilized relative to BD upon cyano substitution. This is likely due to the inclusion of the C≡N bond in the π^* orbitals, allowing for greater delocalization regardless of the CN group location. With the exception of the 1-CNBD **R2Br** MECI, all S_1-S_0 MECIs shown in Figure 4.1 are accessible from the Franck-Condon region, necessitating dynamical simulation to understand the photochemistry of these species.

4.3.2 Nonadiabatic dynamics simulation

Due to the selection criteria that the initial state was the excited state with the maximum transition dipole moment, 87% of the population was initially excited to S_2 for BD. In 1-CNBD and 2-CNBD, 97 and 67% of the initial populations were on S_1, respectively. The

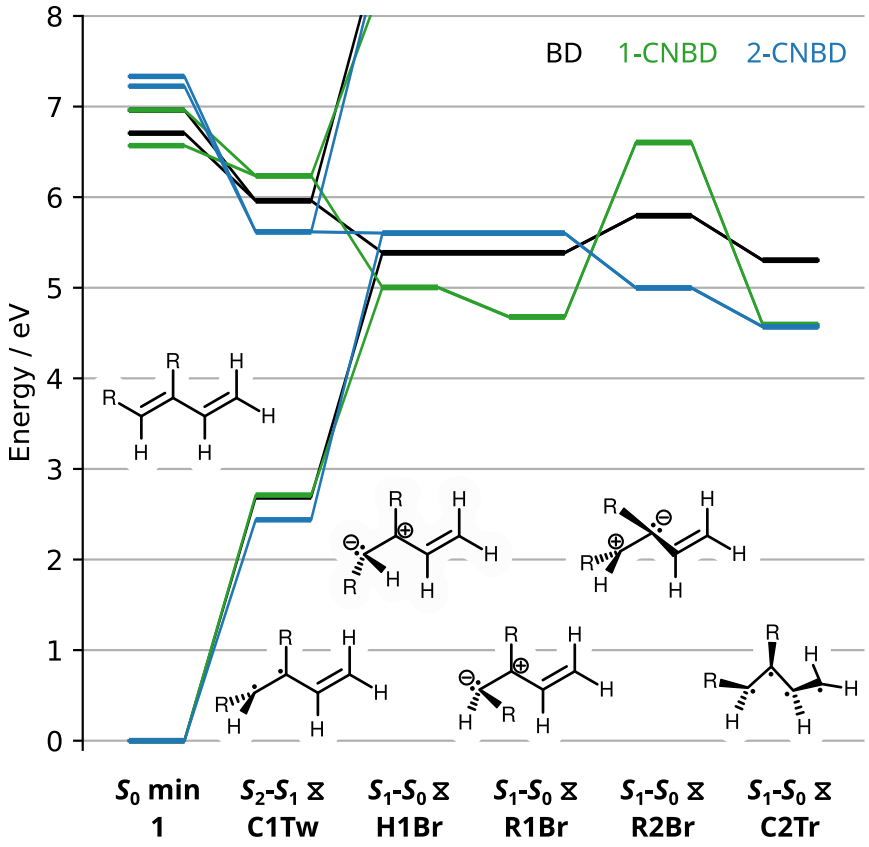

Figure 4.1: MR-CIS/6-31G* potential energies of relevant points on the potential energy surface of BD (black), 1-CNBD (green) and 2-CNBD (blue).

Table 4.1: Decay offsets and lifetimes for the total excited state population of BD, 1-CNBD and 2-CNBD and their associated least-squares uncertainties.

Molecule	t_0 / fs	τ_{ex} / fs	c
BD	71.9 ± 1.1	207 ± 2	0.0675 ± 0.0003
1-CNBD	68.5 ± 0.8	227 ± 2	0.0308 ± 0.0004
2-CNBD	34.3 ± 1.6	194 ± 3	0.0978 ± 0.0011

population curves in Figure 4.2 show a similar trend of rapid inital S_2 decay to S_1, or in the case of 1-CNBD, a plateau on S_1, followed by a slow decay to S_0. The standard deviations in Figure 4.2 are calculated by bootstrap sampling,[177] as detailed in Section C2 of the SI. The initial decay offset is roughly proportional to the initial S_1-S_2 energy gap shown in Figure 4.1, with the shortest offset for 2-CNBD. The S_2-S_1 decay time scales are visibly slower for 1-CNBD relative to BD and 2-CNBD. Due to the initial rapid decay of S_2 populations, the time scales of the total excited state population are comparable between all three molecules. The total excited state decay was fit to an exponential function of the form $f(t) = \exp(-(t - t_0)/\tau_{ex}) + c$, and the values of fit parameters are given in Table 4.1.

Separation of the AIMS spawn geometries into groups based on their similarity to the MECIs was difficult due to the similar frequencies of pyramidalization at both carbon sites. The MECI associated with pyramidalization at different carbons may in fact occur on the same conical intersection seam as has been observed for several other systems.[18,149,178] Nonetheless, there is a general trend of increased pyramidalization or bridging at the substituted site as discussed in the following section.

4.4 Discussion

In our previous work on the effect of different substituents on the excited state dynamics of ethylene,[163] we found that the degree of perturbation of conical intersection seams was dependent on the strength of the π-acceptor or π-donor substituent, *i.e.* the ability of a substituent to induce polarization across the C=C bond. However, although this polarization changes at which carbon the pyramidalization takes place, the reaction is not photochemical in nature: isomerization of the ethylene C=C bond re-produces the original molecule. In contrast, the energetic change caused by substitution of polyenes may be used to favour/inhibit isomerization at a specific site, leading to the desired photochemical products.

As Figure 4.1 shows, the addition of a cyano group leads to significant shifts in the S_2-S_1 and S_1-S_0 MECIs. Semiclassical Ehrenfest calculations for several substituted butadienes have shown that C1 substitution with CH_3, NH_2 and F and C2 substitution with CH_3 (all π-donors) lead to increased C4 twisting, whereas C1 substition of CF_3 (a π-acceptor)

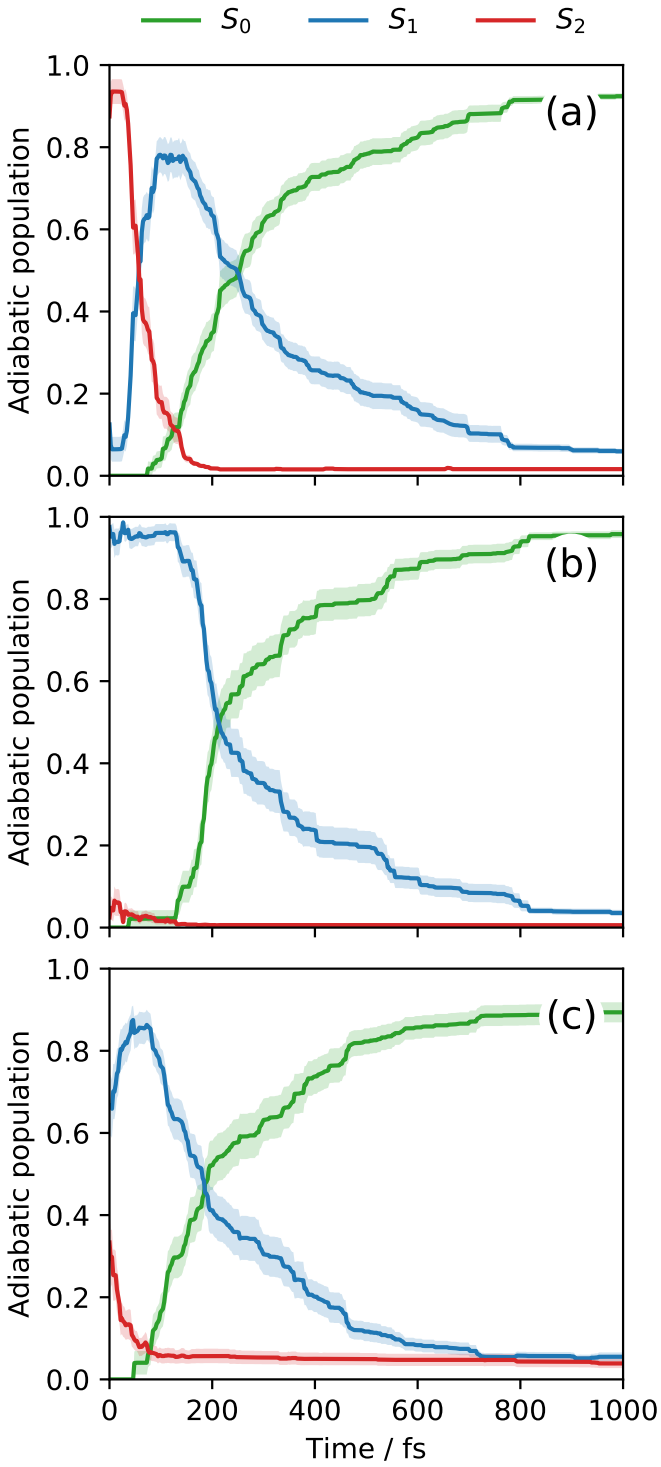

Figure 4.2: Adiabatic populations *vs.* time for (a) BD, (b) 1-CNBD, and (c) 2-CNBD. Shaded regions show one bootstrap standard deviation from the mean.

leads to more favourable twisting at C1 during S_2-S_1 decay.[165] These results suggest that π-acceptors will favour twisting on the substituted bond, which is consistent with potential energy surfaces implied by the energy differences in Figure 4.1. MS-CASPT2 calculations using the MR-CIS optimized geometries (see Figure C6 in the SI) show the opposite energetic trend for 1-CNBD, although the S_2-S_1 energetic difference of the **C1Tw** geometry is greather than the difference between **C1Tw** and **C4Tw** average energies. Fortunately, the S_2-S_1 dynamics does not play a major role in 1-CNBD because the $\pi\pi^*$ state is lower in energy. The initial population on S_2 decays via a higher point on the conical intersection seam corresponding to bond alternation. The S_2-S_1 decay of 2-CNBD behaves much like butadiene with twisting occuring primarily at C1. Assuming the evolution following photoexcitation is largely diabatic, the lower coupling between the bright $\pi\pi^*$ and dark $(\pi^*)^2$ for 1-CNBD and 2-CNBD should lead to less of the excited-state wavepacket having $(\pi^*)^2$ character, and thus less of the wavepacket reaching the **C2Tr** conical intersection region. This trend in S_2-S_1 coupling suggests a more complicated picture for π-donor substitution, where initial isomerization occurs on the unsubstitiuted end of the molecule, potentially avoiding the photoproduct **3** in Scheme 4.1.

The most notable differences in the potential energy surfaces of substituted *vs.* unsubstituted butadiene are the S_1-S_0 conical intersection energies. As predicted, the ethylenic MECIs are lowered in energy when pyramidalization occurs at the substituted carbon and increased in energy for pyramidalization at the adjacent carbons. The overall effect on the transoid MECIs is stabilization with respect to the ethylenic intersections with a slight difference in the **C2Tr** and **C3Tr** energies likely from the π and π^* contributions to the $(\pi^*)^2$ state. These results suggest a similar "tilting" of the potential energy surface as seen for substituted ethylenes,[163] although the energies of the transoid MECIs appear unaffected by the substituent location.

The AIMS simulations of all three molecules result in very similar decay time scales despite the addition of substituents, as shown in Figure 4.2 and Table 4.1. The excited state lifetime can be interpreted as the sum of time delay t_0 and decay constant τ_{ex}. Intuitively, one might expect the decay time scale of the **R2Br** and **C2Tr** pathways to be slower than that of **R1Br** due to the masses involved in motion from the **C1Tw** geometry. Thus, if CN substitution favours pyramidalization at the substituted site, 1-CNBD should have a similar decay time scale to BD (as observed), while that of 2-CNBD should be slower. This, however, assumes that the geometries of the conical intersections are identical while their masses and potential energies differ. In fact, the optimized geometries involving CN bridging (**R1Br** for 1-CNBD and **R2Br** for 2-CNBD) show a C=C−C bend rather than pyramidalization and can thus be reached through a higher-frequency motion than large amplitude pyramidalization involving the relatively massive cyano group. The net result is similar excited state lifetimes for BD and 1-CNBD (279 and 296 fs, respectively) and a

faster lifetime for 2-CNBD (228 fs).

Figure 4.3 shows the S_1 minimum potential energy surface along C1 and C2 pyramidal angles, τ_{C1} and τ_{C2}, respectively. All bond lengths and angles (with the exception of the CCN angle) were relaxed along with the central C2–C3 torsion, while C1–C2 and C3–C4 torsions, out-of-plane angles and C−C≡N linear bending angles were constrained. The $\tau_{C1} = 0$, $\tau_{C2} = 0$ point corresponds to a geometry with a 90° torsion about the C1–C2 bond. The optimized structures of **H1Br**, **R1Br**, **R2Br** and **C2Tr** are shown by the symbols $\times$, $+$, $\star$ and $*$, respectively. Notably, because the **R1Br** structure of 1-CNBD and the **R2Br** structure of 2-CNBD have almost zero pyramidalization at the substituted carbons, the potential energy wells for substituted BD are much closer to the **C1Tw** structure. The potential energy contours clearly show how introducing a cyano group significantly increases the barrier toward either C1 or C2 pyramidalization, thus driving the dynamics along the other coordinate.

Also shown in Figure 4.3 are the magnitudes of population transferred at the AIMS spawn geometries as a function of the spawn geometry, convoluted with Gaussians with widths of 5°. As shown in Section C1 of the SI, the majority of S_1-S_0 population transfer occurs within 2 fs of the spawn time, meaning spawn geometries are representative of transitions between states. The distribution of spawn geometries correspond roughly to the potential energy wells along either pyramidalization coordinate. A barrier lies along τ_{C1} for BD and 2-CNBD, and pyramidalization occurs mainly along C2. The opposite is true for 1-CNBD, where the energy barrier effectively inhibits any trajectory from reaching the **R2Br** or **C2Tr** MECI regions. Thus, it is the relative position of the potential energy barrier between wells that determines the outcome of the photochemical reaction.

To characterize the electronic wavefunction at the AIMS spawn geometries, iterative Hirshfeld charges q_X were computed from the electron density at atom centres X for each spawn geometry. Figure 4.4 shows the magnitude of population transferred during a spawn event as a function of atomic charge difference between C1 and C2 and pyramidalization angle difference between C1 and C2. MECI geometries are also shown for reference. As noted in a previous study of butadiene dynamics,[37] nonadiabatic decay occurs mainly via the **C2Tr** (neutral) and **H1Br** (positive $q_{C2} - q_{C1}$) conical intersections. The Hirshfeld charges of +1 suggest significant amount of charge transfer across the C1–C2 bond, consistent with our previous study on substituted ethylenes.[163] Addition of a CN group to make 1-CNBD strongly favours charge density at C1, leading to the majority of the spawn population transferred in the **R1Br** conical intersection region. In contrast, substitution at C2 inhibits pyramidalization at C1. Although spawn geometries in Figure 4.3 more closely resemble the **C2Tr** geometry, the electron densities suggest that the ethylenic **R2Br** conical intersection dominates the 2-CNBD dynamics. These results are consistent with the decrease in coupling between $\pi\pi^*$ and $(\pi^*)^2$ states in the Franck-Condon region following cyano substitution.

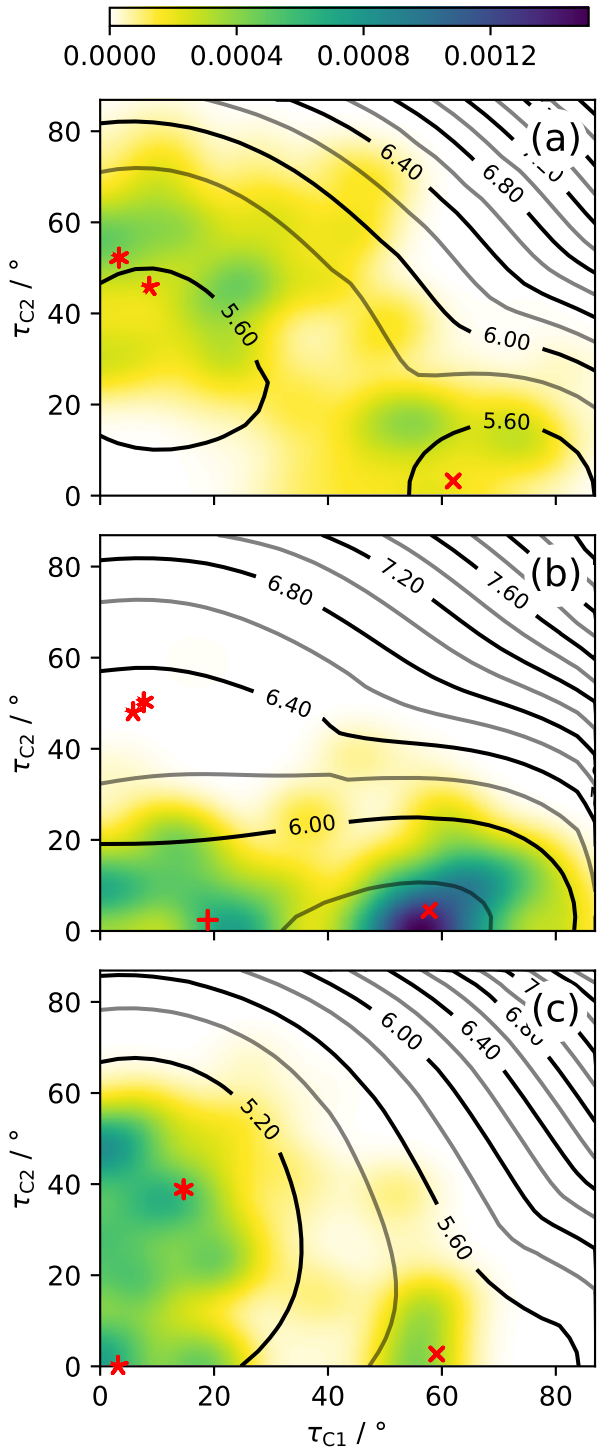

Figure 4.3: Relaxed S_1 potential energy surfaces (contours in eV) of (a) BD, (b) 1-CNBD and (c) 2-CNBD along τ_1 and τ_2. Gaussian convoluted AIMS spawn populations are also shown as a function of pyramidalization angles. Optimized geometries **H1Br**, **R1Br**, **R2Br** and **C2Tr** are given by the red symbols $\times$, $+$, $\star$ and $*$, respectively.

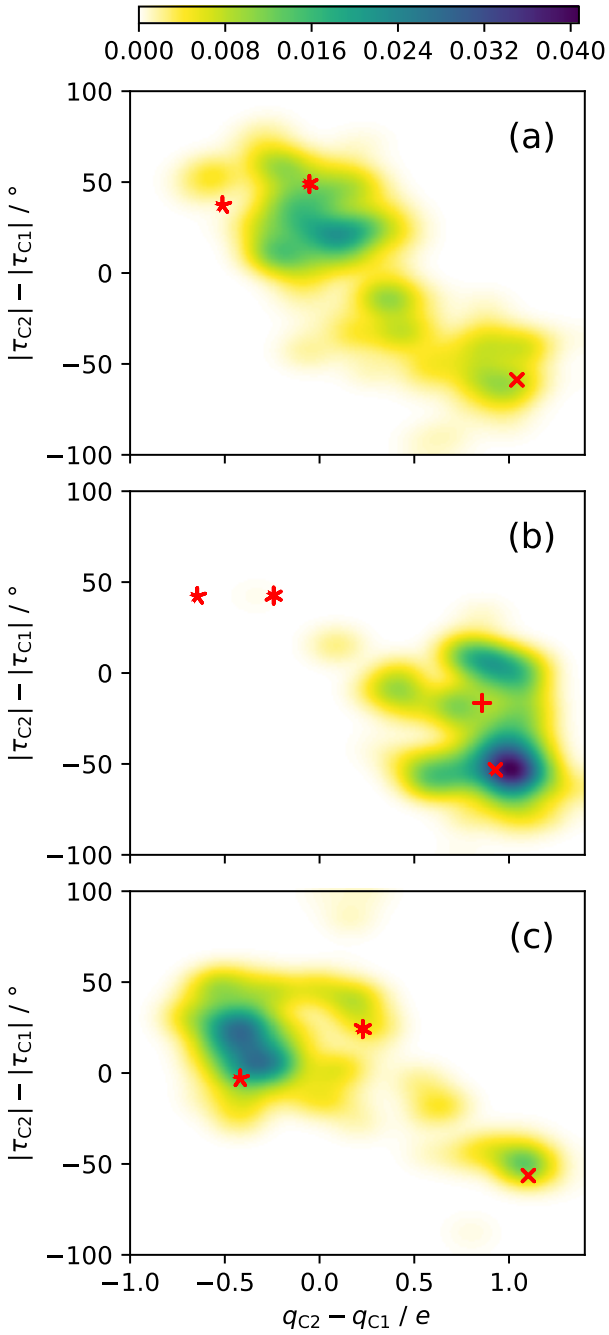

Figure 4.4: Gaussian convoluted AIMS spawn populations of (a) BD, (b) 1-CNBD and (c) 2-CNBD as a function of atomic charge difference and pyramidalization angle difference at C1 and C2. **H1Br**, **R1Br**, **R2Br** and **C2Tr** are given by the red symbols $\times$, $+$, $\star$ and $*$, respectively.

The above data show clear evidence of substituent effects on nonadiabatic dynamics by altering the potential energy surface and increasing or decreasing barriers to certain decay pathways. Using a π-acceptor substituent (CN) leads to the stabilization of bridging conical intersections located at the substituted site and destabilization at adjacent sites. This effect is also manifested in the potential energy surface by significantly increasing the barrier to the unfavourable MECI. Thus, the substituent "directs" the excited state wavepacket along a specific coordinate depending on its position. One might expect that the reverse process (*i.e.* favouring dynamics localized at an adjacent carbon) would be expected by substituting a π-donor; however, the energetic ordering of S_2-S_1 MECIs is likely also interchanged for a π-donor substituted butadiene,[165] which, in turn, could direct the molecule toward **H4Br** for C1 substitution and **H3Br** and **C3Tr** for C2 substitution. By studying the effects of cyano substitution on the nonadiabatic dynamics of butadiene, we move closer to a general set of rules for perturbative substituent effects in photochemistry.

It is important to note that in the gas phase, the excess kinetic energy is distributed throughout the molecule. This energy is significantly greater than isomerization barriers, meaning that a photoproduct could not be readily isolated from a gas-phase experiment. Figure C2 in the SI shows nuclear densities along the torsion of the carbon backbone starting from their spawn time as well as the densities integrated from 200 fs onwards. Although there is a slight increase in *cis* geometries for 2-CNBD, the internal energy of the ground state wavepacket is great enough to overcome the torsional barrier, and the photochemical yield is not measurable. The ultimate fate of excited gas-phase molecules is internal vibrational redistribution and fragmentation if the kinetic energy is sufficiently high.

In contrast, in the condensed phase the solvent acts as a bath, removing excess vibrational energy. A polar solvent would also alter the potential energy surface, favouring the polarized electronic structure seen in isomerization. This effect has been observed in excited-state dynamics simulations of polyenes with implicit[179] and explicit[154,156] solvent. In cyanobutadiene, this would result in a stabilizing effect on the transient dipole that forms in the vicinity of the seam of conical intersection (**H1Br**, **R1Br** and **R2Br**); however, the dynamical effects must also be taken into account. Simulations of solvated rhodopsin and azobenzene show significant increases in excited state lifetime with the inclusion of solvent as well as changes in the branching ratio of photoproducts,[154,180] particularly with increasing solvent polarity. In more extreme cases, solvent reorganization can dramatically effect the electronic character of the excited state,[181] potentially driving a molecule to specific photoproducts.[182] The overall solvent effects on molecules similar to cyanobutadiene are difficult to predict due to the interplay of excited state stabilization, lifetimes, quantum yields and dynamics of the solvent itself. Addition of a solvent may lead to a more dramatic effect from substitution, pushing the reactions to desired photoproducts, or may quench the momentum along the isomerization coordinates. Simulation of substituted polyenes in

solvents will demonstrate the competing solvent and substituent effects on nonadiabatic dynamics, and potentially lead to new light-driven synthesis strategies and other tailored photochemical properties.

4.5 Conclusions

Photoinitiated isomerization processes necessarily involve large amplitude motion on an electronic excited state. The changes in the nuclear geometry that arise from these motions can result in large changes in electronic character, including accessing conical intersection seams. The formation of a large, transient dipole across the double bond of ethylene during the excited state decay is one such example. We show here that chemical substitution may favour or inhibit motion at a predetermined site by altering the topography of relevant regions of the the potential energy surfaces.

We have shown that the concept of functional group substitution is applicable for influencing the potential energy surface and branching ratios of polyenes using cyano-substituted butadiene as a representative molecular system. The π-acceptor substituent preferentially stabilizes transient charge formation at the substituted carbon atom, thus leading to favourable isomerization at that site. This approach, further developed, may be used to exert "chemical control" over ultrafast dynamical processes in organic chromophores. The present study implicitly simulates a gas-phase experiment, thus relaxation to the ground electronic state results in a molecular species with sufficient internal vibrational energy to surmount isomerization barriers, thereby complicating the prediction of photochemical products. Further study of solution-phase photochemistry could reveal new strategies for tuning the excited state properties and reaction outcomes of conjugated molecules.

Acknowledgements

R.J.M. and M.S.S. acknowledge financial support from the Natural Sciences and Engineering Research Council of Canada (NSERC). R.J.M. acknowledges the Government of Ontario for support in the form of an Ontario Graduate Scholarship.

Chapter 5
Substituent effects on nonadiabatic excited state dynamics: Inertial, steric and electronic effects in methylated butadienes

R.J. MacDonell,[1] M.E. Corrales,[2] A.E. Boguslavskiy,[3] L. Bañares,[2] A. Stolow,[1,3,4] and M.S. Schuurman[1,4]

Reprinted with permission from *J. Chem. Phys.* **2020**, *152*, 084308.
https://doi.org/10.1063/1.5139446.

This work shows the importance of electronic effects on excited-state dynamics even with weak (methyl) substituents. I (RJM) characterized potential energy surfaces, performed nonadiabatic dynamics calculations, simulated the TRPES spectra and wrote the interpretation of the results. MEC and AEB performed the TRPES experiments, fit the resulting spectra and wrote the interpretation of experimental results. LB and AS supervised the experimental work and provided feedback. MSS supervised the theoretical work and provided feedback.

[1] Department of Chemistry and Biomolecular Sciences, University of Ottawa, Ottawa, Ontario K1N 6N5, Canada
[2] Departamento de Química Física, Facultad de Ciencias Químicas, Universidad Complutense de Madrid, 28040 Madrid, Spain
[3] Department of Physics, University of Ottawa, Ottawa, Ontario K1N 6N5, Canada
[4] National Research Council of Canada, 100 Sussex Drive, Ottawa, Ontario K1A 0R6, Canada

Abstract

The photochemical dynamics of double-bond-containing hydrocarbons is exemplified by the smallest alkenes, ethylene and butadiene. Chemical substituents can alter both decay timescales and photoproducts through a combination of inertial effects due to substituent mass, steric effects due to substituent size, and electronic (or potential) effects due to perturbative changes to the electronic potential energy surface. Here we demonstrate the interplay of different substituent effects on 1,3-butadiene and its methylated derivatives using a combination of *ab initio* simulation of nonadiabatic dynamics and time-resolved photoelectron spectroscopy (TRPES). The purely inertial effects of methyl substitution are simulated through the use of mass 15 "heavy-hydrogen" atoms. As expected from both inertial and electronic influences, the excited-state dynamics is dominated by pyramidalization at the unsubstituted carbon sites. Although the electronic effects of methyl group substitution are weak, they alter both decay timescales and branching ratios by influencing the initial path taken by the excited wavepacket following photoexcitation.

5.1 Introduction

Conjugated polyenes play an important role throughout chemistry. In organic photochemistry, they are known for their low-lying bright electronic states, typically dominated by $\pi\pi^*$ excitations. Certain polyenes, particularly short-chain or polar polyenes, decay nonradiatively from an electronically excited state by passage through conical intersections between the ground and excited states. Many of these decay pathways are dominated by a single geometric motif: a 90° twist about a C=C bond followed by a pyramidalization at one of the carbon atoms of the twisted bond. Passage through the conical intersection may result in isomerization about the twisted bond. This motion is characteristic of the excited-state dynamics of ethylene, but also occurs in molecules as large as the retinal Schiff base chromophore in rhodopsin, responsible for initiating the vision signal in many organisms.[134,154,155,183] The localization of dynamics to a single carbon-carbon bond is potentially useful in areas of synthesis, light-harvesting and photochemical switching.

The shortest polyene, 1,3-butadiene, serves as a model system for the dynamics of larger polyenes because it exhibits dynamical aspects of both ethylene and longer polyenes. Conjugated polyenes typically have a low-lying, spectroscopically dark $(\pi^*)^2$ state and a bright $\pi\pi^*$ state at higher energy. In butadiene, these two states are nearly degenerate,[32,33] with the dark state roughly 0.2 eV lower in energy than the bright state.[184] The complexity of its UV absorption spectrum,[185,186] in conjunction with its small size, have made butadiene a common benchmark for theoretical[34–37,166,184,187–191] and experimental[164,192–196] spectroscopic studies. The spectrum consists of a series of broad peaks ranging from 216 nm to

200 nm. Using reduced-dimensional linear vibronic coupling models, the form of the absorption spectrum was attributed to excitation to the bright $\pi\pi^*$ state, with initial motion along bond alternation of the carbon backbone and much of the coupling to the dark state due to out-of-plane C=C torsional modes.[34,35] A new paradigm was introduced by Levine and Martínez,[36] wherein both ethylenic and transoid dynamics participated and were in competition. More recently, further corrections to this model revealed a sensitivity of the spectrum to the coupling between excited states, with an additional dependence of the third absorption band due to coupling to a low-lying Rydberg state.[191]

The ultrafast electronic de-excitation of butadiene involves conical intersections of polarized electronic character (*i.e.* ionic pathways similar to the twist-pyramidalization of ethyene, with a lone-pair configuration) and nonpolar character (*i.e.* covalent pathways related to the bond-alternation pathway, transoid and cisoid, with a tetraradical configuration). Recently, the $\pi\pi^*$ excited-state dynamics of butadiene were studied in detail using a combination of time-resolved photoelectron-photoion coincidence spectroscopy (TRPEPICO) and *ab initio* simulation,[37,164] largely corraborating the Levine and Martínez model.[36] Multi-state complete active space second-order perturbation theory (MS-CASPT2) calculations revealed that the C1 pyramidalization and transoid minimum energy conical intersections (MECI) occur at nearly the same energies and thus both contribute to the excited state decay. *Ab initio* multiple spawning (AIMS) simulations revealed that the dynamics were largely dictated by the initial geometry, with a slightly greater proportion of the excited-state wavepacket passing through the transoid conical intersection region. By systematically varying the electronic structure method so as to favour either the $\pi\pi^*$ or $(\pi^*)^2$ states, the dynamics accordingly shifted to either ethylenic or transoid S_1-S_0 intersections.[37] Using TRPEPICO, the excited-state dynamics were characterized in detail, revealing the interplay of the two dynamical pathways. The extreme width of the UV absorption spectrum was also explained in terms of the rapid torsion about a C=C double bond.[164]

In a systematic but phenomenological approach to dynamics at conical intersections, we have focused on the effects of methylation on the nonadiabatic dynamics of small organic molecules.[8] In ethylene, increasing methylation stabilizes of Rydberg-type states relative to the $\pi\pi^*$ valence state, slowing the Rydberg-to-valence dynamics considerably. In substituted ethylenes such as acrolein and acrylonitrile, methylation has a strong inertial effect on the dynamics, depending on the methylated position in the molecule.[54,140] For crotonaldehyde in particular, methylation dramatically increases the decay timescale by decreasing the probability of internal conversion to the ground state, thereby increasing the probability of intersystem crossing from the $n\pi^*$ state.[54] Similarly, methylation of allene leads to the gradual dominance of the twist-bend (central carbon) as opposed to the twist-pyramidalized (terminal carbons) conical intersection, as explained by steric repulsion and slower vibra-

tional frequencies due to the inertial effects of methylation.[56] A more dramatic effect was seen for adenine, where methyl substitution destabilizes a $\pi\sigma^*$ state, thus altering the dynamics by removing a decay pathway.[172,197] Many of these studies assumed that methyl group substitution introduces primarily an inertial effect, decreasing the velocity of the wavepacket along certain directions in coordinate space. The methyl substitution technique thus provides an approach for influencing how the nuclear wavefunction evolves as it passes through a region of strong nonadiabatic coupling.

More recently, it was shown that concepts of electron resonance for displacing electron density within molecules are also relevant for excited states. The dominant decay pathway of ethylene, twist-pyramidalization, occurs with a concurrent increase in charge density at the pyramidalized carbon. By adding a π-accepting CN group to ethylene[140] and butadiene,[198] it was shown that the potential energy surface is "tilted" to favour pyramidalization at the CN-substituted carbon. This effect dominates dynamics even in cases where pyramidalization at the substituted carbon is dynamically disfavoured due to massive substituents.[140] The shift of MECI energies (and, thus, the shift of the potential energy surfaces) can be tuned by the choice of functional group. Finally, dynamical simulations of vinylamine (NH_2-substituted ethylene) showed how π-donors have the opposite effect, *i.e.* the dominant decay pathway is pyramidalization at the neighbouring carbon site.[163]

The observed effects of substituents on nonadiabatic dynamics can be separated into three categories: inertial, steric and electronic (or potential). Inertial effects result from changes in the mass of substituents and thus can be thought of as purely dynamical in nature,[199,200] whereas steric and electronic effects result in changes to the potential energy surfaces. In reality, any functional group substituent will lead to a combination of all three effects, the relative magnitudes of which depend on the mass, geometry and electronic nature of the substituent. With the exception of the slight effects of isotopic substitution, disentangling these effects is difficult in real molecules; however, atomic masses can be readily varied in theoretical simulations. By introducing a "heavy-hydrogen" atom having the same mass as a chemical substituent, it is possible to characterize the purely inertial effects on the dynamics without concomitant changes to the underlying potential energy surface.

Although the methyl group was largely considered to be an "electronically inert" substituent in the past, it is a weak π-donor and should lead to some observable change in potential energy surfaces and associated gradients in the methylated molecule. For example, closer inspection of MECI energies of methylated acrylonitrile show 0.3 eV shifts, small relative to the 1 eV shift due to CN substitution.[140] Here, we study the effects of methyl substitution on the excited-state dynamics of 1,3-butadiene (BD). Specifically, we used symmetrically methylated derivatives of BD: 2,3-dimethyl-1,3-butadiene (central-dimethylbutadiene, C-MeBD) and 2,5-dimethyl-2,4-hexadiene (terminal-tetramethylbutadiene, T-MeBD), stud-

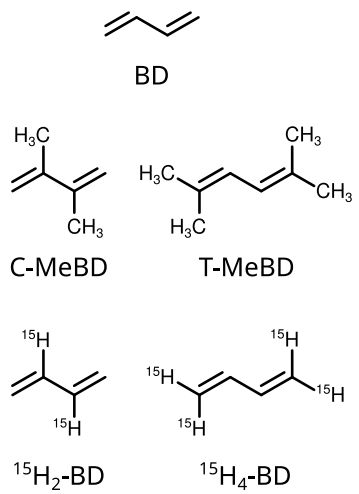

Figure 5.1: Molecular structures of 1,3-butadiene (BD), 2,3-dimethyl-1,3-butadiene (C-MeBD), 2,5-dimethyl-2,4-hexadiene (T-MeBD), 2,3-$^{15}H_2$-1,3-butadiene ($^{15}H_2$-BD) and 1,1,4,4-$^{15}H_4$-1,3-butadiene ($^{15}H_4$-BD).

ied by a combination of time-resolved photoelectron spectroscopy (TRPES) and *ab initio* multiple spawning (AIMS) simulations. In the AIMS calculations, we replaced methyl substituents with hydrogen atoms of mass 15 u, yielding 2,3-$^{15}H_2$-1,3-butadiene ($^{15}H_2$-BD) and 1,1,4,4-$^{15}H_4$-1,3-butadiene ($^{15}H_4$-BD), the analogs of C-MeBD and T-MeBD, respectively. Structures of these molecules are shown in Figure 5.1. By comparing the excited-state dynamics seen in the TRPES data to those calculated for the methylated species and the heavy-hydrogen atom species, we aim to isolate the role of the inertial effects on the nonadiabatic excited-state dynamics of 1,3-butadiene.

5.2 Methods

5.2.1 Experimental methods

TRPES experiments[98] were performed using a magnetic bottle photoelectron spectrometer with a seeded pulsed molecular beam produced by an Even-Lavie 1 kHz pulsed valve. Chemicals for these experiments, 1,3-butadiene (BD, Matheson, 99.9%), 2,3-dimethyl-1,3-butadiene (C-MeBD, Alpha Aesar, 98%), 2,5-dimethyl-2,4-hexadiene (T-MeBD, Alpha Aesar, 96%), were used without further purification. One femtosecond laser was tuned to 237.4 nm so as to be in resonance with the target T-MeBD $\pi\pi^*$ state. The other femtosecond laser was set to 200 nm. Thus, for BD and C-MeBD, the 200 nm pulse was the pump, whereas for T-MeBD the 237 nm pulse was the pump. In all cases, the other fs laser pulse acted as the time-delayed probe which, by single-photon ionization of the excited state, generated the photoelectron spectrum. Tuneable femtosecond UV laser pulses were pro-

duced via frequency mixing the output of a 35 fs, 800 nm, 1 kHz Ti:Sapphire regenerative amplifier (Coherent Legend Elite). The 237.4 nm beam was generated with Light Conversion's TOPAS and its DUV Extension module pumped with 800 nm ($\nu_{pump} + 2(2\nu_{signal})$ nonlinear mixing scheme). The 200.4 nm is the 4th harmonic of the 800 nm. The resulting UV pulses were separated from the fundamental and intermediate frequency counterparts by three or more reflections off suitable dichroic mirrors. Both pump and probe pulses were compressed using VUV-grade CaF_2 prism pairs, thus managing dispersion in air and in the vacuum input window, then combined co-linearly on a thin dichroic mirror. The combined pulses were focused by a deep UV aluminium (DUVA) coated concave spherical mirror ($f = 0.5$ m) into the interaction region of a magnetic bottle photoelectron spectrometer where they intercepted the pulsed seeded (alternatively 1% BD, 1% C-MeBD, or 0.1% T-MeBD in helium) molecular beam. The ensuing energy-resolved photoelectron spectrum, recorded as a function of time delay between pump and probe laser pulses (controlled by a motorized translation stage), thus yields the time-resolved photoelectron spectrum (TRPES). During the time delay scan, the beams were modulated with computer controlled shutters at every time delay and three measurements were taken: pump-probe, pump-only, and probe-only; the latter two were subtracted in all plots presented. Immediately before and after every experimental run, a short scan was used to register the nonresonant [1+1′] ionization of xenon, determining the time zero, t_0, and cross correlation width (instrument response function) later used in fits. Photoelectron kinetic energies were calibrated using the well-known one-colour photoelectron spectrum of BD.

As in previous experiments,[129,140,164] the TRPES data were globally fit to a 2D surface of the form

$$S(E, \Delta t) = g(\Delta t) \otimes \sum_i D_i(E) \exp(-\Delta t/\tau_i), \tag{5.1}$$

where $g(\Delta t)$ is a Gaussian cross-correlation function, and $D_i(E)$ is the i-th time-independent, energy-resolved decay associated spectrum (DAS) correlated with time constant τ_i. Large-amplitude motion of the excited state wavepacket can give rise to a "chirp" in the photoelectron energies as a function of time, an effect which is not included in the DAS. Thus, to account for this, the time zero (t_0) of the exponential decay is included as a variable in the fit as a function of energy, yielding $\Delta t = t - t_0(E)$, where t is the experimental pump-probe time delay.[129] The measured full width at half maxima of the cross-correlation signal used in the fits were 95, 104 and 110 fs for BD, C-MeBD and T-MeBD, respectively.

Electronic absorption spectra were measured for C-MeBD and T-MeBD in the vapour phase using a Varian Cary 5000 UV-Vis-NIR spectrophotometer, shown in Figure 5.2. The UV spectrum of BD is also given for comparison.[185] The broad features around 200–230 nm and 220–250 nm for C-MeBD and T-MeBD, respectively, are assigned to the bright $\pi\pi^*$ absorption band characteristic of alkenes.

5.2.2 Computational methods

Critical points on the potential energy surfaces of BD, C-MeBD and T-MeBD were characterized by optimizing structures using single-excitation multireference configuration interaction (MR-CIS) with a 6-31G* basis and a four electron, four orbital active space for all molecules. State averaging was performed over the three lowest-lying states of the multiconfigurational self-consistent field reference. Ground- and excited-state potential energies were calculated at the MR-CIS/6-31G* level of theory and compared to multi-state complete active space second-order perturbation theory (MS-CASPT2) with a cc-pVTZ basis, as shown in Figures D7 and D8 in the supplementary material (SM). MR-CIS calculations were performed with the COLUMBUS software package,[120] while MS-CASPT2 calculations were performed using Molcas.[147,148]

The MR-CIS calculations showed good agreement with the trends in MS-CASPT2 energies, and thus the MR-CIS/6-31G* level of theory was employed for nonadiabatic molecular dynamics using the *ab initio* multiple spawning (AIMS) formalism.[88,89,119] The molecular wavefunction was expanded over electronic states ψ and nuclear basis functions χ as

$$\mathbf{\Psi}(\mathbf{r},\mathbf{R},t) = \sum_{I=1}^{N_s} \sum_{j=1}^{N_I(t)} c_j^I(t)\psi_j^I(\mathbf{r},\mathbf{R})\chi_j^I(\mathbf{R},t). \tag{5.2}$$

The total number of electronic states, N_s, is three: the ground, $\pi\pi^*$ and $(\pi^*)^2$ states. The number of nuclear basis functions on state I, $N_I(t)$ was changed over time by spawning a new basis function to a coupled state when the coupling exceeded a given threshold. The nuclear basis was composed of frozen-width Gaussian functions with time-dependent, classically-evolving positions, momenta and phases. Expansion coefficients c_j^I were found for each timestep using the time-dependent Schrödinger equation. Initial conditions were sampled from a $v = 0$ vibrational distribution obtained from Hessians calculated at the RI-MP2/cc-pVDZ level of theory using Turbomole.[175,176] The initial position and momentum of the C-MeBD and T-MeBD trajectories were resampled until the initial trajectory was within 150 cm^{-1} of the pump energy plus a correction relative to MS-CASPT2 (6.20 + 0.78 eV for C-MeBD and 5.23 + 0.97 eV for T-MeBD). Each initial condition was treated as a separate simulation according to the independent first-generation approximation.[90] Thus, 40 and 36 initial conditions led to 521 and 702 trajectories over the course of the simulation for C-MeBD and T-MeBD, respectively.

Separate calculations were performed to simulate only inertial effects by artificially changing certain hydrogen-atom masses to the total mass of a methyl group (15.0234 u). The heavy-hydrogen atoms were selected to correspond to methylation of central ($^{15}H_2$-BD) and terminal ($^{15}H_4$-BD) carbons. The Hessian and the nuclear Gaussian widths were

appropriately scaled for the change in mass. Excitation was assumed to be vertical, *i.e.* without the additional pump selection criteria for initial conditions, since there was not a corresponding experiment for the heavy-hydrogen species. As a result of the different initial condition criteria, the initial conditions of methylated species were more tightly distributed along certain vibrational modes relative to the heavy-hydrogen molecules, as shown in Figures D2–D4 in the SM. 40 initial conditions for both systems resulted in 622 and 565 trajectories for $^{15}H_2$-BD and $^{15}H_4$-BD, respectively. Comparisons to unsubstituted BD were done using data from previous published work.[198]

Time-resolved photoelectron spectra were simulated to facilitate direct comparison to experiment. Using the wavefunction expansion given in Equation 5.2, the photoelectron signal is given by[122,123,140]

$$S(E,t) = \sum_{I=1}^{N_s^0} \sum_{j=1}^{N_I(t)} \left|c_j^I(t)\right|^2 \sum_{J=1}^{N_s^+} \sum_{n=1}^{2} w_j^{IJ}(n,t)\delta\left(E - \left[n\omega - \Delta E_j^{IJ}(t)\right]\right), \tag{5.3}$$

$$w_j^{IJ}(n,t) = \begin{cases} \left|\phi_j^{IJ}(t)\right|^2, & n = 1 \\ 0.01, & n = 2 \end{cases} \tag{5.4}$$

where labels 0 and + signify neutral and cation states, $\phi_j^{IJ}(t)$ is the Dyson orbital norm[99] between neutral state I and cation state J of trajectory j at time t, and likewise $\Delta E_j^{IJ}(t)$ is the ionization potential for the same states, trajectory and time. The probe energy is given by $n\omega$, where n is the probe photon count. Based on previous work,[140] Dyson orbital weighting was only used for one-photon signals. A two-photon signal weighted by a factor of 0.01 was used for the unsubstituted BD spectrum only. After generating $S(E,t)$, the final spectrum was calculated by convolution with Gaussian functions along both axes. All spectra used an energy width of $\sigma_E = 0.1$ eV, and time widths of $\sigma_t = 35.25$, 38.22 and 44.16 fs for BD, C-MeBD and T-MeBD, respectively, to agree with experimental parameters.

Iterative Hirshfeld charges were used to characterize the electronic structure of molecules in conical intersection regions by evaluating electronic densities on a molecular grid and finding the difference with spherically-averaged atomic densities.[79,80] In previous work, we have shown that local differences in partial atomic charges and nuclear geometry give a robust separation of different portions of the seam space of small polyenes.[163,198]

5.3 Results and discussion

In Figure 5.2, we show the gas phase UV absorption spectra of BD,[185] C-MeBD and T-MeBD. The dashed red vertical lines indicate the fs laser wavelengths used here. For T-MeBD, the 237 nm pulse acted as the pump, where as for BD and C-MeBD the 200 nm pulse acted as the pump. Although neither BD nor C-MeBD absorb at 237 nm, there is

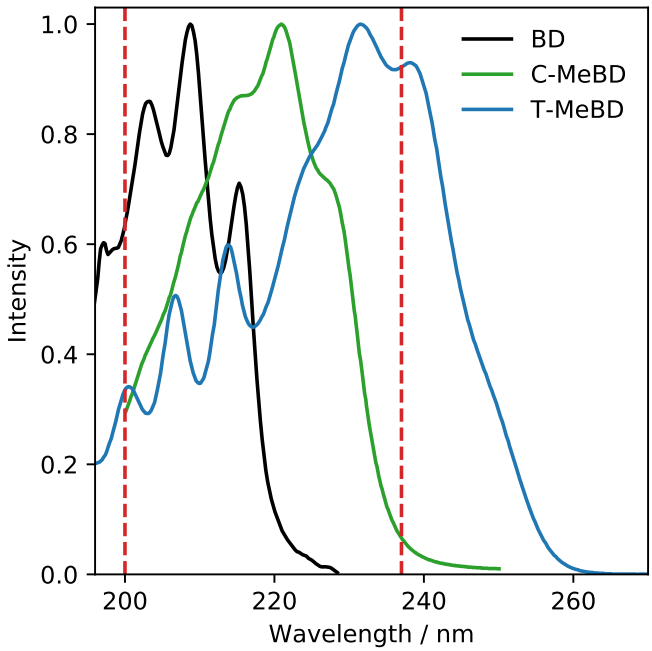

Figure 5.2: Experimental absorption spectra of BD, C-MeBD and T-MeBD. Vertical dashed lines show the pump and probe wavelengths. The BD spectrum is reprinted with permission from Leopold *et al.*, J. Chem. Phys. **81**, 4218–4229 (1984). Copyright 1984 AIP Publishing.

some non-zero absorption by T-MeBD at 200 nm. Therefore, the TRPES data for T-MeBD can contain both pump-probe and probe-pump photoelectron spectra. These overlap only at the time-zero point and can be treated by fitting the data in both positive (pump-probe) and negative (probe-pump) time delay directions.

The MR-CIS/6-31G* potential energies of critical points on the potential energy surfaces of BD, C-MeBD and T-MeBD are shown in Figure 5.3, with the symbol ⧖ used to indicate MECI geometries. In comparison with our previous study of a cyano substituent (a strong π-acceptor),[198] the energy shifts caused by methyl substitution are relatively small. At the optimized ground-state minimum (**1**), methylation led to slight differences in excited-state characters. Unsubstituted BD is known to have nearly degenerate $\pi\pi^*$ and $(\pi^*)^2$ states, and the $(\pi^*)^2$ state is lower in energy (S_1) than the $\pi\pi^*$ state (S_2) at higher levels of theory.[36,37,166] Here, the MR-CIS energies of BD follow the same trend. C-MeBD follows the same state ordering as unsubstituted BD, whereas the $\pi\pi^*$ state of T-MeBD is lower in energy (S_1); however, for all three molecules the near degeneracy of the two states means that the state ordering can swap with small changes in geometry.

The energy of the S_2-S_1 C1C2-twist MECI (**C1Tw**) of C-MeBD (relative to the ground-state minimum) is the same as that of unsubstituted BD, while the T-MeBD **C1Tw** energy is decreased by less than 0.3 eV. For the S_1-S_0 transition, C-MeBD exhibits a decrease in the

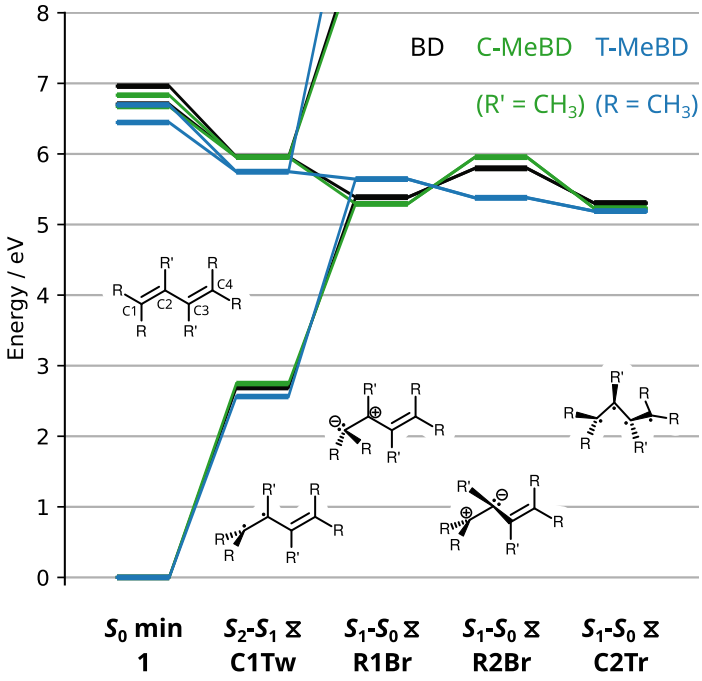

Figure 5.3: Potential energies of critical points for BD (black), C-MeBD (green) and T-MeBD (blue), relative to their respective ground-state minimum energy, optimized and calculated at the MR-CIS/6-31G* level of theory. The carbon backbone numbering and the structures of the S_2-S_1 and S_1-S_0 MECIs are also shown.

R1Br MECI (pyramidalization/bridging of the C1 substituent, *i.e.* H or CH_3) energy and an increase in the **R2Br** MECI (pyramidalization/bridging of the C2 substituent) energy of ∼0.2 eV, while a more pronounced 0.4–0.5 eV shift occurs for T-MeBD. The **R1Br** geometry of T-MeBD appears to be sterically hindered due to the two methyl groups on the pyramidalized carbon atom, leading to C−CH_3 bond lengths of 1.7–1.8 Å. All of the S_1-S_0 MECI energies match the expectations of chemical intuition, based on the weak π-donor characteristic of methyl groups. Notably, the energy of the **C2Tr** MECI (kinked-diene/transoid) decreases with increasing number of substituents, consistent with the independence of substituent position previously seen for cyanobutadienes.[198]

In Figure 5.4a–c, we show the experimental TRPES data for all three molecules, with the positive time representing the delay between pump and probe pulses. All spectra show a spectral shift from higher to lower kinetic energies with increasing time delay, particularly for T-MeBD with the largest observed shift. The T-MeBD spectrum also exhibits a long-lived band from 0 to 2.2 eV which does not appear in the other spectra. The simulated spectra are shown in Figure 5.4d–f and are described and compared to the experimental results below.

The calculated initial adiabatic populations of C-MeBD and T-MeBD are shown in Figures 5.5a and b. The initial conditions were selected based on the experimental pump

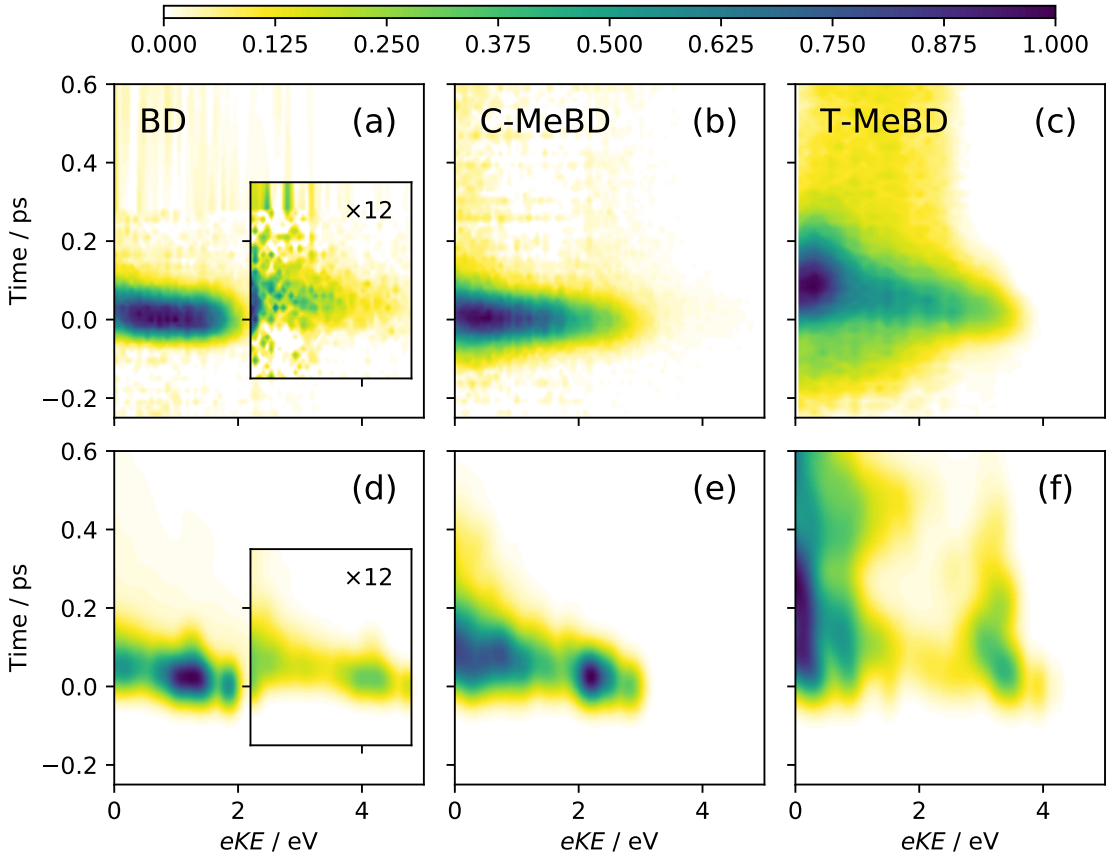

Figure 5.4: Experimental (a-c) and theoretical (d-f) normalized TRPES of BD, C-MeBD and T-MeBD (from left to right, respectively) as a function of electron kinetic energy and pump-probe delay. Inset into (a) and (d) are scaled signals due to the absorption of two probe photons (producing higher kinetic energy photoelectrons) displayed on the same axes as the unscaled spectra.

photon energies and the strength of the electronic transition dipole, resulting in 65% and 43% of the initial population on S_2 for C-MeBD and T-MeBD, respectively. Also shown in Figure 5.5 are the AIMS adiabatic populations as a function of time for C-MeBD and T-MeBD, as well as for the heavy-hydrogen species, $^{15}H_2$-BD and $^{15}H_4$-BD (Figure 5.5c and d). The initial populations of the heavy-hydrogen molecules are in good agreement with each other, as expected because the sampled potential surfaces are the same. The population curves show consistent sequential $S_2 \rightarrow S_1 \rightarrow S_0$ population dynamics, with fast initial decay from S_2 and slower decay from S_1. The populations were fit to a first-order kinetic model of the form

$$S_2 \underset{\tau_{-1}}{\overset{\tau_1}{\rightleftharpoons}} S_1 \underset{\tau_{-2}}{\overset{\tau_2}{\rightleftharpoons}} S_0 \tag{5.5}$$

An inital time delay t_0 was also included. The equations for the populations of each state depend on t_0, the initial S_2 population $p_2(0)$ (assuming $p_1(0) = 1 - p_2(0)$), the forward decay constants τ_1 and τ_2 and the backward decay constants τ_{-1} and τ_{-2}. The full equations for populations as a function of time are given in Section D1 of the supplementary material (SM). Note that the backward decay constants are important for obtaining fits when small populations remain on the excited states and do not necessarily represent the rate of population tranfer from lower-energy to higher-energy states.

Fit values and their least-square uncertainties for the populations in Figure 5.5 are given in Table 5.1. The fit τ_{-2} value of T-MeBD was many orders of magnitude larger than τ_2, and thus could be excluded with no significant changes in other values. The decay of C-MeBD is faster relative to $^{15}H_2$-BD, whereas for T-MeBD the decay is slower than its heavy-hydrogen equivalent. The populations alone suggest a notable difference between the methyl-substituted *vs.* the heavy-hydrogen substituted molecules. Part of this difference may result from differences in initial conditions. Figures D2–D4 show how the use of experimental pump energies for C-MeBD and T-MeBD led to tighter distributions along torsion, pyramidalization and bond alternation modes relative to $^{15}H_2$-BD and $^{15}H_4$-BD. Sampling along the bond alternation mode in particular is shifted from the ground state minimum, which may have the effect of a slight increase/decrease the decay times of C-MeBD/T-MeBD, respectively, contrary to the observed changes in Table 5.1. The increase in mass has a subtle effect on decay timescales, but the effect is greater for the methylated molecules, suggesting that the inertial (mass-weighting) effect does not fully account for the effects of methyl substitution. Comparing molecules, the S_2 decay (τ_1) is fastest for BD, followed by C-MeBD and the much slower T-MeBD. The S_1 decay (τ_2) is similarly slow for T-MeBD (1.30 ps), whereas the C-MeBD τ_2 decay is faster than that of BD by >70 fs. Interestingly, these results suggest faster excited-state decay dynamics for C-MeBD than for unsubstituted BD, despite the addition of heavy methyl groups.

In Figure 5.4d–f, the energy shift seen in the experimental TRPES (Figure 5.4a–c) is

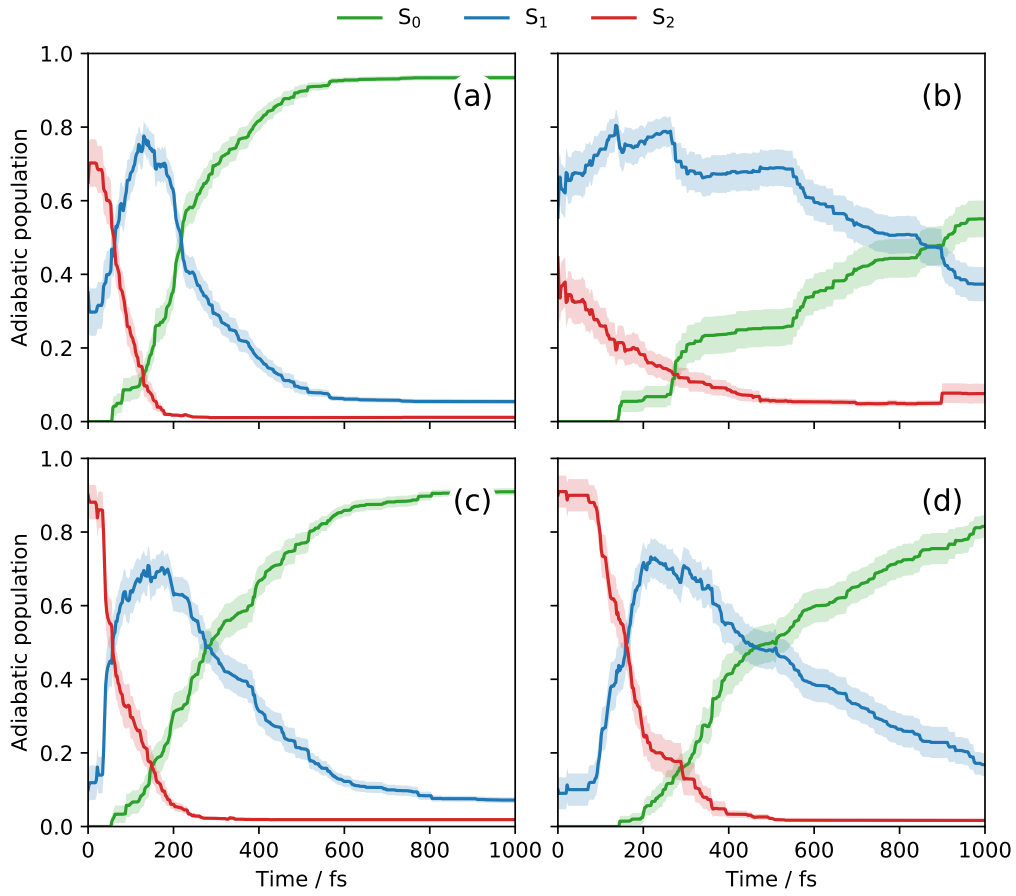

Figure 5.5: Adiabatic populations of (a) C-MeBD, (b) T-MeBD, (c) $^{15}H_2$-BD and (d) $^{15}H_4$-BD as a function of time. Shaded regions show one bootstrap standard deviation from the mean.

Table 5.1: Time delays, inital populations, decay constants and their least-squares uncertainties from fits to the adiabatic populations shown in Figure 5.5.

Molecule	t_0 / fs	$p_2(0)$	τ_1 / fs	τ_{-1} / fs	τ_2 / fs	τ_{-2} / fs
BD	52.2 ± 0.6	0.89 ± 0.01	22.6 ± 0.9	442 ± 25	240 ± 2	4830 ± 120
C-MeBD	69.5 ± 2.1	0.62 ± 0.01	30.5 ± 3.1	2000 ± 1600	168.9 ± 3.3	3590 ± 290
T-MeBD	89.2 ± 7.8	0.31 ± 0.01	111 ± 15	1130 ± 220	1301 ± 17	—
$^{15}H_2$-BD	47.1 ± 1.1	0.83 ± 0.01	41.9 ± 1.5	577 ± 33	234 ± 2	3860 ± 100
$^{15}H_4$-BD	115.5 ± 1.3	0.88 ± 0.01	68.4 ± 1.8	1447 ± 69	455 ± 5	14500 ± 3800

reproduced but overestimated in the simulated spectra of all three molecules, particularly T-MeBD. This overestimation is consistent with past simulated spectra,[37,140] and suggests an under-estimation of the excited state gradients relative to the gradients of the cation states. The experimental and theoretical data for BD and C-MeBD are otherwise in qualitative agreement. The BD spectra show similar features in the two-photon region, shown inset. The full BD spectra are in good agreement with recent results using a 216 nm pump and a 200 nm probe, as well as the corresponding simulated spectra.[37,164] In the theoretical spectrum of C-MeBD, there is a high-amplitude region around 2.2 eV which comes from the $S_2 \rightarrow D_0$ transition. Excluding the Dyson-orbital norm weighting significantly reduces this intensity, suggesting that the ionization probability is over-estimated for that particular band. The $S_2 \rightarrow D_0$ band of T-MeBD appears as an oscillating feature around 3.5 eV. The spectrum without Dyson-orbital norms suggests a similar over-estimation of the band intensity. For comparison, theoretical spectra without Dyson norm weighting factors are given in Figure D6 in the SM.

The theoretical TRPES of T-MeBD, Figure 5.4f, shows significantly more structure than the experimental spectrum, with oscillations in the 1–2 eV range rather than the smooth evolution seen experimentally (Figure 5.4c). The oscillation continues with less intensity around 800 fs (shown in Figure D6f in the SM), suggesting some periodic motion of the excited-state wavepacket. Kinetic energies within that energy range result from $S_1 \rightarrow D_0$ transitions. The shift to lower energies (250 and 630 fs) coincides with pyramidalization at the central carbon in the vicinity of the **C2Tr** MECI for most trajectories, while the return to higher energies (440 and 820 fs) comes from a flattening around C2. The disagreement with experimental data may suggest that the low-frequency pyramidalization modes were under-sampled in the inital condition selection, leading to coherent motion in the theoretical spectrum that is "averaged out" in the experimental spectrum. Indeed, the pyramidalization mode had a particularly tight distribution for the initial conditions shown in Figure D3 in the SM. The long-lived plateau in the experimental spectrum includes photoelectron kinetic energies up to 2.2 eV. This is a significantly higher kinetic energy than one would expect for a hot ground-state spectrum, suggesting that a part of the wavepacket gets trapped on the excited state, in agreement with the theoretical results. The experimental T-MeBD spectrum also has observable dynamics in the negative time direction, which results from the absorption cross section at 200 nm being only somewhat smaller than that at 237 nm (see Figure 5.2), and are not included in the simulation.

For the purpose of quantitative comparison between spectra, in Table 5.2 we show global fits to the TRPES signal. The fit is based on the kinetic model $X \xrightarrow{h\nu} A \xrightarrow{\tau_1} B \xrightarrow{\tau_2} X$. Data errors were calculated by bootstrap sampling over experimental scans and theoretical initial conditions which were then used as weights for χ^2 fitting. The bootstrap standard deviations are given in Figure D5 in the SM. To estimate the confidence interval of fitted

Table 5.2: Decay constants for fits to the experimental and theoretical time-resolved photoelectron spectra. Errors correspond to the 90% confidence interval. See text for details.

	Experimental		Theoretical	
Molecule	τ_1 / fs	τ_2 / fs	τ_1 / fs	τ_2 / fs
BD	$7.8\,^{+1.9}_{-0.8}$	$13.8\,^{+4.2}_{-6.2}$	14.0 ± 2.1	$39.8\,^{+2.0}_{-4.0}$
C-MeBD	$8.0\,^{+2.8}_{-0.8}$	$24\,^{+10}_{-15}$	$40.9\,^{+8.2}_{-4.1}$	82.3 ± 8.2
T-MeBD	$24.8\,^{+9.9}_{-8.7}$	$99\,^{+30}_{-20}$	$149\,^{+67}_{-45}$	$560\,^{+250}_{-220}$

parameters, each fitted parameter was fixed and systematically varied (with all other parameters relaxed in order to minimize χ^2) in increments of 5% of the parameter value until the obtained value of χ^2 reached the threshold for 90% confidence. This error analysis provides the maximum possible variation of a fitting parameter which is consistent with a particular χ^2 range, as it takes into account multi-dimensional correlations which may exist between a given set of parameters. The error bars are thus asymmetric, reflecting the differences between increasing *vs.* decreasing the values of fit constants. The experimental decay time constants are consistent with the observed trend in adiabatic populations, *i.e.* C-MeBD $\approx$ BD $<$ T-MeBD. The first time constants (τ_1) of all three molecules are within the experimental cross-correlation, whereas τ_2 is significantly longer for T-MeBD. The theoretical decay constants all overestimate the experimental results but follow a similar trend. There is a greater difference between C-MeBD and BD in the simulated spectra, and T-MeBD is nearly an order of magnitude greater than the experimental values. The qualitative differences between the simulated and experimental TRPES of T-MeBD likely originate in the propensity for the simulation to trap population on the excited state. This may arise due to an underestimation of the vertical excitation energy, which reduces the available amount of internal energy in the excited-state dynamics. Comparison of MS-CASPT2 energies in Figure D8 show a relatively large separation of S_2-S_1 MECI energies at the MR-CIS-optimized geometries, which indicates a poor description of the two excited states before they reach the S_1-S_0 conical intersection regions.

In Figure 5.6 we show contour maps of the relaxed S_1 adiabatic surfaces as a function of pyramidalization angles of the terminal and central carbons, ϕ_{C1} and ϕ_{C2}, respectively. The $\phi_{C1} = \phi_{C2} = 0$ geometry corresponds to a 90° rotation of the C1–C2 bond and a slight torsion about the central C2–C3 bond, which is in the region of the S_2-S_1 MECI and thus represents a starting point for population on S_1. All points on the surfaces correspond to geometry optimizations with out-of-plane angles and C1–C2 and C3–C4 dihedral angles constrained. For reference, the **R1Br**, **R2Br** and **C2Tr** MECI geometries are given by the symbols $\times$, $\star$ and $*$, respectively. As previously noted, the BD surface (Figure 5.6c and d) has nearly degenerate potential energy wells along both pyramidalization coordinates, with the initial gradient pointing towards C2 pyramidalization. The surfaces of C-MeBD and

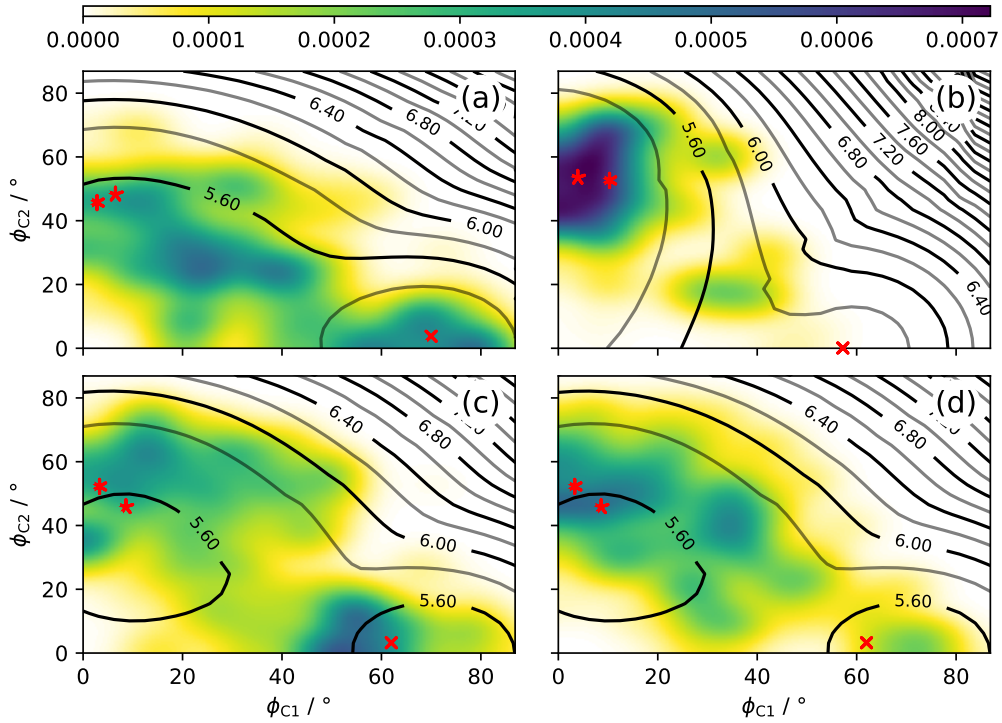

Figure 5.6: Relaxed S_1 adiabatic surfaces (contours) and spawn populations (heatmap) as a function of pyramidalization angles of the terminal and central carbon atoms, ϕ_{C1} and ϕ_{C2}, for (a) C-MeBD, (b) T-MeBD, (c) $^{15}H_2$-BD and (d) $^{15}H_4$-BD. The red symbols $\times$, $\star$ and $*$ represent **R1Br**, **R2Br** and **C2Tr** MECIs, respectively.

T-MeBD are only slightly shifted relative to previous results with cyano-substituted BD.[198] The potential energy well along ϕ_{C1} is lowered in energy for C-MeBD, and increased in energy with a slight barrier in the case of T-MeBD.

Also shown as heatmaps in Figure 5.6 are populations transferred during AIMS spawn events from the parent trajectory on S_1 to the child trajectory on S_0.[163] The S_1-S_0 population transfer is sufficiently localized around the spawn geometry to let us assume that the geometry is constant during population transfer. The heatmap of spawns is convoluted with a Gaussian of $\sigma = 5°$ along both pyramidalization angles. The spawn events show delocalization over the ϕ_{C1} and ϕ_{C2} wells for C-MeBD and the heavy-hydrogen molecules, and localization of T-MeBD spawn populations along ϕ_{C2}. For the methylated species, the difference in spawn geometries can be explained by the changes in the potential energy surfaces. T-MeBD has a large energy barrier to C1 pyramidalization due to steric hindrance and π-donation from the two terminal methyl groups, whereas the **C2Tr** MECI remains energetically accessible for C-MeBD, thus leading to a greater range of geometries. In constrast, the heavy-hydrogen molecules have identical (electronic) potential energies but there is still a notable difference in the spawn distributions. $^{15}H_4$-BD shows a decrease in C1

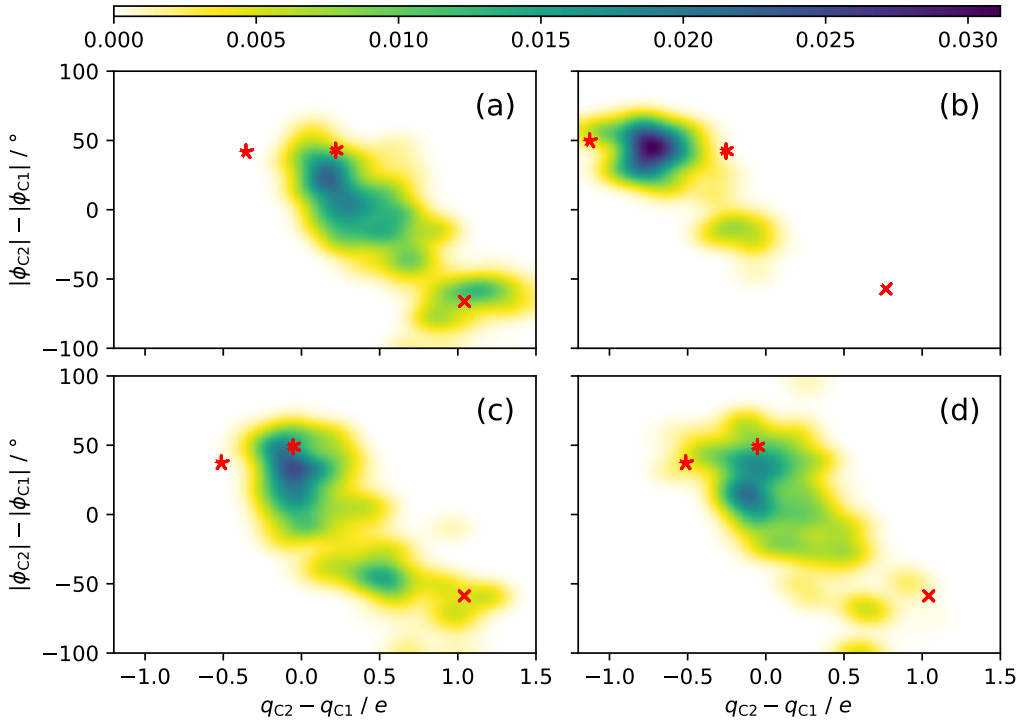

Figure 5.7: S_1-S_0 spawn populations as a function of differences in charge and pyramidalization at C1 and C2 for (a) C-MeBD, (b) T-MeBD, (c) $^{15}H_2$-BD and (d) $^{15}H_4$-BD. The red symbols $\times$, $\star$ and $*$ represent **R1Br**, **R2Br** and **C2Tr** MECIs, respectively.

pyramidalization relative to $^{15}H_2$-BD. This difference is evidence of an inertial effect on the nonadiabatic dynamics in BD: with heavier terminal hydrogens, the C1 pyramidalization has a much lower frequency and the excited state wavepacket takes longer to access the **R1Br** conical intersection region.

Further characterization of the spawn geometries is given by analysis of the difference in electron density across the C1–C2 bond. In Figure 5.7, we show the spawn populations as a function of partial atomic charge differences and pyramidalization differences at C1 and C2, with relevant MECIs given by red symbols as before. This analysis has previously been shown to give a good separation of electronic and nuclear characters into different regions of the conical intersection seam.[163,198] As before, T-MeBD shows the greatest localization with the majority of spawns occuring between **R2Br** and **C2Tr** geometries, *i.e.* with some transfer of electron density from C1 to C2. The spawns for the other systems have most population transfer occuring near **C2Tr**. The amount of **R1Br** population increases from $^{15}H_4$-BD to $^{15}H_2$-BD due to the inertial effect on the nonadiabatic dynamics, then from $^{15}H_2$-BD to C-MeBD due to the electronic effect of CH_3 π-donation.

These and previous results with substituted ethylenes[163] and cyano-substituted butadienes[198] demonstrate the importance of electronic substituent effects (*i.e.* perturbations

to the potential energy surface) on the nonadiabatic dynamics of small organic molecules, particularly polyenes. For strongly interacting substituents such as CN, the potential energies of MECIs may be shifted by more than 1 eV, leading to preference and inhibition of predictable low-frequency motions; however, even small changes due to a weak π-donor such as CH_3 lead to significant differences in wavepacket motion in comparison to unsubstituted BD. Steric repulsion from neighbouring CH_3 groups can further tilt the potential energy surface, as seen in the case of T-MeBD. For both methylated butadienes, the change in decay timescales with respect to BD were underestimated by simulations which implemented heavy-hydrogen atoms at the appropriate positions. The nuclear and electronic character of spawn events for the heavy-hydrogen species closely resembled that of BD, which suggests that the shape of the potential energy surface (both energies and gradients) is likely more important than the relative masses for predicting branching ratios of conical intersection mediated dynamics.

5.4 Conclusions

We are interested in the use of systematic chemical substitution in order to study dynamics at conical intersections. The molecule 1,3-butadiene is a paradigmatic example due to the role it plays in bridging the gap between ethylene and larger polyenes. Here we applied methyl substitution to the case of butadiene. The nonadiabatic dynamics of methylated butadienes show evidence of inertial, steric and electronic effects on both theoretical and experimental decay time constants, as well as on the predicted branching ratios for the substituted molecules. Adding methyl groups to butadiene leads only to small (0.2–0.4 eV) shifts in the energies of twist-pyramidalization MECIs. Despite this, the changes in decay time constants and branching ratios for pyramidalization MECIs are underestimated by inertial effects alone, as in the theoretical simulations for the heavy-hydrogen species $^{15}H_2$-BD and $^{15}H_4$-BD. Closer inspection reveals that transitions to the ground electronic state occur in the lower energy regions of the potential energy surface, despite the small differences in energy. This suggests that electronic (potential) effects on nonadiabatic dynamics are significant even for weak π-donor substituents: methyl substitution cannot be assumed to be purely inertial in nature.

Our findings further reinforce the importance of studying how perturbative changes in electronic structure, *e.g.* resonance in polyenes, can lead to predictable changes in photochemical dynamics. Such predictions may be applied to tailoring photochemical reactions into highly specific products, with potential applications in synthetic organic chemistry, or may be used to alter excited state properties and lifetimes in order to optimize artifical light harvesting, photovoltaics and photoswitching materials. An understanding of "dynamics-function" relationships will be important in the rational design of such materials.

Acknowledgements

R.J.M., A.S. and M.S.S. acknowledge financial support from the Natural Sciences and Engineering Research Council of Canada (NSERC). M.E.C. and L.B. acknowledge financial support for Spanish MCIU under grant PGC2018-096444-B-I00.

Chapter 6
Characterization of partial atomic charges of electronically excited states

R.J. MacDonell,[1] S. Patchkovskii,[2] and M.S. Schuurman[1,3]

Unpublished.

This work shows how partial atomic charges can be used to interpret electronic structure calculations of excited state, and includes a demonstration of the consistent $C-C$ bond polarization of one type of polyene MECIs. I (RJM) performed electronic structure calculations, wrote the scripts for calculating partial atomic charges and interpreted the results in the text. SP wrote the libraries for calculating electron densities on grids and provided feedback. MSS supervised the work and provided feedback.

[1] Department of Chemistry and Biomolecular Sciences, University of Ottawa, Ottawa, Ontario K1N 6N5, Canada

[2]Max-Born-Institut für nichtlineare Optik und Kurzzeitspektroskopie, Max-Born-Straße 2A, 12489 Berlin, Germany.

[3]National Research Council of Canada, 100 Sussex Drive, Ottawa, Ontario K1A 0R6, Canada

Abstract

Partial atomic charges provide useful and intuitive concepts for understanding molecular properties and chemical reaction mechanisms on the ground electronic state. They show how changes within a molecule can lead to an increase or decrease in electron density or electron affinity within a molecule, and thus provide a simple electrostatic picture of molecular interactions. In contrast, partial atomic charges remain relatively unused in the characterization of excited-state properties. We show how partial atomic charge methods perform for interatomic, intermolecular and inter-bond electron transfer. Our results demonstrate the utility of real-space partial atomic charges, particularly the iterative Hirshfeld approach, in understanding changes of electron density at an atomic scale. We use these results to demonstrate the similarities of conical intersection regions of several conjugated polyenes relevant for photochemical isomerization. Atomic charges provide a useful picture for the otherwise complex electronic structure than can result from excited-state processes.

6.1 Introduction

Many widely-used chemical concepts in molecular physics lack a rigorous definition as an observable quantum mechanical quantity. As a result, many approaches have been developed as an attempt to quantify the same properties of atoms and molecules. Several such concepts are fundamental aspects of chemistry such as partial atomic charge, bond order and steric repulsion.[70] Partial atomic charges have garnered a significant amount of attention since they can be used to quantify shifts in electron density such as inter- and intramolecular charge transfer, changes in electronic character and the potential long-range electrostatic interactions.[201,202]

Approaches for defining ab initio partial atomic charges can be broadly divided into two categories. The first are those which are fit to external properties such as dipoles, higher multipoles,[71,72] or the electrostatic potential. An example of the latter is the "charges from electrostatic potentials" (CHELP) family of methods (*e.g.* grid-based, CHELPG),[73,74] which are useful for quantifying intermolecular interactions or long-range intramolecular interactions. These methods may suffer from "screening" the effect of atoms within large molecules by only considering an external observable. Conversely, electron density methods partition the molecular electron density into atomic components. In Mulliken population analysis, this partitioning is done by assigning atomic basis functions to each atom centre and finding

$$\rho_\alpha = \mathrm{Tr}_\alpha(\mathbf{DS}), \tag{6.1}$$

where ρ_α is the density assigned to atom α, Tr_α is the trace over basis functions centred at atom α, $\mathbf{D}$ is the 1-electron reduced density matrix and $\mathbf{S}$ is the atomic basis function

overlap matrix. The atomic charge is then found from the difference in electron density and atomic charge, $q_\alpha = Z_\alpha - \rho_\alpha$. This approach does not readily account for different bases on different atom centres, and may over-assign diffuse basis functions to atoms which are spatially separated from the actual electron density.[75] Other methods, such as Löwdin populations or natural atomic orbitals, provide a more robust determination of partial charges but still depend on assignment based on basis function centres.[76,77] Alternatively, partial charges can be determined without knowledge of the basis functions. For example, intrinsic atomic orbital populations (for single-reference wavefunctions),[203,204] quasi-atomic orbitals[205,206] and Stockholder projector analysis[207,208] are methods which project atomic weights onto the full basis of the molecule, thereby removing the dependence on the atomic centres of the basis set.

Alternatively, real-space density approaches rely on assigning atomic weights on a grid and integrating the density corresponding to each atom. As a result, they depend uniquely on the electron density, meaning their only form of basis set dependence is the convergence of the density. Population-based approaches are of the form

$$q_\alpha = Z_\alpha - \int \mathrm{d}\mathbf{r}\, w_\alpha(\mathbf{r})\rho_{mol}(\mathbf{r}), \tag{6.2}$$

where Z_α is the nuclear atomic charge, $w_\alpha(\mathbf{r})$ is the weight function and $\rho_{mol}(\mathbf{r})$ is the molecular electron density at cartesian coordinate $\mathbf{r}$. The total electron density is integrated over defined regions of space to give the atomic populations, and charges are defined as the difference between nuclear charges and populations. Alternatively, "promolecular" approaches rely on densities of spherically-symmetric, non-interacting atoms (the promolecule), *i.e.* $\rho_{pro}(\mathbf{r}) = \sum_\alpha \rho^\alpha_{at}(\mathbf{r})$. The difference between promolecular and molecular densities is known as the deformation density, yielding charges of the form

$$q_\alpha = \int \mathrm{d}\mathbf{r}\, w_\alpha(\mathbf{r}) \left[\rho_{pro}(\mathbf{r}) - \rho_{mol}(\mathbf{r})\right]. \tag{6.3}$$

Real-space approaches to calculating partial charges thus depend on the representation of atomic charge (point charges or promolecular densities) and the form of $w_\alpha(\mathbf{r})$. In Bader's quantum theory of atoms in molecules (QTAIM), 3D space is partitioned according to the electron density topography, with weight functions of 0 or 1 depending on the atom reached by steepest-ascent of the density.[78] Alternatively, Becke charges use the same formalism as Becke's spherical grids, with size-adjusted Voronoi cells and a sigmoid functional form of $w_\alpha(\mathbf{r})$ between atomic sites.[209] The Hirshfeld approach uses Equation 6.3 with a weight function of $w_\alpha(\mathbf{r}) = \rho^\alpha_{at}(\mathbf{r})/\rho_{pro}(\mathbf{r})$, *i.e.* it assigns atomic weights based on contributions to the promolecular densities.[79] A simpler form, which yields similar results to Hirshfeld charges, is the Voronoi deformation density (VDD) approach, which assigns a weight of

unity to the nearest atomic site of each grid point, thus dividing 3D space into Voronoi cells. These deformation density approaches generally use neutral, ground-state atomic densities to form the promolecule, and their magnitudes tend to be significantly lower than other approaches.[210] An extension to the Hirshfeld approach treats q_α in Equation 6.3 as a change in charge and uses weighted sums of charged atomic densities to yield charges independent of the starting conditions. This method, known as iterative Hirshfeld (IH), effectively "fits" atomic densities to the molecular density and yields charges in good agreement with CHELPG and QTAIM.[80]

Although each of the partial atomic charge approaches listed above have been extensively used for the analysis of ground state molecules, there are comparatively far fewer examples for which these techniques have been used for the analysis of excited-state wavefunctions. Calculating consistent values of charge requires converged electron densities, which themselves require additional computational effort for the more complex, multi-reference electronic characters of molecules in excited states. Nonetheless, the charge methods discussed above are equally applicable for excited state properties. For example, QTAIM analysis has been used to evaluate charges and bonding interactions of excited formaldehyde.[211] A range of charge methods were assessed for charge-transfer excitations of a series of conjugated push-pull organic compounds, and showed that electrostatic potential methods best reproduce differences in dipole moments for vertical excitations.[202] Other approaches have been used for bonding analyses[212] and to quantify non-covalent interactions[213] for excited molecules.

For example, excited-state charge transfer is a characteristic of many photochemical processes, and is thus frequently the subject of experimental and theoretical study.[214–216] Many heteronuclear diatomics have well-studied covalent and ion-pair states with an avoided crossing between states as the molecule dissociates for which a strong shift in charges can be observed and quantified by the dipole moment.[214,217,218] Molecular complexes may also have charge transfer states if the differences in electron affinity between molecules is sufficiently high. This results in the loss of an electron from the donor molecule into an unoccupied (or partially occupied) orbital of an acceptor molecule, creating an ion pair. Some examples of this are tetracyanoethylene (TCNE) with tetramethylethylene (TME),[219] benzene and polycyclic aromatic hydrocarbons.[213,215,216] The ethylene π-bond of TCNE acts as an electron acceptor, and excitation of the complexed molecule gives the transition TCNE-X $\rightarrow$ $TCNE^{-}$-X^{+} which leads to a stronger intermolecular bond in the excited state.[213,216]

Charge transfer can play a role over shorter distances in the ultrafast photochemistry of molecules. One well-known example is the "sudden polarization" of ethylene: following excitation to the $\pi\pi^*$ state, ethylene undergoes internal conversion to the ground state by a torsion about the C=C bond followed by a pyramidalization of a single methylene (CH_2) group to reach a conical intersection between the two states, shown in Scheme 6.1 (with

the ⧖ symbol representing conical intersections, R = R' = H, and labels **C***n***Pyr** represent pyramidalization at carbon n). The electronic character on the excited state resembles that of a lone pair on the pyramidalized carbon, and has a dipole across the C=C bond.[16,20,21] This pathway is not unique to ethylene: it is common to substituted ethylenes (R or R' ≠ H in Scheme 6.1),[163] as well as many larger alkenes such as butadiene,[37,39,166] substituted butadienes,[174,198,220] hexatriene and cyclohexadiene[39,221] and larger biomolecules such as the retinal chromophore,[134,155,183] all of which may undergo photochemical isomerization by Scheme 6.1 to yield a photoproduct **2** different from the starting molecule **1**. Polyenes with two or more conjugated C=C bonds also have a low-lying $(\pi^*)^2$ which can undergo internal conversion through nonpolar conical intersections (*e.g.* "kinked-diene" MECIs such as "transoid", labelled **C***n***Tr** for displacement about carbon n).[33] Thus, understanding the branching ratios of excited-state decay can be aided by characterizing local changes in electron density.[163,198,220]

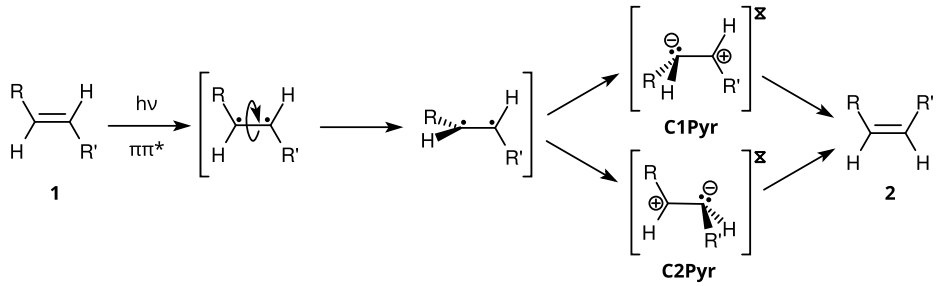

Scheme 6.1

It should be noted that the electronic character of a state at a point of conical intersection is not uniquely defined. To gain a better understanding of ultrafast photochemistry, it is desirable to study the properties of the excited state approaching the conical intersection region. At the point of degeneracy, the states are intermixed but can be resolved by projecting onto a geometry on the decay pathway before reaching the conical intersection, or by making an infinitesimal displacement along branching space coordinates. In Section 6.5, we use the latter approach to study trends in charges of characteristic MECIs of polyenes.

In this paper, we show how a variety of partial atomic charge methods perform for characterization of excited-state wavefunctions. We focus on examples where the charge-transfer character is well known: interatomic charge-transfer of LiH and LiF, intermolecular charge transfer of the benzene-TCNE (B-TCNE) complex and the sudden polarization effect of ethylene, 1,3-butadiene, 1,3,5-hexatriene, 1,3-cyclohexadiene and their derivatives substituted with amino (π-donor) and cyano (π-acceptor) groups. We show how partial atomic charges can be used as a coarse-grained view of the otherwise complex electronic characters of excited states, and how similarities in charge differences may plan an important role in identifying motifs characteristic of photochemistry.

6.2 Computational methods

Electron densities and their gradients were calculated at each point of a Becke molecular grid[209] with Lebedev spherical quadrature.[222–224] Densities and calculated charges were converged with a small number of radial and spherical points. All calculations employ 70 radial and 110 angular points, *i.e.* 770 grid points per atom. Density values were calculated from the one-electron reduced density matrix (1-RDM) or, equivalently, from natural molecular orbitals and their respective populations.

Ground-state atomic densities for the deformation density promolecule were calculated for atoms with charges of -3 to $+3$ using restricted open-shell second order Møller-Plesset perturbation theory (ROMP2) with an aug-cc-pVTZ basis in the GAMESS electronic structure package.[225,226] Details of the symmetrization of atomic densities are given in Section E1 in the supporting information (SI, Appendix E). These promolecule densities were used in the calculation of Hirshfeld, IH and VDD charges. Becke charges were calculated using the same weighting procedure as the Becke grids. Thus, the points of each spherical grid were assigned to the nucleus at its centre.[227] Charges calculated with Bader's Quantum Theory of Atoms in Molecules were also calculated on the Becke grid by following steepest ascent paths to local maxima in the electron density.[228]

A series of test calculations were also performed to assess the charges and their basis set dependence. The charges for several small molecular are shown in Figure E1 in the SI, where the basis set label indicates the basis used to calculate the electron density of the molecule. For comparison, Mulliken charges are shown with the expected divergence as the size of the atomic basis increases. As previously reported, Hirshfeld and VDD charges closely resemble each other and have nearly the same value as the Mulliken cc-pVDZ charges.[210] Becke charges are also similar to Hirshfeld and VDD with slightly greater magnitudes for most molecules. IH has the same sign as the other grid-based charges, but is much greater for all cases except carbon atom of HCN. This greater magnitude is consistent with QTAIM and CHELPG results.[80] The only significant basis set dependence of the grid-based methods occurs for formaldehyde (OCH_2), which is due to an unconverged electron density of the molecule with the smaller cc-pVDZ and cc-pVTZ bases.

For the purpose of comparing the applicability of partial atomic charges on excited states, we choose a level of theory suitable for producing accurate electron densities for each molecule. All comparisons are thus made with the same electron density. Mulliken charges calculated by the electronic structure software are shown for comparison, despite their known defficiencies. Ground- and excited-state calculations of LiH and LiF were performed using multi-state complete active space second-order perturbation theory with a Dunning augmented triple-zeta basis (MS-CASPT2/aug-cc-pVTZ) with a 2-electron, 5-orbital complete active space averaged over three complete active space self-consistent field

reference states (SA3-2,5-CAS) for LiH, and a SA2-6,6-CAS reference for LiF. B-TCNE geometries were optimized using resolution-of-the-identity Møller-Plesset perturbation theory (RI-MP2) with a double-zeta basis (cc-pVDZ) using the Q-Chem electronic structure package,[229] and excited-state calculations were performed with MS-CASPT2 with an augmented double-zeta basis (aug-cc-pVDZ) using a SA4-4,4-CAS reference. Both sets of MS-CASPT2 calculations were performed using the Molcas electronic structure package.[147,148] Minimum-energy conical intersections (MECIs) were optimized and excited-state properties of polyenes were calculated with multi-reference single-excitation configuration interaction (MR-CIS) and a 6-31G* basis using the COLUMBUS electronic structure package.[120] Due to the low-lying π3s Rydberg states of ethylene and vinylamine, a diffuse s-type basis function was added to the centre of mass of ethylene and the nitrogen atom of vinylamine. Ground- and excited-state minimum energy geometries and minimum energy conical intersections (MECIs) were optimized at the same level of theory. Additional details on the level of theory for each example molecule are given in Table E3 in the SI.

6.3 Interatomic charge transfer

One of the simplest examples of charge transfer in chemistry are the covalent and charge-transfer states of heteronuclear diatomics. Figure 6.1a shows the lowest two singlet states of LiF with Σ^+ symmetry as a function of the bond length. There is a narrow avoided crossing at an interatomic distance of 6.2 Å. From a Lewis picture, the ground state has an ionic Li^+-F^- character whereas the first excited state is covalent, Li−F. At the dissociation limit, the ground state is made up of neutral atoms (Li + F) and the excited state is the corresponding atoms (Li^+ + F^-).[217] The partial atomic charges in Figure 6.1b show suggest a more complex evolution of the electronic character. At bond lengths shorter than equilibrium, there are two qualitatively different behaviours: Mulliken and Becke charges are negative for both states (Li^-F^+ for $\Delta q = q_{\mathbf{Li}} - q_{\mathbf{F}} = -2$), whereas Hirshfeld, VDD and IH charges are positive for S_0 ($1\ ^1\Sigma^+$) and close to zero for S_1 ($2\ ^1\Sigma^+$). In the vicinity of the equilibrium bond length, only IH matches the Lewis picture with $\Delta q = 2$, whereas Hirshfeld, VDD and Mulliken charges have $\Delta q \approx 1$ on the ground state. All methods have a crossing in partial charges at 4 Å, which significantly precedes the avoided crossing. At bond lengths greater than 5 Å, all charge methods match the neutral and ionic characters expected. Of these methods, IH and Mulliken are closest to the expected charge difference from the ground-state equilibrium to greater bond length, and only IH matches intuition for shorter bond lengths.

A more complex example is given by LiH. The lowest $^1\Sigma^+$ state of LiH is ionic in nature much like LiF. The two lowest $^1\Sigma^+$ excited states of LiH both correspond to neutral Li−H. Approaching the dissociation limit, the ground state corresponds to the ground-state

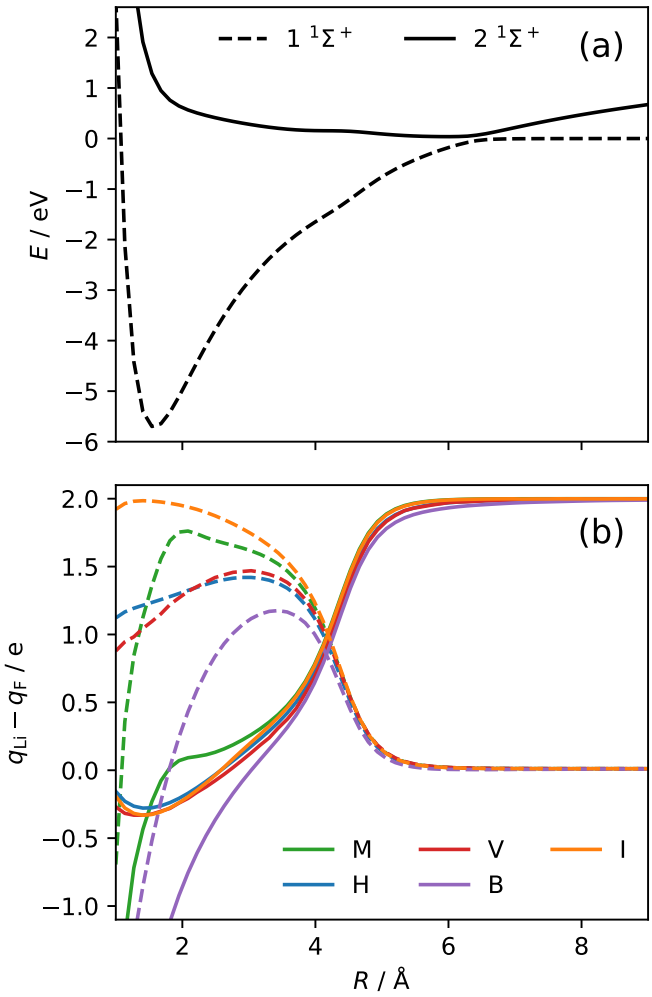

Figure 6.1: (a) MS-CASPT2 potential energy curves of LiF and (b) charge differences as a function of bond length. Charges in (b) are M: Mulliken; H: Hirshfeld; V: VDD; B: Becke; and I: IH. Line styles correspond to electronic states in (a) and (b).

ions Li(2s) + H(1s), S_1 involves an excitation of Li to give Li(2p) + H(1s) and S_2 is the ionic state, $Li(1s)^+ + H(1s)^-$. At longer bond lengths, S_2 re-crosses a higher dissociative state.[218] The ionic state thus passes through both neutral states during dissociation. Figure 6.2 shows potential energies and differences in charge for these three states as a function of bond length. The avoided crossing around 3–4 Å is significanly larger than LiF, with an energy difference of 1.2 eV at the narrowest. In Figure 6.2b, the partial atomic charges show very different behaviours at short bond lengths, similar charges with different magnitudes between the two avoided crossings and nearly identical values approaching the dissociation limit. At bond lengths shorter than equilibrium, Mulliken gives negative charge differences for all three states, whereas VDD and Hirshfeld show similar behaviours on S_0 ($\Delta q \approx 0.9$), and Becke and IH are qualitatively differenct ($\Delta q = 0.4$ and 2.0, respectively). On S_1, Becke and VDD have similar magnitudes near -0.5, and Hirshfeld and IH are also similar near -0.1. The state characters change in the vicinity of the first avoided crossing to yield maximum charges on S_1 of $\sim$1.1 for VDD and IH, 0.8 for Mulliken and Hirshfeld, and 0.6 for Becke, before all going to the dissociation limit of neutral atoms. S_2 charges of all grid-based methods are similar to the S_0 values at short bond lengths, then increase to values from 0.8 to 1.1 in the avoided crossing region before reaching values of 2 at the dissocation limit.

The trends in charges give some indication of the suitability of methods for different analyses: all methods give qualitatively similar results at longer bond lengths. Mulliken and Becke do not match chemical intuition at short bond lengths where the orbital overlap is highest for Mulliken and the Becke weight function is most significant near the atom centres. Hirshfeld and VDD charges give charges whose sign matches expected values, but whose magnitude is small. Only IH gives the expected signs and magnitudes of charges for the full dissociation path in both LiF and LiH. These results, particularly the small magnitudes of Hirshfeld and VDD,[80] have been noted previously for small molecules.

6.4 Intermolecular charge transfer

Charge transfer states in molecular complexes correspond to the excitation of an electron from an occupied orbital in one molecule to an unoccupied or partially occupied orbital in another. These occur in π-stacked donor-acceptor complexes, where the acceptor has a higher electron affinity and can take an electron from the donor. An example of this is the benzene-tetracyanoethylene (B-TCNE) complex, with TCNE acting as the acceptor and benzene as the donor. The B-TCNE complex has two low energy structures with C_{2v} symmetry with nearly identical energies. Figure 6.3 shows the two structures, denoted "parallel" and "perpendicular", as well as labelled symmetry-equivalent atoms. The centres of mass of the two molecules are separated by a distance of 3.1 Å at the minimum energy

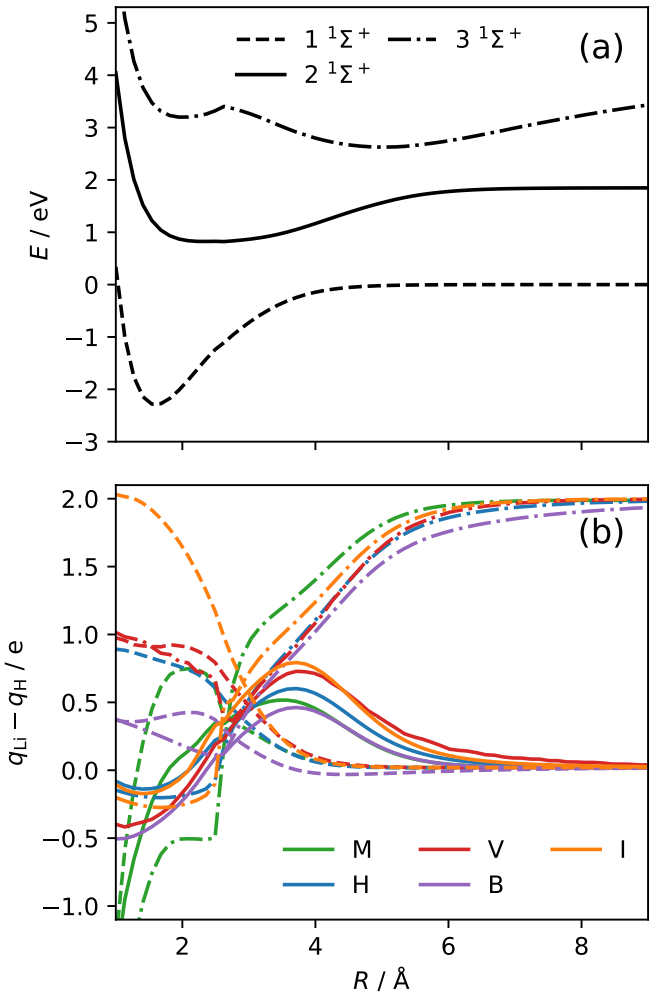

Figure 6.2: (a) MS-CASPT2 potential energy curves of LiH and (b) charge differences as a function of bond length. Charges in (b) are M: Mulliken; H: Hirshfeld; V: VDD; B: Becke; and I: IH. Line styles correspond to electronic states in (a) and (b).

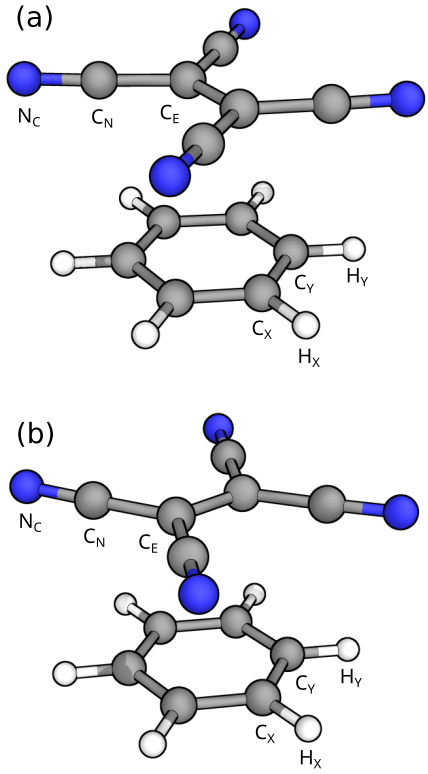

Figure 6.3: Structures of the B-TCNE complex in (a) parallel and (b) perpendicular geometries. Labels for symmetry-equivalent atoms are shown for both.

point.

Table 6.1 shows the energies and differences in molecular charge ($\Delta q_{\text{B-T}}$) for the ground state and the three lowest-lying excited states: two charge-transfer states followed by a π3s Rydberg state. The charge differences show a significant variation for different charge methods considering the distance between the two molecules. Hirshfeld, VDD and IH charges are in good agreement for all states of both geometries, and are for the most part smaller in magnitude than Mulliken and Becke charges. All methods suggest a $\Delta q_{\text{B-T}}$ of roughly 2 e for S_1 and a smaller value for S_2. The greatest disparity appears for S_3, in which an electron from TCNE is excited into a 3s Rydberg orbital with a centre closer to TCNE. Relative to the Hirshfeld, VDD and IH values, the Mulliken charges are appear underestimated whereas the Becke charges are overestimated. For Mulliken, this is naturally explained by its tendency to assign diffuse electron density to all atom centres with diffuse functions despite the large distance to the atom centres. Becke appears to have the opposite effect: the Voronoi weighting assigns more of the space to TCNE than benzene compared to the approaches other than VDD. Interestingly, the VDD charges of the neutral states of

Table 6.1: Potential energies (E) and molecular charge differences ($\Delta q_{\text{B-T}}$) for the ground and excited states of The B-TCNE complex.

			$\Delta q_{\text{B-T}}$ / e				
Geometry	State	Energy / eV	Mulliken	Hirshfeld	VDD	Becke	IH
parallel	S_0	0.01	0.28	0.15	0.18	0.31	0.09
	S_1	3.60	2.03	1.77	1.83	1.96	1.87
	S_2	3.66	1.82	1.58	1.63	1.76	1.67
	S_3	7.08	0.11	0.34	0.34	0.61	0.29
perpendicular	S_0	0.00	0.37	0.16	0.19	0.32	0.11
	S_1	3.59	2.09	1.78	1.84	1.96	1.88
	S_2	3.69	1.88	1.58	1.64	1.76	1.68
	S_3	6.88	0.29	0.44	0.44	0.69	0.43

B-TCNE appear to more closely resemble IH despite the difference in weighting factors.

The molecular charge differences reveal the charge-transfer states of the B-TCNE complex but does not otherwise distinguish between the two other than a small difference in magnitude. The two charge-transfer states result from excitation of an electron from nearly degenerate benzene π-orbitals (E_{1g} symmetry for D_{6h} benzene) to the empty π^*-orbital of TCNE. The presence of TCNE breaks the benzene orbital symmetry, leading to one orbital with lobes at the C_X atoms, and the other with nodes in the same positions. This is observed by the charges of equivalent atoms in Figure 6.4 which shows values for S_1 and S_2. The Mulliken approach predicts charges much greater in magnitude than the other methods, and thus had to be scaled by an order of magnitude. All other approaches are roughly in agreement with smaller differences in magnitude. The difference between states can be seen particularly from the C_X and C_Y charges, which change in sign from one state to the other. Comparing Figure 6.4a and b also reveals that the state characters swap from the parallel to the perpendicular structure. Importantly, this demonstrates how partial atomic charges may be used to identify the electronic character by quantifying the differences in electron density.

6.5 Photodynamics of polyenes

The characteristic motion of the excited state dynamics of ethylene is a twisting of the C=C bond followed by the pyramidalization of one methylene (CH_2) group to reach the **C1Pyr** twist-pyramidalization MECI (Scheme 6.1). Concurrent with this geometric change is the sudden polarization of ethylene, which involves a shift of electron density to the pyramidalized site. This is illustrated by the evolution from the twisted (symmetric) S_2-S_1 MECI to the **C1Pyr** MECI, shown in Figure 6.5. The geometries between MECIs were generated by interpolating along natural internal coordinates, which mainly consisted of the

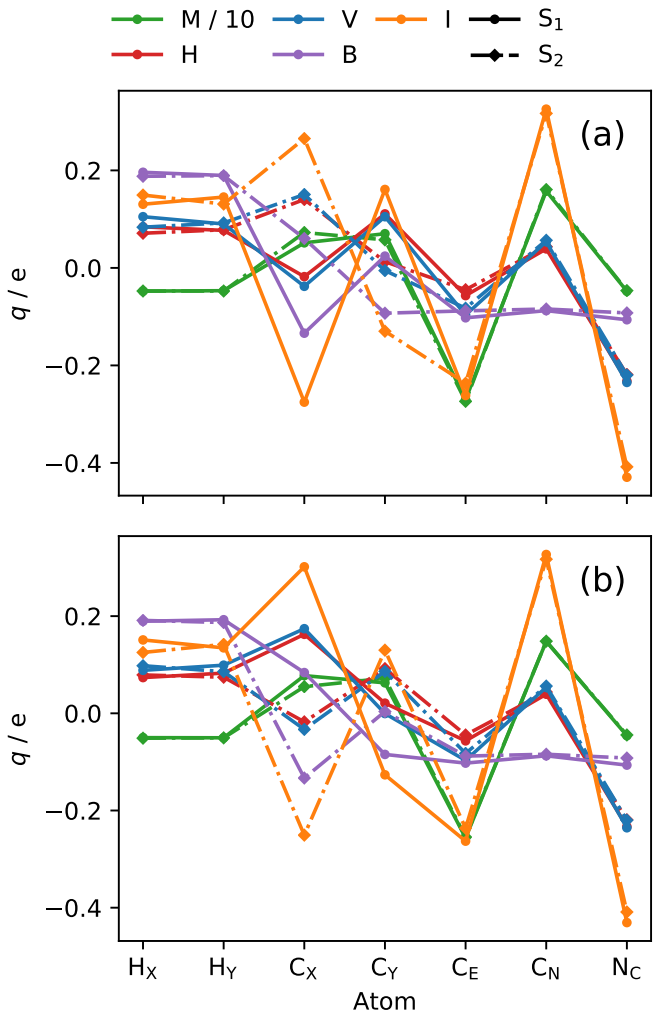

Figure 6.4: Charges of symmetry-equivalent atoms for (a) parallel and (b) perpendicular geometries of B-TCNE. Charge labels are M: Mulliken; H: Hirshfeld; V: VDD; B: Becke; and I: IH. Mulliken charges were scaled by a factor of 10 to fit on the same scale.

out-of-plane pyramidalization motion, CH_2 scissoring and the methylene tilt. Also included are geometries from the **C1Pyr** MECI to the ground state minimum. The pyramidalization and scissoring motion have been shown before to dominate the coupling between the $\pi\pi^*$ state and ground state,[22] whereas the tilt has a relatively minor effect lowering the potential energy and reducing the molecule to C_1 symmetry overall. Without the tilt, there is a point on the conical intersection seam only 0.3 eV bove the MECI with C_s symmetry which bridges between equivalent MECI geometries.[18] As the molecular geometry evolves, so too does the electronic character. Figure 6.5a shows the dominant configurations of the MR-CIS wavefunction as a function of the geometry for the ground and excited state, along with the "highest-occupied" and "lowest-unoccupied" molecular orbitals (HOMO and LUMO, respectively, assuming a closed-shell ground-state configuration). Initially, the ground state (dashed lines) is mostly in a closed-shell π^2 configuration whereas the excited state (solid lines) is in the open-shell $\pi\pi^*$ configuration. As pyramidalization occurs, the symmetry between carbons is broken and the configurations swap. The excited-state character is mostly $(\text{HOMO})^2$, which resembles a lone-pair orbital at the pyramidalized carbon.

Figure 6.5b shows the change in atomic charge difference across the C=C bond as a function of the geometry using several methods. Here, C1 represents the carbon atom at which pyramidalization takes place. Each of the methods show qualitatively similar behaviour of pyramidalization leading to polarization across the C=C bond on S_1, with more negative charge at C1. Each method exhibits a maximum charge diference on S_1 before reaching the **C1Pyr** conical intersection region. In this respect, Mulliken charges disagree with other methods with the onset of polarization and the maximum value occuring much later in the interpolated path. Becke charges yield similar results to the promolecular methods (Hirshfeld and VDD) with maximum charge differences around 0.5 e, whereas IH yields maximum charge differences around 1.4 e around the same geometry, with a decrease to 1.0 e at the **C1Pyr** MECI. Also shown in Figure 6.5b are the differences in ground-state charges. With the exception of Mulliken charges, each method undergoes a gradual decrease in charge with the minima at the S_1-S_0 MECI. Mulliken charge differences on S_0 initially decrease, then increase in the region of the S_1 maxima for mother methods, then decrease to a minimum value before the MECI. The difference between Mulliken charges and other methods may in part be from the Rydberg 3s basis function located between carbon atoms, to which Mulliken populations may be assigned.

The sudden polarization effect and twist-pyramidalization conical intersection motif is not unique to ethylene. It is in fact common for larger polyenes to have similar geometric motifs to the **C1Pyr** MECI of ethylene (**C***n***Pyr** for pyramidalization at carbon n), while also having competitive (and dominant, for longer chain lengths) MECIs which are nonpolar and have a greater multireference character. These kinked-diene (**C***n***Tr**) MECIs have mixed electronic structures which resemble a tetraradicals. In the case of the ethylenic MECIs, the

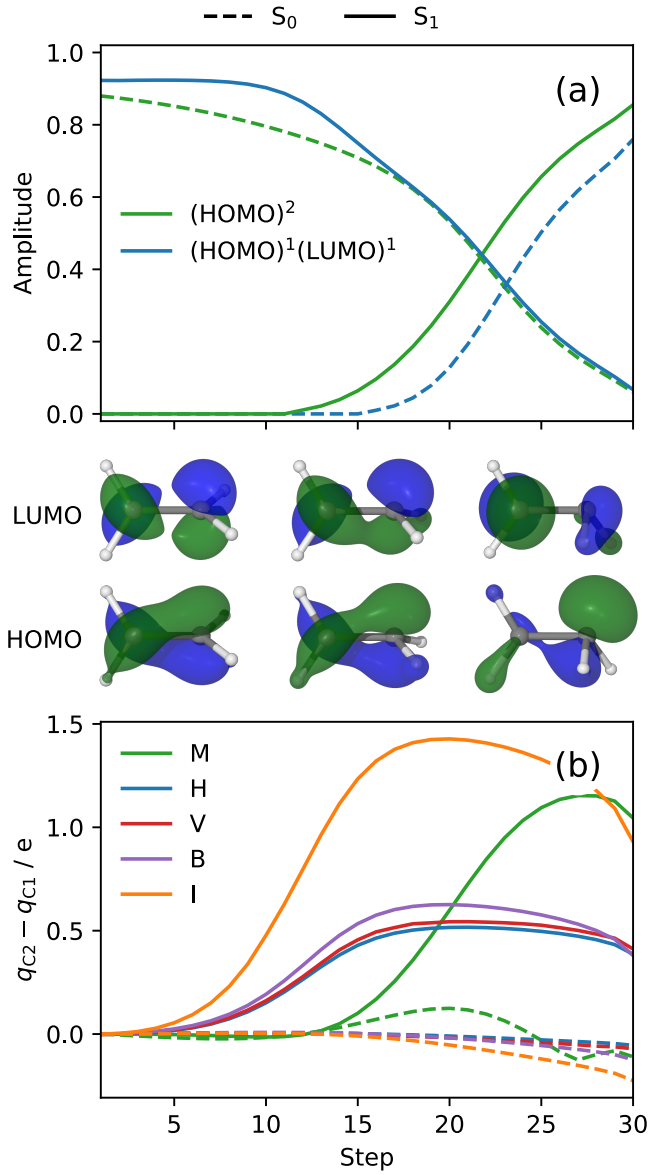

Figure 6.5: Evolution of (a) electronic character and (b) charge differences along interpolated internal coordinates from the S_2-S_1 twisted MECI to the **C1Pyr** S_1-S_0 MECI. The HOMO and LUMO are shown at representative points of the path. Charges in (b) are M: Mulliken; H: Hirshfeld; V: VDD; B: Becke; and I: IH. Solid lines represent the ground state (S_0) and dashed lines represent the excited state (S_1) in (a) and (b).

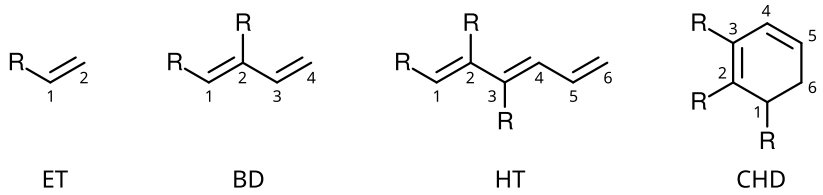

Figure 6.6: Carbon numbering and possible substituent positions for the polyenes ET, BD, HT and CHD. Indices of CHD were chosen to match HT.

valence orbitals are "localized" about the pyramidalized group and the potential energy is largely invariant with chain length. This localization also appears for other systems such as silicon nanoparticles, and may be a general trait of conical intersections due to the relatively small energetic cost of achieving degeneracy between the localized HOMO and LUMO at symmetry-broken geometries.[230,231] The kinked-diene MECIs are more delocalized than the ethylenic MECIs, and do not exhibit the sudden polarization effect.

To demonstrate the similar electronic structures of polyenes conical intersections, a set of 148 MECIs of ethylene (ET), 1,3-butadiene (BD), 1,3,5-hexatriene (HT), 1,3-cyclohexadiene (CHD) and their amino (Am) and cyano (CN) singly-substituted derivatives were optimized at the MR-CIS/6-31G* level of theory. Their labeling used in the text is given in Figure 6.6. Each geometry was displaced by 1 pm along the gradient-difference vector in order to break the MECI degeneracy so that the state characters could be assigned. If the two state characters remained unresolved, the displacement along the nonadiabatic coupling vector was sufficient to resolve them. Charges on the closed-shell state of ethylenic geometries and the mixed tetraradical state of kinked-diene MECIs at the pyramidalized (or central) carbon and the double-bonded (DB) and single-bonded (SB) carbons are shown in Figure 6.7 (note that bond orders correspond to Figure 6.6, except for the ring-closure MECIs of CHD where the C1–C6 bond is DB for the sake of clarity). The state characters were chosen to match that of ET and BD on S_1 approaching the **C1Pyr** and **C2Tr** MECIs, respectively. IH charges were chosen as an example due to their relatively large magnitudes similar to QTAIM and CHELPG results.[80]

The charges in Figure 6.7 are divided into ethylenic and kinked-diene groups (Figure 6.7a and b, respectively) to show the differences in electron density between the two conical intersection types. Most optimized ethylenic MECIs show a strong polarization of the pyramidalized carbon relative to the adjacent carbons, whereas kinked-diene geometries have values closer to zero with several MECIs showing the opposite trend in charge. This becomes clearer when comparing the average polarization across the carbon-carbon bonds: for ethylenic geometries, $\Delta q_{\mathrm{DB}} = q_{\mathrm{DB}} - q_N = 0.92 \pm 0.29$ and $\Delta q_{\mathrm{SB}} = 0.65 \pm 0.24$, whereas for the kinked-diene geometries, $\Delta q_{\mathrm{DB}} = 0.12 \pm 0.43$ and $\Delta q_{\mathrm{SB}} = 0.15 \pm 0.40$. The outliers in Figure 6.7 are all amino-substituted molecules (filled shapes), and all correspond to the site

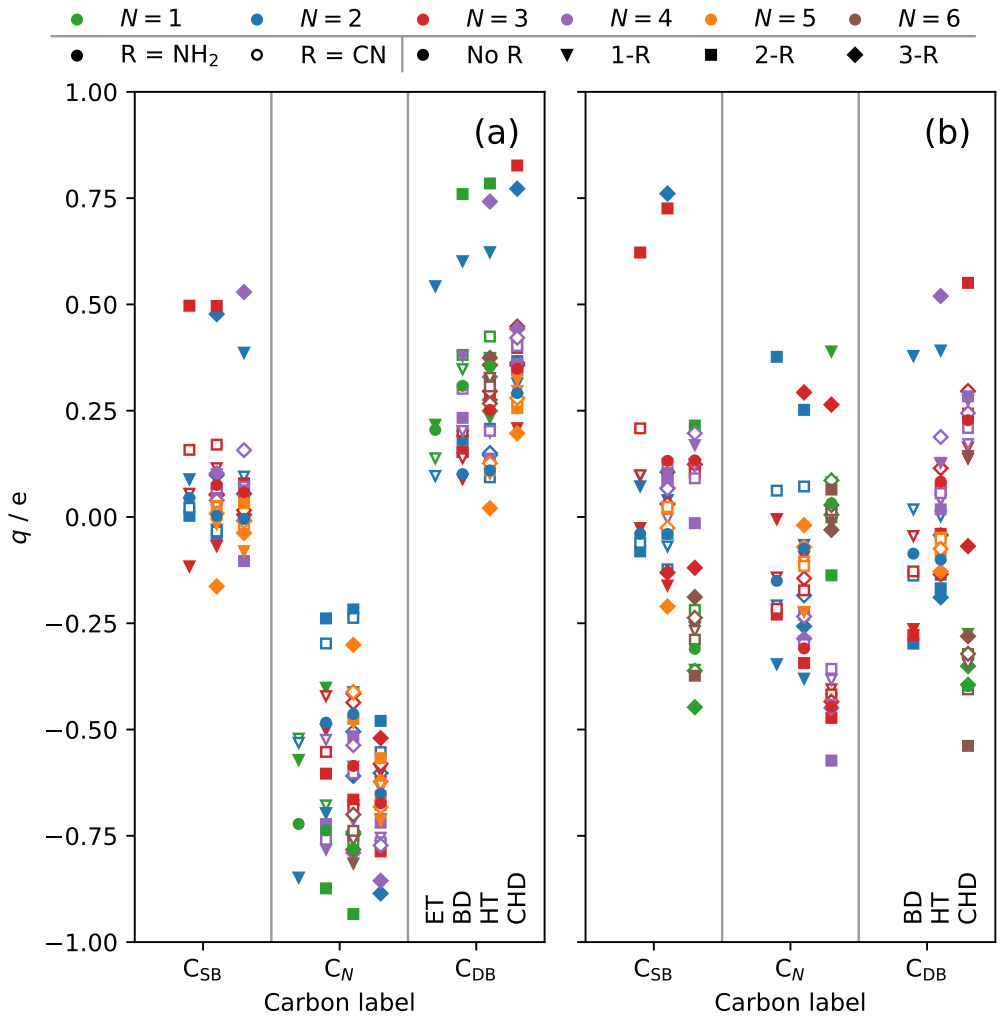

Figure 6.7: Iterative Hirshfeld charges of polyene MECI geometries at pyramidalized (C_N) sites, and sites double-bonded (C_{DB}) and single-bonded (C_{SB}) to C_N. Ethylenic geometries are shown in (a), and kinked-diene geometries are given in (b). Colours represent pyramidalization position (N), shapes represent substituent position and filled/open shapes represent the amino/cyano substituent identity. From left to right in each section is ET, BD, HT and CHD.

adjacent to the substituted carbon atom. Interestingly, these outliers have more positive charges, contrary to the partial negative charge expected from resonance of an amino π-donor. Also noteworthy are the geometries in 6.7b with significantly large charge differenes, such as the **C3Tr** MECIs of 2-AmBD, 2-AmHT and 2-AmCHD (red filled squares), or polarization in the opposite direction such as the **C2Tr** MECIs of 2-AmBD and 2-AmHT (blue filled squares). It should be noted that the alternation of charge continues down the polyene backbone for most MECIs, much like the resonance picture.

The variability in charges of polyene and substituted polyene MECIs shows that great care must be taken in using charges alone to assign branching ratios for nonadiabatic dynamics; however, in previous studies[163,198,220] we have shown that differences in pyramidalization angles in addition to differences in charge often provide a robust separation of different MECIs. Substituents have a minor effect on the charge at MECIs, but they have a significant effect on the potential energy gradients which direct an excited wavepacket to different MECIs. Figures E2–E5 in the SI show the energies at S_1-S_0 MECIs relative to the ground-state minimum energy. In all cases, cyano-substitution lowers the energy of pyramidalization at the substituted site relative to adjacent sites, whereas amino-substitution has the opposite effect. This change in MECI energies is readily predicted by the resonance picture of π-acceptor and π-donor substituents and their stabilization of electron density (*i.e.* during pyramidalization) at specific sites. Due to the corresponding changes gradients on the $\pi\pi^*$ state,[163,198,220] these results help substantiate the claim that functional group substituents can be used to steer photochemical reactions in a predictable manner.

6.6 Conclusions

The concept of partial atomic charges has long been employed to characterize difference in the electronic structure for ground-state molecules and reaction mechanisms. The lack of a quantum mechanical observable have led to many different definitions of these charges. Real-space charges in particular can be efficiently implemented on a grid, and offer a robust determination of charge with no explicit dependence on atomic basis sets. We have shown that the same charge approaches can be used for the characterization of excited-state properties. Partial atomic charges provide a coarse-grained view of otherwise complex electronic structure within a molecule.

In our examples, partial atomic charges have been used to identify charge transfer on excited states. All methods that we tested readily identify the ion-pair states for large atomic separation, but only IH identify the same character for bond lengths shorter than equilibrium. All approaches readily identify the differences in B-TCNE charge transfer states and minimum-energy geometries with the exception of the Mulliken results. The real-space methods also show consistent onset of sudden polarization of ethylene on the

excited state and the lack of polarization on the ground state. From these results, we have identified that IH produce charges consistent with chemical intuition that are easily differentiated due to their large magnitudes. We used IH charges to begin to gain an intuition for the photodynamics of polyenes: ET, BD, HT and CHD showed a consistent trend of local carbon-carbon bond polarization at ethylenic conical intersections, but no trend for kinked-diene conical intersections. These results point towards a simple picture of polyene excited-state dynamics which can be used to predict and design novel photochemical properties.

Acknowledgements

R.J.M. and M.S.S. acknowledge financial support from the Natural Sciences and Engineering Research Council of Canada (NSERC).

Chapter 7
Conclusions and future work

This thesis has demonstrated the potential for chemical substitution to direct photochemical processes of polyenes to particular reactive outcomes. Changes in the stability of certain conical intersection regions (and in the PES as a whole) can be predicted using the basic concepts of steric repulsion, electronic resonance, and frequency changes due to mass. This has been shown by time-dependent theoretical simulation, validated by time-resolved spectroscopic measurements, of substituted ethylenes and butadienes, and the observation of consistent trends for substituted polyenes.

The electronic effect of a cyano substituent was readily demonstrated by acrylonitrile (cyanoethylene) and its methyl-substituted analogs in Chapter 2. The cyano group has a π-acceptor effect which inhibits electron density, and thus pyramidalization, at the unsubstituted site. As a result, the excited-state decay proceeds almost exclusively through pyramidalization at the substituted carbon in the region of the lower-energy MECI. Adding methyl groups to acrylonitrile demonstrates the strength of π-acceptor effect. The dynamics of methyl-substituted molecules are slowed at the substituted sites; however, even methacrylonitrile (1-cyano-1-methylethylene) undergoes pyramidalization at the CN-substituted site due to the strong π-acceptor effect, despite the fact that CH_2 pyramidalization is dynamically favoured. This led to relatively slow excited-state lifetimes and TRPES singal decay for methacrylonitrile relative to acrylonitrile and crotonitile.

Chapter 3 showed the trends in substituted ethylenes with a series of electronic (π-donor and π-acceptor) substituents. The difference in twist-pyramidalization MECI energies on opposite sites of the C$-$C bond shows a correlation between the magnitudes of structure deformation required to reach the conical intersection and the relative energies of the potential crossings. This can be explained in term of a 2-electron-2-orbital biradical model used to represent the ground, $\pi\pi^*$ and $(\pi^*)^2$ states of ethylene, whereby changes in the initial polarization across the C$-$C bond by a substituent lead to less/more pyramidalization required to reacher the lower/higher energy conical intersection region. The results of nonadiabatic dynamics simulations validate this model for acrylonitrile and vinylamine (aminoethylene). The majority of the transitions to the ground electronic state proceed with pyramidalization at the favoured carbon atom (cyano-substituted, and amino-unsubstituted). Electronic substituents consistently led to predictable perturbation in electronic struture and dynamics of ethylene.

The ability of chemical substitution to strongly influence photochemical reactions (*i.e.* with distinct isomerization products) was shown in Chapter 4. After photoexcitation to the $\pi\pi^*$ state, 1,3-butadiene can proceed to the ground state via decay pathways similar to ethylene or kinked-diene pathways with no C$-$C bond polarization. Substitution with a cyano group lowers the relative MECI energy for ethylenic pyramidalzation at the substituted site while also lowering the energy of the kinked-diene MECI independent of the substituent position. Here, the difference in gradients on the inital $\pi\pi^*$ state play an impor-

tant role by directing the excited wavepacket towards pyramidalization. Thus, substitution shows the potential to direct the ultrafast dynamics of butadiene towards specific regions of the PES which may correspond to different photoproducts.

Several past studies have used methyl substitution as an inertial substituent due to its weak π-donor ability in comparison to other functional groups. In Chapter 5, it was shown that the electronic effect of methyl groups should not be neglected in dynamics simulations. TRPES experiments gave a relatively slow decay timescale for terminal-methyl-substituted butadiene relative to unsubsititued butadiene and central-methyl-substituted butadiene. Excited-state dynamics simulations using hydrogen atoms with an artificial mass of 15 u resulted in an underestimated change in decay timescales relative to unsubstituted butadiene. This is once again explained in terms of changes of excited-state gradients of the substituted molecules. Methyl substitution leads to a greater amount of the excited-state wavepacket undergoing internal conversion with pyramidalization at the unsubstited sites, whereas mass-weighting alone evolves on the same PES as unsubsituted butadiene and decays through similar geometries to the unweighted molecule.

The previous results show the utility the concept of partial atomic charge for interpreting the electronic structures that arise due to excited-state nuclear dynamics. Chapter 6 gives an overview of grid-based partial atomic charge methods and their comparison the atomic-orbital-based Mulliken approach. Changes in electronic character such as interatomic and intermolecular charge transfer are clearly shown by the analysis of partial atomic charges. For ethylene, 1,3-butadiene, 1,3,5-hexatriene, 1,3-cyclohexadiene and their amino- and cyano-substituted analogs, analysis of partial atomic charges shows a clear trend in the sudden polarization effect across a C$-$C bond for MECIs similar the ethylene. Kinked-diene geometries, however, show no consistent trend in charge differences. This demonstrates how the principles charge localization can be applied to larger molecules to influence photochemical reactions.

This work represents a first step towards predictive models of substituent effects on ultrafast photochemistry, particularly the photoisomerization of conjugated polyenes. It has the potential to be applied to larger molecular systems to obtain desired isomerized photoproducts, or to be used in light-harvesting and molecular motors to tune the photochemical properties of molecules. For universal application in photochemistry, there remain several open questions. Firstly, all systems studied in this thesis are isolated molecules which represent the gas phase at low pressures, whereas most chemical reactions take place within a solvent. The gas-phase simulations do not include intermolecular interactions, thus the absorbed photon energy is conserved and converted to vibrational kinetic energy, which is sufficiently high to overcome isomerization and bond-dissociation energies on the ground state. The addition of a solvent would serve as an energetic bath which would stabilize products on the ground state; however, a polar solvent may also influence the local envi-

ronment during pyramidalization. It remains to be seen if solvents enhance or weaken the effect of electronic substituents for excited-state processes.

The subject of this thesis is the photoisomerization of polyenes, which represents an important class of internal conversion processes in organic molecules. This involves excitation exclusively to alkene $\pi\pi^*$ states. There are, however, other types of ultrafast internal conversion processes which may results in different isomerization or bond cleavage. In principle, the substituent effects above may be applicable to other other electronic characters, for example by stabilizing/destabilizing a radical at a specific site in $\pi\sigma^*$ dissociative dynamics. As in other aspects of chemistry, substituents effects serve as a toolbox for inhibiting/favouring nuclear motion and electron density within molecules. Simulation and characterization of substituent effects on a different types of ultrafast decay processes is required to gain an intuition of the overarching rules of internal conversion photochemistry.

References

(1) Kasha, M. *Discuss. Faraday Soc.* **1950**, *9*, 14–19.

(2) Turro, N. J.; Ramamurthy, V.; Scaiano, J. C. *Modern Molecular Photochemistry of Organic Molecules*; University Science Books: Sausalito, CA, 2010.

(3) Eyring, H. *J. Chem. Phys.* **1935**, *3*, 107–115.

(4) Evans, M. G.; Polanyi, M. *Trans. Faraday Soc.* **1935**, *31*, 875–894.

(5) Pechukas, P. *Adv. Rev. Phys. Chem.* **1981**, *31*, 159–177.

(6) Truhlar, D. G.; Garrett, B. C.; Klippenstein, S. J. *J. Phys. Chem.* **1996**, *100*, 12771–12800.

(7) Levine, B. G.; Martínez, T. J. *Annu. Rev. Phys. Chem.* **2007**, *58*, 613–634.

(8) Schuurman, M. S.; Stolow, A. *Annu. Rev. Phys. Chem.* **2018**, *69*, 427–450.

(9) Berry, M. V.; Wilkinson, M. *Proc. R. Soc. Lond. A* **1984**, *392*, 15–43.

(10) Yarkony, D. R. *Rev. Mod. Phys.* **1996**, *68*, 985–1013.

(11) Yarkony, D. R. In *Conical Intersections: Electronic Structure, Dynamics & Spectroscopy*; Domcke, W., Yarkony, D. R., Köppel, H., Eds.; World Scientific Publishing Co. Pte. Ltd.: Singapore, 2004; pp 41–127.

(12) Klessinger, M. *Angew. Chem. Int. Ed.* **1995**, *34*, 549–551.

(13) Bernardi, F.; Olivucci, M.; Robb, M. A. *Chem. Soc. Rev.* **1996**, *25*, 321–328.

(14) Salem, L. *Acc. Chem. Res.* **1979**, *12*, 87–92.

(15) Dugave, C.; Demange, L. *Chem. Rev.* **2003**, *103*, 2475–2532.

(16) Bonačić-Koutecký, V.; Bruckmann, P.; Hiberty, P.; Koutecký, J.; Leforestier, C.; Salem, L. *Angew. Chem. Int. Ed.* **1975**, *14*, 575–576.

(17) Allison, T. K.; Tao, H.; Glover, W. J.; Wright, T. W.; Stooke, A. M.; Khurmi, C.; van Tilborg, J.; Liu, Y.; Falcone, R. W.; Martínez, T. J.; Belkacem, A. *J. Chem. Phys.* **2012**, *136*, 124317.

(18) Mori, T.; Martínez, T. J. *J. Chem. Theory Comput.* **2013**, *9*, 1155–1163.

(19) Sellner, B.; Barbatti, M.; Müller, T.; Domcke, W.; Lischka, H. *Mol. Phys.* **2013**, *111*, 2439–2450.

(20) Wulfman, C. E. *Science* **1971**, *172*, 1061.

(21) Brooks, B. R.; Schaefer III, H. F. *J. Am. Chem. Soc.* **1979**, *101*, 307–311.

(22) Viel, A.; Krawczyk, R. P.; Manthe, U.; Domcke, W. *Angew. Chem. Int. Ed.* **2003**, *42*, 3434–3436.

(23) Dauben, W. G.; Ritscher, J. S. *J. Am. Chem. Soc.* **1970**, *92*, 2925–2926.

(24) Dauben, W. G.; Seeman, J. I.; Vietmeyer, N. D.; Wendschuh, P. H. *Pure Appl. Chem.* **1973**, *33*, 197–215.

(25) Squillacote, M. E.; Semple, T. C. *J. Am. Chem. Soc.* **1987**, *109*, 892–894.

(26) Schuddeboom, W.; Jonker, S. A.; Warman, J. M.; de Haas, M. P.; Vermeulen, M. J. W.; Jager, W. F.; de Lange, B.; Feringa, B. L.; Fessenden, R. W. *J. Am. Chem. Soc.* **1993**, *115*, 3286–3290.

(27) Erbas-Cakmak, S.; Leigh, D. A.; McTernan, C. T.; Nussbaumer, A. L. *Chem. Rev.* **2015**, *115*, 10081–10206.

(28) Feringa, B. L. *Angew. Chim. Int. Ed.* **2017**, *56*, 11060–11078.

(29) Hall, C. R.; Browne, W. R.; Feringa, B. L.; Meech, S. R. *Angew. Chim. Int. Ed.* **2018**, *57*, 6203–6207.

(30) Feringa, B. L. *Acc. Chem. Res.* **2001**, *34*, 504–513.

(31) Wang, J.; Feringa, B. L. *Science* **2011**, *331*, 1429–1432.

(32) Fuß, W.; Haas, Y.; Zilberg, S. *Chem. Phys.* **2000**, *259*, 273–295.

(33) Garavelli, M. *Theor. Chem. Acc.* **2006**, *116*, 87–105.

(34) Komainda, A.; Ostojić, B.; Köppel, H. *J. Chem. Phys. A* **2013**, *117*, 8782–8793.

(35) Komainda, A.; Lefrancois, D.; Dreuw, A.; Köppel, H. *Chem. Phys.* **2017**, *482*, 27–38.

(36) Levine, B. G.; Martínez, T. J. *J. Phys. Chem. A* **2009**, *113*, 12815–12824.

(37) Glover, W. J.; Mori, T.; Schuurman, M. S.; Boguslavskiy, A. E.; Schalk, O.; Stolow, A.; Martínez, T. J. *J. Chem. Phys.* **2018**, *148*, 164303.

(38) Wilsey, S.; Houk, K. N. *Photochem. Photobiol.* **2002**, *76*, 616–621.

(39) Norton, J. E.; Houk, K. N. *Mol. Phys.* **2006**, *104*, 993–1008.

(40) Ernst, O. P.; Lodowski, D. T.; Elstner, M.; Hegemann, P.; Brown, L. S.; Kandori, H. *Chem. Rev.* **2014**, *114*, 126–163.

(41) Wright, C. B.; Redmond, T. M.; Nickerson, J. M. In *Progress in Molecular Biology and Translational Science, Vol. 134*; Hejtmancik, J. F., Nickerson, J. M., Eds.; Elsevier Inc.: Amsterdam, Netherlands, 2015; pp 443–448.

(42) Bonačić-Koutecký, V.; Koutecký, J.; Michl, J. *Angew. Chem. Int. Ed.* **1987**, *26*, 170–189.

(43) Virshup, A. M.; Levine, B. G.; Martínez, T. J. *Theor. Chem. Acc.* **2014**, *133*, 1506.

(44) Cembran, A.; Bernardi, F.; Olivucci, M.; Garavelli, M. *Proc. Natl. Acad. Sci.* **2005**, *102*, 6255–6260.

(45) Martínez, T. J. *Acc. Chem. Res.* **2006**, *39*, 119–126.

(46) Olsen, S.; Lamothe, K.; Martínez, T. J. *J. Am. Chem. Soc.* **2010**, *132*, 1192–1193.

(47) Ko, C.; Levine, B.; Toniolo, A.; Manohar, L.; Olsen, S.; Werner, H.-J.; Martínez, T. J. *J. Am. Chem. Soc.* **2003**, *125*, 12710–12711.

(48) Freedman, K. A.; Becker, R. S. *J. Am. Chem. Soc.* **1986**, *108*, 1245–1251.

(49) Ohta, K.; Naitoh, Y.; Tominaga, K.; Hirota, N.; Yoshihara, K. *J. Phys. Chem. A* **1998**, *102*, 35–44.

(50) Ingold, C. K. *Chem. Rev.* **1934**, *15*, 225–274.

(51) Hammett, L. P. *J. Am. Chem. Soc.* **1937**, *59*, 96–103.

(52) Ozimiński, W. P.; Dobrowolski, J. C. *J. Phys. Org. Chem.* **2009**, *22*, 769–778.

(53) Scudder, P. H. *Electron Flow in Organic Chemistry: A Decision Based Guide to Organic Mechanisms*, 2nd ed.; John Wiley & Sons, Inc.: Hoboken, NJ, 2013.

(54) Lee, A. M. D.; Coe, J. D.; Ullrich, S.; Ho, M.-L.; Lee, S.-J.; Cheng, B.-M.; Zgierski, M. Z.; Chen, I.-C.; Martínez, T. J.; Stolow, A. *J. Phys. Chem. A* **2007**, *111*, 11948–11960.

(55) Schalk, O.; Boguslavskiy, A. E.; Stolow, A. *J. Phys. Chem. A* **2010**, *114*, 4058–4064.

(56) Neville, S. P.; Wang, Y.; Boguslavskiy, A. E.; Stolow, A.; Schuurman, M. S. *J. Chem. Phys.* **2016**, *144*, 014305.

(57) Lochbrunner, S.; Schultz, T.; Schmitt, M.; Shaffer, J. P.; Zgierski, M. Z.; Stolow, A. *J. Chem. Phys.* **2001**, *114*, 2519–2522.

(58) Cederbaum, L. S. In *Conical Intersections: Electronic Structure, Dynamics & Spectroscopy*; Domcke, W., Yarkony, D. R., Köppel, H., Eds.; World Scientific Publishing Co. Pte. Ltd.: Singapore, 2004; pp 3–40.

(59) Hartree, D. R. *Proc. Camb. Phil. Soc.* **1928**, *24*, 89–110.

(60) Szabo, A.; Ostlund, N. S. *Modern Quantum Chemistry: Introduction to Advanced Electronic Structure Theory*; McGraw-Hill, Inc.: New York, NY, 1989.

(61) Fock, V. *Z. Physik* **1930**, *61*, 126–148.

(62) Boys, S. F. *Proc. R. Soc. Lond. A* **1950**, *200*, 542–554.

(63) Sherrill, C. D.; Schaefer III, H. F. *Adv. Quantum Chem.* **1999**, *34*, 143–269.

(64) Roos, B. O.; Taylor, P. R.; Siegbahn, P. E. M. *Chem. Phys.* **1980**, *48*, 157–173.

(65) Andersson, K.; Malmqvist, P.-Å.; Roos, B. O. *J. Chem. Phys.* **1991**, *96*, 1218–1226.

(66) Finley, J.; Malmqvist, P.-Å.; Roos, B. O.; Serrano-Andrés, L. *Chem. Phys. Lett.* **1998**, *288*, 299–306.

(67) Kraemer, W. P.; Roos, B. O.; Siegbahn, P. E. M. *Chem. Phys.* **1982**, *69*, 305–321.

(68) Lengsfield III, B. H.; Saxe, P.; Yarkony, D. R. *J. Chem. Phys.* **1984**, *81*, 4549–4553.

(69) Lischka, H.; Dallos, M.; Szalay, P. G.; Yarkony, D. R.; Shepard, R. *J. Chem. Phys.* **2003**, *120*, 7322–7329.

(70) Gonthier, J. F.; Steinmann, S. N.; Wodrich, M. D.; Corminboeuf, C. *Chem. Soc. Rev.* **2012**, *41*, 4671–4687.

(71) Cioslowski, J. *J. Am. Chem. Soc.* **1989**, *111*, 8333–8336.

(72) Ferenczy, G. *J. Comput. Chem.* **1991**, *12*, 913–917.

(73) Chirlian, L. E.; Francl, M. M. *J. Comput. Chem.* **1987**, *8*, 894–905.

(74) Breneman, C. M.; Wiberg, K. B. *J. Comput. Chem.* **1990**, *11*, 361–373.

(75) Mulliken, R. S. *J. Chem. Phys.* **1955**, *23*, 1833–1840.

(76) Löwdin, P.-O. *J. Chem. Phys.* **1950**, *18*, 365–375.

(77) Reed, A. E.; Weinstock, R. B.; Weinhold, F. *J. Chem. Phys.* **1985**, *83*, 735–746.

(78) Bader, R. F. W. *Atoms in Molecules: A Quantum Theory*; Oxford University Press: Oxford, UK, 1990.

(79) Hirshfeld, F. L. *Theoret. Chim. Acta.* **1977**, *44*, 129–138.

(80) Bultinck, P.; Alsenoy, C. V.; Ayers, P. W.; Carbó-Dorca, R. *J. Chem. Phys.* **2007**, *126*, 144111.

(81) Köppel, H.; Domcke, W.; Cederbaum, L. S. In *Conical Intersections: Electronic Structure, Dynamics & Spectroscopy*; Domcke, W., Yarkony, D. R., Köppel, H., Eds.; World Scientific Publishing Co. Pte. Ltd.: Singapore, 2004; pp 323–368.

(82) Worth, G. A.; Meyer, H.-D.; Köppel, H.; Cederbaum, L. S.; Burghardt, I. *Int. Rev. Phys. Chem.* **2008**, *27*, 569–606.

(83) Richings, G. W.; Polyak, I.; Spinlove, K. E.; Worth, G. A.; Burgharrdt, I.; Lasorne, B. *Int.*

Rev. Phys. Chem. **2015**, *34*, 269–308.

(84) Tully, J. C. *J. Chem. Phys.* **1990**, *93*, 1061–1071.

(85) Ben-Nun, M.; Martínez, T. J. In *Adv. Chem. Phys., Vol. 121*; Prigogine, I., Rice, S. A., Eds.; John Wiley & Sons, Inc.: Hoboken, NJ, 2002; pp 439–512.

(86) Makhov, D. V.; Glover, W. J.; Martínez, T. J.; Shalashilin, D. V. *J. Chem. Phys.* **2014**, *141*, 054110.

(87) Richings, G. W.; Worth, G. A. *Chem. Phys. Lett.* **2017**, *683*, 606–612.

(88) Martínez, T. J.; Ben-Nun, M.; Levine, R. D. *J. Phys. Chem.* **1996**, *100*, 7884–7895.

(89) Ben-Nun, M.; Quenneville, J.; Martínez, T. J. *J. Phys. Chem. A* **2000**, *104*, 5161–5175.

(90) Hack, M. D.; Wensmann, A. M.; Truhlar, D. G.; Ben-Nun, M.; Martínez, T. J. *J. Chem. Phys.* **2001**, *115*, 1172–1186.

(91) Mignolet, B.; Curchod, B. F. E. *J. Chem. Phys.* **2018**, *148*, 134110.

(92) Scherer, N. F.; Knee, J. L.; Smith, D. D.; Zewail, A. H. *J. Phys. Chem.* **1985**, *89*, 5141–5143.

(93) Zewail, A. H. *Science* **1988**, *242*, 1645–1653.

(94) Zewail, A. H. *J. Phys. Chem. A* **2000**, *104*, 5660–5694.

(95) Neumark, D. M. *Adv. Rev. Phys. Chem.* **2001**, *52*, 255–277.

(96) Blanchet, V.; Zgierski, M. Z.; Seideman, T.; Stolow, A. *Nature* **1999**, *401*, 52–54.

(97) Stolow, A. *Adv. Rev. Phys. Chem.* **2003**, *54*, 89–119.

(98) Stolow, A.; Bragg, A. E.; Neumark, D. M. *Chem. Rev.* **2004**, *104*, 1719–1758.

(99) Spanner, M.; Patchkovskii, S.; Zhou, C.; Matsika, S.; Kotur, M.; Weinacht, T. C. *Phys. Rev. A* **2012**, *86*, 053406.

(100) Okabe, H.; Dibeler, V. H. *J. Chem. Phys.* **1973**, *59*, 2430–2435.

(101) West, G. A.; Berry, M. J. *J. Chem. Phys.* **1974**, *61*, 4700–4716.

(102) Halpern, J. B.; Miller, G. E.; Okabe, H.; Nottingham, W. *J. Photochem. Photobiol. A* **1987**, *42*, 63–72.

(103) Gandini, A.; Hackett, P. A. *Can. J. Chem.* **1978**, *56*, 2096–2098.

(104) Du, W.-N.; Luo, C.; Li, Z.-S. *J. Chem. Phys.* **2008**, *129*, 174309.

(105) Bird, C. A.; Donaldson, D. J. *Chem. Phys. Lett.* **1996**, *249*, 40–45.

(106) Oh, C. Y.; Shin, S. K.; Kim, H. L.; Park, C. R. *J. Phys. Chem. A* **2003**, *107*, 4333–4338.

(107) Mullen, P. A.; Orloff, M. K. *Theoret. Chim. Acta* **1971**, *23*, 278–284.

(108) Motte-Tollet, F.; Messina, D.; Hubin-Franskin, M.-J. *J. Chem. Phys.* **1995**, *103*, 90–89.

(109) Eden, S.; Limão-Vieira, P.; Kendall, P.; Mason, N. J.; Hoffmann, S. V.; Spyrou, S. M. *Eur. Phys. J. D* **2003**, *26*, 201–210.

(110) Ilakovac, V.; Carniato, S.; Gallet, J.-J.; Kukk, E.; Horvatić, D.; Ilakovac, A. *Phys. Rev. A* **2008**, *77*, 012516.

(111) Ilakovac, V.; Houari, Y.; Carniato, S.; Gallet, J.-J.; Kukk, E.; Horvatić, D. *Phys. Rev. A* **2012**, *85*, 062521.

(112) Wang, K.; McKoy, V.; Hockett, P.; Schuurman, M. S. *Phys. Rev. Lett.* **2014**, *112*, 113007.

(113) Schuurman, M. S.; Giegerich, J.; Pachner, K.; Lang, D.; Kiendl, B.; MacDonell, R. J.; Krueger, A.; Fischer, I. *Chem. Eur. J.* **2015**, *21*, 14486–14495.

(114) Wu, G.; Boguslavskiy, A. E.; Schalk, O.; Schuurman, M. S.; Stolow, A. *J. Chem. Phys.* **2011**, *135*, 165309.

(115) Wolf, T. J. A.; Kuhlman, T. S.; Schalk, O.; Martínez, T. J.; Møller, K. B.; Stolow, A.; Unterreiner, A.-N. *Phys. Chem. Chem. Phys.* **2014**, *16*, 11770–11779.

(116) Schalk, O.; Schuurman, M. S.; Wu, G.; Lang, P.; Mucke, M.; Feifel, R.; Stolow, A. *J. Phys. Chem. A* **2014**, *118*, 2279–2287.

(117) Eland, J. H. D.; Vieuxmaire, O.; Kinugawa, T.; Lablanquie, P.; Hall, R. I.; Penent, F. *Phys. Rev. Lett.* **2003**, *90*, 053003.

(118) Kłoda, T.; Matsuda, A.; Karlsson, H. O.; Elshakre, M.; Linusson, P.; Eland, J. H. D.; Feifel, R.; Hansson, T. *Phys. Rev. A* **2010**, *82*, 033431.

(119) Martínez, T. J.; Ben-Nun, M.; Levine, R. D. *J. Phys. Chem. A* **1997**, *101*, 6389–6402.

(120) Lischka, H. et al. *COLUMBUS, an ab initio electronic structure program, release 7.0*; 2012.

(121) Hariharan, P. C.; Pople, J. A. *Theor. Chim. Acta* **1973**, *28*, 213–222.

(122) Hudock, H. R.; Levine, B. G.; Thompson, A. L.; Satzger, H.; Townsend, D.; Gador, N.; Ullrich, S.; Stolow, A.; Martínez, T. J. *J. Phys. Chem. A* **2007**, *111*, 8500–8508.

(123) Hudock, H. R.; Martínez, T. J. *ChemPhysChem* **2008**, *9*, 2486–2490.

(124) Mori, T.; Glover, W. J.; Schuurman, M. S.; Martínez, T. J. *J. Phys. Chem. A* **2012**, *116*, 2808–2818.

(125) Houk, K. N.; Munchausen, L. L. *J. Am. Chem. Soc.* **1976**, *98*, 937–946.

(126) Delwiche, J.; Gochel-Dupuis, M.; Collin, J. E.; Heinesch, J. *J. Electron Spectrosc. Relat. Phenom.* **1993**, *66*, 65–74.

(127) Willett, G. D.; Baer, T. *J. Am. Chem. Soc.* **1980**, *102*, 6774–6779.

(128) Chrostowska, A.; Nguyen, T. X. M.; Dargelos, A.; Khayar, S.; Graciaa, A.; Guillemin, J.-C. *J. Phys. Chem. A* **2009**, *113*, 2387–2396.

(129) Schalk, O.; Boguslavskiy, A. E.; Stolow, A.; Schuurman, M. S. *J. Am. Chem. Soc.* **2011**, *133*, 16451–16458.

(130) Ohno, K.; Matsumoto, S.; Imai, K.; Harada, Y. *J. Phys. Chem.* **1984**, *88*, 206–209.

(131) Ben-Nun, M.; Martínez, T. J. *Chem. Phys.* **2000**, *259*, 237–248.

(132) Barbatti, M.; Ruckenbauer, M.; Lischka, H. *J. Chem. Phys.* **2005**, *122*, 174307.

(133) Weingart, O. *J. Am. Chem. Soc.* **2007**, *129*, 10618–10619.

(134) Polli, D.; Altoe, P.; Weingart, O.; Spillane, K. M.; Manzoni, C.; Brida, D.; Tomasello, G.; Orlandi, G.; Kukura, P.; Mathies, R. A.; Garavelli, M.; Cerullo, G. *Nature* **2010**, *467*, 440–443.

(135) Quenneville, J.; Martínez, T. J. *J. Phys. Chem. A* **2003**, *107*, 829–837.

(136) Takeuchi, S.; Ruhman, S.; Tsuneda, T.; Chiba, M.; Taketsugu, T.; Tahara, T. *Science* **2008**, *322*, 1073–1077.

(137) Fuß, W.; Kosmidis, C.; Schmid, W. E.; Trushin, S. A. *Angew. Chem. Int. Ed.* **2004**, *43*, 4178–4182.

(138) Kobayashi, T.; Horio, T.; Suzuki, T. *J. Phys. Chem. A* **2015**, *119*, 9518–9523.

(139) Champenois, E. G.; Shivaram, N. H.; Wright, T. W.; Yang, C.-S.; Belkacem, A.; Cryan, J. P. *J. Chem. Phys.* **2016**, *144*, 014303.

(140) MacDonell, R. J.; Schalk, O.; Geng, T.; Thomas, R. D.; Feifel, R.; Hansson, T.; Schuur-

man, M. S. *J. Chem. Phys.* **2016**, *145*, 114306.

(141) Michl, J.; Bonačić-Koutecký, V. *Tetrahedron* **1988**, *44*, 7559–7585.

(142) Nenov, A.; Cordes, T.; Herzog, T. T.; Zinth, W.; de Vivie-Riedle, R. *J. Chem. Phys. A* **2010**, *114*, 13016–13030.

(143) Saebø, S.; Radom, L. *J. Mol. Struct.* **1982**, *89*, 227–233.

(144) Brown, R. D.; Godfrey, P.; Kleibomer, B.; Pierlot, A. P.; McNaughton, D. *J. Molec. Spec.* **1990**, *142*, 195–204.

(145) Pillsbury, N. R.; Drucker, S. *J. Mol. Spec.* **2004**, *224*, 188–193.

(146) Frank, I.; Grimme, S.; Peyerimhoff, S. D. *J. Phys. Chem.* **1996**, *100*, 16187–16194.

(147) Aquilante, F. et al. *J. Comput. Chem.* **2016**, *37*, 506–541.

(148) Vancoillie, S.; Delcey, M. G.; Lindh, R.; Vysotskiy, V.; Malmqvist, P.-Å.; Veryazov, V. *J. Comput. Chem.* **2013**, *34*, 1937–1948.

(149) Coe, J. D.; Ong, M. T.; Levine, B. G.; Martínez, T. J. *J. Phys. Chem. A* **2008**, *112*, 12559–12567.

(150) Martín, M. E.; Losa, A. M.; Fdez.-Galván, I.; Aguilar, M. A. *J. Chem. Phys.* **2004**, *121*, 3710–3716.

(151) Aidas, K.; Møgelhøj, A.; Nilsson, E. J. K.; Johnson, M. S.; Mikkelsen, K. V.; Christiansen, O.; Söderhjelm, P.; Kongsted, J. *J. Chem. Phys.* **2008**, *128*, 194503.

(152) Slee, T.; Larouche, A.; Bader, R. F. W. *J. Phys. Chem.* **1988**, *92*, 6219–6227.

(153) Wiberg, K. B.; Rablen, P. R.; Marquez, M. *J. Am. Chem. Soc.* **1992**, *114*, 8654–8668.

(154) Punwong, C.; Owens, J.; Martínez, T. J. *J. Phys. Chem. B* **2015**, *119*, 704–714.

(155) Nogly, P. et al. *Science* **2018**, *361*, eeat0094.

(156) Toniolo, A.; Olsen, S.; Manohar, L.; Martínez, T. J. *Faraday Discuss.* **2004**, *127*, 149–163.

(157) Fang, C.; Frontiera, R. R.; Tran, R.; Mathies, R. A. *Nature* **2009**, *462*, 200–204.

(158) Acharya, A.; Bogdanov, A. M.; Grigorenko, B. L.; Bravaya, K. B.; Nemukhin, A. V.; Lukyanov, K. A.; Krylov, A. I. *Chem. Rev.* **2017**, *117*, 758–795.

(159) Vassiliev, S.; Comte, P.; Mahboob, A.; Bruce, D. *Biochemistry* **2010**, *49*, 1873–1881.

(160) Ogata, K.; Yuki, T.; Hatakeyama, M.; Uchida, W.; Nakamura, S. *J. Am. Chem. Soc.* **2013**, *135*, 15670–15673.

(161) Kupitz, C. et al. *Nature* **2014**, *513*, 261–265.

(162) Deb, S.; Weber, P. M. *Annu. Rev. Phys. Chem.* **2011**, *62*, 19–39.

(163) MacDonell, R. J.; Schuurman., M. S. *Chem. Phys.* **2018**, *515*, 360–368.

(164) Boguslavskiy, A. E.; Schalk, O.; Gador, N.; Glover, W. J.; Mori, T.; Schultz, T.; Schuurman, M. S.; Martínez, T. J.; Stolow, A. *J. Chem. Phys.* **2018**, *148*, 164302.

(165) Ichikawa, H.; Takatsuka, K. *J. Phys. Chem. A* **2017**, *121*, 315–325.

(166) Olivucci, M.; Ragazos, I. N.; Bernardi, F.; Robb, M. A. *J. Am. Chem. Soc.* **1993**, *115*, 3710–3721.

(167) Fuß, W.; Lochbrunner, S.; A. M. Müller, T. S.; Schmid, W. E.; Trushin, S. A. *Chem. Phys.* **1998**, *232*, 161–174.

(168) Liu, R. S. H. *Acc. Chem. Res.* **2001**, *34*, 555–562.

(169) Müller, A. M.; Lochbrunner, S.; Schmid, W. E.; Fuß, W. *Angew. Chem. Int. Ed.* **1998**, *37*, 505–507.

(170) Ostojić, B.; Domcke, W. *Chem. Phys.* **2001**, *269*, 1–10.

(171) Krawczyk, R. P.; Malsch, K.; Hohlneicher, G.; Gillen, R. C.; Domcke, W. *Chem. Phys. Lett.* **2000**, *320*, 535–541.

(172) Satzger, H.; Townsend, D.; Zgierski, M. Z.; Patchkovskii, S.; Ullrich, S.; Stolow, A. *Proc. Natl. Acad. Sci.* **2006**, *103*, 10196–10201.

(173) Garavelli, M.; Frabboni, B.; Fato, M.; Celani, P.; Bernardi, F.; Robb, M. A.; Olivucci, M. *J. Am. Chem. Soc.* **1999**, *121*, 1537–1545.

(174) Olivucci, M.; Bernardi, F.; Ottani, S.; Robb, M. A. *J. Am. Chem. Soc.* **1994**, *116*, 2034–2048.

(175) Ahlrichs, R.; Bär, M.; Häser, M.; Horn, H.; Kölmel, C. *Chem. Phys. Lett.* **1989**, *162*, 165–169.

(176) Weigend, F.; Häser, M. *Theor. Chem. Acc.* **1997**, *97*, 331–340.

(177) Efron, B. *Ann. Stat.* **1979**, *7*, 1–26.

(178) Hunt, P. A.; Robb, M. A. *J. Am. Chem. Soc.* **2005**, *127*, 5720–5726.

(179) Sifain, A. E.; Gifford, B. J.; Gao, D. W.; Lystrom, L.; Nelson, T. R.; Tretiak, S. *J. Phys. Chem. A* **2018**, *122*, 9403–9411.

(180) Cusati, T.; Granucci, G.; Persico, M. *J. Am. Chem. Soc.* **2011**, *133*, 5109–5123.

(181) Goyal, P.; Hammes-Schiffer, S. *ACS Energy Lett.* **2017**, *2*, 512–519.

(182) Boggio-Pasqua, M.; Robb, M. A.; Groenhof, G. *J. Am. Chem. Soc.* **2009**, *131*, 13580–13581.

(183) Gröbner, G.; Burnett, I. J.; Glaubitz, C.; Choi, G.; Mason, A. J.; Watts, A. *Nature* **2000**, *405*, 810–813.

(184) Watson, M. A.; Chan, G. K.-L. *J. Chem. Theory Comput.* **2012**, *8*, 4013–4018.

(185) Leopold, D. G.; Pendley, R. D.; Roebber, J. L.; Hemley, R. J.; Vaida, V. *J. Chem. Phys.* **1984**, *81*, 4218–4229.

(186) Orlandi, G.; Zerbetto, F.; Zgierski, M. Z. *Chem. Rev.* **1991**, *91*, 867–891.

(187) SerranoâĂŘAndrís, L.; Merchán, M.; NebotâĂŘGil, I.; Lindh, R.; Roos, B. O. *J. Chem. Phys.* **1993**, *98*, 3151–3162.

(188) Watts, J. D.; Gwaltney, S. R.; Bartlett, R. J. *J. Chem. Phys.* **1996**, *105*, 6979–6988.

(189) Dallos, M.; Lischka, H. *Theor. Chem. Acc.* **2004**, *112*, 16–26.

(190) Chien, A. D.; Holmes, A. A.; Otten, M.; Umrigar, C. J.; Sharma, S.; Zimmerman, P. M. *J. Phys. Chem. A* **2018**, *122*, 2714–2722.

(191) Rabidoux, S. M.; Cave, R. J.; Stanton, J. F. *J. Phys. Chem. A* **2019**, *123*, 3255–3271.

(192) Rothberg, L. J.; Gerrity, D. P.; Vaida, V. *J. Chem. Phys.* **1980**, *73*, 5508–5513.

(193) Phillips, D. L.; Zgierski, M. Z.; Myers, A. B. *J. Phys. Chem.* **1993**, *97*, 1800–1809.

(194) Assenmacher, F.; Gutmann, M.; Hohlneicher, G.; Stert, V.; Radloff, W. *Phys. Chem. Chem. Phys.* **2001**, *3*, 2981–2982.

(195) Fuß, W.; Schmid, W. E.; Trushin, S. A. *Chem. Phys. Lett.* **2001**, *342*, 91–98.

(196) Hockett, P.; Ripani, E.; Rytwinski, A.; Stolow, A. *J. Mod. Opt.* **2013**, *60*, 1409–1425.

(197) Kang, H.; Jung, B.; Kim, S. K. *J. Chem. Phys.* **2003**, *118*, 6717–6719.

(198) MacDonell, R. J.; Schuurman., M. S. *J. Phys. Chem. A* **2019**, *123*, 4693–4701.

(199) Corrales, M. E.; Loriot, V.; Balerdi, G.; González-Vázquez, J.; de Nalda, R.; Bañares, L.; Zewail, A. H. *Phys. Chem. Chem. Phys.* **2014**, *16*, 8812–8818.

(200) Murillo-Sánchez, M. L.; Poullain, S. M.; Bajo, J. J.; Corrales, M. E.; González-Vázquez, J.; Solá, I. R.; Bañares, L. *Phys. Chem. Chem. Phys.* **2018**, *20*, 20766–20778.

(201) Gross, K. C.; Seybold, P. G.; Hadad, C. M. *Int. J. Quantum Chem.* **2002**, *90*, 445–458.

(202) Jacquemin, D.; Bahers, T. L.; Adamo, C.; Ciofini, I. *Phys. Chem. Chem. Phys.* **2012**, *14*, 5383–5388.

(203) Knizia, G. *J. Chem. Theory Comput.* **2013**, *9*, 4834–4843.

(204) Knizia, G.; Klein, J. E. M. N. *Angew. Chim. Int. Ed.* **2015**, *54*, 5518–5522.

(205) West, A. C.; Schmidt, M. W.; Gordon, M. S.; Ruedenberg, K. *J. Phys. Chem. A* **2015**, *119*, 10360–10367.

(206) West, A. C.; Duchimaza-Heredia, J. J.; Gordon, M. S.; Ruedenberg, K. *J. Phys. Chem. A* **2017**, *121*, 8884–8898.

(207) Vanfleteren, D.; Neck, D. V.; Bultinck, P.; Ayers, P. W.; Waroquier, M. *J. Chem. Phys.* **2010**, *133*, 231103.

(208) Vanfleteren, D.; Neck, D. V.; Bultinck, P.; Ayers, P. W.; Waroquier, M. *J. Chem. Phys.* **2012**, *136*, 014107.

(209) Becke, A. D. *J. Chem. Phys.* **1988**, *88*, 2547–2553.

(210) Guerra, C. F.; Handgraaf, J.-W.; Baerends, E. J.; Bickelhaupt, F. M. *J. Comput. Chem.* **2004**, *25*, 189–210.

(211) Ferro-Costas, D.; Pendás, Á. M.; González, L.; Mosquera, R. A. *Phys. Chem. Chem. Phys.* **2014**, *16*, 9249–9258.

(212) Jara-Cortés, J.; Guevara-Vela, J. M.; Pendás, Á. M.; Hernández-Trujillo, J. *J. Comput. Chem.* **2017**, *38*, 957–970.

(213) Vannay, L.; Brémond, E.; de Silva, P.; Corminboeuf, C. *Chem. Eur. J.* **2016**, *22*, 18422–18449.

(214) Rodríguez-Mayorga, M.; Ramos-Cordoba, E.; Salvador, P.; Solà, M.; Matito, E. *Mol. Phys.* **2015**, *114*, 1345–1355.

(215) Chiu, C.-C.; Hung, C.-C.; Chen, C.-L.; Cheng, P.-Y. *J. Phys. Chem. B* **2013**, *117*, 9734–9756.

(216) Aquino, A. A. J.; Borges Jr., I.; Nieman, R.; Köhn, A.; Lischka, H. *Phys. Chem. Chem. Phys.* **2014**, *16*, 20586–20597.

(217) Varandras, A. J. C. *J. Chem. Phys.* **2009**, *131*, 124128.

(218) Jasik, P.; Sienkiewicz, J. E.; Domsta, J.; Henriksen, N. E. *Phys. Chem. Chem. Phys.* **2017**, *19*, 19777–19783.

(219) Li, X.-Y.; Hu, C.-X. *J. Comput. Chem.* **2002**, *23*, 874–886.

(220) MacDonell, R. J.; Corrales, M. E.; Boguslavskiy, A. E.; Bañares, L.; Stolow, A.; Schuurman, M. S. Under review.

(221) Wolf, T. J. A. et al. *Nature Chem.* **2019**, *11*, 504–509.

(222) Lebedev, V. I. *Comput. Math. Math. Phys.* **1975**, *15*, 44–51.

(223) Lebedev, V. I. *Comput. Math. Math. Phys.* **1976**, *16*, 10–24.

(224) Lebedev, V. I.; Laikov, D. N. *Doklady Math.* **1999**, *59*, 477–481.

(225) Knowles, P. J.; Andrews, J. S.; Amos, R. D.; Handy, N. C.; Pople, J. A. *Chem. Phys. Lett.*

1991, *186*, 130–136.

(226) Schmidt, M. W.; Baldridge, K. K.; Boatz, J. A.; Elbert, S. T.; Gordon, M. S.; Jensen, J. H.; Koseki, S.; Matsunaga, N.; Nguyen, K. A.; Su, S.; Windus, T. L.; Dupuis, M.; Montgomery Jr., J. A. *J. Comput. Chem.* **1993**, *14*, 1347–1363.

(227) Lehtola, S.; Jónsson, H. *J. Chem. Theory Comput.* **2014**, *1*-, 642–649.

(228) Rodríguez, J. I.; Köster, A. M.; Ayers, P. W.; Santos-Valle, A.; Vela, A.; Merino, G. *J. Comput. Chem.* **2009**, *30*, 1082–1092.

(229) Shao, Y. et al. *Mol. Phys.* **2015**, *113*, 184–215.

(230) Levine, B. G.; Peng, W.-T.; Esch, M. P. *Phys. Chem. Chem. Phys.* **2019**, *21*, 10870–10878.

(231) Levine, B. G.; Esch, M. P.; Fales, B. S.; Hardwick, D. T.; Peng, W.-T.; Shu, Y. *Adv. Rev. Phys. Chem.* **2019**, *70*, 21–43.

(232) Pemberton, C. C. Reaction Paths of Photoinduced Electrocyclic Ring-Opening: 1,3-Cyclohexadiene and α-Terpinene. Ph.D. thesis, Brown University, Providence, RI, 2015.

(233) Roger A. Sayle, E. J. M.-W. *Trends. Biochem. Sci.* **1995**, *20*, 374–376.

(234) Herráez, A. *Biochem. Mol. Biol. Educ.* **2006**, *34*, 255–261.

(235) West, D. H. D. *Comm. ACM* **1979**, *22*, 532–535.

(236) Andraos, J. *J. Chem. Educ.* **1999**, *76*, 1578–1583.

Appendix A

Supplementary material — Excited state dynamics of acrylonitrile: Substituent effects at conical intersections interrogated via time-resolved photoelectron spectroscopy and *ab initio* simulation (Chapter 2)

A1 Geometries

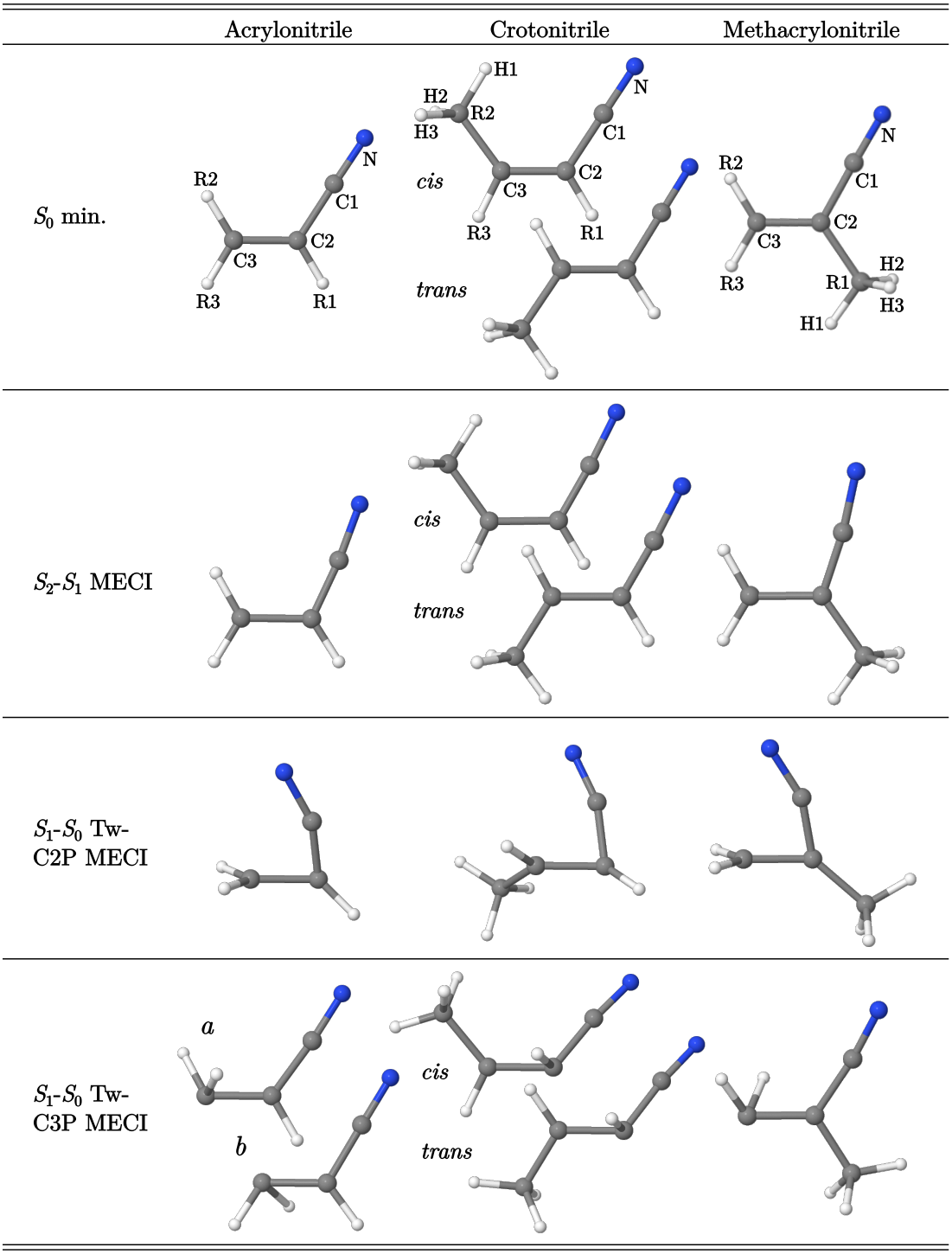

Figure A1: MR-FOCI/6-31G* optimized molecular geometries with atomic labels.

Table A1: Bond lengths for geometries optimized with MR-FOCI using a 6-31G* basis.

		Bond length / Å						
	Geometry	NC1	C1C2	C2C3	C2R1	C3R2	C3R3	RH
AN	S_0 min.	1.1718	1.4331	1.3530	1.0757	1.0758	1.0752	—
	S_2-S_1 MECI	1.2601	1.3576	1.4760	1.0712	1.0746	1.0743	—
	S_1-S_0 Tw-C2P	1.2176	1.3652	1.4593	1.0657	1.0811	1.0816	—
	S_1-S_0 Tw-C3P$_a$	1.1757	1.4464	1.4102	1.0813	1.0873	1.1941	—
	S_1-S_0 Tw-C3P$_b$	1.1746	1.4342	1.4070	1.0873	1.0865	1.1982	—
CrN	*cis*-S_0 min.	1.1754	1.4333	1.3532	1.0749	1.5033	1.0783	1.0848
	trans-S_0 min.	1.1752	1.4325	1.3521	1.0760	1.0789	1.5025	1.0852
	cis-S_2-S_1 MECI	1.2644	1.3489	1.4689	1.0746	1.4930	1.0762	1.0876
	trans-S_2-S_1 MECI	1.2693	1.3465	1.4581	1.0764	1.0766	1.4947	1.0875
	S_1-S_0 Tw-C2P	1.2113	1.3767	1.4597	1.0686	1.4956	1.0845	1.0817
	cis-S_1-S_0 Tw-C3P	1.1817	1.4058	1.4102	1.1601	1.5087	1.0835	1.0844
	trans-S_1-S_0 Tw-C3P	1.1806	1.4106	1.4122	1.1585	1.0881	1.4906	1.0848
MeAN	S_0 min.	1.1749	1.4399	1.3523	1.5117	1.0756	1.0758	1.0841
	S_2-S_1 MECI	1.2559	1.3666	1.4950	1.5058	1.0749	1.0760	1.0863
	S_1-S_0 Tw-C2P	1.2285	1.3511	1.4598	1.4935	1.0816	1.0821	1.0852
	S_1-S_0 Tw-C3P	1.1764	1.4544	1.4150	1.4997	1.1788	1.0926	1.0840

Table A2: Bond angles for geometries optimized with MR-FOCI using a 6-31G* basis.

		Bond angle / °							
	Geometry	NC1C2	C1C2C3	C1C2R1	C2C3R2	C2C3R3	CRH1	CRH2	CRH3
AN	S_0 min.	179.20	122.33	116.28	121.59	120.46	—	—	—
	S_2-S_1 MECI	175.09	114.69	122.31	119.97	121.07	—	—	—
	S_1-S_0 Tw-C2P	157.57	80.45	131.65	120.85	123.59	—	—	—
	S_1-S_0 Tw-C3P$_a$	173.16	126.48	113.35	119.51	71.76	—	—	—
	S_1-S_0 Tw-C3P$_b$	178.01	120.10	112.83	117.64	71.03	—	—	—
CrN	*cis*-S_0 min.	179.80	123.37	115.89	126.28	116.86	112.05	110.25	110.25
	trans-S_0 min.	179.85	122.26	116.25	118.56	124.12	111.58	110.55	110.55
	cis-S_2-S_1 MECI	176.85	120.53	119.33	124.82	116.60	112.16	110.99	110.99
	trans-S_2-S_1 MECI	177.18	120.20	118.85	118.35	122.37	111.47	111.30	111.30
	S_1-S_0 Tw-C2P	160.79	82.95	126.77	123.04	121.40	112.45	111.01	106.46
	cis-S_1-S_0 Tw-C3P	174.09	127.51	101.44	127.62	116.85	111.39	111.44	108.64
	trans-S_1-S_0 Tw-C3P	173.71	125.35	101.72	122.04	121.50	106.82	109.79	113.24
MeAN	S_0 min.	178.77	119.22	116.49	121.49	49.01	110.35	110.77	110.77
	S_2-S_1 MECI	173.89	109.20	126.39	119.08	49.11	109.73	112.46	112.45
	S_1-S_0 Tw-C2P	157.85	79.29	139.75	121.72	29.98	109.36	111.29	112.34
	S_1-S_0 Tw-C3P	171.86	123.51	115.45	76.16	20.65	106.16	113.88	108.87

Table A3: Dihedral, out-of-plane and pyramidal angles for geometries optimized with MR-FOCI using a 6-31G* basis.

		Dihedral angle / °					Out-of-plane angle / °	
	Geometry	NCCC	CCCR	CCRH1	CCRH2	CCRH3	R1	C3R2R3 pyr.
AN	S_0 min.	180.00	0.00	—	—	—	0.00	0.00
	S_2-S_1 MECI	0.43	0.14	—	—	—	0.19	0.14
	S_1-S_0 Tw-C2P	15.97	100.41	—	—	—	26.55	3.04
	S_1-S_0 Tw-C3P$_a$	53.88	21.83	—	—	—	4.70	55.45
	S_1-S_0 Tw-C3P$_b$	91.12	162.58	—	—	—	5.87	56.76
CrN	*cis*-S_0 min.	180.00	0.00	0.00	120.77	120.77	0.00	0.00
	trans-S_0 min.	180.00	180.00	0.00	120.58	120.58	0.00	0.00
	cis-S_2-S_1 MECI	0.01	0.01	0.02	120.78	120.73	0.00	0.00
	trans-S_2-S_1 MECI	0.01	180.0	0.02	120.49	120.45	0.00	0.00
	S_1-S_0 Tw-C2P	19.80	106.23	144.52	20.06	97.51	33.64	1.13
	cis-S_1-S_0 Tw-C3P	156.85	34.70	178.44	57.10	60.69	76.45	6.59
	trans-S_1-S_0 Tw-C3P	154.34	148.60	69.75	45.15	168.94	77.41	6.98
MeAN	S_0 min.	180.00	0.00	0.00	120.19	120.19	0.00	0.00
	S_2-S_1 MECI	0.16	0.04	0.14	119.24	118.95	0.00	0.04
	S_1-S_0 Tw-C2P	6.10	93.89	178.20	62.88	58.37	9.33	1.30
	S_1-S_0 Tw-C3P	42.38	58.40	165.87	72.97	41.68	2.79	60.90

A2 Potential energy surface characterization

Table A4: S_0, S_1 and S_2 energies at critical points on the potential energy surface at the MR-FOCI/6-31G* and CASPT2/cc-pVTZ levels of theory for geometries optimized at the MR-FOCI/6-31G* level of theory.

		E(MR-FOCI/6-31G*) / eV			E(CASPT2/cc-pVTZ) / eV		
	Geometry	S_0	S_1	S_2	S_0	S_1	S_2
AN	S_0 min.	0.00	7.30	7.36	0.00	6.62	6.92
	S_2-S_1 MECI	0.86	6.64	6.64	0.91	6.11	6.31
	S_1-S_0 Tw-C2P	4.91	4.91	8.67	4.28	4.45	7.83
	S_1-S_0 Tw-C3P$_a$	6.00	6.00	10.71	3.92	5.15	10.02
	S_1-S_0 Tw-C3P$_b$	6.68	6.68	11.42	4.70	5.18	9.80
CrN	*cis*-S_0 min.	0.00	7.28	7.32	0.00	6.39	7.01
	trans-S_0 min.	0.00	7.26	7.33	0.02	6.42	7.04
	cis-S_2-S_1 MECI	0.79	6.61	6.61	0.86	5.95	6.35
	trans-S_2-S_1 MECI	0.80	6.59	6.59	0.89	5.98	6.34
	S_1-S_0 Tw-C2P	4.63	4.63	8.67	4.07	4.27	8.01
	cis-S_1-S_0 Tw-C3P	5.97	5.97	9.44	4.16	4.74	8.44
	trans-S_1-S_0 Tw-C3P	5.13	5.13	9.26	2.72	4.66	8.18
MeAN	S_0 min.	0.00	7.38	7.46	0.00	7.11	7.12
	S_2-S_1 MECI	0.95	6.79	6.79	1.05	6.26	6.56
	S_1-S_0 Tw-C2P	4.85	4.85	8.38	4.41	4.46	7.72
	S_1-S_0 Tw-C3P	5.63	5.63	10.33	4.49	4.98	8.44

A3 Initial condition selection

To account for the near degeneracy of S_1 and S_2 in the Franck-Condon region, the probability of populating excited state I was found by

$$p_I(\mathbf{R}) \propto \frac{\Delta E_{0I}(\mathbf{R})\mu_{0I}(\mathbf{R})^2}{\left(\frac{\omega_1 - \Delta E_{0I}(\mathbf{R})}{\Delta\omega_1}\right)^2 + 1}, \tag{A1}$$

where ΔE_{0I} is the potential energy difference between the ground state and state I, μ_{0I} is the transition dipole moment from the ground state, and ω_1 and $\Delta\omega_1$ are the energy and bandwidth of the experimental pump pulse and p_I is normalized such that $p_1(\mathbf{R}) + p_2(\mathbf{R}) = 1$. Trajectories were calculated starting from unselected states with a probability of greater than 5% using the same initial positions and momenta as the corresponding selected state, and the populations were weighted by $p_I(\mathbf{R})$.

A4 Topography analysis

To quantitatively investigate the role of seam topography on the efficacy of population transfer at the spawn points, the seam coordinate $\mathbf{s}$, gradient difference vector $\mathbf{g}$ and nonadiabatic coupling vector $\mathbf{h}$ between states i and j are defined by:

$$\mathbf{s}_{ij} = \nabla_{\mathbf{R}}(E_i(\mathbf{R}) + E_j(\mathbf{R}))/2, \tag{A2}$$

$$\mathbf{g}_{ij} = \nabla_{\mathbf{R}}(E_i(\mathbf{R}) - E_j(\mathbf{R}))/2, \tag{A3}$$

$$\mathbf{h}_{ij} = \langle\psi_i|\nabla_{\mathbf{R}}|\psi_j\rangle\,(E_i - E_j), \tag{A4}$$

where $\nabla_{\mathbf{R}}$ is the nuclear gradient operator. From these, the slopes s_x and s_y, the pitch δ_{gh} and the asymmetry Δ_{gh} can be calculated as follows:

$$s_x = \mathbf{s}\cdot\mathbf{x} = \mathbf{s}\cdot\mathbf{g}/g, \tag{A5}$$

$$s_y = \mathbf{s}\cdot\mathbf{y} = \mathbf{s}\cdot\mathbf{h}/h, \tag{A6}$$

$$\delta_{gh}^2 = (g^2 + h^2)/2, \tag{A7}$$

$$\Delta_{gh} = (g^2 - h^2)/(g^2 + h^2), \tag{A8}$$

where g and h are the norms of the similarly named vectors, *i.e.* $g = |\mathbf{g}|$ and $h = |\mathbf{h}|$. s_x and s_y can be thought of as the slopes of a line through the centre of the double cone formed by the coupled surfaces in the branching space, while δ_{gh} is related to the angle of the double cone itself. Δ_{gh} is a measure of the ellipticity of the cone.[11]

The topographical values were binned and plotted for all nonadiabatic spawn events from the *ab initio* dynamics simulations in order to observe differences in the topography between molecules. One such difference is visible for the distribution of slopes, shown in Figure A2. AN show a tight distribution about the origin, suggesting a vertical double cone. While the peak in the CrN and MeAN distribitions also occur near $(s_x, s_y) = (0, 0)$, there is clearly a broader distribution in slopes. The lower frequency motion in CrN and MeAN relative to AN leads to a more shallow potenial in

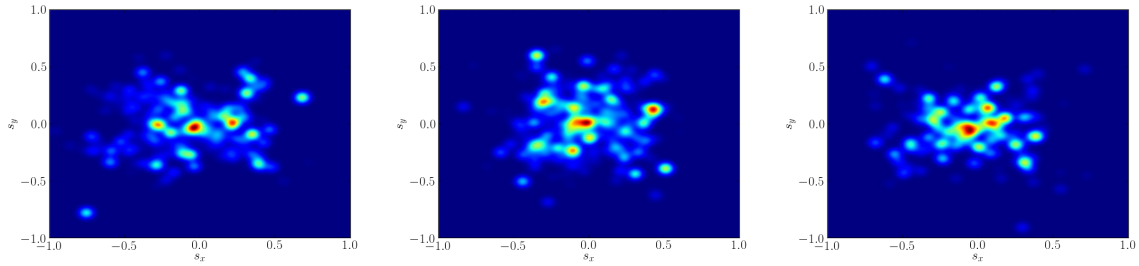

(a) (b) (c)

Figure A2: Conical intersection slope (s_x, s_y) distribution for all AIMS spawn events as a function of time for (a) acrylonitrile, (b) crotonitrile and (c) methacrylonitrile. Each point is weighted by population transferred and convoluted with a Gausssian function.

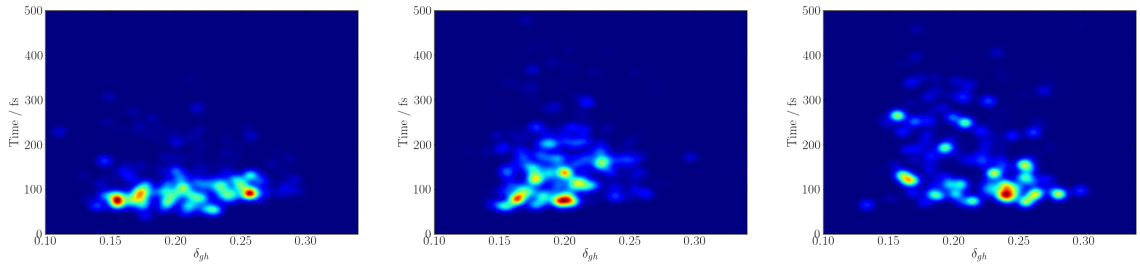

(a) (b) (c)

Figure A3: Conical intersection pitch δ_{gh} distribution for all AIMS spawn events as a function of time for (a) acrylonitrile, (b) crotonitrile and (c) methacrylonitrile. Each point is weighted by population transferred and convoluted with a Gausssian function.

the region of the Tw-C2P intersection seam, thus leading to a greater exploration of the seam.

The distribution of pitch and asymmetry of the CI can be found in Figures A3 and A4. δ_{gh} and Δ_{gh} of AN both have relatively broad distributions relative to CrN and MeAN. The peaks of the pitch and asymmetry are highest for MeAN and lowest for CrN. This suggests that the MeAN wavepacket generally travels through more irregular CIs for the passage to the ground state, which may have some effect on the time taken for de-excitation. MeAN also shows a weak trend towards a small pitch with time as the wavepacket samples the conical intersection seam.

At a true conical intersection, the energy difference between states is zero by definition; however, in the AIMS method a spawning event between states is based on a threshold for coupling between states. The energy gap ΔE is therefore a measure of the degree of coupling. Figure A5 gives this energy difference as a function of time for all three molecules. AN and CrN both have energy gaps greater than 0.3 eV with a significant transfer of population, whereas the S_1 and S_0 energies differed by roughly 0.1 eV for CrN. As with δ_{gh}, the ΔE_{CI} distribution of MeAN tends to lower energies as longer times. This suggests that CrN spawns occur closer to the CI seam and MeAN geometries tend to spawn closer to the seam at later times. Overall, the topographic distributions suggest relatively efficient and inefficient passage through CIs for CrN and MeAN, respectively, in comparison to AN.

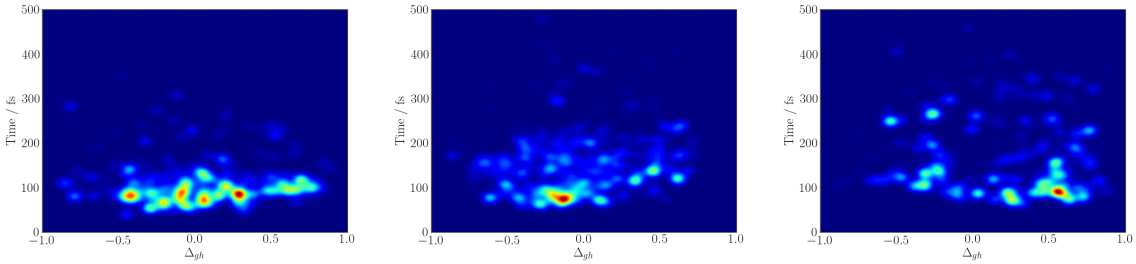

Figure A4: Conical intersection asymmetry Δ_{gh} for all AIMS spawn events as a function of time for (a) acrylonitrile, (b) crotonitrile and (c) methacrylonitrile. Each point is weighted by population transferred and convoluted with a Gausssian function.

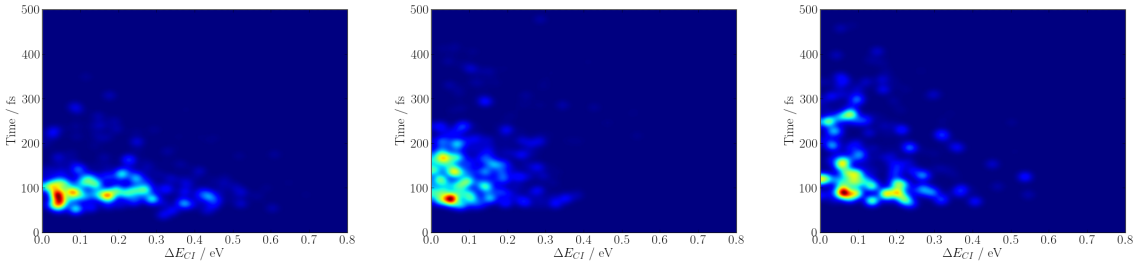

Figure A5: Conical intersection energy difference (ΔE_{CI}) for all AIMS spawn events as a function of time for (a) acrylonitrile, (b) crotonitrile and (c) methacrylonitrile. Each point is weighted by population transferred and colvoluted with a Gaussian function.

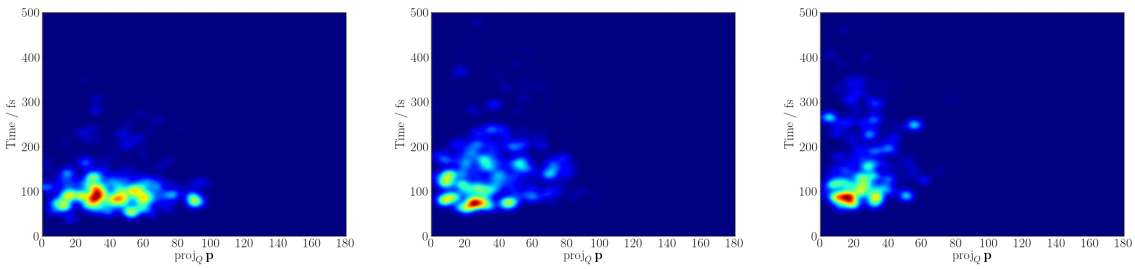

Figure A6: Projection of the momentum $\mathbf{p}$ onto the branching space of all AIMS spawn events as a function of time for (a) acrylonitrile, (b) crotonitrile and (c) methacrylonitrile. Each point is weighted by population transferred and convoluted with a Gaussian function.

A5 Momentum analysis

The branching space Q, defined by the space spanned by vectors $\mathbf{g}$ and $\mathbf{h}$, is the space along which the degenerate adiabatic state energies is lifted to first order. For a molecule to efficiently transfer population through a conical intersection, it will typically need to move within this branching space. In other words, the momentum of the molecule must for the most part be within Q for an efficient transition. This principle is similar to the selection of spawn in the AIMS algorithm, which employs a threshold for the value of $\mathbf{p} \cdot \mathbf{h}$.[88,89,119] Here, we define the projection of the momentum $\mathbf{p}$ onto the branching space by:

$$\mathrm{proj}_Q\, \mathbf{p} = \mathrm{proj}_{\mathbf{x}}\, \mathbf{p} + \mathrm{proj}_{\mathbf{y}'}\, \mathbf{p} = (\mathbf{p} \cdot \mathbf{x})\mathbf{x} + (\mathbf{p} \cdot \mathbf{y}')\mathbf{y}', \tag{A9}$$

$$\mathbf{y}' = (\mathbf{y} - \mathrm{proj}_{\mathbf{x}}\, \mathbf{y})/|\mathbf{y} - \mathrm{proj}_{\mathbf{x}}\, \mathbf{y}|, \tag{A10}$$

where the $\mathbf{x}$ and $\mathbf{y}$ are defined as unit vectors in the direction of $\mathbf{g}$ and $\mathbf{h}$, respectively. The calculated values for $\mathrm{proj}_Q\, \mathbf{p}$ *vs.* time from *ab initio* results are given in Figure A6. Comparison of these figures shows a thin distribution for the methyl substituted molecules relative to AN. This is to be expected seeing both molecules rely on lower frequency motions than the non-substituted AN. Having less momentum in the branching space at the point of a conical intersection is cause for less population being tranferred to the coupled state. The overall CrN distribution in $\mathrm{proj}_Q\, \mathbf{p}$ is wider than that of MeAN. An inverse relation between distribution width in $\mathrm{proj}_Q\, \mathbf{p}$ and and time can be seen from these figures, which is to be expected due to the coupling between states and subsequent population transfer with greater motion in the branching space.

A6 Assignment of photoelecton spectra

The decay associated spectrum of the first exponential time constant of AN is shown in Figure A7. It exhibits several discrete peaks on a continuous background. We tentatively fitted the peak and the background to a set of Gaussian functions. While the broad band stems from direct ionization with two photons, the discrete peaks can be assigned to ionization through Rydberg states, *i.e.* the first probe pulse populates a Rydberg state and the second pulse ionizes the molecules from there.

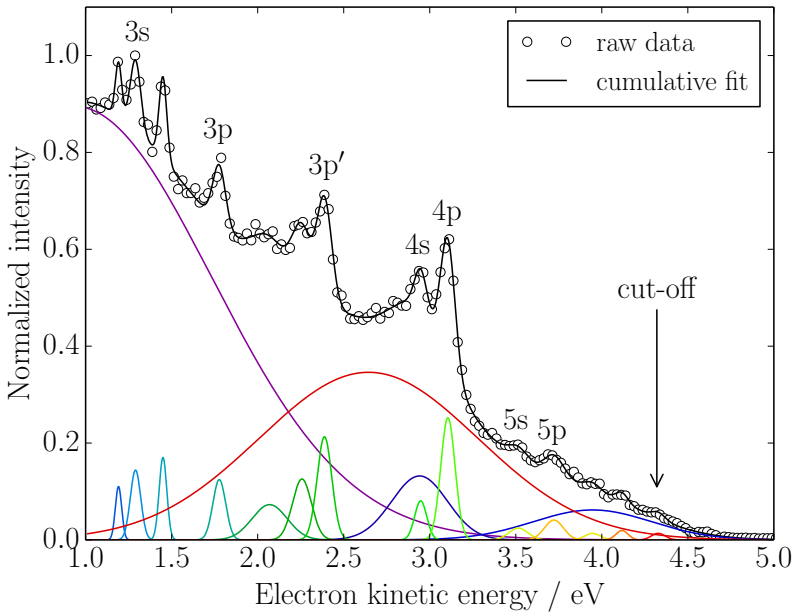

Figure A7: Decay associated spectrum of the monoexponential decay of acrylonitrile. Gaussian fits of the spectrum are also included.

Since the Rydberg state and the ionic state have (almost) the same shape of the potential energy surface, the peak position only depends on the probe wavelength, the principle quantum number of the Rydberg state n and the quantum defect δ. The peak positions are given by

$$E_B = \frac{Ry}{(n-\delta)^2} = \omega_2 - E_{kin}, \tag{A11}$$

where Ry is the Rydberg constant, ω_2 the energy of the probe photon and E_{kin} the kinetic energy of the photoelectron. In this case, we can assign most of the peaks to two Rydberg series. The s-Rydberg series exhibits a quantum defect of $\delta_s = 0.90$ while the p-Rydberg series shows a quantum defect of $\delta_p = 0.75$. An in depth descussion on intermediate states can be found in ref. 232. The weakness of the peaks shows that resonant two photon probe is a minor process and does not affect the analysis of the data significantly.

In addition, we saw a similar structure superimposed on the [1+2′] band of MeAN because of the intermediate Rydberg states, but no peaks were assignable to ionization to higher lying states. The peaks are relatively weak when compared with the two photon spectra of some other molecules, most prominently 1,3-cyclohexadiene.[232] We did not observe any additional structure on the photoelectron signal of CrN.

Appendix B

Supporting information — Substituent effects on the nonadiabatic dynamics of ethylene: π-donors and π-acceptors (Chapter 3)

B1 Electronic structure details

Table B1: Basis set used for MR-FOCI, active space, number of CASSCF states and MR-FOCI (CASPT2) state index for the $\pi\pi^*$ state for all substituted ethylenes.

Molecule	Basis set	N_{elec}	N_{orb}	N_{states}	Ind. $\pi\pi^*$
VNt	6-31G*	8	6	8[†]	5
VCN	6-31G*	6	6	5	2
VIm	6-31G*	6	5	6	2
VAl	6-31G*	6	5	6	4
ET	6-31G* + Ryd3s	2	3	5	2
VCl	6-31G*	6	6	7	2
VMe	6-31G*	4	4	5	1
VOH	6-31G*	4	4	5	2
VAm	6-31G* + Ryd3s	4	4	8	2

[†]5 states used for MECI optimization due to lack of convergence

Table B2: CASPT2/cc-pVTZ ground state and $\pi\pi^*$ state energies at the Franck-Condon point and at pyramidalization MECIs.

	E_{FC} / eV		E_{C1Pyr} / eV		E_{C2Pyr} / eV	
Molecule	gs	$\pi\pi^*$	gs	$\pi\pi^*$	gs	$\pi\pi^*$
VNt	−282.612747	−282.389890	−282.492450	−282.481586	−282.448683	−282.423469
VCN	−170.476301	−170.215502	−170.313972	−170.317587	−170.302246	−170.287407
VIm	−171.672029	−171.411220	−171.494100	−171.501471	−171.491880	−171.502794
VAl	−191.538862	−191.295901	−191.366141	−191.377613	−191.355853	−191.365111
ET	−78.397086	−78.109141	−78.219573	−78.225175	−78.219573	−78.225175
VCl	−537.517920	−537.236935	−537.360221	−537.351641	−537.348495	−537.360723
VMe	−117.623890	−117.321198	−117.444242	−117.434701	−117.467149	−117.440707
VOH	−153.523935	−153.264987	−153.343193	−153.337327	−153.369253	−153.393081
VAm	−133.666665	−133.428139	−133.505918	−133.500775	−133.557661	−133.550161

Table B3: XYZ file for VNt S_0 minimum MR-FOCI optmized geometry.

```
 8

C          0.724134         -0.628705         -0.000020
C          1.871255          0.064701          0.000018
N         -0.560344          0.024914          0.000002
O         -0.603679          1.233924         -0.000189
O         -1.524872         -0.711727          0.000219
H          0.638698         -1.696313         -0.000077
H          1.876505          1.138147          0.000081
H          2.807113         -0.462874         -0.000012
```

Table B4: XYZ file for VNt C1Pyr MECI MR-FOCI optmized geometry.

```
 8

C        -0.465678        -0.801328         0.018432
C        -1.561684         0.036871        -0.457765
N         0.651347        -0.042163         0.161175
O         0.468956         1.167914        -0.144531
O         1.744885        -0.425012         0.539438
H        -0.425269        -1.846370         0.249055
H        -1.742644         0.164096        -1.510681
H        -2.218420         0.533719         0.234611
```

Table B5: XYZ file for VNt C2Pyr MECI MR-FOCI optmized geometry.

```
 8

C        -0.807483        -0.070484         0.473469
C        -1.838824         0.030792        -0.446854
N         0.573861         0.072000         0.049817
O         0.972712         1.041269        -0.533997
O         1.185251        -0.931419         0.333705
H        -0.824504        -0.209906         1.548735
H        -2.706140        -0.603418        -0.277673
H        -2.186348         0.902971         0.237237
```

Table B6: XYZ file for VCN S_0 minimum MR-FOCI optmized geometry.

```
 7

N         1.811068        -0.214787         0.000000
C        -0.693737         0.510927         0.000000
C         0.682628         0.110948         0.000000
C        -1.707823        -0.381287         0.000000
H        -0.879238         1.569931         0.000000
H        -1.525753        -1.441619         0.000000
H        -2.729161        -0.045861         0.000000
```

Table B7: XYZ file for VCN C1Pyr MECI MR-FOCI optmized geometry.

```
 7

N         0.839691        -0.987668        -0.830812
C        -0.692138         0.725680         0.244029
C         0.294724        -0.014657        -0.338793
C        -1.491540        -0.397463        -0.232835
H        -0.844666         1.778325         0.311096
H        -1.787046        -1.192202         0.437892
H        -1.772661        -0.534213        -1.268346
```

Table B8: XYZ file for VCN C2Pyr MECI MR-FOCI optmized geometry.

```
 7

N         1.528628        -3.037785        -2.054120
C        -0.748496        -3.157674        -0.788411
C         0.513430        -3.082753        -1.467357
C        -1.627840        -2.059672        -0.822326
H        -0.951497        -4.145891        -0.382845
H        -2.419966        -2.027722        -0.079428
H        -2.117720        -2.967583        -1.431211
```

Table B9: XYZ file for VIm S_0 minimum MR-FOCI optmized geometry.

```
 9

C         1.813754        -0.143227         0.000000
C         0.583272         0.421307         0.000000
C        -0.654791        -0.353864         0.000000
N        -1.803521         0.230935         0.000000
H         1.941469        -1.214055         0.000000
H         2.707442         0.455759         0.000000
H         0.470283         1.493736         0.000000
H        -0.548318        -1.435858         0.000000
H        -2.542383        -0.454923         0.000000
```

Table B10: XYZ file for VIm C1Pyr MECI MR-FOCI optmized geometry.

9			
C	1.733132	-0.279638	-0.273129
C	0.582598	0.196546	0.363888
C	-0.773483	-0.293880	0.394574
N	-1.788621	0.288422	-0.157154
H	2.718859	-0.027691	0.096101
H	1.732490	-0.760345	-1.248308
H	0.655033	0.824300	-0.620235
H	-0.879765	-1.174132	1.025009
H	-2.633344	-0.194820	0.100627

Table B11: XYZ file for VIm C2Pyr MECI MR-FOCI optmized geometry.

9			
C	1.833558	-0.369540	-0.102039
C	0.593671	0.311992	-0.133860
C	-0.668173	-0.419326	-0.019533
N	-1.760036	0.247371	0.152136
H	1.790318	0.286803	0.883182
H	2.692231	0.166885	-0.505325
H	0.449749	1.391761	-0.110871
H	-0.602382	-1.497375	-0.082529
H	-2.554019	-0.374327	0.189302

Table B12: XYZ file for VAl S_0 minimum MR-FOCI optmized geometry.

8			
C	1.770428	-0.143599	0.000017
C	0.550871	0.442213	-0.000033
C	-0.683442	-0.351895	0.000007
O	-1.799023	0.137223	0.000007
H	2.677098	0.435112	0.000056
H	1.873659	-1.216906	-0.000042
H	0.440037	1.514354	0.000011
H	-0.558115	-1.439127	-0.000038

Table B13: XYZ file for VAl C1Pyr MECI MR-FOCI optmized geometry.

8			
C	1.728581	-0.284637	-0.264957
C	0.562533	0.214253	0.298195
C	-0.794421	-0.275966	0.381136
O	-1.850132	0.238189	0.049014
H	2.700540	-0.053099	0.153093
H	1.769107	-0.808263	-1.215518
H	0.713551	0.877619	-0.641175
H	-0.804761	-1.208012	0.956434

Table B14: XYZ file for VAl C2Pyr MECI MR-FOCI optmized geometry.

8			
C	-1.526250	0.799404	0.469858
C	-0.654058	-0.305319	0.496513
C	0.655467	-0.241808	-0.200130
O	1.373504	-1.223088	-0.297743
H	-2.333483	0.862984	1.193047
H	-2.009931	-0.092653	-0.159090
H	-0.868490	-1.290836	0.907059
H	0.929916	0.729027	-0.607313

Table B15: XYZ file for ET S_0 minimum MR-FOCI optmized geometry.

6			
C	0.672161	0.000000	0.000000
C	-0.672161	0.000000	0.000000
H	1.235916	0.918621	0.000000
H	1.235916	-0.918621	0.000000
H	-1.235916	0.918621	0.000000
H	-1.235916	-0.918621	0.000000

Table B16: XYZ file for ET C1Pyr MECI MR-FOCI optmized geometry.

```
 6

C          0.736862          0.241832         -0.272543
C         -0.625052         -0.035421          0.000607
H          1.304924         -0.527040         -0.796648
H          0.780066         -0.329064          0.756183
H         -1.035800         -1.023398          0.197967
H         -1.319654          0.769402          0.189901
```

Table B17: XYZ file for VCl S_0 minimum MR-FOCI optmized geometry.

```
 6

C         -0.566984          0.505298          0.000000
C         -1.651203         -0.287991          0.000000
Cl         1.065711         -0.061915          0.000002
H         -0.635614          1.587832          0.000000
H         -1.577337         -1.360252          0.000000
H         -2.629193          0.158542          0.000001
```

Table B18: XYZ file for VCl C1Pyr MECI MR-FOCI optmized geometry.

```
 6

C         -0.755913         -0.932221          0.097798
C         -1.462823          0.312246         -0.003834
Cl         0.822925          0.422486          0.099564
H         -0.556700         -1.492642         -0.806414
H         -1.536315          0.915671         -0.901997
H         -1.944279          0.719751          0.871529
```

Table B19: XYZ file for VCl C2Pyr MECI MR-FOCI optmized geometry.

```
 6

C          0.585828         -0.435232         -0.001854
C          1.587107          0.504379         -0.000823
Cl        -1.143005         -0.007636          0.016601
H          0.564146         -1.529193         -0.013064
H          2.199850          0.009600          0.799493
H          2.185924          0.025927         -0.821310
```

Table B20: XYZ file for VMe S_0 minimum MR-FOCI optmized geometry.

```
 9

C          1.292165        -0.229560         0.000001
C          0.130608         0.468362         0.000001
C         -1.242840        -0.160212        -0.000001
H          1.298120        -1.308960        -0.000001
H          2.246471         0.256642         0.000002
H          0.183853         1.588362         0.000003
H         -1.390134        -0.783471         0.874679
H         -1.390134        -0.783466        -0.874685
H         -2.024950         0.582629         0.000001
```

Table B21: XYZ file for VMe C1Pyr MECI MR-FOCI optmized geometry.

```
 9

C          1.143501        -0.209081        -0.128170
C          0.322212         0.816673         0.376984
C         -1.078603        -0.302007         0.009118
H          1.775799        -0.783292         0.537750
H          1.098190        -0.617954        -1.137732
H         -0.005634         1.581758        -0.318225
H         -1.808719         0.354607         0.458312
H         -1.009383        -1.227964         0.557342
H         -1.245322        -0.467648        -1.047166
```

Table B22: XYZ file for VMe C2Pyr MECI MR-FOCI optmized geometry.

```
 9

C          1.252892        -0.431941         0.337740
C          0.124003         0.324923        -0.087671
C         -1.257872        -0.151225         0.028527
H          1.747299         0.470105         0.838214
H          1.850169        -0.189540        -0.607317
H          0.177646         1.341470        -0.547151
H         -1.306091        -1.130065         0.480819
H         -1.716431        -0.163847        -0.959306
H         -1.842354         0.566564         0.601881
```

Table B23: XYZ file for VOH S_0 minimum MR-FOCI optmized geometry.

7			
C	1.232566	-0.184337	0.000000
C	0.029467	0.423342	0.000000
O	-1.134292	-0.291877	0.000000
H	1.320570	-1.255437	0.000000
H	2.127030	0.409821	0.000000
H	-0.091150	1.489017	0.000000
H	-1.895387	0.295476	0.000000

Table B24: XYZ file for VOH C1Pyr MECI MR-FOCI optmized geometry.

7			
C	0.961725	-0.169322	-0.114133
C	0.055743	0.950885	0.134091
O	-0.920356	-0.275006	0.360691
H	1.511181	-0.604442	0.702869
H	1.042662	-0.692036	-1.061248
H	-0.269364	1.503669	-0.734119
H	-1.300581	-0.527572	-0.477984

Table B25: XYZ file for VOH C2Pyr MECI MR-FOCI optmized geometry.

7			
C	1.237421	-0.269607	0.001019
C	0.022366	0.401938	-0.002727
O	-1.116553	-0.218682	0.001748
H	1.800905	0.087208	0.868531
H	1.800186	0.075979	-0.871011
H	-0.275113	1.599135	-0.010215
H	-1.842501	0.399340	-0.001790

Table B26: XYZ file for VAm S_0 minimum MR-FOCI optmized geometry.

```
 8

C         1.208501        -0.453045        -0.206953
C         1.284058         0.820052         0.244338
N         1.090504         1.980282        -0.499022
H         1.047561        -0.682028        -1.248480
H         1.275980        -1.274316         0.482725
H         1.438459         1.007567         1.295202
H         1.141277         1.868490        -1.491050
H         1.591139         2.783241        -0.179355
```

Table B27: XYZ file for VAm C1Pyr MECI MR-FOCI optmized geometry.

```
 8

C         1.205152        -0.554587        -0.122840
C         1.202579         0.826318         0.339745
N         0.994462         1.261938        -1.059949
H         0.290690        -1.119854        -0.201582
H         2.061475        -0.994481        -0.637065
H         2.108663         1.235225         0.746898
H         0.068709         1.155915        -1.424248
H         1.707858         1.092107        -1.766514
```

Table B28: XYZ file for VAm C2Pyr MECI MR-FOCI optmized geometry.

```
 8

C         1.190522        -0.478768        -0.180051
C         1.291317         0.881495         0.318701
N         1.180027         1.952465        -0.512804
H         0.270582        -1.027836        -0.060626
H         2.084401        -1.059054        -0.342113
H         1.456605         1.142113         1.357124
H         1.026921         1.804675        -1.489849
H         1.249992         2.891959        -0.171838
```

B2 Comparison of ground and excited state partial charges

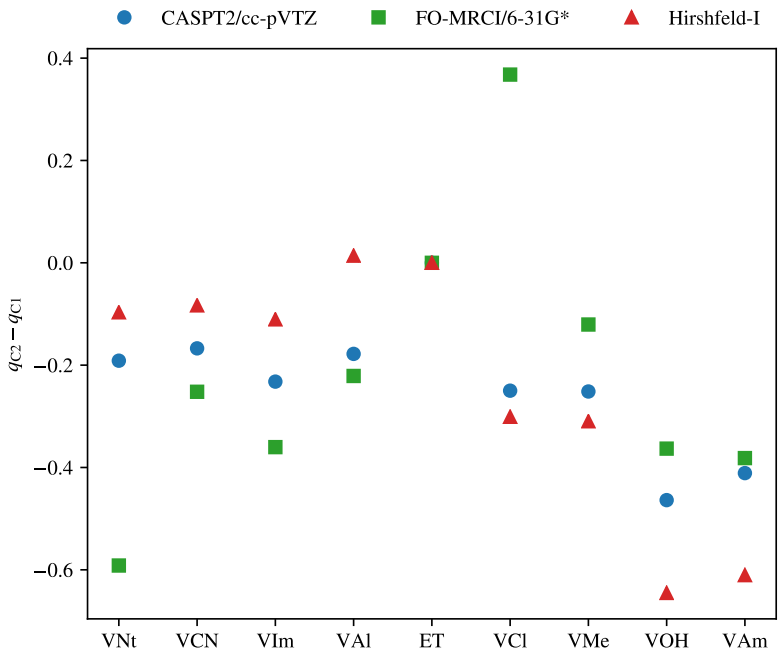

Figure B1: Ground state CASPT2/cc-pVTZ and MR-FOCI/6-31G* Mulliken charge difference and MR-FOCI/6-31G* iterative Hirshfeld charge difference for all molecules.

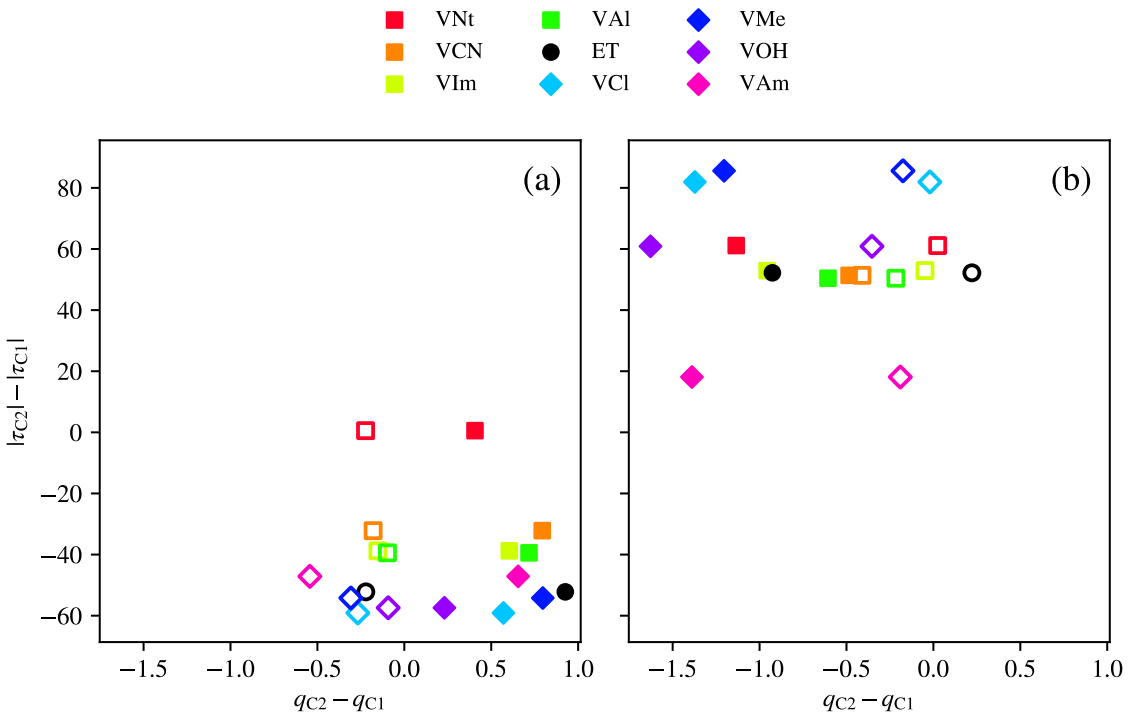

Figure B2: Iterative Hirshfeld charges *vs.* pyramidalization angle at (a) C1Pyr and (b) C2Pyr geometries. Squares represent π-acceptors, and diamonds represent π-donors. Filled shapes are charges from the state with a dominant closed-shell configuration, and open shapes are open shell. Intermediate values such as VAm C1Pyr and VCN C2Pyr have nearly equal contributions from the two main configurations.

B3 Critical points on the potential energy surfaces of VCN and VAm

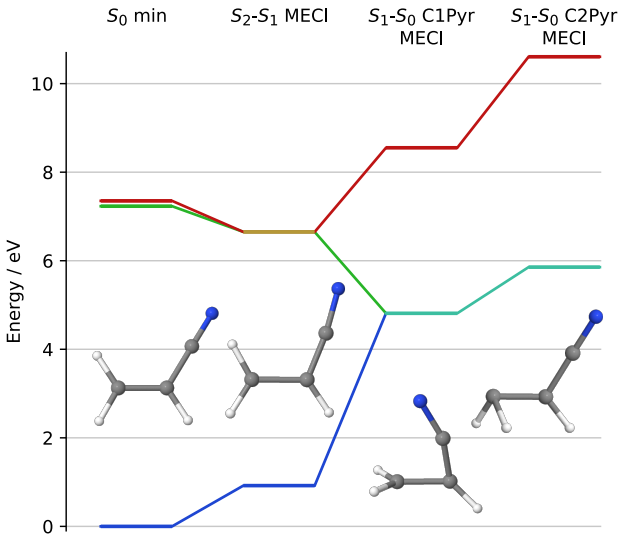

Figure B3: MR-FOCI/6-31G* minima and minimum energy conical intersections for VCN.

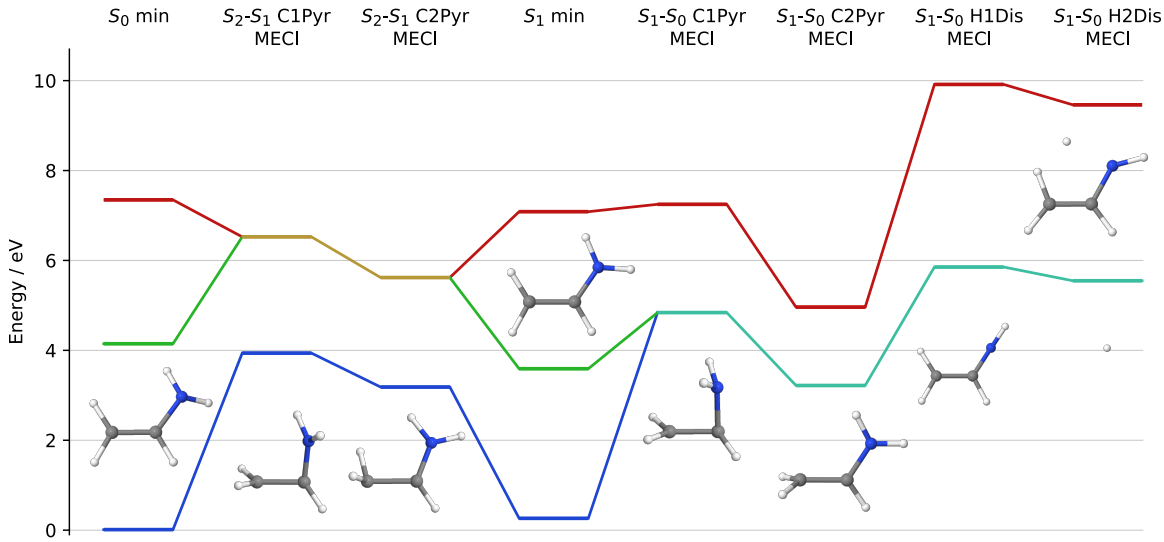

Figure B4: MR-FOCI/6-31G* minima and minimum energy conical intersections for VAm.

Table B29: XYZ file for VCN S_2-S_1 MECI MR-FOCI optmized geometry.

```
 7

N         1.694962        -0.513850        -0.146036
C        -0.649959         0.634697         0.026347
C         0.604329         0.107718        -0.060571
C        -1.706339        -0.414488        -0.002033
H        -0.852007         1.681352         0.101487
H        -1.416541        -1.446558        -0.082445
H        -2.751985        -0.173384         0.057251
```

Table B30: XYZ file for VAm S_2-S_1 C1Pyr MECI MR-FOCI optmized geometry.

```
 8

C         1.178579        -0.611769        -0.031980
C         1.272757         0.838753         0.221832
N         0.981195         1.251198        -1.060227
H         0.262574        -1.156268         0.010455
H         1.989836        -1.020656        -0.618420
H         2.088140         1.275403         0.742845
H         0.114390         1.009705        -1.509855
H         1.706754         1.684916        -1.659895
```

Table B31: XYZ file for VAm S_2-S_1 C2Pyr MECI MR-FOCI optmized geometry.

```
 8

C         1.148596        -0.517607        -0.185441
C         1.391134         0.886195         0.394500
N         1.100095         1.807142        -0.472652
H         0.498821        -0.335791        -1.027236
H         2.024028        -0.878286        -0.649229
H         1.394012         1.096001         1.420639
H         0.629474         1.579949        -1.390154
H         1.147019         2.756351        -0.298145
```

Table B32: XYZ file for VAm S_1 minimum MR-FOCI optmized geometry.

```
 8

C         1.185623        -0.466888        -0.221571
C         1.284294         0.860570         0.252148
N         1.183568         1.927131        -0.507417
H         1.018235        -0.689455        -1.256804
H         1.281866        -1.274062         0.479582
H         1.452276         1.047030         1.294982
H         1.025163         1.871532        -1.504438
H         1.263213         2.859579        -0.109145
```

Table B33: XYZ file for VAm S_1-S_0 H1Dis MECI MR-FOCI optmized geometry.

```
 8

C        -1.363115         0.100504        -0.007898
C        -0.094085        -0.371949         0.094818
N         0.982653         0.325646        -0.197530
H        -1.550969         1.108317        -0.328098
H        -2.205438        -0.527000         0.221374
H         0.024080        -1.412363         0.387091
H         1.675343         0.937680         0.171849
H         4.645403        -0.917206         1.802393
```

Table B34: XYZ file for VAm S_1-S_0 H2Dis MECI MR-FOCI optmized geometry.

```
 8

C        -1.190550         0.188910         0.183918
C        -0.116081        -0.455609        -0.169217
N         1.112350         0.160899         0.009159
H        -0.935375         1.141638         0.634685
H        -2.204296        -0.031740        -0.034249
H        -0.082973        -1.447848        -0.618521
H         0.395368         1.941815         0.008930
H         2.048615        -0.227314        -0.004121
```

B4 Determination of bonded and dissociated geometries

The bond connectivity $N_{b,i}$ for atom i of VAm was was found by comparing the distance between all other atoms to the sum of their covalent radii plus an allowance factor c

$$b_{ij} = \begin{cases} 1, & |\mathbf{R}_i - \mathbf{R}_j| < r_i + r_j + c \\ 0, & \text{otherwise} \end{cases}, \tag{B1}$$

$$N_{b,i} = \sum_{j}^{N_{atom}} b_{ij}, \tag{B2}$$

where $\mathbf{R}_i$ is cartesian position of atom i, r_i is its covalent radius and c is the allowance factor. The covalent radii used were 0.32 Å, 0.72 Å, and 0.68 Å for H, C and N, respectively. The allowance factor was set to a generous value of 0.56 Å, giving a maximum N−H bond distance of 1.56 Å.[233,234]

Appendix C

Supporting information — Site-selective isomerization of cyano-substituted butadienes: Chemical control of nonadiabatic dynamics (Chapter 4)

C1 Spawning

As per the original definition of FMS on adiabtic surfaces,[89] a spawning event occurs when the dot product of the nonadiabatic coupling vector $\mathbf{d}$ and the velocity v exceeds a set threshold. This threshold is chosen such that only sharp peaks in $\mathbf{d} \cdot \mathbf{v}$ exceed it in a set of test calculations. Thresholds of 0.014, 0.015 and 0.015 a.u. were chosen for BD, 1-CNBD and 2-CNBD, respectively. New trajectories are also required to conserve the classical energy of the nuclear basis, thus their momentum was scaled by the energy difference between states. Cases with kinetic energy less than the potential energy difference are rejected.

Although the choice of spawning is arbitrary and does not necessarily correspond to a change in state population, the choice of spawning criteria given above generally results in population transfer occuring at or near the spawn time. Figure C1 shows the population of new trajectories on the ground electronic state and their derivatives as a function of the time difference from t_{spawn}. The opacity for each trajectory is given by the total "population transferred" of that spawning event. The spawn time occurs within 10 a.u. of the inflection point in all cases, and population changes tend to occur within ∼60 a.u. of the spawning event. Given the relatively slow vibrational periods of the molecules, assigning properties based on the spawn geometry yields nearly identical results to measuring properties weighted by $\mathrm{d}p_c/\mathrm{d}t$ for all times. The former was used for data in Figures 4.3 and 4.4. It should be noted that this assumption is only valid for certain systems, namely those with localized, peaked conical intersection regions (*e.g.* polar polyenes and small non-polar polyenes).

C2 Bootstrap sampling

The standard deviation is a poor measure of the error associated with the mean adiabatic populations $\bar{\mathbf{p}}$ due to the variation between initial conditions. Instead, "bootstrap samples" are generated by sampling the set of initial conditions with replacement, *i.e.* an initial condition may be included more than once, but the total number of initial conditions remains the same for each sample. Averaging over initial conditions in a sample i generates sample populations $\mathbf{p}_i$. The mean values $\langle \mathbf{p} \rangle$ and standard deviations $\boldsymbol{\sigma}$ can then be calculated from multiple bootstrap samples. As the number of samples increases, the bootstrap mean $\langle \mathbf{p} \rangle$ converges to the true mean $\bar{\mathbf{p}}$ where each initial condition is included once.[177]

To avoid storing adiabatic populations for thousands of bootstrap samples, the mean and variance are updated incrementally.[235] For sample number n, let

$$\langle \mathbf{p} \rangle_n = \frac{1}{n} \sum_{i=0}^{n} \mathbf{p}_i, \tag{C1}$$

$$\boldsymbol{\Delta}_n = \sum_{i=0}^{n} (\mathbf{p}_i - \langle \mathbf{p} \rangle_n)^2. \tag{C2}$$

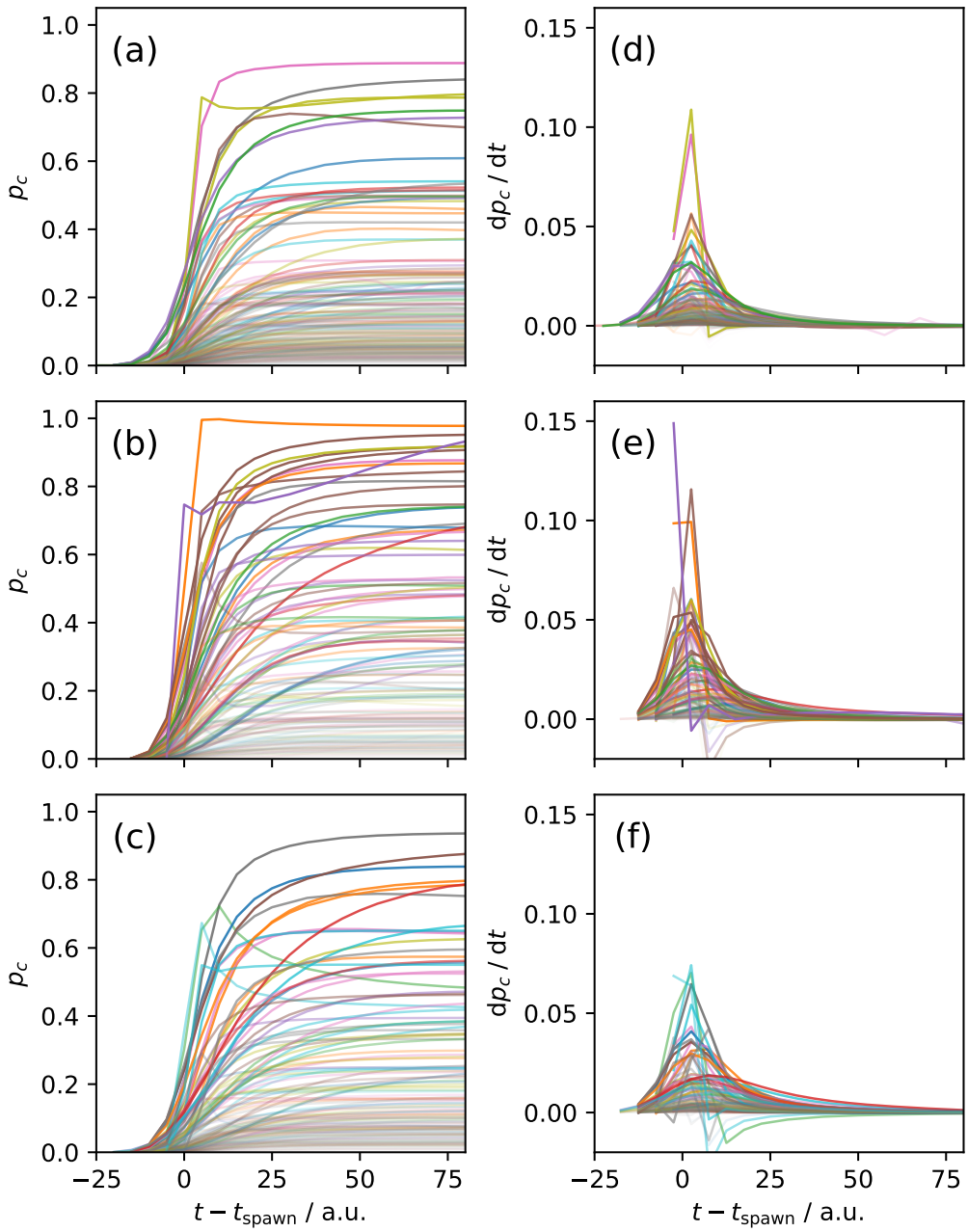

Figure C1: Ground state trajectory populations (a-c) and their time derivatives (d-f) as a function of time from spawn. Plots are given for BD, 1-CNBD and 2-CNBD from top to bottom. Line opacity is proportional to the total population transferred.

These values are updated by generating a new bootstrap sample $\mathbf{p}_{n+1}$, then

$$\mathbf{e}_{n+1} = \mathbf{p}_{n+1} - \langle \mathbf{p} \rangle_n, \tag{C3}$$

$$\langle \mathbf{p} \rangle_{n+1} = \langle \mathbf{p} \rangle_n + \frac{\mathbf{e}_{n+1}}{n+1}, \tag{C4}$$

$$\boldsymbol{\Delta}_{n+1} = \boldsymbol{\Delta}_n + \mathbf{e}_{n+1} \left(\mathbf{p}_{n+1} - \langle \mathbf{p} \rangle_{n+1} \right). \tag{C5}$$

Convergence is achieved when $\max |\langle \mathbf{p} \rangle_n - \bar{\mathbf{p}}| < \delta$ for all times and states with a set threshold δ. The standard deviation is then given by

$$\boldsymbol{\sigma}_n = \sqrt{\frac{\boldsymbol{\Delta}_n}{n-1}}. \tag{C6}$$

Only the current values of $\langle \mathbf{p} \rangle_n$ and $\boldsymbol{\Delta}_n$ need to be stored, and they are updated until convergence. We use a convergence threshold of $\delta = 10^{-3}$, requiring roughly 3000–8000 bootstrap samples for each molecule.

C3 Photochemical yield

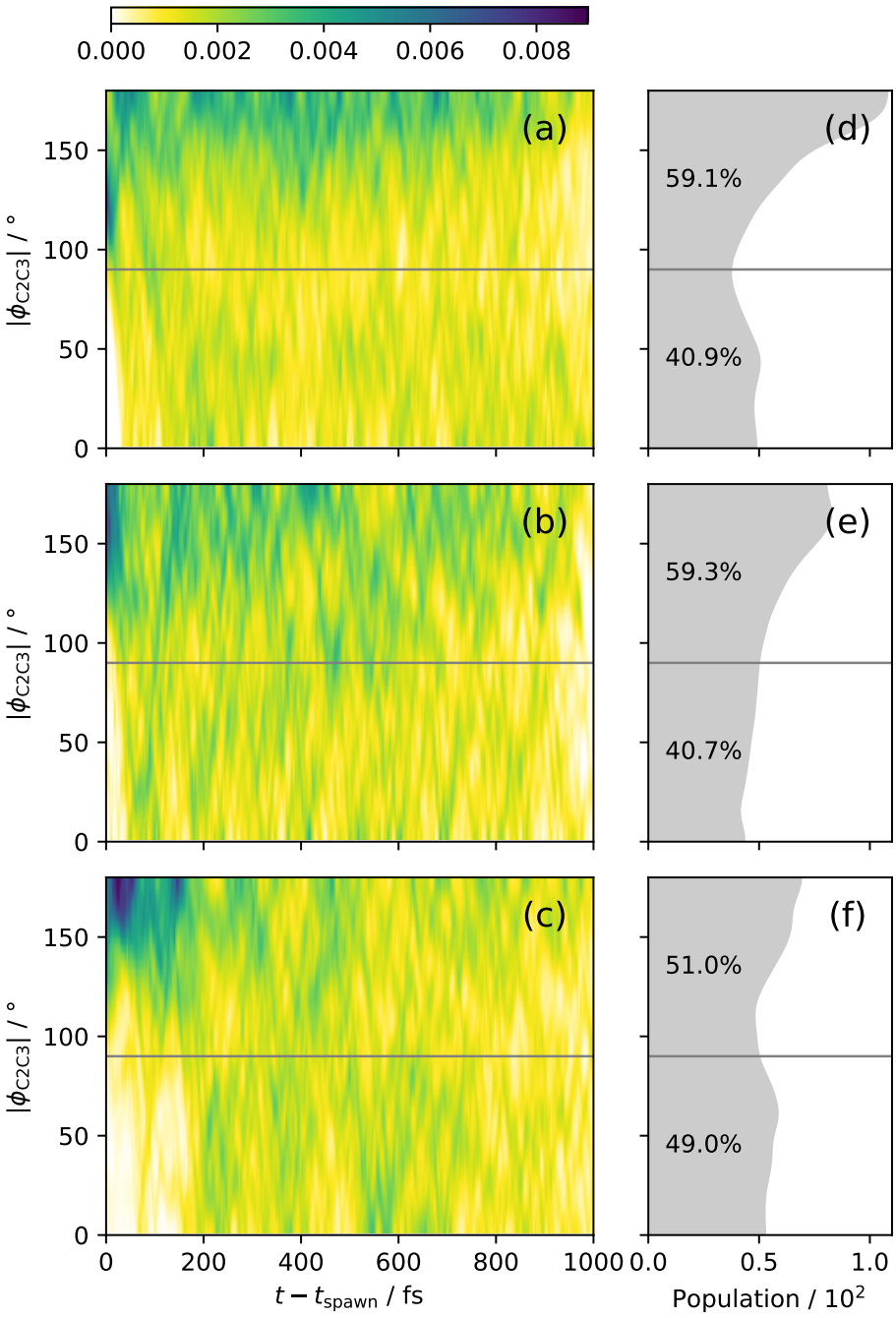

Figure C2: Ground state wavefunction density (a-c) as a function of time from spawn and C2-C3 dihedral angle and (d-f) densities integrated from 200 fs to the end of the simulation. Plots are given for BD, 1-CNBD and 2-CNBD from top to bottom.

C4 Potential energy surfaces

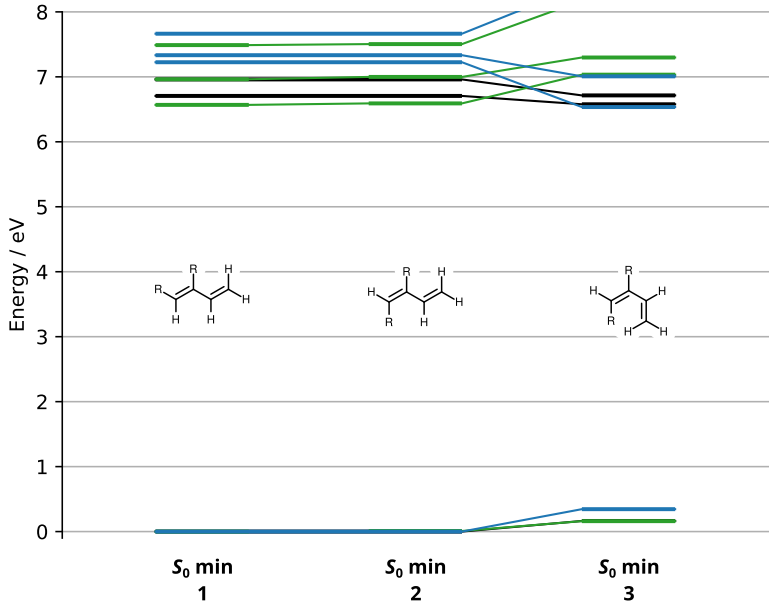

Figure C3: MR-CIS/6-31G* ground state potential energy minima of BD (black), 1-CNBD (green) and 2-CNBD (blue).

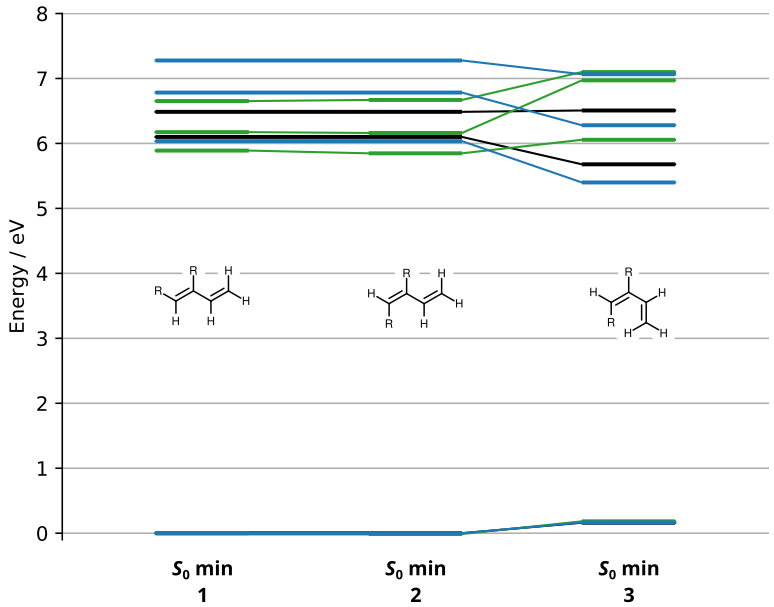

Figure C4: MS-CASPT2/cc-pVTZ ground state potential energy minima of BD (black), 1-CNBD (green) and 2-CNBD (blue).

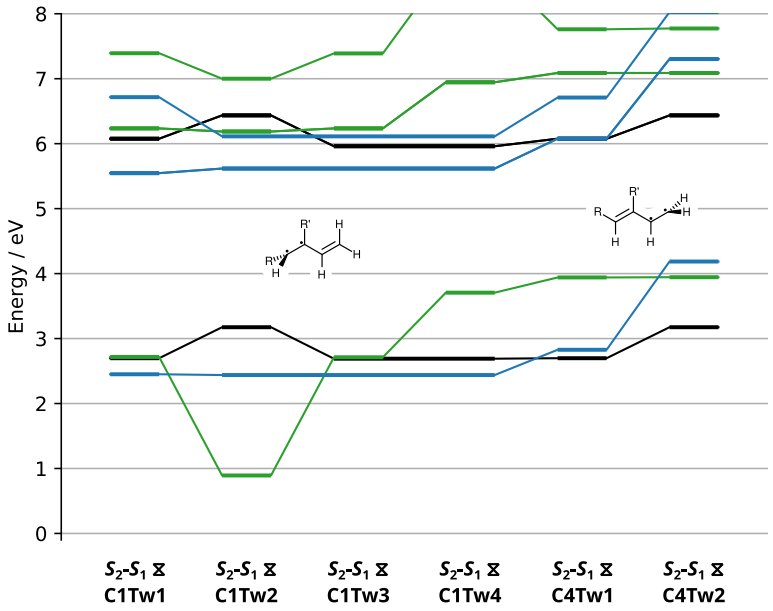

Figure C5: MR-CIS/6-31G* S_2-S_1 minimum energy conical intersections of BD (black), 1-CNBD (green) and 2-CNBD (blue).

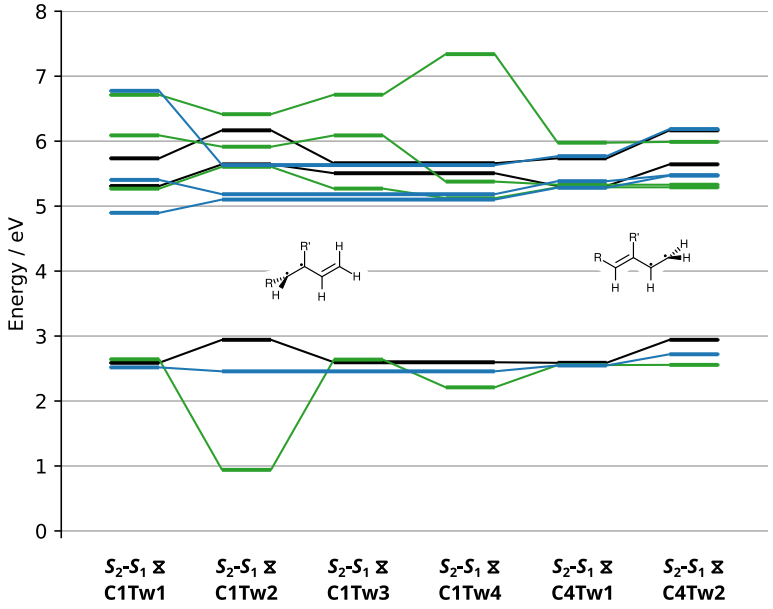

Figure C6: MS-CASPT2/cc-pVTZ S_2-S_1 minimum energy conical intersections of BD (black), 1-CNBD (green) and 2-CNBD (blue).

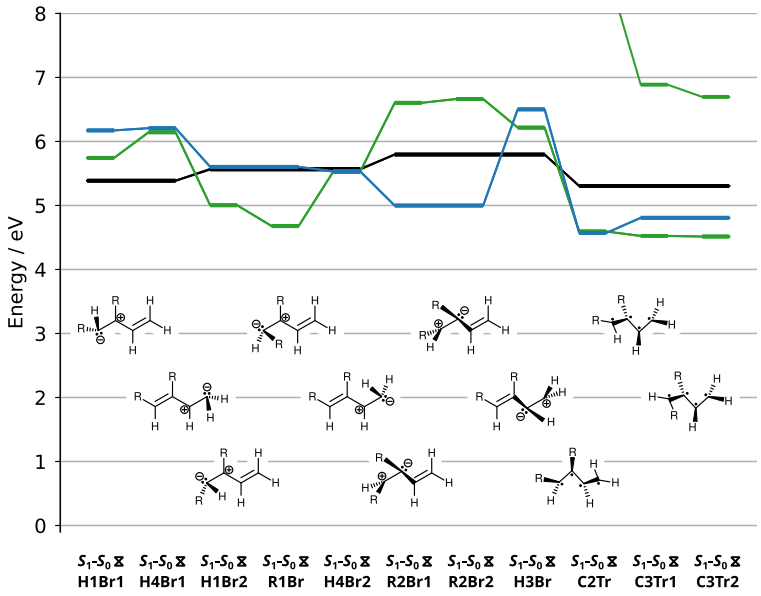

Figure C7: MR-CIS/6-31G* S_1-S_0 minimum energy conical intersections of BD (black), 1-CNBD (green) and 2-CNBD (blue).

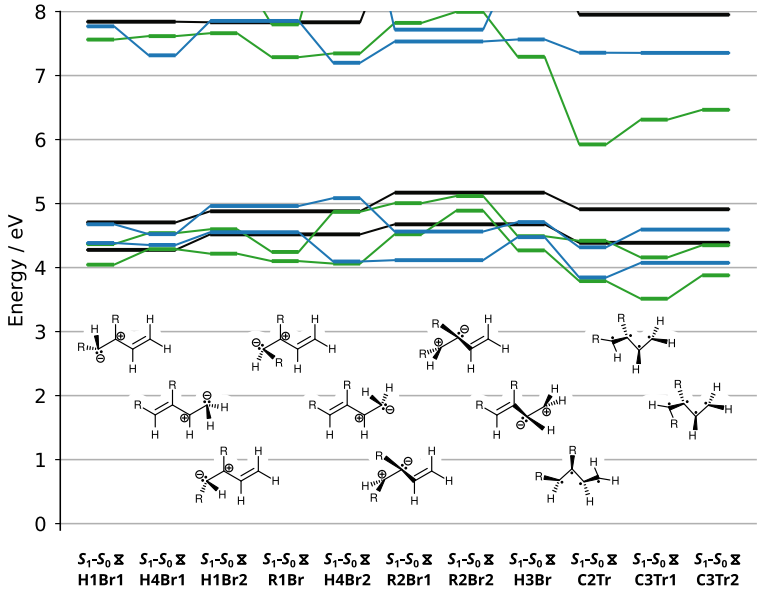

Figure C8: MS-CASPT2/cc-pVTZ S_1-S_0 minimum energy conical intersections of BD (black), 1-CNBD (green) and 2-CNBD (blue).

Table C1: MR-CIS/6-31G* potential energies of BD critical geometries.

	Energy / E_h		
Geometry	S_0	S_1	S_2
1, **2**	−155.0487659848	−154.8023180095	−154.7929770444
3	−155.0427635433	−154.8070399811	−154.8020210437
C1Tw1	−154.9496358805	−154.8254668870	−154.8254666863
C1Tw2	−154.9321085728	−154.8122623407	−154.8122593724
C1Tw3	−154.9499109734	−154.8297179987	−154.8297177233
H1Br1	−154.8508456793	−154.8508002978	−154.7223639172
H1Br2	−154.8443901889	−154.8440556562	−154.7230354871
R2Br	−154.8357835236	−154.8357827967	−154.7201466902
C2Tr	−154.8538763952	−154.8538759847	−154.7243602701

Table C2: MS-CASPT2/cc-pVTZ potential energies of BD critical geometries.

	Energy / E_h		
Geometry	S_0	S_1	S_2
1, **2**	−155.6306958100	−155.4065201300	−155.3923249700
3	−155.6247728700	−155.4220104500	−155.3915592800
C1Tw1	−155.5355936100	−155.4355877100	−155.4199125000
C1Tw2	−155.5225787400	−155.4233142600	−155.4040742500
C1Tw3	−155.5352839700	−155.4283392800	−155.4226845300
H1Br1	−155.4735417100	−155.4577659400	−155.3425458300
H1Br2	−155.4646306900	−155.4513795900	−155.3428776000
R2Br	−155.4588620900	−155.4406867500	−155.2921998400
C2Tr	−155.4694743700	−155.4502166500	−155.3384971600

Table C3: MR-CIS/6-31G* potential energies of 1-CNBD critical geometries.

	Energy / E_h			
Geometry	S_0	S_1	S_2	S_3
1	−246.8632743906	−246.6218919031	−246.6074049901	−246.5880712070
2	−246.8629440915	−246.6210547072	−246.6060775154	−246.5875072641
3	−246.8573730484	−246.6047986267	−246.5950889742	−246.5629670549
C1Tw1	−246.7634362285	−246.6341441598	−246.6341437323	−246.5916144552
C1Tw2	−246.8304813130	−246.6359008680	−246.6359004088	−246.6060318113
C1Tw3	−246.7636254079	−246.6341537353	−246.6341381080	−246.5917248165
C1Tw4	−246.7270660037	−246.6080431135	−246.6080385566	−246.5430115999
C4Tw1	−246.7184599539	−246.6027920761	−246.6027919646	−246.5780674151
C4Tw2	−246.7183228552	−246.6027931429	−246.6027885431	−246.5776190214
H1Br1	−246.6522304733	−246.6522277098	−246.5221665464	−246.4788705343
H1Br2	−246.6794031198	−246.6793986446	−246.5560059647	−246.5139941484
R1Br	−246.6914048680	−246.6913191255	−246.5574593428	−246.5504069342
H4Br1	−246.6375616378	−246.6374304288	−246.5160617173	−246.4282369893
H1Br2	−246.6602059297	−246.6602057744	−246.5540061989	−246.4687262240
R2Br1	−246.6206117638	−246.6206112720	−246.5061234267	−246.4407299288
R2Br2	−246.6184085511	−246.6184078753	−246.5051928366	−246.4438697749
H3Br	−246.6348541739	−246.6348539726	−246.5245336240	−246.4527965779
C2Tr	−246.6944600286	−246.6944588016	−246.5426425418	−246.5201656531
C3Tr1	−246.6970237748	−246.6970222584	−246.6101849836	−246.5182850048
C3Tr2	−246.6973757240	−246.6973631652	−246.6172215143	−246.5162664935

Table C4: MS-CASPT2/cc-pVTZ potential energies of 1-CNBD critical geometries.

	Energy / E_h			
Geometry	S_0	S_1	S_2	S_3
1	−247.7067678600	−247.4903136800	−247.4798788100	−247.4623051100
2	−247.7072183800	−247.4918705700	−247.4803570800	−247.4616745900
3	−247.7000435800	−247.4842104700	−247.4505843400	−247.4458892900
C1Tw1	−247.6101142600	−247.5135896100	−247.4834568900	−247.4605100700
C1Tw2	−247.6726562400	−247.5012213000	−247.4898758400	−247.4714675700
C1Tw3	−247.6102928900	−247.5135540300	−247.4834746900	−247.4604541400
C1Tw4	−247.6259953800	−247.5190032000	−247.5095919400	−247.4374942400
C4Tw1	−247.6133855400	−247.5128161700	−247.5113802700	−247.4875813200
C4Tw2	−247.6132805100	−247.5128360700	−247.5113692600	−247.4871355700
H1Br1	−247.5585597000	−247.5467543900	−247.4293206200	−247.3828396000
H1Br2	−247.5522384900	−247.5382214600	−247.4256642100	−247.3874315900
R1Br	−247.5565040800	−247.5512542200	−247.4394207100	−247.4206030400
H4Br1	−247.5496610100	−247.5404505800	−247.4273368100	−247.3695342300
H1Br2	−247.5579315700	−247.5281952800	−247.4372605200	−247.3489481700
R2Br1	−247.5410882600	−247.5232399100	−247.4197465900	−247.3767235800
R2Br2	−247.5275486700	−247.5191587800	−247.4133994100	−247.3688083200
H3Br	−247.5503574900	−247.5422009900	−247.4391995700	−247.3854166400
C2Tr	−247.5679759800	−247.5448434000	−247.4895202400	−247.3418191700
C3Tr1	−247.5780956400	−247.5543770700	−247.4752856100	−247.3660278200
C3Tr2	−247.5646703400	−247.5473978900	−247.4696391900	−247.3899376100

Table C5: MR-CIS/6-31G* potential energies of 2-CNBD critical geometries.

	Energy / E_h			
Geometry	S_0	S_1	S_2	S_3
1, **2**	−246.8603834900	−246.5948739612	−246.5908934589	−246.5787428078
3	−246.8477063319	−246.6202250232	−246.6028584544	−246.5515283499
C1Tw1	−246.7703332099	−246.6565598182	−246.6565582769	−246.6135780176
C1Tw2	−246.7707722917	−246.6539653452	−246.6539523321	−246.6357572570
C4Tw1	−246.7564833086	−246.6370519566	−246.6370511952	−246.6137962889
C4Tw2	−246.7065589193	−246.5920359423	−246.5919898002	−246.5654673608
H1Br1	−246.6335584040	−246.6335549670	−246.5098198611	−246.4375786765
H1Br2	−246.6545112795	−246.6544643456	−246.5383163368	−246.4570723320
H4Br1	−246.6322890345	−246.6322329912	−246.5188105271	−246.4194012591
H1Br2	−246.6571960362	−246.6568765291	−246.5611297824	−246.4534244850
R2Br	−246.6767213983	−246.6766708377	−246.5615694334	−246.5171429661
H3Br	−246.6214800789	−246.6214456805	−246.5124063245	−246.4379719313
C2Tr	−246.6924649718	−246.6924631922	−246.5559024593	−246.5325728726
C3Tr	−246.6837276638	−246.6837270385	−246.5505183670	−246.5285977122

Table C6: MS-CASPT2/cc-pVTZ potential energies of 2-CNBD critical geometries.

	Energy / E_h			
Geometry	S_0	S_1	S_2	S_3
1, **2**	−247.7045445700	−247.4778939000	−247.4519492000	−247.4484063600
3	−247.6987831900	−247.5064193700	−247.4740609300	−247.4452037800
C1Tw1	−247.6120231400	−247.5245918400	−247.5059554900	−247.4555723600
C1Tw2	−247.6142612600	−247.5170876000	−247.5140581400	−247.4975736800
C4Tw1	−247.6109386400	−247.5103978800	−247.5066845800	−247.4925245900
C4Tw2	−247.6046102500	−247.5035325800	−247.5032914900	−247.4772000500
H1Br1	−247.5434272800	−247.5326866900	−247.4190434700	−247.3251915000
H1Br2	−247.5372499500	−247.5221932000	−247.4159433100	−247.3325593300
H4Br1	−247.5445574100	−247.5383547100	−247.4356873100	−247.3663247200
H1Br2	−247.5540529300	−247.5176837800	−247.4399708500	−247.3337885900
R2Br	−247.5532906400	−247.5368529100	−247.4277511500	−247.4209478600
H3Br	−247.5400696200	−247.5314285600	−247.4265780400	−247.3780333100
C2Tr	−247.5632162900	−247.5458888600	−247.4342062300	−247.4008474600
C3Tr	−247.5548263200	−247.5357324900	−247.4342906800	−247.3566684000

C5 Molecular geometries

All geometries are given in units of Ångström.

Table C7: MR-CIS optimized geometry of the BD S_0 *trans* minimum (**1**, **2**).

C	−0.061215	0.255384	−0.048985
C	0.778184	0.905738	0.792956
C	1.704173	0.243114	1.698536
C	2.543572	0.893468	2.540478
H	−0.728595	0.792149	−0.700659
H	−0.088870	−0.821546	−0.094479
H	0.772877	1.986403	0.805882
H	1.709481	−0.837551	1.685611
H	2.571226	1.970398	2.585973
H	3.210951	0.356703	3.192153

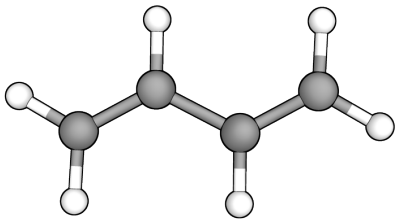

Table C8: MR-CIS optimized geometry of the BD S_0 *cis* minimum (**3**).

C	−0.108735	0.330951	−0.094729
C	0.763613	0.890255	0.778704
C	1.686701	0.194211	1.680851
C	1.847620	−1.144455	1.817874
H	−0.740867	0.947227	−0.710110
H	−0.206809	−0.735678	−0.210179
H	0.795802	1.968293	0.829027
H	2.298849	0.835122	2.297489
H	1.278988	−1.856536	1.243208
H	2.561379	−1.542961	2.517748

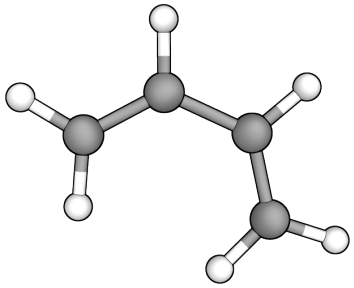

Table C9: MR-CIS optimized geometry of the BD S_2-S_1 C1 twist MECI 1 (**C1Tw1**).

C	−1.771535	−1.246620	−0.023181
C	−1.444413	0.129504	0.018663
C	−0.068024	0.587764	0.028609
C	0.340074	1.965622	−0.005373
H	−2.793232	−1.580530	−0.038327
H	−0.997381	−1.994505	−0.032692
H	−2.223901	0.871766	0.018181
H	0.656683	−0.231675	0.030489
H	0.478275	2.467695	−0.948634
H	0.423848	2.538142	0.903145

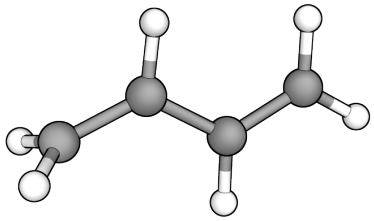

Table C10: MR-CIS optimized geometry of the BD S_2-S_1 C1 twist MECI 2 (**C1Tw2**).

C	1.447207	−1.402569	1.056560
C	0.405946	−1.179757	0.114504
C	−0.684324	−0.247416	0.141261
C	−2.002149	−0.472441	−0.259515
H	2.487433	−1.473361	0.755386
H	1.288885	−1.693567	2.096831
H	0.104853	−2.218843	−0.125220
H	−0.409066	0.774487	0.366534
H	−2.349236	−1.455664	−0.532702
H	−2.695176	0.346053	−0.337128

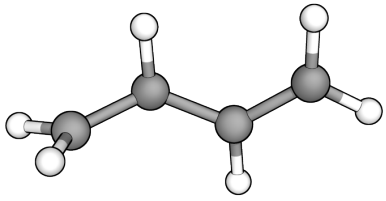

Table C11: MR-CIS optimized geometry of the BD S_2-S_1 C1 twist MECI 3 (**C1Tw3**).

C	−1.831586	−0.525265	0.194469
C	−0.549356	−0.097798	−0.336322
C	0.671398	−0.111266	0.452131
C	1.978019	0.067339	−0.117750
H	−2.165698	−1.542577	0.066945
H	−2.490360	0.161963	0.700317
H	−0.432013	0.155099	−1.386854
H	0.583316	−0.314804	1.505727
H	2.101539	0.232896	−1.173480
H	2.855174	0.070598	0.502653

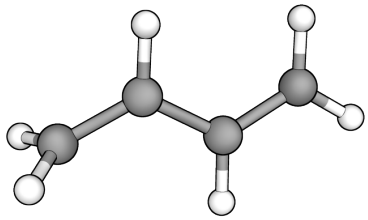

Table C12: MR-CIS optimized geometry of the BD S_1-S_0 H1 bridging MECI 1 (**H1Br1**).

C	1.841822	0.081208	0.057792
C	0.689252	−0.634436	−0.026686
C	−0.601895	0.013296	−0.099864
C	−1.816004	−0.716548	0.021817
H	2.804941	−0.398401	0.083936
H	1.828613	1.158278	0.096778
H	0.686535	−1.710895	−0.041153
H	−0.526662	1.104012	−0.129623
H	−2.674613	−0.198314	−0.418122
H	−1.816590	−0.006067	0.962993

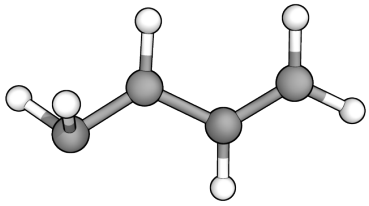

Table C13: MR-CIS optimized geometry of the BD S_1-S_0 H1 bridging MECI 2 (**H1Br2**).

C	1.859253	0.103075	0.022560
C	0.748132	−0.676460	−0.046586
C	−0.577449	−0.077563	−0.007071
C	−1.853416	−0.695048	0.135308
H	2.839597	−0.319624	0.156861
H	1.788075	1.177231	−0.027326
H	0.825900	−1.750959	0.014039
H	−0.550199	0.996762	−0.177030
H	−1.828743	−1.660216	0.653989
H	−1.411920	−1.164271	−0.851898

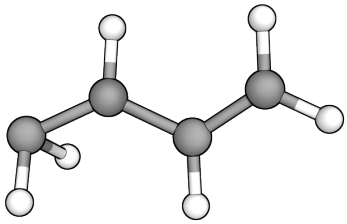

Table C14: MR-CIS optimized geometry of the BD S_1-S_0 H2 bridging MECI (**R2Br**).

C	1.363655	−1.476755	1.033233
C	0.534891	−0.949371	0.036100
C	−0.670060	−0.158282	0.076533
C	−1.952814	−0.537649	−0.176377
H	2.387908	−1.747906	0.815252
H	1.012393	−1.807281	2.008700
H	0.204967	−2.070707	0.266985
H	−0.474465	0.895795	0.220505
H	−2.217818	−1.566881	−0.361516
H	−2.737363	0.195240	−0.243732

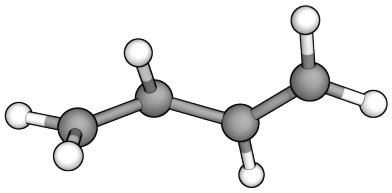

Table C15: MR-CIS optimized geometry of the BD S_1-S_0 C2 transoid MECI (**C2Tr**).

C	1.311740	−0.522258	0.966044
C	0.385161	−0.489594	−0.176401
C	−0.147032	0.757933	−0.623599
C	−1.486348	0.287422	−0.307643
H	2.173392	0.123071	0.955778
H	1.011290	−0.939779	1.911243
H	0.143552	−1.388069	−0.717179
H	0.236749	1.687881	−0.240237
H	−1.988066	−0.424395	−0.939287
H	−1.980353	0.592607	0.598953

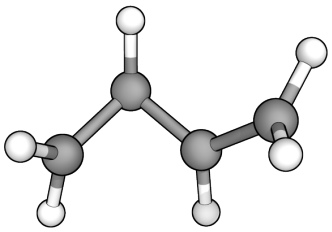

Table C16: MR-CIS optimized geometry of the 1-CNBD S_0 *trans-trans* minimum (**1**).

C	2.689834	−0.026590	0.000000
C	1.367798	−0.567234	0.000001
C	0.258458	0.222320	−0.000001
C	−1.098097	−0.312622	−0.000001
C	−2.181219	0.449072	0.000001
N	3.780057	0.416736	0.000001
H	1.288882	−1.640211	0.000002
H	0.376470	1.292962	−0.000002
H	−1.197811	−1.386013	−0.000002
H	−2.118357	1.523782	0.000002
H	−3.168407	0.023779	0.000001

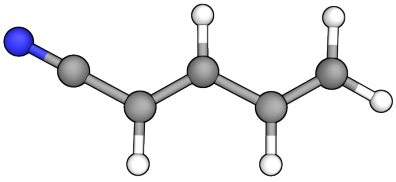

Table C17: MR-CIS optimized geometry of the 1-CNBD S_0 *cis-trans* minimum (**2**).

C	−0.135856	−1.173381	−0.146745
C	−0.053411	0.250616	−0.041228
C	0.796001	0.890189	0.810384
C	1.728049	0.232683	1.722031
C	2.533712	0.903062	2.530843
N	−0.209025	−2.344566	−0.238832
H	−0.710106	0.809965	−0.681941
H	0.779825	1.966727	0.812437
H	1.743734	−0.844082	1.719491
H	2.543999	1.979381	2.559085
H	3.212138	0.397642	3.193968

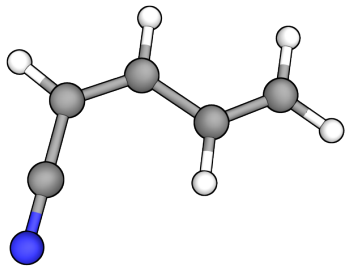

Table C18: MR-CIS optimized geometry of the 1-CNBD S_0 *cis-cis* minimum (**3**).

C	−0.589568	−1.082014	−0.019071
C	−0.073958	0.250527	−0.125918
C	0.841937	0.787898	0.715819
C	1.477529	0.113745	1.873723
C	2.122145	−1.035001	1.812484
N	−1.039565	−2.169066	0.026680
H	−0.467477	0.834936	−0.938253
H	1.123413	1.813738	0.537671
H	1.411860	0.641050	2.811297
H	2.226581	−1.583609	0.893319
H	2.568925	−1.470196	2.687955

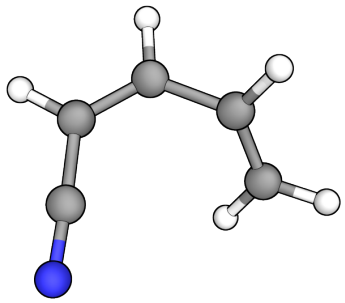

Table C19: MR-CIS optimized geometry of the 1-CNBD S_2-S_1 C1 twist MECI 1 (**C1Tw1**).

C	0.795804	2.612871	−1.119732
C	0.280518	1.978683	0.024379
C	−0.083934	0.562464	0.000674
C	−1.402440	0.101669	−0.002818
C	−1.748979	−1.215943	−0.016401
N	1.825570	2.686303	−1.852119
H	−0.008818	2.609994	0.848880
H	0.720159	−0.155411	−0.056386
H	−2.188698	0.838536	0.021491
H	−1.004051	−1.991083	−0.042342
H	−2.777267	−1.524047	0.009704

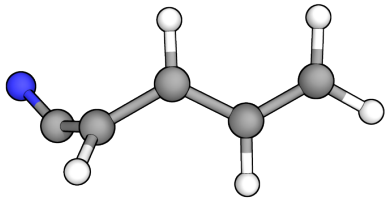

Table C20: MR-CIS optimized geometry of the 1-CNBD S_2-S_1 C1 twist MECI 2 (**C1Tw2**).

C	2.658087	−1.996892	0.816966
C	1.570311	−1.236078	0.888234
C	0.377534	−1.293179	0.085405
C	−0.702220	−0.408576	0.285036
C	−1.847549	−0.404591	−0.429181
N	3.722782	−2.706128	0.781331
H	1.656235	−0.493920	1.675818
H	0.318556	−2.037054	−0.688944
H	−0.595056	0.320371	1.074125
H	−2.016537	−1.104075	−1.229282
H	−2.631508	0.300264	−0.223756

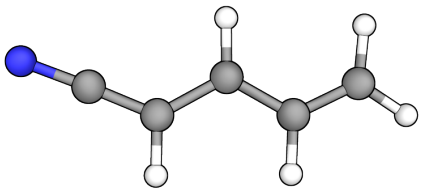

Table C21: MR-CIS optimized geometry of the 1-CNBD S_2-S_1 C1 twist MECI 3 (**C1Tw3**).

C	−2.388561	−1.756905	0.071252
C	−1.781429	−0.489997	0.117192
C	−0.431386	−0.282047	−0.406058
C	0.689687	−0.079247	0.401348
C	1.947916	0.125422	−0.080048
N	−2.903588	−2.598910	−0.721557
H	−2.266028	0.267563	0.711569
H	−0.302722	−0.325828	−1.476892
H	0.541255	−0.071046	1.469033
H	2.150587	0.125529	−1.136142
H	2.776476	0.304876	0.578834

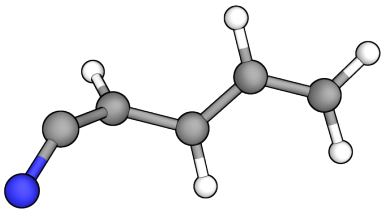

Table C22: MR-CIS optimized geometry of the 1-CNBD S_2-S_1 C1 twist MECI 4 (**C1Tw4**).

C	2.642135	0.849098	0.695447
C	2.016678	−0.100944	−0.121536
C	0.725297	−0.669515	0.274328
C	−0.475641	−0.133249	−0.318782
C	−1.777998	−0.213352	0.288910
N	3.142996	1.614448	1.389638
H	2.484999	−0.354341	−1.055839
H	0.648942	−1.275186	1.162954
H	−0.377125	0.410976	−1.242760
H	−1.904282	−0.624428	1.299739
H	−2.660907	0.070302	−0.253411

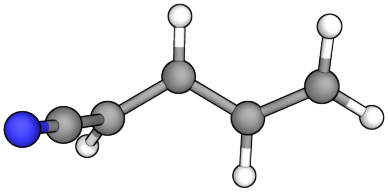

Table C23: MR-CIS optimized geometry of the 1-CNBD S_2-S_1 C4 twist MECI 1 (**C4Tw1**).

C	−3.170670	−1.582788	−0.063118
C	−1.799508	−1.235738	−0.030925
C	−1.402053	0.102898	0.041917
C	−0.060550	0.582972	0.100490
C	0.305422	1.938336	−0.044412
N	−4.278176	−1.865603	−0.090663
H	−1.082192	−2.034097	−0.089353
H	−2.187889	0.839799	0.101186
H	0.770852	−0.099948	−0.061696
H	0.361098	2.506226	−1.020017
H	0.626448	2.573172	0.778458

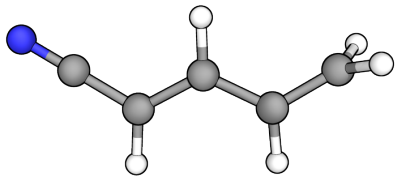

Table C24: MR-CIS optimized geometry of the 1-CNBD S_2-S_1 C4 twist MECI 2 (**C4Tw2**).

C	−2.857064	0.677328	−0.353170
C	−1.974069	−0.427776	−0.372864
C	−0.700475	−0.336243	0.197319
C	0.285461	−1.366324	0.229978
C	1.466294	−1.311420	1.001323
N	−3.573338	1.568461	−0.337939
H	−2.331510	−1.343093	−0.808519
H	−0.421418	0.620325	0.611012
H	0.024394	−2.379245	−0.070119
H	1.534624	−1.483299	2.116195
H	2.457423	−1.145108	0.585387

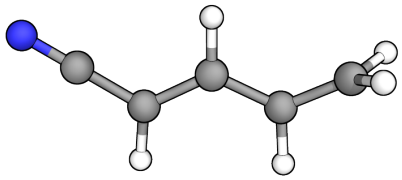

Table C25: MR-CIS optimized geometry of the 1-CNBD S_1-S_0 H1 bridging MECI 1 (**H1Br1**).

C	−2.906004	0.012653	−0.830780
C	−1.776645	−0.553291	−0.155878
C	−0.512721	0.107111	−0.156281
C	0.717304	−0.619057	−0.033122
C	1.902790	0.029501	0.144966
N	−3.828865	0.388718	−1.386835
H	−1.860764	0.062944	0.874069
H	−0.407248	1.190536	−0.090163
H	0.664094	−1.691435	−0.108461
H	1.943501	1.102092	0.239503
H	2.835775	−0.504295	0.187598

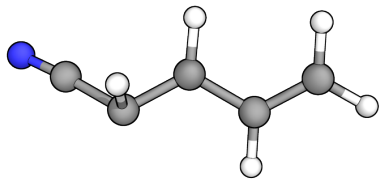

Table C26: MR-CIS optimized geometry of the 1-CNBD S_1-S_0 H1 bridging MECI 2 (**H1Br2**).

C	−2.093289	−1.761498	0.492156
C	−1.798453	−0.518754	−0.136539
C	−0.495926	0.033859	−0.087643
C	0.778583	−0.653261	−0.090617
C	1.908121	0.062629	0.134371
N	−2.420185	−2.733307	1.035999
H	−1.318684	−0.913118	−1.120836
H	−0.399827	1.114832	−0.141666
H	0.785712	−1.730669	−0.107528
H	1.888813	1.139361	0.162155
H	2.852423	−0.417321	0.321484

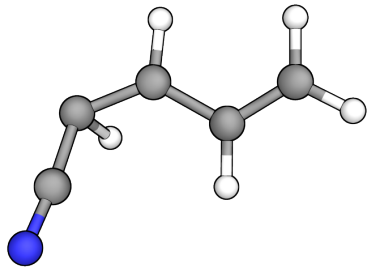

Table C27: MR-CIS optimized geometry of the 1-CNBD S_1-S_0 R1 bridging MECI (**R1Br**).

C	1.487555	−0.846603	−1.044237
C	1.517970	−0.583923	0.282284
C	0.319103	0.177172	−0.042397
C	−1.035834	−0.373060	−0.076021
C	−2.093726	0.424847	−0.073239
N	1.125492	−0.728552	−2.206073
H	1.970051	−1.004994	1.147758
H	0.392420	1.241793	−0.232795
H	−1.130385	−1.441661	−0.005639
H	−1.996605	1.494147	−0.145207
H	−3.092103	0.036728	0.010894

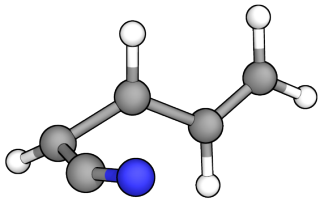

Table C28: MR-CIS optimized geometry of the 1-CNBD S_1-S_0 H4 bridging MECI 1 (**H4Br1**).

C	3.133477	−0.598549	−0.062397
C	1.856423	0.053081	−0.040089
C	0.680554	−0.641046	0.038257
C	−0.595076	0.031550	0.104510
C	−1.810432	−0.698094	0.011123
N	4.154225	−1.098790	−0.081444
H	1.870845	1.128299	−0.079824
H	0.670487	−1.717141	0.058983
H	−0.526176	1.121780	0.111280
H	−1.769014	−0.019488	−1.006519
H	−2.704012	−0.167452	0.348955

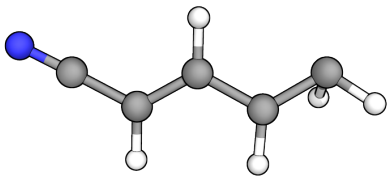

Table C29: MR-CIS optimized geometry of the 1-CNBD S_1-S_0 H4 bridging MECI 2 (**H4Br2**).

C	3.169787	−0.527616	0.136100
C	1.871922	0.044190	−0.011619
C	0.738281	−0.712934	−0.114341
C	−0.568981	−0.080119	−0.024248
C	−1.825537	−0.689467	0.207512
N	4.229194	−0.979788	0.251508
H	1.820894	1.119982	−0.017007
H	0.798697	−1.788966	−0.092629
H	−0.546993	0.991891	−0.193851
H	−1.838951	−1.687743	0.644410
H	−1.420732	−1.063342	−0.846343

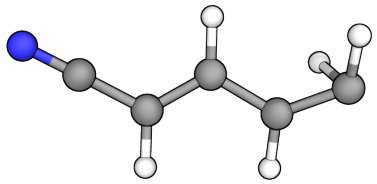

Table C30: MR-CIS optimized geometry of the 1-CNBD S_1-S_0 H2 bridging MECI 1 (**R2Br1**).

C	2.713621	−1.848863	0.776282
C	1.342434	−1.476098	1.008991
C	0.570618	−0.894607	−0.018160
C	−0.661071	−0.140663	0.070363
C	−1.933981	−0.561080	−0.148938
N	3.794965	−2.160797	0.612878
H	0.954785	−1.786697	1.973888
H	0.171683	−2.074708	0.189903
H	−0.484323	0.916109	0.211359
H	−2.167580	−1.596872	−0.339008
H	−2.747060	0.142027	−0.173446

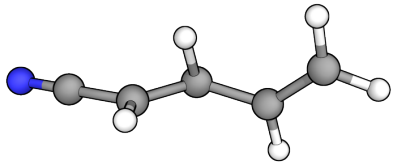

Table C31: MR-CIS optimized geometry of the 1-CNBD S_1-S_0 H2 bridging MECI 2 (**R2Br2**).

C	0.840096	−1.936294	2.321140
C	1.338068	−1.500478	1.029068
C	0.571289	−0.879856	0.019346
C	−0.662229	−0.126846	0.066388
C	−1.931558	−0.562174	−0.147343
N	0.466959	−2.229553	3.354515
H	2.363552	−1.777415	0.836780
H	0.169556	−2.068659	0.163781
H	−0.490300	0.936170	0.155805
H	−2.160652	−1.607488	−0.282249
H	−2.745754	0.136172	−0.221070

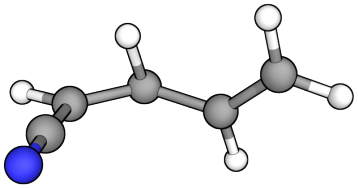

Table C32: MR-CIS optimized geometry of the 1-CNBD S_1-S_0 H3 bridging MECI (**H3Br**).

C	−2.992557	0.475228	−0.299530
C	−1.969709	−0.520189	−0.235198
C	−0.681699	−0.195903	0.109651
C	0.470784	−1.026819	0.083119
C	1.412210	−1.438632	1.035204
N	−3.816863	1.260441	−0.344386
H	−2.253654	−1.526255	−0.490371
H	−0.460127	0.837845	0.327354
H	0.107961	−2.159180	0.387514
H	2.412579	−1.717216	0.732373
H	1.159241	−1.679473	2.064302

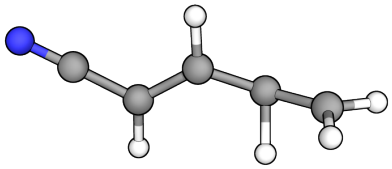

Table C33: MR-CIS optimized geometry of the 1-CNBD S_1-S_0 C2 transoid MECI (**C2Tr**).

C	0.746298	−1.851081	2.112188
C	0.953061	−1.016163	0.992466
C	0.271924	−1.236122	−0.288815
C	−0.700387	−0.219411	−0.118124
C	−2.116781	−0.565467	−0.142166
N	0.590861	−2.557383	3.024251
H	1.519198	−0.115157	1.153639
H	−0.038973	−2.228635	−0.564846
H	−0.376829	0.796179	0.042426
H	−2.459863	−1.402705	0.437847
H	−2.720583	−0.258765	−0.980443

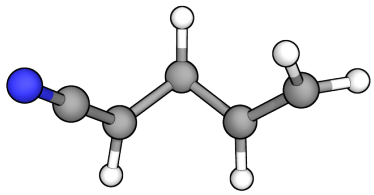

Table C34: MR-CIS optimized geometry of the 1-CNBD S_1-S_0 C3 transoid MECI 1 (**C3Tr1**).

C	−2.880344	−0.125542	−1.197741
C	−2.092068	−0.579329	−0.124718
C	−0.727038	−0.095279	0.040543
C	0.285233	−0.958860	−0.435820
C	1.075918	−1.125775	0.764034
N	−3.532139	0.266359	−2.079707
H	−2.390763	−1.482540	0.373744
H	−0.472409	0.819176	0.549206
H	0.050040	−1.773062	−1.096464
H	1.487434	−0.261213	1.256124
H	1.037555	−2.040256	1.331982

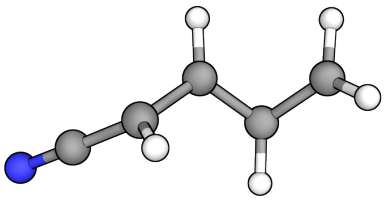

Table C35: MR-CIS optimized geometry of the 1-CNBD S_1-S_0 C3 transoid MECI 2 (**C3Tr2**).

C	−2.566492	−1.568401	0.731475
C	−2.104201	−0.496610	−0.052258
C	−0.719854	−0.058459	0.039745
C	0.244929	−0.986468	−0.418721
C	1.061294	−1.129232	0.762356
N	−2.955675	−2.441950	1.396185
H	−2.713250	−0.173676	−0.879760
H	−0.411442	0.871203	0.488670
H	−0.048689	−1.827933	−1.019457
H	1.504926	−0.259336	1.215612
H	1.007723	−2.023320	1.360712

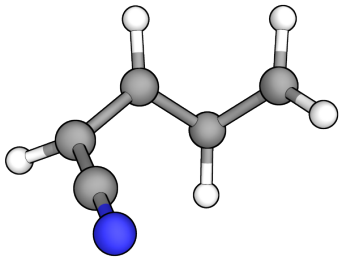

Table C36: MR-CIS optimized geometry of the 2-CNBD S_0 *trans* minimum (**1**, **2**).

C	−1.756856	−0.659866	−0.000001
C	−0.596775	0.044967	0.000000
C	0.732306	−0.600965	0.000001
C	1.888822	0.035939	−0.000001
C	−0.653764	1.484496	0.000001
N	−0.690521	2.660076	0.000003
H	−2.713044	−0.168640	−0.000001
H	−1.742496	−1.735643	0.000000
H	0.710116	−1.677587	0.000003
H	2.816658	−0.506130	−0.000001
H	1.955480	1.109353	−0.000003

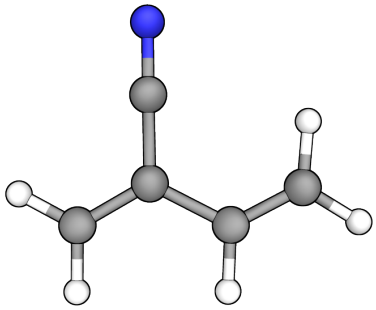

Table C37: MR-CIS optimized geometry of the 2-CNBD S_0 *cis* minimum (**3**).

C	−1.799524	−0.645493	−0.000004
C	−0.617802	0.016763	−0.000000
C	0.732963	−0.589379	−0.000007
C	1.018988	−1.914705	0.000006
C	−0.632464	1.445276	0.000011
N	−0.622078	2.603666	0.000021
H	−2.730524	−0.109732	0.000005
H	−1.844537	−1.718840	−0.000015
H	1.549863	0.111724	−0.000022
H	2.040993	−2.248355	0.000001
H	0.257277	−2.675006	0.000023

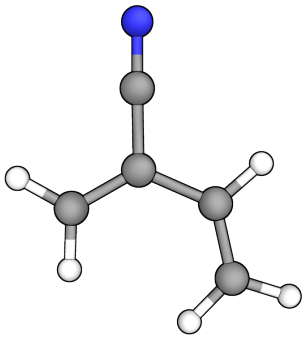

Table C38: MR-CIS optimized geometry of the 2-CNBD S_2-S_1 C1 twist MECI 1 (**C1Tw1**).

C	0.229584	2.049547	0.001871
C	−0.059888	0.615390	−0.000175
C	−1.413215	0.107024	−0.001289
C	−1.756897	−1.266558	−0.003809
C	1.010826	−0.319560	−0.000566
N	1.922458	−1.047729	−0.000813
H	0.689762	2.423488	−0.902371
H	0.688222	2.420942	0.907823
H	−2.183128	0.857570	−0.000114
H	−2.788359	−1.566050	−0.004352
H	−1.004144	−2.034112	−0.005136

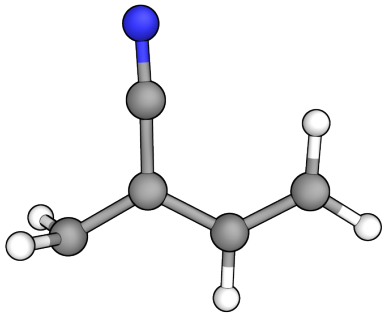

Table C39: MR-CIS optimized geometry of the 2-CNBD S_2-S_1 C1 twist MECI 2 (**C1Tw2**).

C	1.480630	−1.337981	1.014580
C	0.234657	−1.376347	0.281881
C	−0.721444	−0.297496	0.200104
C	−1.994321	−0.364278	−0.355772
C	0.044250	−2.693027	−0.150920
N	−0.041927	−3.813577	−0.483719
H	2.436156	−1.204659	0.524809
H	1.530561	−1.522825	2.080278
H	−0.397341	0.641859	0.620308
H	−2.627531	0.503466	−0.350428
H	−2.376150	−1.272543	−0.787355

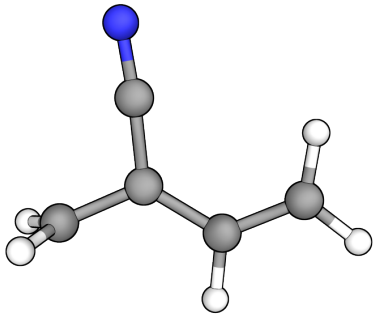

Table C40: MR-CIS optimized geometry of the 2-CNBD S_2-S_1 C4 twist MECI 1 (**C4Tw1**).

C	0.346617	2.004460	−0.022195
C	−0.123243	0.693254	0.017365
C	−1.464648	0.181774	0.046550
C	−1.606229	−1.246116	0.089758
C	0.839115	−0.389010	0.034029
N	1.538920	−1.315530	0.049878
H	1.402388	2.198800	−0.039911
H	−0.335706	2.834703	−0.035319
H	−2.348195	0.797952	0.041512
H	−1.682457	−1.870952	−0.797376
H	−1.657498	−1.818779	1.013197

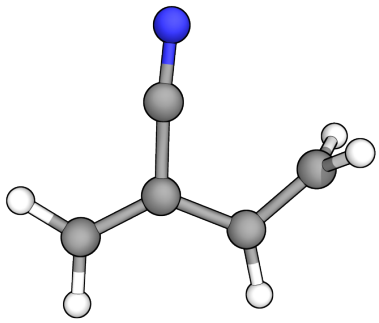

Table C41: MR-CIS optimized geometry of the 2-CNBD S_2-S_1 C4 twist MECI 2 (**C4Tw2**).

C	−1.994390	−0.403264	−0.382713
C	−0.712595	−0.351157	0.152810
C	0.279389	−1.395887	0.224032
C	1.463668	−1.230147	0.984132
C	−0.229323	0.928837	0.628668
N	0.228280	1.886769	1.041255
H	−2.627259	0.463282	−0.349751
H	−2.394331	−1.324243	−0.767129
H	−0.012588	−2.433437	0.100256
H	1.550083	−1.245762	2.117033
H	2.453908	−1.116596	0.548141

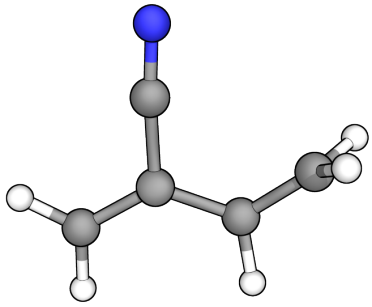

Table C42: MR-CIS optimized geometry of the 2-CNBD S_1-S_0 H1 bridging MECI 1 (**H1Br1**).

C	−1.754736	−0.791762	0.167362
C	−0.584113	0.002146	−0.003012
C	0.728489	−0.609404	−0.000883
C	1.901264	0.080113	0.015333
C	−0.605037	1.472587	−0.081086
N	−0.667467	2.603107	−0.175859
H	−2.676217	−0.303671	−0.170727
H	−1.767504	−0.084333	1.161713
H	0.708801	−1.685038	−0.006157
H	2.841219	−0.442316	−0.005798
H	1.933106	1.155677	0.042757

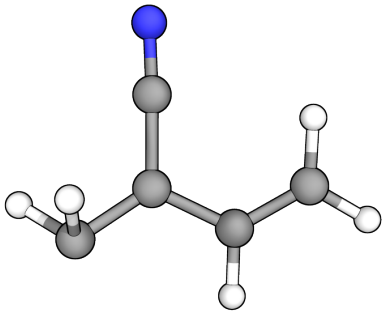

Table C43: MR-CIS optimized geometry of the 2-CNBD S_1-S_0 H1 bridging MECI 2 (**H1Br2**).

C	−1.842147	−0.695637	0.164194
C	−0.586782	−0.044720	0.045248
C	0.756853	−0.630417	−0.038939
C	1.903057	0.091561	0.023158
C	−0.634083	1.401315	−0.080228
N	−0.673266	2.551303	−0.208788
H	−1.796721	−1.711490	0.562507
H	−1.349482	−1.031791	−0.863681
H	0.790747	−1.707481	−0.034166
H	2.855699	−0.403623	0.085040
H	1.902145	1.167313	0.035975

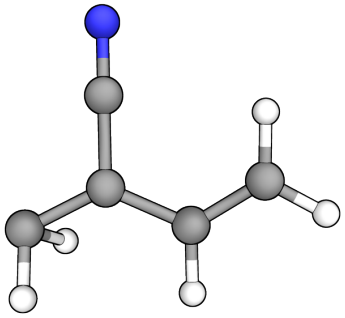

Table C44: MR-CIS optimized geometry of the 2-CNBD S_1-S_0 H4 bridging MECI 1 (**H4Br1**).

C	−1.730500	−0.668597	−0.049986
C	−0.563969	0.042437	0.020426
C	0.728317	−0.613378	0.106732
C	1.948848	0.096263	0.000022
C	−0.621177	1.493272	0.021194
N	−0.745040	2.620714	0.026914
H	−2.687129	−0.180220	−0.081539
H	−1.709528	−1.744211	−0.067098
H	0.636397	−1.700245	0.143316
H	1.941495	−0.605323	−0.994967
H	2.823496	−0.430487	0.389329

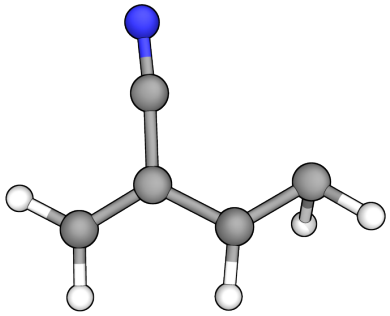

Table C45: MR-CIS optimized geometry of the 2-CNBD S_1-S_0 H4 bridging MECI 2 (**H4Br2**).

C	−1.737085	−0.687205	0.010185
C	−0.622672	0.094792	−0.050046
C	0.712870	−0.522917	−0.010757
C	1.986849	0.061700	0.133105
C	−0.730804	1.527448	0.015431
N	−0.804507	2.680805	0.041344
H	−2.718004	−0.266790	0.137083
H	−1.649397	−1.758136	−0.044228
H	0.655185	−1.593524	−0.180149
H	2.054274	1.046153	0.594060
H	1.538698	0.472944	−0.884624

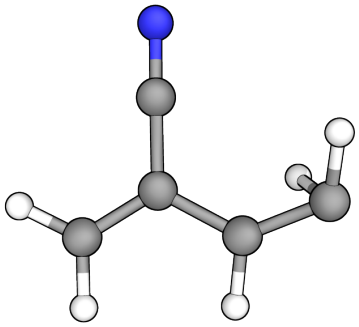

Table C46: MR-CIS optimized geometry of the 2-CNBD S_1-S_0 R2 bridging MECI (**R2Br**).

C	1.407936	−1.543479	0.892778
C	0.084501	−1.241828	0.376216
C	−0.827060	−0.151065	0.188970
C	−2.066283	−0.214187	−0.357631
C	0.211395	−2.582171	0.172381
N	0.829014	−3.617407	0.240210
H	2.291515	−1.473105	0.278306
H	1.574505	−1.791167	1.929162
H	−0.455564	0.802530	0.529266
H	−2.665450	0.673677	−0.449414
H	−2.486517	−1.140135	−0.713637

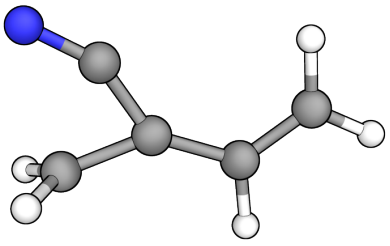

Table C47: MR-CIS optimized geometry of the 2-CNBD S_1-S_0 H3 bridging MECI (**H3Br**).

C	−1.953690	−0.545712	−0.169919
C	−0.661936	−0.160270	0.076990
C	0.550390	−0.950754	0.016490
C	1.366066	−1.473951	1.038760
C	−0.408100	1.256838	0.283289
N	−0.204713	2.357266	0.476277
H	−2.740854	0.180512	−0.248875
H	−2.194301	−1.581244	−0.340398
H	0.128900	−2.107091	0.181477
H	2.395535	−1.730502	0.832572
H	0.986958	−1.820842	1.995885

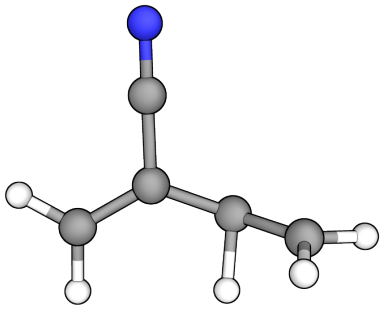

Table C48: MR-CIS optimized geometry of the 2-CNBD S_1-S_0 C2 transoid MECI (**C2Tr**).

C	−1.560288	−0.660640	0.217686
C	−0.577256	0.168815	−0.487767
C	0.569179	−0.634809	−0.295475
C	1.790470	−0.080503	0.285611
C	−0.578096	1.585177	−0.423536
N	−0.612787	2.745706	−0.415880
H	−1.764494	−0.490000	1.260054
H	−1.868133	−1.599474	−0.208048
H	0.516730	−1.668141	−0.591207
H	2.665105	0.014401	−0.336547
H	1.718055	0.576732	1.132971

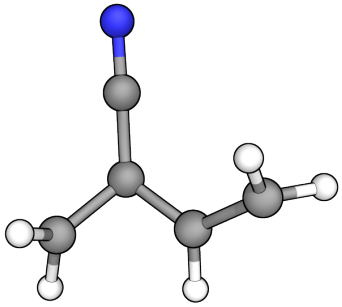

Table C49: MR-CIS optimized geometry of the 2-CNBD S_1-S_0 C3 transoid MECI (**C3Tr**).

C	−2.049167	−0.719305	−0.279523
C	−0.698568	−0.183816	−0.139414
C	0.383291	−1.085495	−0.378673
C	1.080437	−1.068029	0.907336
C	−0.483693	1.181004	0.235813
N	−0.349453	2.298806	0.513937
H	−2.612078	−0.503209	−1.171772
H	−2.312411	−1.596529	0.281264
H	0.186566	−1.998973	−0.908950
H	1.604483	−0.182840	1.223209
H	0.814618	−1.774712	1.677427

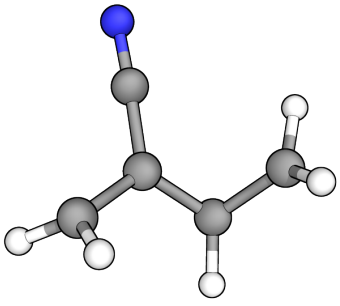

Appendix D

Supplementary material — Substituent effects on nonadiabatic excited state dynamics: Inertial, steric and electronic effects in methylated butadienes (Chapter 5)

D1 Adiabatic population kinetic model

Adiabatic populations were fit to a first-order kinetic model of the form

$$\mathrm{S}_2 \underset{\tau_{-1}}{\overset{\tau_1}{\rightleftharpoons}} \mathrm{S}_1 \underset{\tau_{-2}}{\overset{\tau_2}{\rightleftharpoons}} \mathrm{S}_0, \tag{D1}$$

where τ are decay lifetimes, *i.e.* $\tau_i = 1/k_i$ for decay constants k_i. Finding the forms of the populations as a function of time involves solving the set of differential equations [236]

$$\frac{\mathrm{d}p_2}{\mathrm{d}t} = -k_1 p_2 + k_{-2} p_1, \qquad \frac{\mathrm{d}p_1}{\mathrm{d}t} = k_1 p_2 + k_{-2} p_0 - (k_{-1} + k_2) p_1, \qquad \frac{\mathrm{d}p_0}{\mathrm{d}t} = k_2 p_1 - k_{-2} p_0, \tag{D2}$$

where p_i are the populations for state i. Doing so yields the following populations:

$$\begin{aligned} p_2(t) = {} & \frac{p_2(0)k_1(\gamma_1 - k_2 - k_{-2}) + p_1(0)k_{-1}(k_{-2} - \gamma_1)}{\gamma_1(\gamma_1 - \gamma_2)} \exp(-\gamma_1 t) \\ & + \frac{p_2(0)k_1(\gamma_2 - k_2 - k_{-2}) + p_1(0)k_{-1}(k_{-2} - \gamma_2)}{\gamma_2(\gamma_2 - \gamma_1)} \exp(-\gamma_2 t) + \frac{k_{-1}k_{-2}}{\gamma_1\gamma_2}(p_2(0) + p_1(0)), \end{aligned} \tag{D3}$$

$$\begin{aligned} p_1(t) = {} & \frac{p_2(0)k_1(k_{-2} - \gamma_1) + p_1(0)(\gamma_1 - k_1)(\gamma_1 - k_{-2})}{\gamma_1(\gamma_1 - \gamma_2)} \exp(-\gamma_1 t) \\ & + \frac{p_2(0)k_1(k_{-2} - \gamma_2) + p_1(0)(\gamma_2 - k_1)(\gamma_2 - k_{-2})}{\gamma_2(\gamma_2 - \gamma_1)} \exp(-\gamma_2 t) + \frac{k_1 k_{-2}}{\gamma_1\gamma_2}(p_2(0) + p_1(0)), \end{aligned} \tag{D4}$$

$$\begin{aligned} p_0(t) = p_2(0) + p_1(0) - p_2(t) - p_1(t) = {} & \frac{p_2(0)k_1k_2 + p_1(0)k_2(k_1 - \gamma_1)}{\gamma_1(\gamma_1 - \gamma_2)} \exp(-\gamma_1 t) \\ & + \frac{p_2(0)k_1k_2 + p_1(0)k_2(k_1 - \gamma_2)}{\gamma_2(\gamma_2 - \gamma_1)} \exp(-\gamma_2 t) + \frac{k_1k_2}{\gamma_1\gamma_2}(p_2(0) + p_1(0)), \end{aligned} \tag{D5}$$

where

$$\gamma_1\gamma_2 = k_{-1}k_{-2} + k_1(k_2 + k_{-2}), \qquad \gamma_1 + \gamma_2 = k_1 + k_{-1} + k_2 + k_{-2}. \tag{D6}$$

The equations can be further simplified by letting $\sum_i p_i(t) = 1$ for all times, with $p_0(0) = 0$. To give an initial delay in the population, the time can be replaced by $t = t' - t_0$. The final fit depends on 6 parameters: initial population $p_2(0)$, time delay t_0 and decay constants k_1, k_{-1}, k_2 and k_{-2} (or equivalently, lifetimes $\tau_i = 1/k_i$).

Figure D1 and Table D1 show fits to the adiabatic populations of unsubstituted BD (from ref. 198) and the values of fit parameters. By excluding certain parameters, their role in the model become more clear. Removing τ_{-1} converges on the fit with all parameters after ∼400 fs, but overestimates the S_2 decay. Conversely, removing τ_{-2} leads to large deviations from the raw data after the S_1 population peak around 150 fs. Excluding both backwards time constants leads the overestimation in S_2 decay at short times and under-estimation of S_1 decay at later times. Notably, the fit parameters are sensitive to the presence/absence of backwards constants, with a 13 fs shift in τ_1 and a 70 fs shift in τ_2.

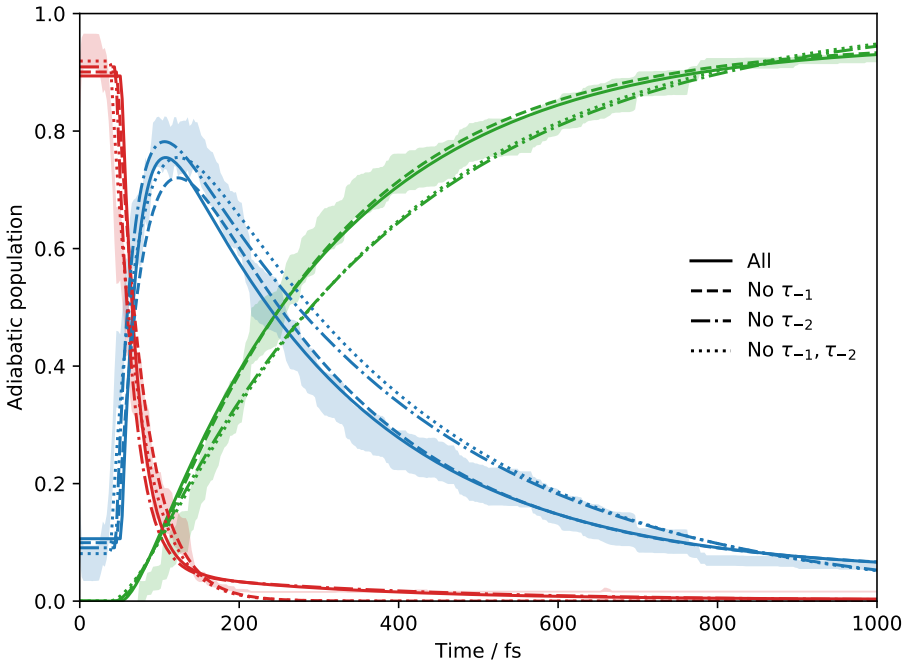

Figure D1: Adiabatic populations of BD[198] with one bootstrap standard deviation from the mean (shaded regions) and fit population functions for the kinetic model above, excluding indicated parameters.

Table D1: Time delays, inital populations, decay constants and their least-squares uncertainties for fits to the adiabatic populations of BD, excluding indicated parameters.

Trials	t_0 / fs	$p_2(0)$	τ_1 / fs	τ_{-1} / fs	τ_2 / fs	τ_{-2} / fs
All	52.2 ± 0.6	0.89 ± 0.01	22.6 ± 0.9	442 ± 25	240 ± 2	4830 ± 120
No τ_{-1}	47.0 ± 0.7	0.90 ± 0.01	35.2 ± 0.7	—	240 ± 2	4594 ± 112
No τ_{-2}	45.1 ± 0.7	0.91 ± 0.01	23.1 ± 0.9	486 ± 27	307 ± 1	—
No τ_{-1}, τ_{-2}	38.5 ± 0.7	0.92 ± 0.01	36.0 ± 0.7	—	313 ± 1	—

D2 Initial condition sampling

To compare initial condition sampling of different vibrational modes for different molecules, the displacement along normal modes was scaled by

$$d_\nu = \sqrt{2\nu} \sum_i Q_{\nu i} \Delta x_i \sqrt{m_i} \tag{D7}$$

where Δx_i is the i-th cartesian coordinate with mass m_i, and $Q_{\nu i}$ is the cartesian-to-normal mode matrix element (*i.e.* the eigenvector matrix of the mass-weighted Hessian) for frequency ν and cartesian coordinate i. Thus, with sufficient sampling each distribution should have a standard deviation of 1, or $d_\nu = 0 \pm 1$.

Given the limited number of initial conditions, the standard deviation of d_ν can vary significantly. Nonetheless, the average d_ν values of C-MeBD and T-MeBD (0.882 and 0.868, respectively) are smaller than those of $^{15}H_2$-BD and $^{15}H_4$-BD (0.935 for both molecules). Modes with particularly tight distributions are shown in Figures D2–D4 below with comparisons to their heavy-H equivalents. The methyl twisting modes of C-MeBD and T-MeBD also had standard deviations of around 0.6–0.7, but do not have equivalent heavy-H modes.

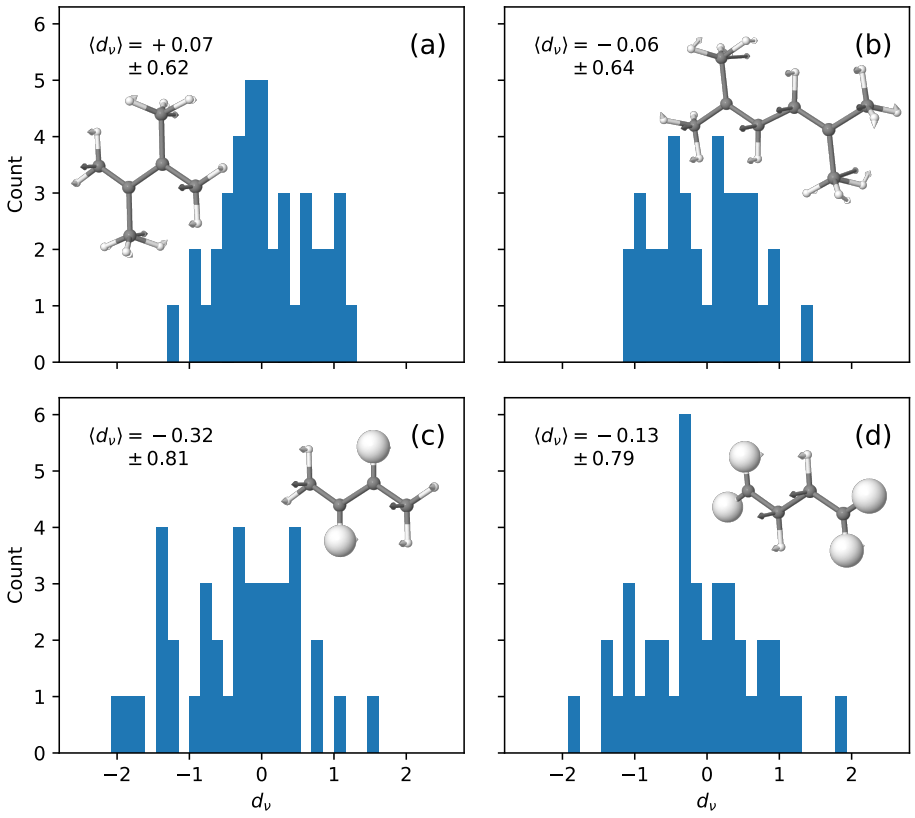

Figure D2: Scaled initial condition distributions along the central C−C torsional normal mode of (a) C-MeBD, (b) T-MeBD, (c) $^{15}H_2$-BD and (d) $^{15}H_4$-BD. Positive values correspond to the direction of the arrows in the inset structures.

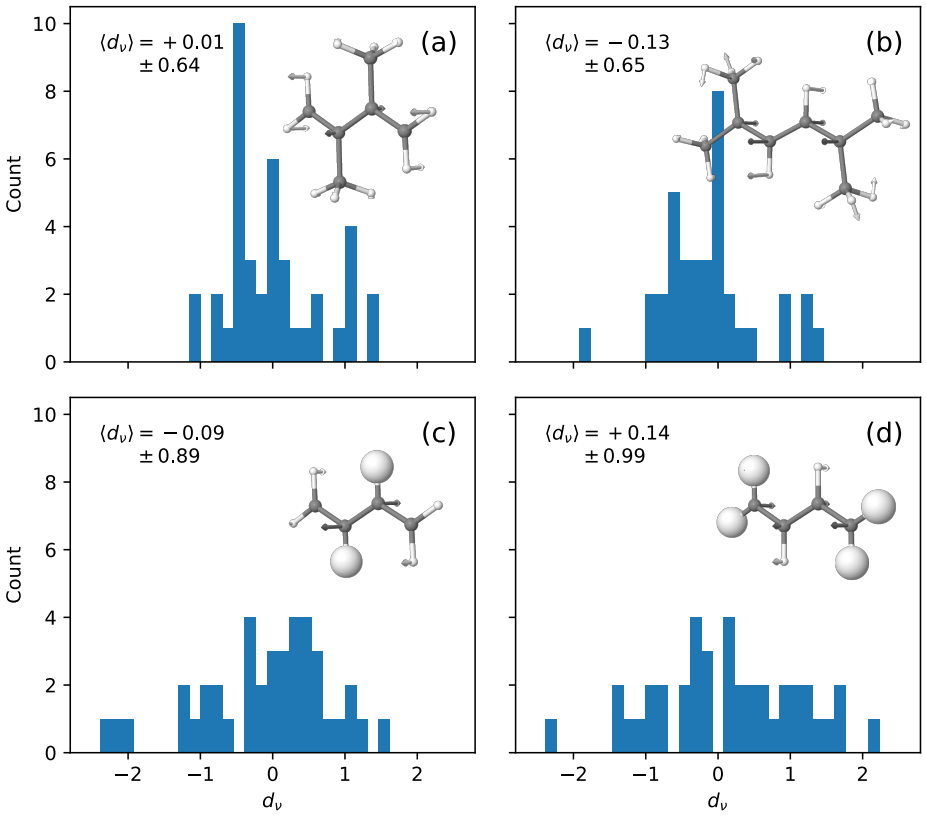

Figure D3: Scaled initial condition distributions along the central-carbon pyramidalization normal mode of (a) C-MeBD, (b) T-MeBD, (c) $^{15}H_2$-BD and (d) $^{15}H_4$-BD. Positive values correspond to the direction of the arrows in the inset structures.

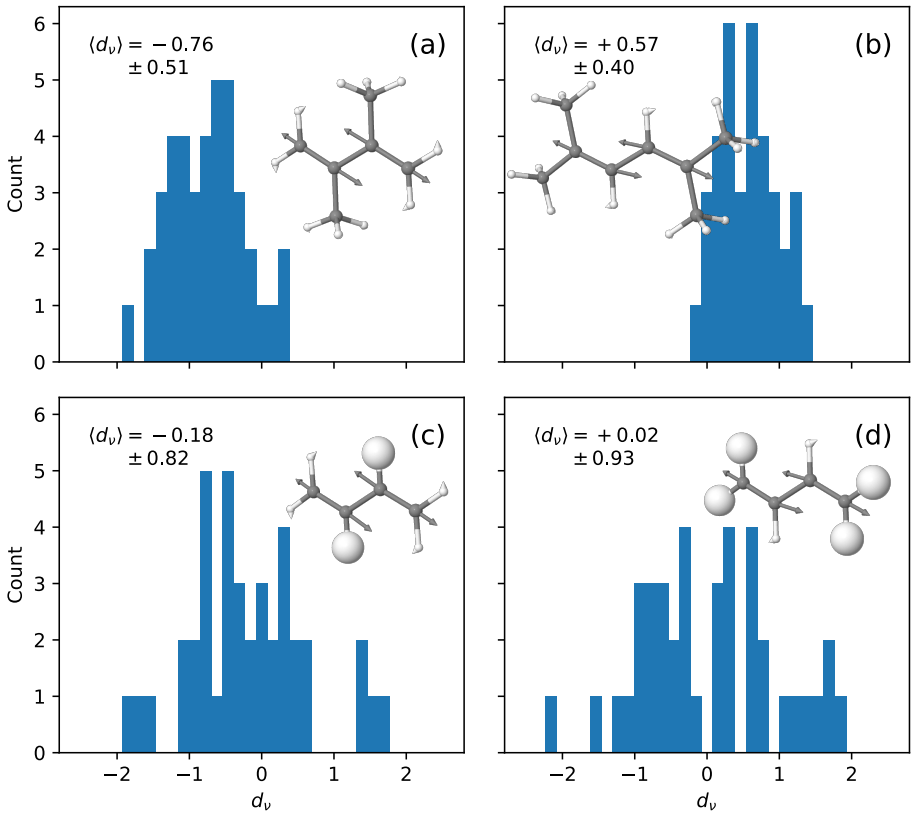

Figure D4: Scaled initial condition distributions along the bond alternation normal mode of (a) C-MeBD, (b) T-MeBD, (c) $^{15}H_2$-BD and (d) $^{15}H_4$-BD. Positive values correspond to the direction of the arrows in the inset structures.

D3 Time-resolved photoelectron spectra

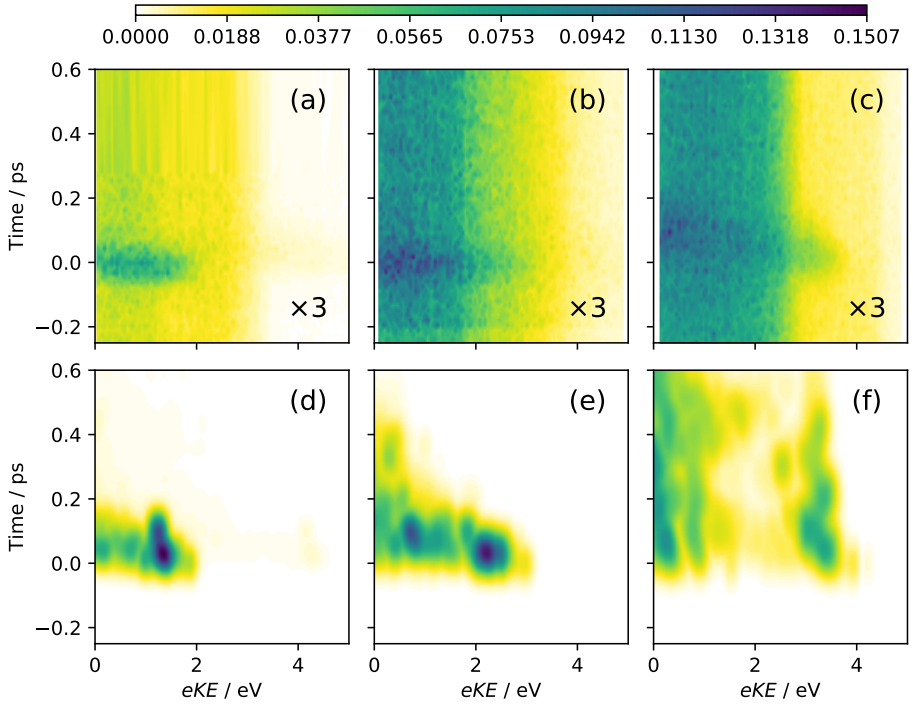

Figure D5: Experimental (a-c) and theoretical (d-f) bootstrap standard deviations of time-resolved photoelectron spectra for BD, C-MeBD and T-MeBD (from left to right, respectively) as a function of electron kinetic energy and pump-probe delay. Experimental values are scaled by a factor of 3.

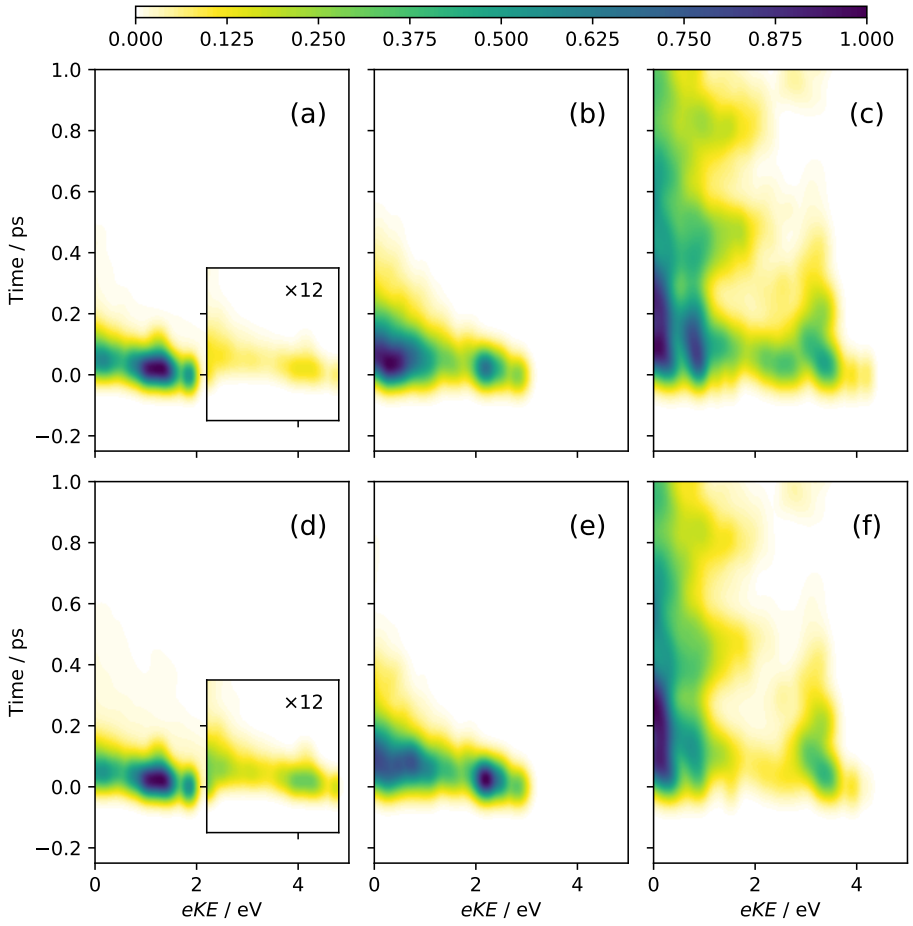

Figure D6: Theoretical time-resolved photoelectron spectra without Dyson orbital weighting (a-c) and with Dyson orbital weighting (d-f) for BD, C-MeBD and T-MeBD (from left to right, respectively) as a function of electron kinetic energy and pump-probe delay. The time range is extended to 1 ps to show the oscillation in the T-MeBD data.

D4 Potential energy surfaces

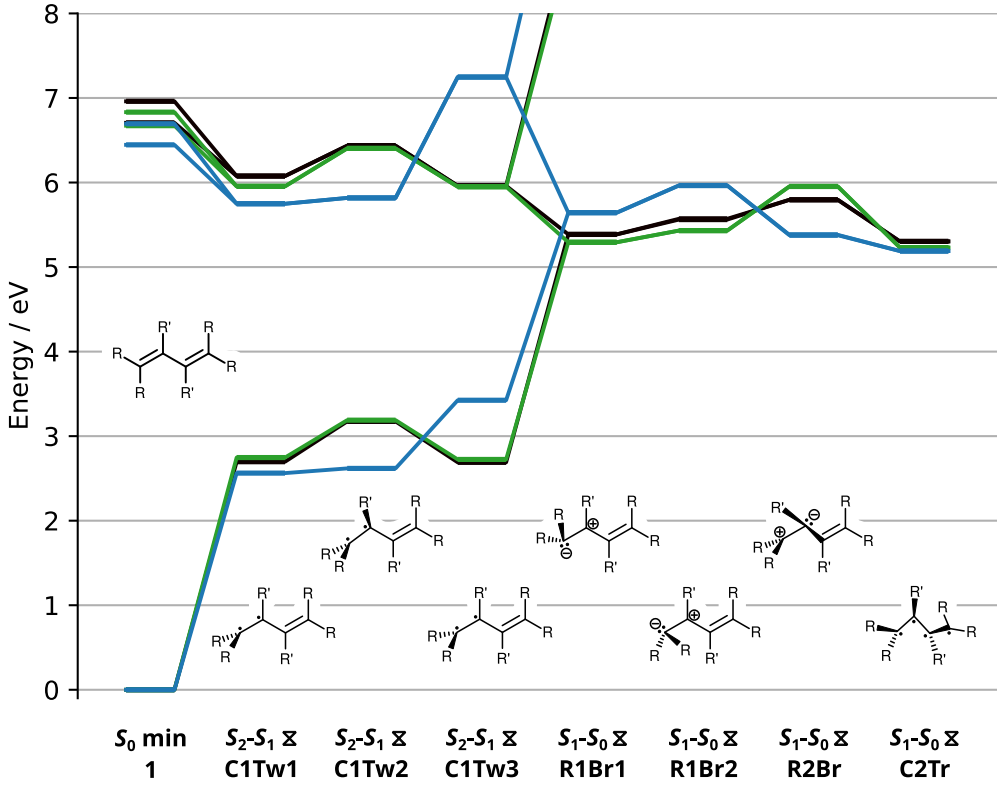

Figure D7: MR-CIS/6-31G* potential energies of BD (black), C-MeBD (green) and T-MeBD (blue).

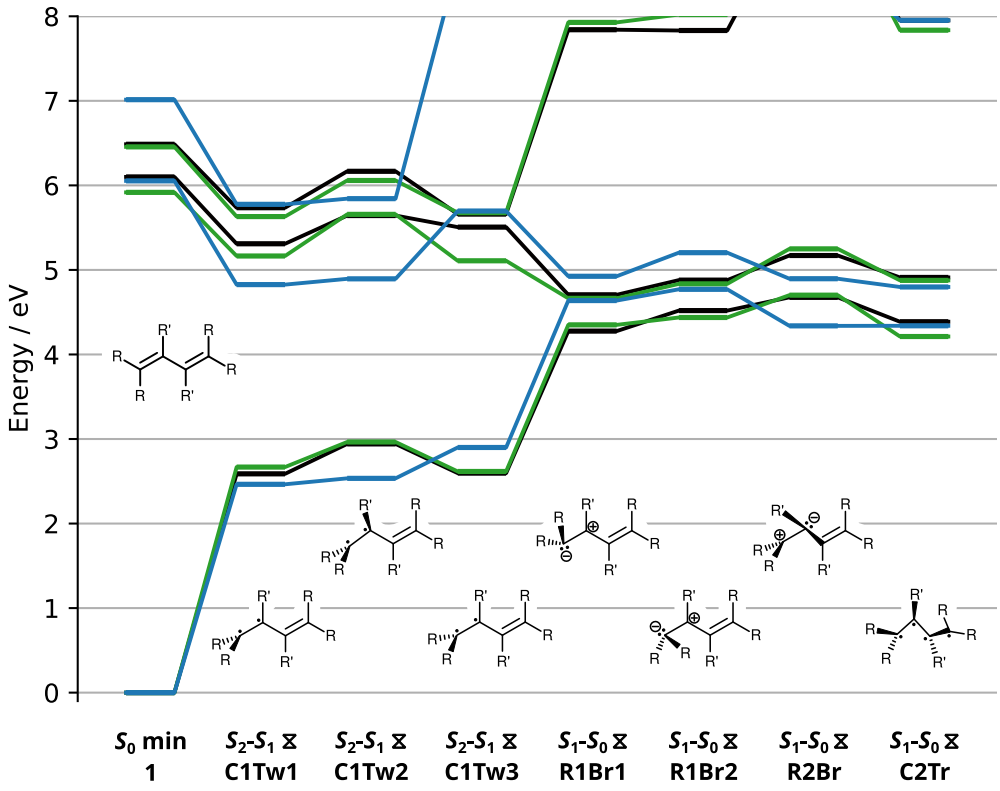

Figure D8: MS-CASPT2/cc-pVTZ potential energies of BD (black), C-MeBD (green) and T-MeBD (blue).

D5 Molecular geometries

Table D2: MR-CIS optimized geometry of the BD S_0 *trans* minimum (**1**).

C	−0.061215	0.255384	−0.048985
C	0.778184	0.905738	0.792956
C	1.704173	0.243114	1.698536
C	2.543572	0.893468	2.540478
H	−0.728595	0.792149	−0.700659
H	−0.088870	−0.821546	−0.094479
H	0.772877	1.986403	0.805882
H	1.709481	−0.837551	1.685611
H	2.571226	1.970398	2.585973

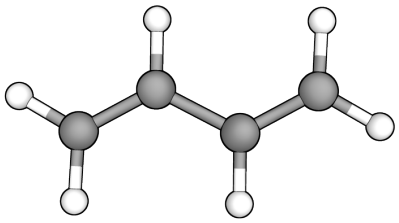

Table D3: MR-CIS optimized geometry of the BD S_2-S_1 C1 twist MECI 1 (**C1Tw1**).

C	−1.771535	−1.246620	−0.023181
C	−1.444413	0.129504	0.018663
C	−0.068024	0.587764	0.028609
C	0.340074	1.965622	−0.005373
H	−2.793232	−1.580530	−0.038327
H	−0.997381	−1.994505	−0.032692
H	−2.223901	0.871766	0.018181
H	0.656683	−0.231675	0.030489
H	0.478275	2.467695	−0.948634

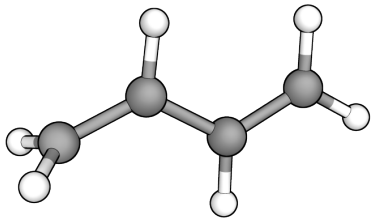

Table D4: MR-CIS optimized geometry of the BD S_2-S_1 C1 twist MECI 2 (**C1Tw2**).

C	1.447207	1.402569	1.056560
C	0.405946	1.179757	0.114504
C	−0.684324	0.247416	0.141261
C	−2.002149	0.472441	−0.259515
H	2.487433	1.473361	0.755386
H	1.288885	1.693567	2.096831
H	0.104853	2.218843	−0.125220
H	−0.409066	−0.774487	0.366534
H	−2.349236	1.455664	−0.532702

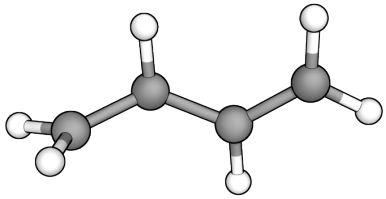

Table D5: MR-CIS optimized geometry of the BD S_2-S_1 C1 twist MECI 3 (**C1Tw3**).

C	−1.831586	−0.525265	0.194469
C	−0.549356	−0.097798	−0.336322
C	0.671398	−0.111266	0.452131
C	1.978019	0.067339	−0.117750
H	−2.165698	−1.542577	0.066945
H	−2.490360	0.161963	0.700317
H	−0.432013	0.155099	−1.386854
H	0.583316	−0.314804	1.505727
H	2.101539	0.232896	−1.173480

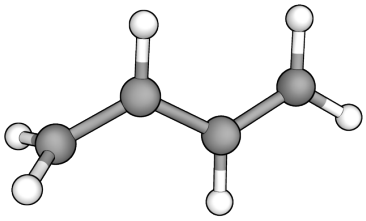

Table D6: MR-CIS optimized geometry of the BD S_1-S_0 H1 bridging MECI 1 (**R1Br1**).

C	1.841822	0.081208	0.057792
C	0.689252	−0.634436	−0.026686
C	−0.601895	0.013296	−0.099864
C	−1.816004	−0.716548	0.021817
H	2.804941	−0.398401	0.083936
H	1.828613	1.158278	0.096778
H	0.686535	−1.710895	−0.041153
H	−0.526662	1.104012	−0.129623
H	−2.674613	−0.198314	−0.418122

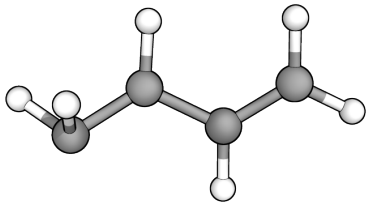

Table D7: MR-CIS optimized geometry of the BD S_1-S_0 H1 bridging MECI 2 (**R1Br2**).

C	1.859253	0.103075	−0.022560
C	0.748132	−0.676460	0.046586
C	−0.577449	−0.077563	0.007071
C	−1.853416	−0.695048	−0.135308
H	2.839597	−0.319624	−0.156861
H	1.788075	1.177231	0.027326
H	0.825900	−1.750959	−0.014039
H	−0.550199	0.996762	0.177030
H	−1.828743	−1.660216	−0.653989

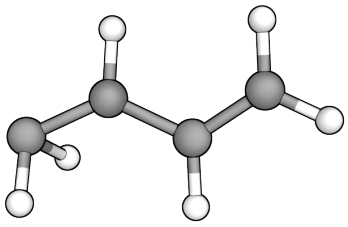

Table D8: MR-CIS optimized geometry of the BD S_1-S_0 H2 bridging MECI (**R2Br**).

C	1.363655	−1.476755	1.033233
C	0.534891	−0.949371	0.036100
C	−0.670060	−0.158282	0.076533
C	−1.952814	−0.537649	−0.176377
H	2.387908	−1.747906	0.815252
H	1.012393	−1.807281	2.008700
H	0.204967	−2.070707	0.266985
H	−0.474465	0.895795	0.220505
H	−2.217818	−1.566881	−0.361516

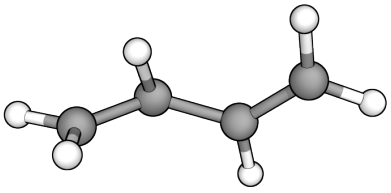

Table D9: MR-CIS optimized geometry of the BD S_1-S_0 C2 transoid MECI (**C2Tr**).

C	1.311740	−0.522258	0.966044
C	0.385161	−0.489594	−0.176401
C	−0.147032	0.757933	−0.623599
C	−1.486348	0.287422	−0.307643
H	2.173392	0.123071	0.955778
H	1.011290	−0.939779	1.911243
H	0.143552	−1.388069	−0.717179
H	0.236749	1.687881	−0.240237
H	−1.988066	−0.424395	−0.939287

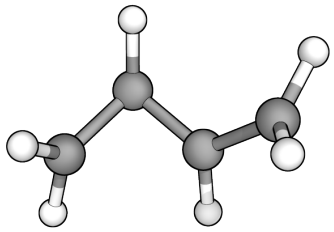

Table D10: MR-CIS optimized geometry of the C-MeBD S_0 *trans* minimum (**1**).

C	−1.733535	0.666608	0.000000
C	−0.374990	0.635314	0.000000
C	0.398792	1.940482	0.000000
C	−0.398791	−1.940483	0.000000
C	0.374990	−0.635314	0.000000
C	1.733534	−0.666606	0.000000
H	−2.263478	1.603937	0.000000
H	−2.335167	−0.224135	0.000000
H	−0.279543	2.785737	0.000000
H	1.033608	2.021889	0.876147
H	1.033608	2.021889	−0.876147
H	−1.033607	−2.021891	−0.876147
H	−1.033607	−2.021891	0.876147
H	0.279545	−2.785738	0.000000
H	2.335164	0.224138	0.000000

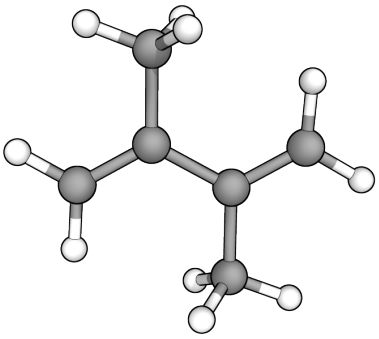

Table D11: MR-CIS optimized geometry of the C-MeBD S_2-S_1 C1 twist MECI 1 (**C1Tw1**).

C	0.310395	1.955047	0.008751
C	−0.055651	0.548624	0.002125
C	1.014905	−0.525587	−0.005454
C	−2.535811	1.179964	0.006896
C	−1.458359	0.125511	0.002640
C	−1.835803	−1.251474	−0.001986
H	0.412419	2.499346	−0.915558
H	0.413963	2.490645	0.937930
H	1.991586	−0.063879	−0.011255
H	0.941286	−1.167698	0.871148
H	0.930246	−1.168147	−0.880480
H	−2.453796	1.817257	−0.867003
H	−2.438366	1.826163	0.872405
H	−3.522864	0.730193	0.017352
H	−1.112083	−2.043910	−0.006967

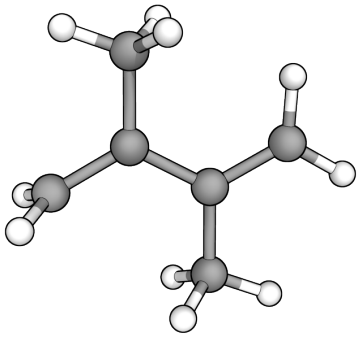

Table D12: MR-CIS optimized geometry of the C-MeBD S_2-S_1 C1 twist MECI 2 (**C1Tw2**).

C	1.422748	−1.258067	1.022367
C	0.372585	−1.220156	0.061318
C	−0.016020	−2.705434	−0.159547
C	−0.274156	1.147933	0.531860
C	−0.685353	−0.243394	0.094312
C	−1.991199	−0.449888	−0.344198
H	2.473279	−1.255260	0.745424
H	1.272832	−1.462864	2.086527
H	0.820625	−3.395290	−0.077023
H	−0.789475	−3.027469	0.538221
H	−0.397383	−2.799577	−1.171022
H	0.346321	1.633039	−0.215605
H	0.314064	1.104940	1.453047
H	−1.135016	1.779597	0.717567
H	−2.326585	−1.393429	−0.737734

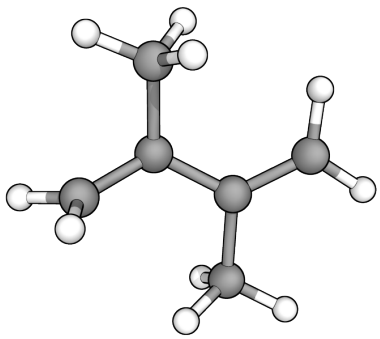

Table D13: MR-CIS optimized geometry of the C-MeBD S_2-S_1 C1 twist MECI 3 (**C1Tw3**).

C	−1.816796	−0.509479	0.192382
C	−0.535211	−0.119181	−0.357814
C	−0.423803	0.255506	−1.823346
C	0.565995	−0.463565	1.925205
C	0.679857	−0.133810	0.457209
C	1.964876	0.108942	−0.094178
H	−2.155050	−1.529914	0.114030
H	−2.422171	0.194661	0.738703
H	−1.401670	0.527105	−2.195372
H	0.264698	1.077082	−2.001641
H	−0.074115	−0.597594	−2.404745
H	0.294232	−1.504776	2.062920
H	−0.212734	0.125981	2.393959
H	1.504802	−0.283195	2.438254
H	2.120580	0.263997	−1.144745

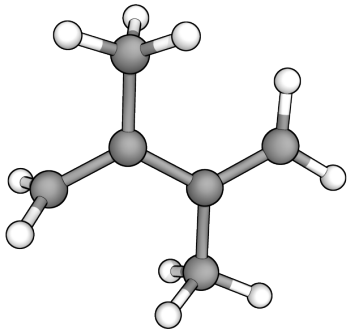

Table D14: MR-CIS optimized geometry of the C-MeBD S_1-S_0 H1 bridging MECI 1 (**R1Br1**).

C	−1.763944	−0.737219	0.102109
C	−0.572392	0.052097	−0.020369
C	−0.550505	1.573071	−0.078192
C	0.713633	−2.162070	−0.069557
C	0.722579	−0.651434	0.006378
C	1.895337	0.034885	0.107489
H	−2.625497	−0.223757	−0.348148
H	−1.822479	−0.050249	1.048960
H	−1.562100	1.952207	−0.040839
H	0.020776	2.024904	0.725643
H	−0.105144	1.883895	−1.018399
H	0.091437	−2.494274	−0.888521
H	0.292208	−2.588262	0.829878
H	1.723751	−2.536319	−0.204297
H	1.943000	1.105904	0.175546

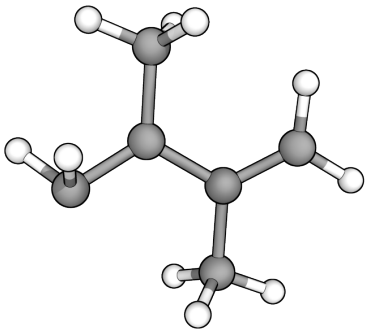

Table D15: MR-CIS optimized geometry of the C-MeBD S_1-S_0 H1 bridging MECI 2 (**R1Br2**).

C	−1.780912	0.624006	−0.350514
C	−0.519384	0.007236	−0.040691
C	−0.584794	−1.488943	0.122052
C	0.848310	2.182551	0.182972
C	0.807737	0.676604	0.034779
C	1.961078	−0.024868	−0.119418
H	−1.780014	1.637290	0.091283
H	−1.161933	1.037010	−1.250005
H	−1.360663	−1.657049	0.860114
H	0.324173	−1.996942	0.412515
H	−0.967984	−1.902596	−0.801972
H	0.428085	2.671134	−0.687500
H	0.272187	2.499998	1.043631
H	1.869130	2.524457	0.306236
H	1.984679	−1.088164	−0.261456

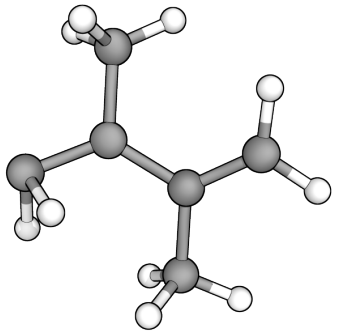

Table D16: MR-CIS optimized geometry of the C-MeBD S_1-S_0 R2 bridging MECI (**R2Br**).

C	1.314913	−1.350032	1.040346
C	0.397809	−1.009278	0.051842
C	−0.052683	−2.600906	0.323964
C	−0.354941	1.348214	0.292664
C	−0.731422	−0.115444	0.070144
C	−2.037966	−0.428182	−0.175903
H	1.050162	−1.564950	2.075107
H	2.352811	−1.556689	0.810313
H	0.702313	−3.374007	0.400963
H	−0.787291	−2.700509	1.112310
H	−0.492401	−2.712427	−0.660074
H	0.709204	1.466354	0.464604
H	−0.882324	1.750764	1.151572
H	−0.614883	1.950659	−0.570871
H	−2.378798	−1.433663	−0.354765

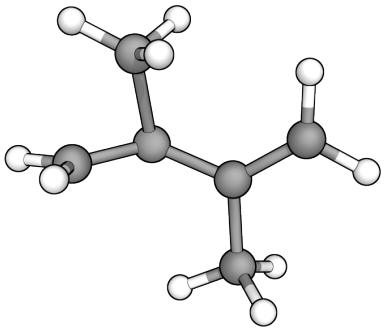

Table D17: MR-CIS optimized geometry of the C-MeBD S_1-S_0 C2 transoid MECI (**C2Tr**).

C	−1.514857	0.340421	−0.181918
C	−0.169218	0.763330	−0.533253
C	0.406774	2.100536	−0.173946
C	0.133659	−1.770440	−0.997856
C	0.332914	−0.529769	−0.157260
C	1.252356	−0.590278	0.991915
H	−1.933313	0.629599	0.769551
H	−2.104345	−0.299996	−0.810424
H	−0.053584	2.865543	−0.792470
H	0.218352	2.373655	0.863444
H	1.478917	2.132163	−0.339794
H	−0.551439	−1.600635	−1.820103
H	−0.227410	−2.606379	−0.407159
H	1.094391	−2.061307	−1.417381
H	2.088051	0.084680	1.048419

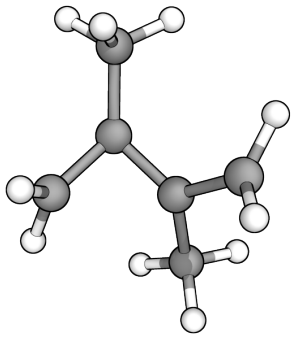

Table D18: MR-CIS optimized geometry of the T-MeBD S_0 *trans* minimum (**1**).

C	−3.073692	−0.836305	0.000000
C	−1.151097	−2.501742	0.000000
C	−1.575896	−1.050180	0.000000
C	−0.727241	0.016950	0.000000
C	0.727239	−0.016949	0.000000
C	1.575896	1.050181	0.000000
C	1.151098	2.501743	0.000000
C	3.073692	0.836303	0.000000
H	−3.331957	0.217109	0.000000
H	−3.529615	−1.293757	0.874364
H	−3.529615	−1.293757	−0.874364
H	−0.078095	−2.637333	0.000000
H	−1.549296	−3.010186	0.874102
H	−1.549296	−3.010186	−0.874103
H	−1.190036	0.990629	0.000000
H	1.190034	−0.990628	0.000000
H	1.549298	3.010187	0.874102
H	1.549298	3.010186	−0.874103
H	0.078097	2.637335	0.000000
H	3.529615	1.293755	0.874364
H	3.529615	1.293755	−0.874364

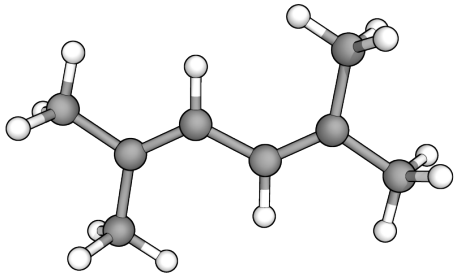

Table D19: MR-CIS optimized geometry of the T-MeBD S_2-S_1 C1 twist MECI 1 (**C1Tw1**).

C	0.344670	2.573592	−1.323234
C	0.550737	2.886141	1.224778
C	0.295440	1.977643	0.056583
C	−0.001151	0.581555	0.280896
C	−1.342772	0.083038	0.165734
C	−1.738718	−1.263102	−0.044540
C	−0.733048	−2.379768	−0.129042
C	−3.197350	−1.618964	−0.153537
H	0.111391	1.837502	−2.081584
H	1.333708	2.986494	−1.528378
H	−0.358347	3.402588	−1.414038
H	1.295031	2.452830	1.890016
H	0.881738	3.874434	0.921846
H	−0.358838	2.994981	1.816963
H	0.821234	−0.112932	0.411099
H	−2.128549	0.825728	0.179966
H	−0.432669	−2.741616	0.855172
H	−1.139040	−3.230363	−0.670063
H	0.173178	−2.064875	−0.641688
H	−3.506762	−2.293780	0.645155
H	−3.417117	−2.127387	−1.092197

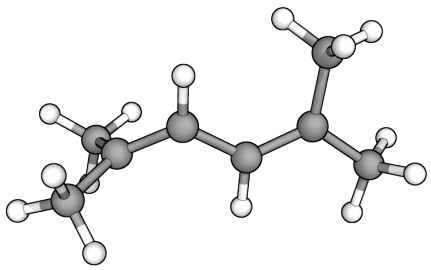

Table D20: MR-CIS optimized geometry of the T-MeBD S_2-S_1 C1 twist MECI 2 (**C1Tw2**).

C	2.846034	−1.280445	0.583955
C	1.240156	−1.692008	2.561718
C	1.446918	−1.529150	1.076239
C	0.322270	−1.593098	0.173796
C	−0.595221	−0.489270	0.077585
C	−1.949127	−0.518829	−0.344114
C	−2.627677	−1.771069	−0.833579
C	−2.811923	0.707196	−0.202994
H	2.908948	−1.375121	−0.493278
H	3.553315	−1.970473	1.042741
H	3.177694	−0.274082	0.850017
H	0.809253	−2.668370	2.783556
H	2.171024	−1.599058	3.112084
H	0.540798	−0.953327	2.946540
H	0.071033	−2.541494	−0.287345
H	−0.231566	0.454057	0.460489
H	−3.182795	−2.263908	−0.033246
H	−3.344306	−1.538724	−1.617436
H	−1.930620	−2.495102	−1.238964
H	−3.643734	0.534092	0.481138
H	−3.249969	0.997835	−1.157161

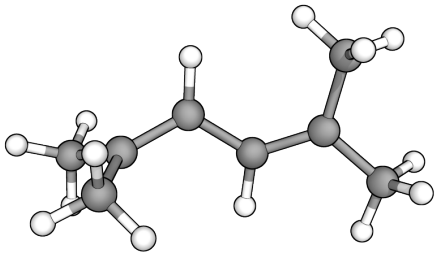

Table D21: MR-CIS optimized geometry of the T-MeBD S_2-S_1 C1 twist MECI 3 (**C1Tw3**).

C	−2.375777	−1.914873	−0.299587
C	−2.854328	0.571810	0.557418
C	−1.963484	−0.511609	0.028954
C	−0.520860	−0.053638	−0.495435
C	0.649559	−0.104575	0.299635
C	1.894294	0.265657	−0.091387
C	2.279450	0.805705	−1.440597
C	3.044166	0.149764	0.868662
H	−1.616390	−2.665036	−0.047582
H	−2.631638	−2.108283	−1.356376
H	−3.258405	−2.189581	0.274628
H	−3.283128	1.255246	−0.196537
H	−3.703126	0.136266	1.080706
H	−2.363227	1.225131	1.288581
H	−0.376685	0.326276	−1.513312
H	0.512400	−0.476075	1.300932
H	2.724089	1.788505	−1.313121
H	3.045439	0.167553	−1.871489
H	1.461656	0.883694	−2.136616
H	3.505435	1.123081	1.010924
H	3.806077	−0.504201	0.453600

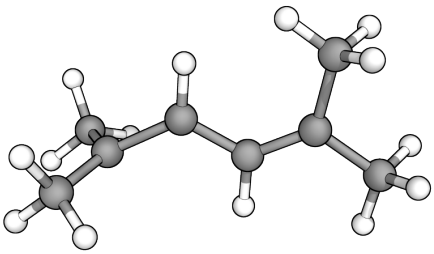

Table D22: MR-CIS optimized geometry of the T-MeBD S_1-S_0 R1 bridging MECI 1 (**R1Br1**).

C	−2.973582	−0.070295	−1.170154
C	−2.125729	0.294385	1.250606
C	−1.802581	−0.550360	−0.333714
C	−0.599109	0.195328	−0.307776
C	0.690829	−0.436954	−0.123059
C	1.869021	0.170902	0.074551
C	2.082903	1.658622	0.193896
C	3.133478	−0.641929	0.189801
H	−2.845393	−0.443028	−2.182335
H	−3.082059	1.018926	−1.233589
H	−3.909670	−0.473248	−0.799032
H	−1.343853	0.167141	1.985270
H	−2.405534	1.335921	1.131305
H	−2.968776	−0.341347	1.484044
H	−0.608085	1.285238	−0.334532
H	0.662110	−1.511877	−0.168807
H	2.630836	1.880936	1.105977
H	2.691874	2.014745	−0.633536
H	1.166561	2.229915	0.206543
H	3.607354	−0.475859	1.154469
H	3.850972	−0.341933	−0.570334

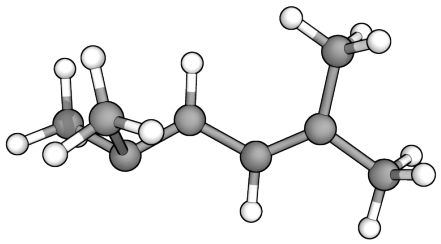

Table D23: MR-CIS optimized geometry of the T-MeBD S_1-S_0 R1 bridging MECI 2 (**R1Br2**).

C	−1.764731	−2.111264	−1.212394
C	−1.438250	−1.451937	1.203752
C	−1.743280	−0.859713	−0.350238
C	−0.549163	−0.139478	−0.070050
C	0.816150	−0.626805	0.031241
C	1.918660	0.186277	0.083310
C	1.908351	1.656479	0.432773
C	3.285773	−0.369774	−0.236511
H	−1.798017	−1.817713	−2.257900
H	−2.674536	−2.671369	−1.020463
H	−0.929632	−2.813021	−1.094014
H	−1.260318	−0.739287	2.001131
H	−2.461012	−1.791146	1.329722
H	−0.730757	−2.272828	1.285222
H	−0.644616	0.926440	0.093342
H	0.978898	−1.667520	−0.194850
H	2.621116	1.839650	1.231428
H	2.225829	2.249680	−0.420541
H	0.946367	2.022555	0.761400
H	3.954955	−0.240321	0.609784
H	3.726044	0.161191	−1.076628

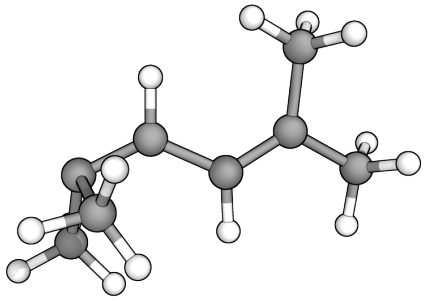

Table D24: MR-CIS optimized geometry of the T-MeBD S_1-S_0 H2 bridging MECI (**R2Br**).

C	−2.999820	0.524788	−0.183729
C	−2.494617	−1.944014	−0.609126
C	−1.976894	−0.588051	−0.190403
C	−0.667063	−0.333685	0.087224
C	0.524712	−1.172953	−0.043009
C	1.383652	−1.555907	1.009762
C	0.936912	−1.897968	2.414397
C	2.852706	−1.761917	0.761029
H	−2.561749	1.470640	0.120227
H	−3.821704	0.306336	0.496601
H	−3.439031	0.669440	−1.170027
H	−1.794344	−2.745527	−0.392562
H	−3.425978	−2.181733	−0.099099
H	−2.699153	−1.977970	−1.678034
H	−0.415859	0.689473	0.335532
H	0.157601	−2.238575	0.251082
H	1.241655	−2.897366	2.711958
H	1.431292	−1.201115	3.088072
H	−0.132455	−1.787174	2.528413
H	3.203820	−2.720604	1.128917
H	3.381626	−0.991553	1.322429

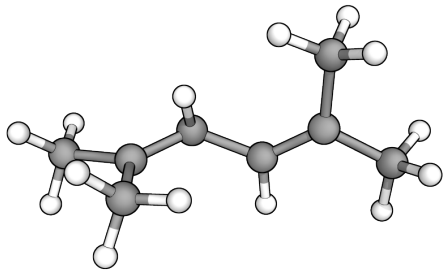

Table D25: MR-CIS optimized geometry of the T-MeBD S_1-S_0 C2 transoid MECI (**C2Tr**).

C	−2.259759	0.678716	0.931746
C	−2.275627	−0.666432	−1.273125
C	−1.516955	0.170147	−0.276705
C	−0.185642	0.699386	−0.594100
C	0.407796	−0.493414	−0.105758
C	1.411852	−0.517476	0.989822
C	2.569519	0.442163	0.940684
C	1.024166	−1.116700	2.313792
H	−1.588837	1.136153	1.650695
H	−2.803890	−0.116549	1.436746
H	−2.992015	1.433921	0.642922
H	−1.608443	−1.176486	−1.960444
H	−2.901706	−1.410698	−0.788302
H	−2.927086	−0.032955	−1.875759
H	0.142833	1.658182	−0.226960
H	0.179515	−1.421387	−0.604924
H	2.342024	1.382209	1.447503
H	3.438794	0.019799	1.436826
H	2.848654	0.681879	−0.079721
H	0.452696	−0.413822	2.922859
H	1.902862	−1.396785	2.887865

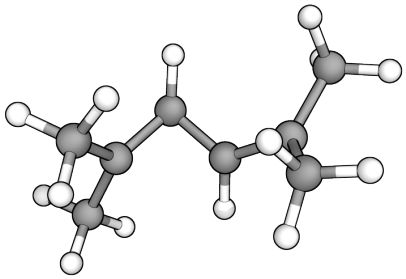

Appendix E
Supporting information — Characterization of partial atomic charges of electronically excited states (Chapter 6)

E1 Spherically averaged atomic densities

Due to the degeneracy of atomic orbitals with like angular momentum l, there are a wide range of asymmetric solutions for the electron density of an atom which give the same energy. In the absence of interactions to break the spherical symmetry (as assumed for atomic components of the promolecular density), the wavefunction is a state or superposition of states that is spherically symmetric. It can be shown that the radial density of a spherically symmetric atomic wavefunction is the same as an asymmetric density integrated over the angular components.

To store ab initio radial densities, we note that the total density is given by

$$\rho_{tot} = \mathrm{Tr}(\mathbf{DS}) = \sum_{ij} D_{ij} S_{ij} = \sum_{ij} D_{ij} A_{ij} R_{ij}, \tag{E1}$$

where $\mathbf{D}$ is the one-electron reduced density matrix (1-RDM), $\mathbf{S}$ is the overlap matrix, $\mathbf{A}$ is the angular overlap matrix and $\mathbf{R}$ is the radial overlap matrix. Given the angular overlaps, the 1-RDM can be reduced to a purely radial form with only $N_{shell} \times N_{shell}$ terms

$$D'_{R,ij} = D_{ij} A_{ij}, \tag{E2}$$

$$\mathbf{D}_R = \mathbf{T}^T \mathbf{D}'_R \mathbf{T}, \tag{E3}$$

where $\mathbf{T}$ is an $N_{basis} \times N_{shell}$ matrix which sums over all basis functions in the same shell.

Given a cartesian atomic orbital basis of the form

$$\psi_i(x,y,z) = N_i x^{a_i} y^{b_i} z^{c_i} \sum_j c_{ij} \exp\left(-\zeta_{ij}(x^2+y^2+z^2)\right), \tag{E4}$$

where x, y and z are cartesian distances from the atom centre, a_i, b_i and c_i are their respective exponents, c_{ij} are contraction coefficients and ζ_{ij} are primitive exponents of the Gaussian basis. The elements of $\mathbf{A}$ for the cartesian basis are then given by

$$A_{ij} = N_i N_j \int_0^{2\pi} \mathrm{d}\theta \, \cos^{a_i+a_j}\theta \sin^{b_i+b_j}\theta \int_0^{\pi} \mathrm{d}\phi \, \sin^{1+a_i+a_j+b_i+b_j}\phi \cos^{c_i+c_j}\phi, \tag{E5}$$

where N_i and N_j satisfy $A_{ii} = 1$. Integration yields zero if $x_i + x_j$ is odd for $x \in a, b, c$, otherwise

$$A_{ij} = \frac{\sqrt{(2l_i+1)!!(2l_j+1)!!}}{(l_i+l_j+1)!!} \prod_x \frac{(x_i+x_j-1)!!}{\sqrt{(2x_i-1)!!(2x_j-1)!!}}, \tag{E6}$$

$$l_i = \sum_x x_i = a_i + b_i + c_i. \tag{E7}$$

Thus, $\mathbf{A}$ can be used to calculate $\mathbf{D}_R$ from Equation E3, and the radial wavefunction $\psi_l(r)$ and

density $\rho(r)$ at radial distance $r = \sqrt{x^2 + y^2 + z^2}$ are given by

$$\psi_l(r) = \frac{r^l}{\sqrt{2l+1}} \sum_j c_{lj} \exp(-\zeta_{lj} r^2), \tag{E8}$$

$$\rho(r) = \sum_{kl} D_{R,kl} \psi_k(r) \psi_l(r). \tag{E9}$$

E2 Example partial charge calculations

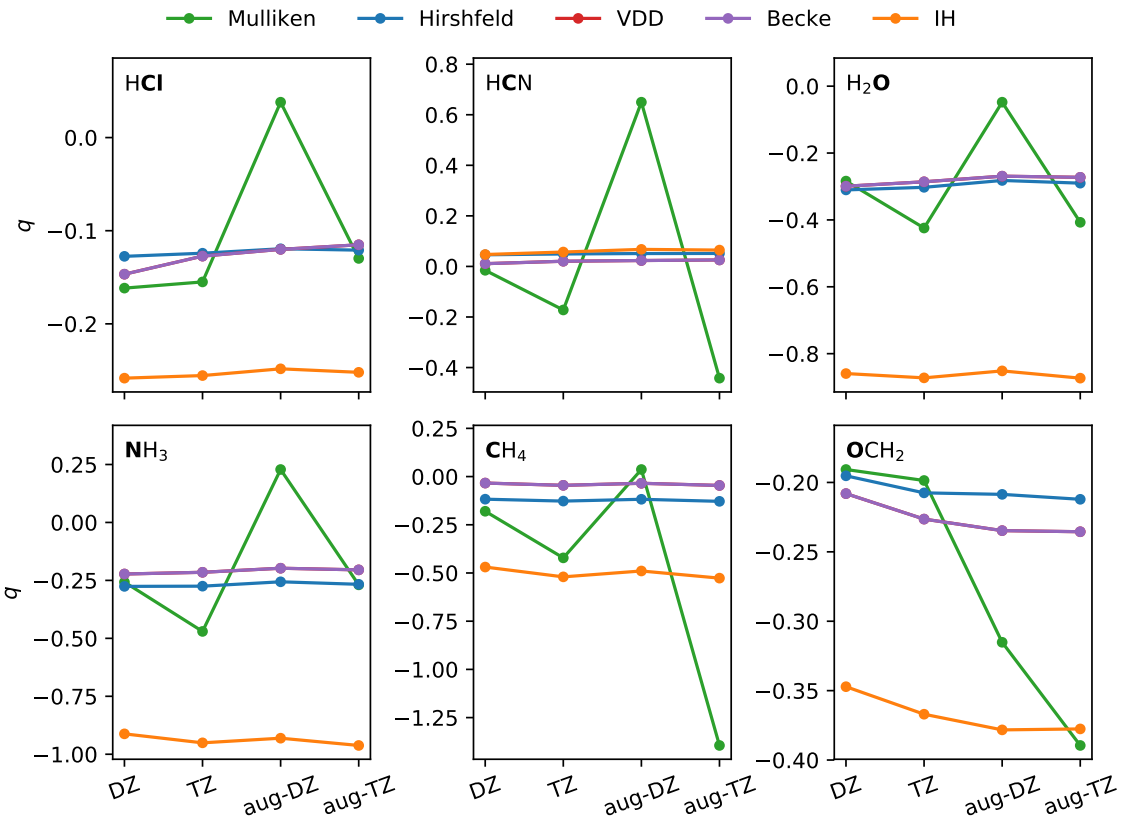

Figure E1: Partial charges of atoms (shown in bold) with increasing basis set size. Basis labels correspond to Dunning basis sets (cc-pV*).

E3 B-TCNE optimized geometries

Table E1: RI-MP2/cc-pVDZ optimized geometry of the B-TCNE parallel conformer.

C	1.0000000000	1.4040633832	1.8493301258
C	1.2197368544	0.7021233104	1.8561422595
C	1.2197368544	−0.7021233104	1.8561422595
C	0.0000000000	−1.4040633832	1.8493301258
C	−1.2197368544	−0.7021233104	1.8561422595
C	−1.2197368544	0.7021233104	1.8561422595
H	2.1660545174	1.2513015032	1.8577501554
H	0.0000000000	2.4990849330	1.8518337101
H	−2.1660545174	1.2513015032	1.8577501554
H	−2.1660545174	−1.2513015032	1.8577501554
H	0.0000000000	−2.4990849330	1.8518337101
H	2.1660545174	−1.2513015032	1.8577501554
C	0.0000000000	0.6904506291	−1.1697854202
C	0.0000000000	−0.6904506291	−1.1697854202
C	1.2314008601	1.4268422850	−1.2069454010
C	−1.2314008601	1.4268422850	−1.2069454010
C	−1.2314008601	−1.4268422850	−1.2069454010
C	1.2314008601	−1.4268422850	−1.2069454010
N	−2.2459005156	2.0470839090	−1.2611267878
N	−2.2459005156	−2.0470839090	−1.2611267878
N	2.2459005156	−2.0470839090	−1.2611267878
N	2.2459005156	2.0470839090	−1.2611267878

Table E2: RI-MP2/cc-pVDZ optimized geometry of the B-TCNE perpendicular conformer.

C	−1.4076730501	0.0000000000	−1.8558029762
C	−0.7038691863	−1.2166816375	−1.8573170043
C	0.7038691863	−1.2166816375	−1.8573170043
C	1.4076730501	0.0000000000	−1.8558029762
C	0.7038691863	1.2166816375	−1.8573170043
C	−0.7038691863	1.2166816375	−1.8573170043
H	−1.2524695502	−2.1637363787	−1.8633247472
H	−2.5019811575	0.0000000000	−1.8546607995
H	−1.2524695502	2.1637363787	−1.8633247472
H	1.2524695502	2.1637363787	−1.8633247472
H	2.5019811575	0.0000000000	−1.8546607995
H	1.2524695502	−2.1637363787	−1.8633247472
C	0.0000000000	0.6902938444	1.1741729407
C	0.0000000000	−0.6902938444	1.1741729407
C	−1.2321386545	1.4254549796	1.2107417227
C	1.2321386545	1.4254549796	1.2107417227
C	1.2321386545	−1.4254549796	1.2107417227
C	−1.2321386545	−1.4254549796	1.2107417227
N	2.2481732506	2.0431132417	1.2665360124
N	2.2481732506	−2.0431132417	1.2665360124
N	−2.2481732506	−2.0431132417	1.2665360124
N	−2.2481732506	2.0431132417	1.2665360124

E4 Polyene electronic structure details

Table E3: Basis set, active space and CASSCF state-averaging for MR-CIS calculations of polyenes. ET: ethylene; BD: 1,3-butadiene; HT: 1,3,5-hexatriene; CHD: 1,3-cyclohexadiene; Am: amino; CN: cyano; 3s: diffuse s-type Rydberg orbital; CAS: complete active space.

Molecule	Basis set	CAS electrons	CAS orbitals	Number of states
ET	6-31G* + 3s(X)	2	3	5
VAm	6-31G* + 3s(N)	4	4	8
VCN	6-31G*	6	6	5
BD	6-31G*	4	4	3
1-AmBD	6-31G*	4	4	3
2-AmBD	6-31G*	4	4	3
1-CNBD	6-31G*	6	6	5
2-CNBD	6-31G*	6	6	5
HT	6-31G*	6	6	3
1-AmHT	6-31G*	6	6	3
2-AmHT	6-31G*	6	6	3
3-AmHT	6-31G*	6	6	3
1-CNHT	6-31G*	6	6	3
2-CNHT	6-31G*	6	6	3
3-CNHT	6-31G*	6	6	3

E5 Polyene potential energies

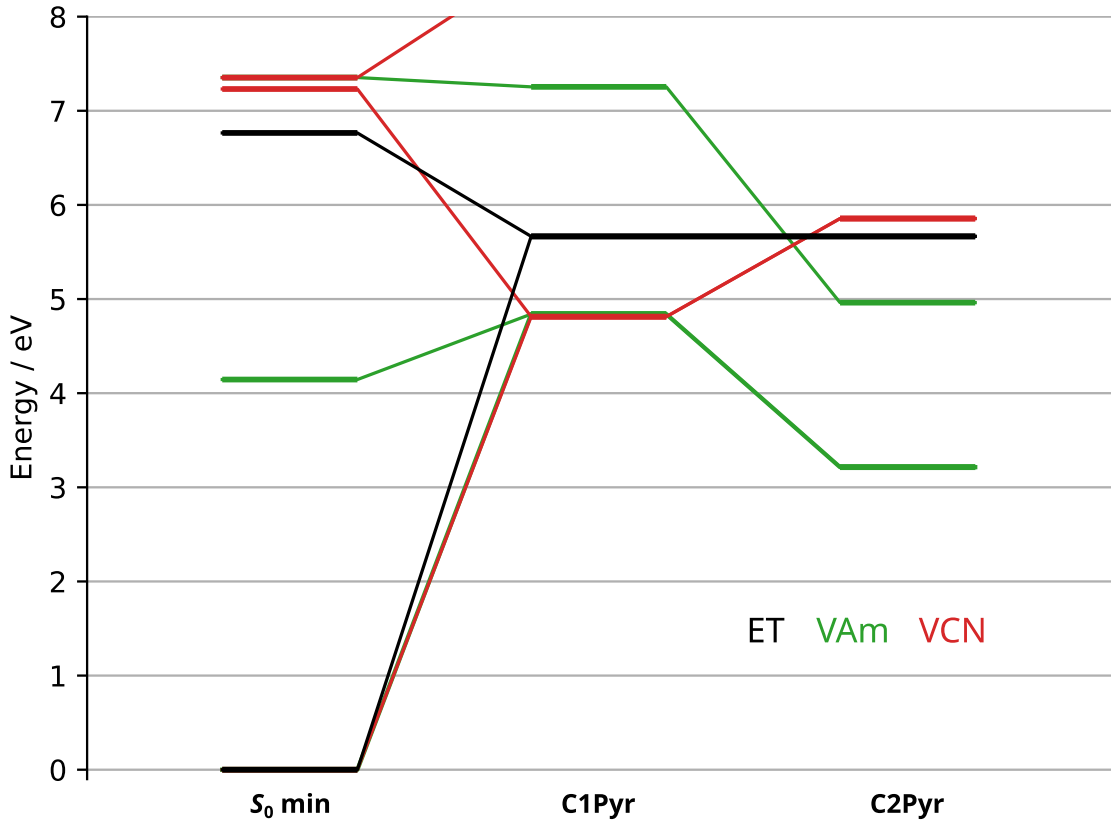

Figure E2: MR-CIS/6-31G* potential energies of ET (black), VAm (green) and VCN (red).

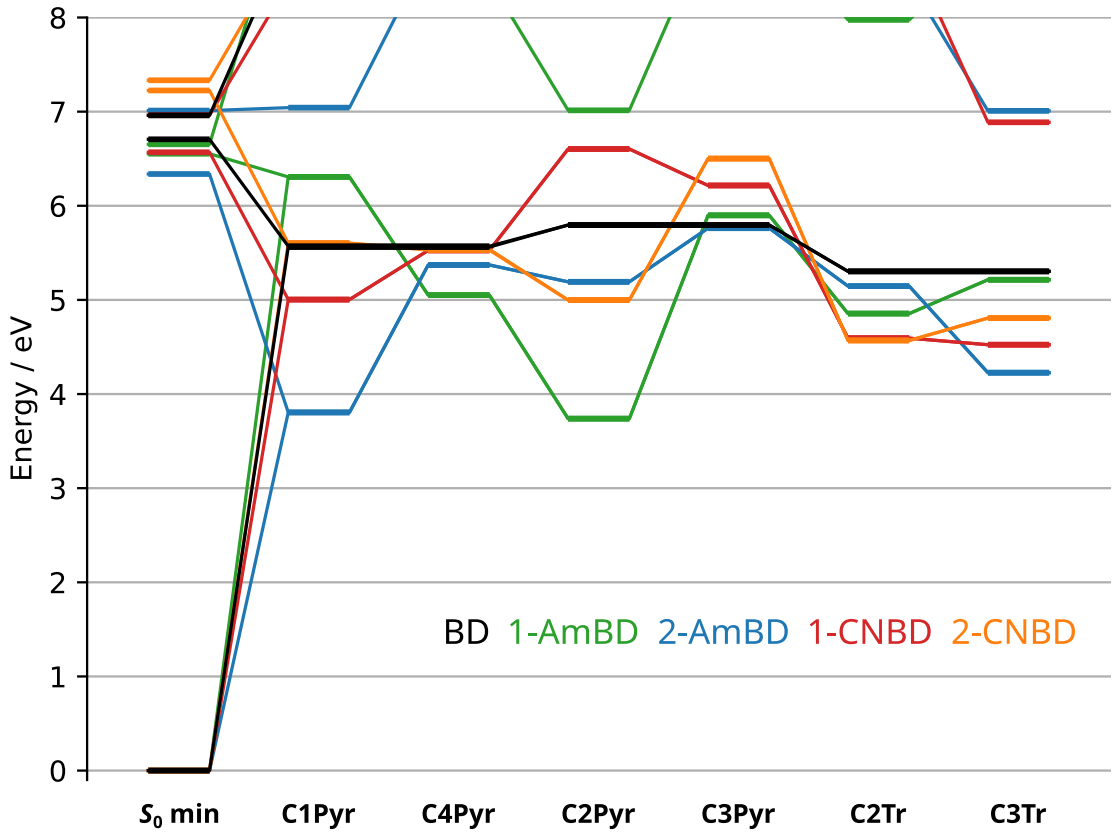

Figure E3: MR-CIS/6-31G* potential energies of BD (black), 1-AmBD (green), 2-AmBD (blue), 1-CNBD (red) and 2-CNBD (orange).

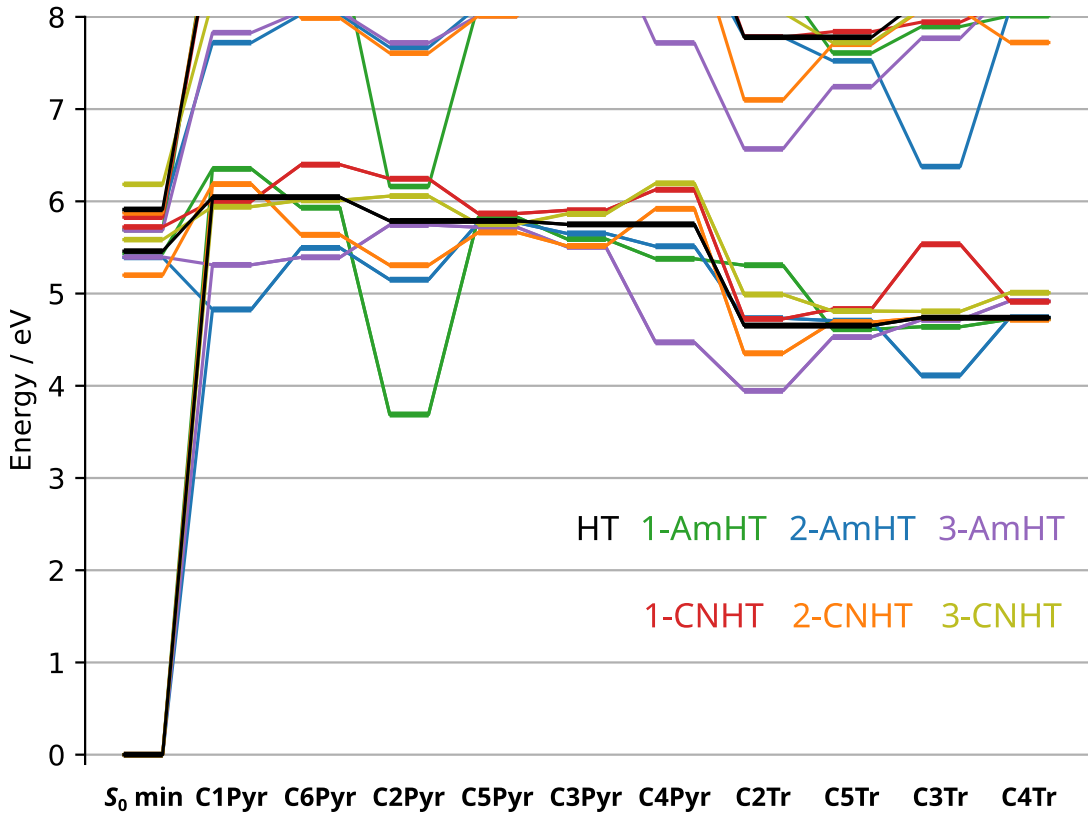

Figure E4: MR-CIS/6-31G* potential energies of HT (black), 1-AmHT (green), 2-AmHT (blue), 3-AmHT (purple), 1-CNHT (red), 2-CNHT (orange) and 3-CNHT (yellow).

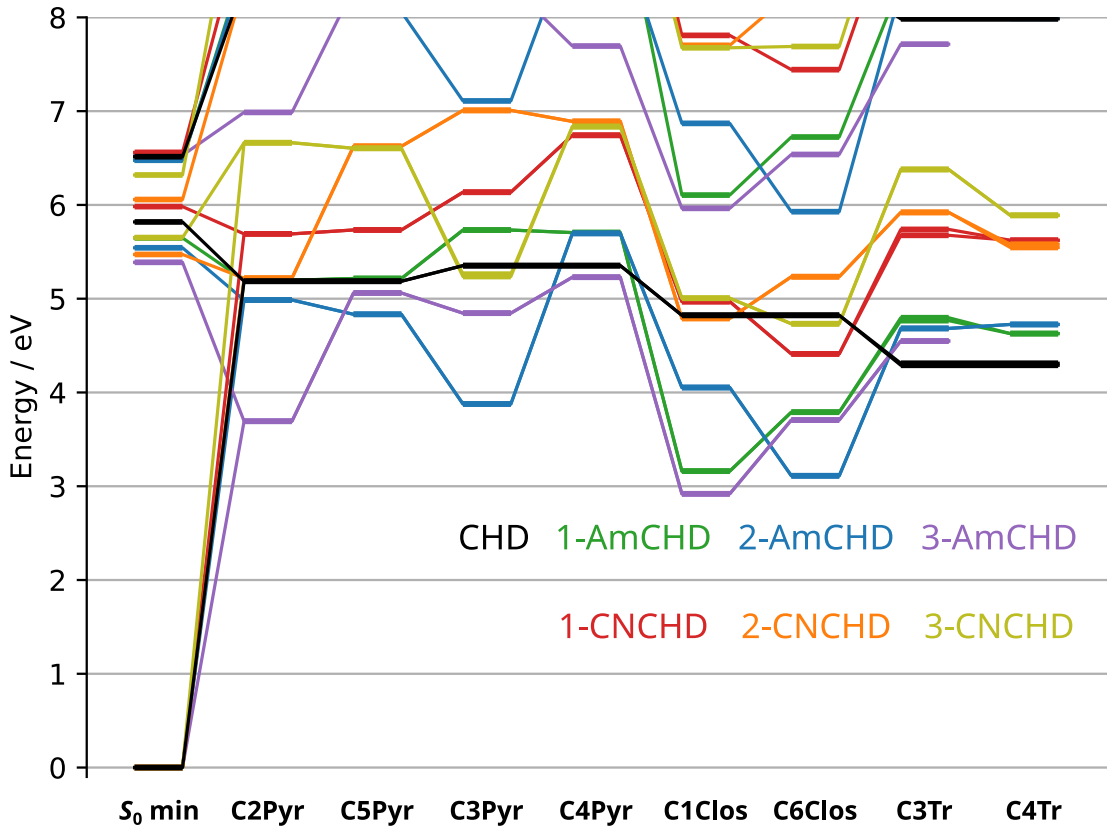

Figure E5: MR-CIS/6-31G* potential energies of CHD (black), 1-AmCHD (green), 2-AmCHD (blue), 3-AmCHD (purple), 1-CNCHD (red), 2-CNCHD (orange) and 3-CNCHD (yellow). Note that the **C4Tr** MECI of 3-AmCHD was not found.

E6 Polyene properties

Geometries, nonadiabatic coupling vectors, gradient difference vectors, charges and energies of optimized ground-state minima and MECIs are organized in a dataset on `https://github.com/ryjmacdonell/polyene-meci-dataset`.